

Université de Montréal

**The regulation and induction of clathrin-mediated endocytosis
through a protein aqueous-aqueous phase separation mechanism**

par

Louis-Philippe Bergeron-Sandoval

Département de biochimie et médecine moléculaire

Programme de Biochimie

Faculté de médecine

Université de Montréal

Thèse présentée à la Faculté des études supérieures
en vue de l'obtention du grade Philosophiae Doctor (Ph.D) en biochimie

Décembre 2016

© Louis-Philippe Bergeron-Sandoval, 2016

Sommaire

La morphologie des cellules et leurs interactions avec l'environnement découlent de divers procédés mécaniques qui contribuent à la richesse et à la diversité de la vie qui nous entoure. À titre d'exemple, les cellules mammifères se conforment à différentes géométries en fonction de l'architecture de leur cytosquelette tandis que les bactéries et les levures adoptent une forme circulaire par turgescence.

Je présente, dans cette thèse, la découverte d'un mécanisme de morphogénèse supplémentaire, soit la déformation de surface cellulaire via l'assemblage de protéines par démixture de phases aqueuses non miscibles et l'adhésion entre les matériaux biologiques. J'expose de façon spécifique comment ce mécanisme régule le recrutement et le mouvement dynamique des protéines qui induisent l'invagination de la membrane plasmique lors de l'endocytose clathrine-dépendante (CME).

Le phénomène de démixture des protéines dans le cytoplasme est analogue à la séparation de phase de l'huile en solution aqueuse. Il constitue un mécanisme cellulaire important et conservé, où les protéines s'agglomèrent grâce aux interactions intermoléculaires qui supplantent la tendance du système à former un mélange homogène.

Plusieurs exemples de compartiments cellulaires dépourvus de membrane se forment par démixture de phase, tels que le nucléole et les granules de traitement de l'ARN [1-6]. Ces organes ou compartiments dénommés NMO, du terme anglais « *non-membranous organelles* », occupent des fonctions de stockage, de traitement et de modification chimique des molécules dans la cellule. J'explore ici les questions suivantes : est-ce que les NMO occupent d'autres fonctions à caractère morphologique ? Quels signaux cellulaires régulent la démixture de phase des protéines dans la formation des NMO ?

Fondée sur la physique mécanique du contact entre les matériaux, j'é mets l'hypothèse que des compartiments cellulaires nanoscopiques, formés par démixture de phase, génèrent des forces mécaniques par adhésion interfaciale. Le travail mécanique ainsi obtenu déforme le milieu cellulaire et les surfaces membranaires adjacents au NMO nouvellement créé.

Le but de mon doctorat est de comprendre comment les cellules orchestrent, dans le temps et l'espace, la formation des NMO associés au CME et comment ceux-ci génèrent des forces mécaniques.

Mes travaux se concentrent sur les mécanismes de démixture de phase et d'adhésion de contact dans le processus d'endocytose chez la levure *Saccharomyces cerevisiae*. Pour enquêter sur le rôle des modifications post-traductionnelles dans ces mécanismes, nous avons premièrement analysé la cinétique de phosphorylation des protéines en conditions de stress. Mes résultats démontrent que le recrutement et la fonction de certaines protéines impliquées dans le CME se régulent via des mécanismes de phosphorylation.

Outre les processus de contrôle post-traductionnel, nous avons élucidé le rôle des domaines de faible complexité dans l'assemblage de plusieurs protéines associées avec le CME. De concert avec les modifications de phosphorylation, des domaines d'interaction protéine-protéine de type PrD (du terme « *prion-like domains* ») modulent directement le recrutement des protéines au sein des NMO associés au CME. La nature intrinsèquement désordonnée de ces PrD favorise un mécanisme d'assemblage des protéines par démixture de phase tel que postulé. Finalement, mes travaux confirment que la formation de ces NMO spécifiques génère des forces mécaniques qui déforment la membrane plasmique et assurent le processus de CME.

D'un point de vue fondamental, mes recherches permettent de mieux comprendre l'évolution d'une stratégie cellulaire pour assembler des compartiments cellulaires

sans membrane et pour fixer les dimensions biologiques associées au CME. De manière plus appliquée, cette étude a le potentiel de générer des retombées importantes dans la compréhension et le traitement de maladies neurodégénératives souvent associées à une séparation de phase aberrante et à la formation d'agrégats protéiques liés à la pathologie.

mots-clés

démixtion des protéines, séparation de phases aqueuses, organelles sans membrane, endocytose clathrine-dépendante, cinétique de phosphorylation, phosphosites fonctionnels, domaine PrD, adhésion de contact, biomécanique

Abstract

Evolution has resulted in distinct mechanical processes that determine the shapes of living cells and their interactions with each other and with the environment. These molecular mechanisms have contributed to the wide variety of life we observe today. For example, mammalian cells rely on a complex cytoskeleton to adapt specific shapes whereas bacteria, yeast and plants use a combination of turgor pressure and cell walls to have their characteristic bloated form.

In this dissertation, I describe my discovery of an unforeseen additional mechanism of morphogenesis: protein aqueous-aqueous phase separation and adhesive contact between biomaterials as a simple and efficient ways for cells to organize internal matter and accomplish work to shape internal structures and surfaces. I specifically describe how a fundamental process of phospholipid membrane and membrane-embedded protein recycling, clathrin-mediated endocytosis (CME), is driven by this mechanism.

Analogous to water and oil emulsions, proteins, and biopolymers in general, can phase separate from single to a binary aqueous phase. For proteins that de-mix from the bulk environment, the intermolecular interactions (or cohesive energy) that favors protein condensation only needs to overcome the low mixing entropy of the system and represents a conserved and energy efficient cellular strategy [2, 3, 7, 8].

So far, various examples of phase separated cellular compartments, termed non-membranous organelles (NMOs), have been discovered. These include the nucleoli, germ line P granules and P bodies, to name a few [1-6]. NMOs are involved in many conserved biological processes and can function as storage, bioreactor or signaling bodies. Cells use phase separation as a scheme to organize internal matter, but do NMOs occupy other complex functions, such as morphogenesis? What specific signals trigger protein phase separation?

Based on mechanical contact theory, I proposed that hundreds of nanometer- to micron-scale phase separated bodies can deform the cellular environment, both cytoplasm and membranes, through interfacial adhesion.

I studied how mechanical contact between a phase-separated protein fluid droplet and CME nucleation sites on membranes drive endocytosis in the model organism budding yeast, *Saccharomyces cerevisiae*. Specifically, this dissertation describes first, my investigations of post-translational modifications (phosphorylation) of several CME-mediating proteins and the implications of these modifications in regulating CME. I then describe how my efforts to understand what was distinct about the proteins that are phosphorylated led me to propose their phase separation into droplets capable of driving invagination and vesicle formation from plasma membrane.

I used fluorescence microscopy, mass spectrometry and micro rheology techniques to respectively determine the spatiotemporal dynamics, phosphorylation modifications and material properties of coalesced CME-mediating proteins. I further investigated how phase separation of these proteins might generate mechanical force.

I demonstrate that changes in the phosphorylation of some endocytic proteins regulates their recruitment to CME nucleation sites. We achieved reliable predictions of functional phosphosites by combining information on the conservation of the post-translational modifications with analysis of the proportion of a protein that is dynamically phosphorylated with time.

The same dynamically phosphorylated proteins were enriched for low amino acid compositional complexity “prion-like domains”, which we demonstrated were essential to these proteins undergoing aqueous-aqueous phase separation on CME nucleation sites. I then demonstrate how phase separated droplet can produce mechanical work to invaginate membranes and drive CME to completion.

In summary, I have discovered a fundamental molecular mechanism by which phase separated biopolymers and membranes could apply work to shape each other. This mechanism determines the natural selection of spatial scale and material properties of CME. Finally, I discuss broader implications of this dissertation to mechanistic understandings of the origins of neurodegenerative diseases, which likely involve pathological forms of protein phase separation and/or aggregation.

key words

phase separation, non-membranous organelles, clathrin-mediated endocytosis, dynamic phosphorylation, prion-like domains, protein function, adhesive contact

Table of contents

Sommaire	ii
<i>mots-clés</i>	iv
Abstract	v
<i>key words</i>	vii
List of figures	xi
List of tables	xiv
Abbreviations.....	xv
Acknowledgements.....	xviii
Dédicace	xxi
CHAPTER 1 Introduction	1
Chemical systems of life and their restrictions	1
<i>Evolutionary and physical constraints on molecular system function</i>	<i>2</i>
<i>Spatial organization of proteins: single chains to complex networks.....</i>	<i>3</i>
<i>Entropy in proteins: from chain conformation to complex systems</i>	<i>4</i>
Mechanisms and consequences of macromolecular phase separation.....	5
<i>What are the hallmarks of liquid-liquid phase separated protein droplets?</i>	<i>8</i>
<i>Amino acid sequence characteristics of droplet-forming proteins</i>	<i>8</i>
<i>Does biological matter transform into distinct coalesced states?</i>	<i>10</i>
<i>What is the nature of the interactions among molecules in a liquid droplet?.....</i>	<i>12</i>
<i>What do molecular interactomes mean in the context of liquid droplets?</i>	<i>19</i>
Investigate protein organization and function with mass spectrometry and micro rheology techniques	23
<i>Molecular system under study: clathrin-mediated endocytosis</i>	<i>24</i>
<i>Detection of protein phosphorylation by mass spectrometry</i>	<i>26</i>
<i>Optical Tweezers: an active microrheology technique to probe the material properties of biological systems</i>	<i>30</i>
Structure of this thesis	33
CHAPTER 2 A Cell Signaling Network Temporally Resolves Specific versus	
Promiscuous Phosphorylation	35
Authors contributions	36
Context of the research	36
Highlights	38
Summary	39
Introduction.....	41

Results.....	43
<i>Dynamic phosphoproteomics at sub-minute temporal resolution.....</i>	43
<i>Recapitulation of the canonical HOG pathway.....</i>	46
<i>Anticipatory Signaling downstream of the canonical HOG pathway.....</i>	48
<i>Global dynamic properties of the HOG signaling response.....</i>	50
<i>Dynamic phosphorylation suggests a dense kinase-phosphatase network.....</i>	54
<i>Dynamic phosphosites are more conserved than static phosphosites.....</i>	58
<i>Conserved phosphosites of pathway-specific proteins are functional.....</i>	59
<i>HOG modulates cytoskeletal and morphogenic pathways.....</i>	63
<i>Actin structures and microtubule mobility are regulated by HOG.....</i>	64
<i>Dynamic phosphoproteomic analysis provides functional insights into polarization.....</i>	66
Supplemental Results	72
<i>Identification of putative phosphosites that regulate actin structures and microtubules..</i>	72
Discussion	73
Extended Experimental Procedures	75
<i>Cell culture.....</i>	75
<i>Cell stimulations</i>	76
<i>Cell lysis</i>	76
<i>Protein extraction.....</i>	76
<i>Enzymatic digestion.....</i>	77
<i>Phosphopeptide isolation</i>	77
<i>Off-line fractionation of phosphopeptides.....</i>	78
<i>nanoLC- MS/MS.....</i>	79
<i>MS Data processing and analysis</i>	79
<i>Data quality filtering</i>	80
<i>Assessing significance of phosphosites</i>	81
<i>Fitting of dynamic profiles.....</i>	82
<i>Clustering of kinetic profiles, GO and PPI network analysis.....</i>	84
<i>Rates of evolution of phosphosites.....</i>	85
<i>Site-directed mutagenesis.....</i>	86
<i>Assessment of phospho-null mutant fitness through competition-growth</i>	87
<i>Fluorescent protein-tagged reporter strains</i>	88
<i>Microscopy</i>	89
Supplementary information.....	91
Acknowledgements.....	91
 CHAPTER 3 Endocytosis caused by liquid-liquid phase separation of proteins	
	92
Authors contributions.....	93
Context of the research	93
Summary	97
Introduction.....	98
Results and discussion	103
<i>PLD-containing CME proteins accumulate and phase separate at cortical sites</i>	103
<i>Cortical droplets can mechanically deform both cytosol and membrane</i>	110
<i>Cortical droplet binding to cytosol provides energy to drive membrane invagination....</i>	122
Materials and Methods.....	128

<i>Cell culture, gene manipulations and fluorescent reporters</i>	128
<i>Truncation and site-directed mutagenesis within ORFs</i>	128
<i>Diffraction-limited fluorescence microscopy</i>	129
<i>Fluorescent probes to quantify endocytosis or detect amyloid structures</i>	131
<i>Cell treatment with water-glycerol solutions, 1,6 hexanediol and latrunculin-A</i>	132
<i>Direct stochastic optical reconstruction microscopy (dSTORM)</i>	133
<i>Fluorescence recovery after photobleaching</i>	134
<i>Centroid tracking of Sla1 foci</i>	136
<i>Quantification of membrane in nascent vesicles under HD titration</i>	136
<i>Effect of 1,6-hexanediol (HD) titration on droplet stability</i>	137
<i>Polystyrene beads and Dextran-FITC osmoporation</i>	139
<i>Optical tweezers measurements and calibration</i>	140
<i>Dimensions and geometry of membrane contour and cortical droplets</i>	142
<i>Calculation of the energies that counteract membrane invagination</i>	143
<i>Cortical droplet material properties and contact angle</i>	146
<i>Theoretical model based on elastic and adhesive contact mechanics</i>	148
Supplementary information	161
Acknowledgments	161
CHAPTER 4 Discussion	162
<i>Detection of functional phosphosites on CME-mediating proteins</i>	162
<i>Are heat shock proteins required to regulate phase separation of cortical droplet?</i>	163
<i>Aberrant phase separation of endocytic proteins in neurodegenerative pathologies?</i>	164
<i>Implications of cortical droplets in regulation and function of CME</i>	164
<i>Evolution of phase separated NMOs and specific length scales</i>	166
APPENDIX 1 Mechanisms and consequences of macromolecular phase separation	168
Summary	169
Introduction	169
<i>What are the hallmarks of liquid-liquid phase separated protein droplets?</i>	171
<i>Amino acid sequence characteristics of droplet-forming proteins</i>	172
<i>Does biological matter transform into distinct coalesced states?</i>	174
<i>What is the nature of the interactions among molecules in a liquid droplet?</i>	176
<i>What do molecular interactomes mean in the context of liquid droplets?</i>	181
<i>Are droplets (and other alternative organizations of matter) important?</i>	185
Conclusions	189
Acknowledgements	189
APPENDIX 2	191
Supplemental Movies	191
Supplemental Files	191
Supplemental Tables	192
BIBLIOGRAPHY	202

List of figures

Figure 1 Protein interactomes contain more disorder than ordered protein complexes.	6
Figure 2 Molecular structures and interactions in distinct solvent regimes.	15
Figure 3 A liquid droplet view of protein and protein-nucleic acid interactomes.....	20
Figure 4 Graphical abstract	40
Figure 5 The origins of complexity in signaling networks	42
Figure 6 Summary of phosphopeptide identification	45
Figure 7 Dynamic phosphorylation within the canonical HOG pathway	47
Figure 8 Regulation of the aquaglyceroporin Fps1 in response to changes in extracellular osmolarity	49
Figure 9 Kinetic analysis of signaling response.....	51
Figure 10 Analysis of dynamic phosphorylation profiles.....	53
Figure 11 Temporal complexity of the kinase-phosphatase network and relationships with dynamic substrates.....	55
Figure 12 Combinatorial explosion of signal complexity and kinase predictions for phosphosites	57
Figure 13 Dynamic phosphosites of the HOG responses are globally more conserved than static phosphosites and conserved phosphosites affect cell fitness.	60
Figure 14 Fitness of phospho-null mutants was assessed by competition-growth under high salt and non-stressed conditions.....	62
Figure 15 Dynamic phosphosite proteins are enriched for both main HOG and complementary responses.	65
Figure 16 GO enrichment analysis for differentially regulated phosphoproteins following osmotic shock.	67

Figure 17 Syp1 dynamic phosphosites are involved in regulation of morphogenesis.	69
Figure 18 Characterization of OE Syp1 and S347, S405 mutant strains.	71
Figure 19 Adaptor-coat endocytic proteins predicted to be intrinsically disordered and behave as globules in poor solvent regime.....	94
Figure 20 Assembly of proteins into a cortical droplet drive clathrin-mediated endocytosis.	99
Figure 21 Syp1 protein is the only BAR domain protein recruited to CME nucleation sites prior to F-actin polymerization and is not required for CME.	101
Figure 22 <i>GPD1Δ</i> cells cannot maintain turgor.	102
Figure 23 Membrane-associated probe (FM4-64) uptake.....	103
Figure 24 Geometry of coat protein distribution at cortical sites with super-resolution (dSTORM) fluorescence imaging of Alexa647-labeled Sla1-GFP.	104
Figure 25 CME adaptor and coat proteins phase separate to form droplets.....	105
Figure 26 Cortical patch-associated PLD-containing proteins fail to form puncta in cells treated with 1,6-hexanediol (HD)	107
Figure 27 Pulse-chase experiments with HD show that HD-dependent dissolution of Sla1 puncta is reversible.	107
Figure 28 We observed no colocalization of Thioflavin T (ThT) to Sla1-mCherry puncta.	109
Figure 29 Mutations of PLDs that prevent phase separation of proteins also disrupt CME.	110
Figure 30 Cytosol and cortical droplets are composed of a viscoelastic amorphous network of interacting proteins	113
Figure 31 Osmoporation of polystyrene beads and micro-rheology.....	115
Figure 32 We measured displacement of expressed viral capsid microNS particles labeled with GFP in both untreated and osmoporated cells.....	116
Figure 33 Dynamic mechanical analysis of cytosol with optical tweezers.....	117
Figure 34 Centroid tracking within a confocal volume of Sla1-GFP foci in <i>GPD1Δ</i> mutant strains treated with LatA.....	119

Figure 35 Colocalization of different sized dextran-FITC revealed that cortical droplets exclude objects of diameters > 5.8 nm.....	120
Figure 36 Fluorescence recovery after photobleaching (FRAP) of dextran within cortical droplets or cytosol regions of interest.	121
Figure 37 Cortical droplets do mechanical work to deform the membrane and cytosol	123
Figure 38 Cortical droplets apply mechanical stress that deform the membrane...	124

List of tables

Table 1 Definition of terms related to protein phase separation	190
Table 2 Temporal profiles of 5453 phosphopeptides on 1656 proteins.....	192
Table 3 We identified 596 dynamic phosphopeptides from 332 proteins	192
Table 4 MaxQuant “parameters.txt” and “experimentalDesign.txt” files	192
Table 5 Yeast strains and mutagenic primer pairs to generate all phosphosite mutants used in Chapter 2	193
Table 6 Terminology. Chapter 2.	196
Table 7 Table S1. Chapter 3. strains used in this study	197
Table 8 Table S2. Chapter 3. parameters and variables used in our theoretical framework were either measured in this study or obtained from the literature .	199
Table 9 Table S3. Chapter 3. Constants and equations used in the elasto-adhesion model for the deformation of the membrane by protein droplets on cortical sites	200
Table 10 Table S4. Chapter 3. Summary of the indentations and energies predicted with our elasto-adhesive contact model	201

Abbreviations

+TIP	plus end tracking protein
ARG4	argininosuccinate lyase
BAR	Bin, Amphisin, Rvs
CCV	clathrin-coated vesicles
CE	cation exchange
CID	collision-induced
CK2	casein kinase 2
CME	clathrin-mediated endocytosis
COP	coat protein
CTDs	C-terminal domains
D motif	MAPK-docking site
D-domain	MAPK docking region
DLC	dimensional liquid chromatography
DNA	deoxy ribonucleic acid
dSTORM	direct stochastic optical reconstruction microscopy
E	Young's modulus
EM	electron microscopy
ESI	electrospray ionization
FC	fold change
FDR	false discovery rate
FM4-64	N-3-Triethylammoniumpropyl-4-6-4-Diethylamino Phenyl Hexatrienyl Pyridinium Dibromide
fps	frames per second
FRAP	fluorescence recovery after photobleaching
G'	storage modulus
G''	loss modulus
G*	complex modulus
GFP	green fluorescent protein
GO	gene ontology
GUVs	giant unilamellar vesicles
HD	1,6-hexanediol
HOG	high osmolarity glycerol
HT	1,2,3-hexanetriol
IDP	intrinsically disordered proteins
JKR	Johnson-Kendall-Roberts (theory)
LatA	latrunculin A

LC	liquid chromatography
LCDs	Low complexity domains
LFM	low fluorescence medium
LLPS	liquid-liquid phase separation
LTQ	linear ion trap
LY	lucifer yellow
LYS1	saccharopine dehydrogenase
m/z	mass-to-charge ratio
MIND	Mtw1 including Nnf1/Nsl1 and Dsn1
MS	mass spectrometry
MSD	mean square displacements
NA	numerical aperture
NASA	National Aeronautics and Space Agency
NLS	nuclear localization sequence
NMOs	non-membranous organelles
OD	optical density
OE	over expressed
ORF	open reading frame
OT	optical tweezer
PAKA	basophilic PKA and PAK kinases
PBS	phosphate buffered saline
PCR	polymerase chain reaction
PhD	Philosophiae Doctor
PM	plasma membrane
PML	promyelocytic leukemia
PPI	protein-protein interactions
PrDs	Prion-like domains
PRM	proline rich motifs
PSD	position-sensitive detector
PTMs	post translational modifications
RNA	ribonucleic acid
ROI	region of interest
SCX	strong cation exchange
SD	synthetic dextrose
SI	Supplementary Information
SILAC	sable isotope labeling with amino acids in cell culture
TCA	trichloroacetic acid
ThT	thioflavin T

TR	Tandem repeat
WASP	Wiscott-Aldrich Syndrome Protein
YFP	yellow fluorescent protein
YKO	yeast knock-out

Acknowledgements

First, I express my sincere gratitude to my supervisor Steve for being a great mentor. Your support and guidance made this thesis possible. You encouraged me to think outside the box and to investigate fascinating questions on life's organization and function. Thank you for allowing me to work on topics I am passionate about and for all your personal and professional advice.

I also want to thank all the Michnick lab members that encouraged and helped me to complete this work. Special thanks to Jacqueline and Jean-Francois who made all my research possible. I have shared great moments in the lab with all the past members (Vincent, Poe Hien, Arturo, Luz, Emmanuelle, Emmanuel, Eugene, Abdellali, Lara) and present members (Diala, Sinan, Bram, Lidice, Shelly, Konstantin). I wish to all success in your research, career and personal life. I also want to express my gratitude to Mohan for his support and friendship, you really encouraged me to complete this thesis.

Many professors from all the universities in Montréal (Jackie V, Daniel Z, Pierre T, Allen E, Adam H, François O) gave me advice and shared ideas that improved my thesis, I am thankful for all the collegial discussions, the warm weather workshops and the advice that helped me complete my doctoral studies. Special thanks to Allen who kindly reviewed sections of this thesis.

Finally, I want to acknowledge the jury members of this thesis for the time and work invested in the evaluation. Thank you all.

Remerciements

Écrire ces remerciements est un exercice réconfortant. Je me considère choyer d'avoir un support et un amour inconditionnel de ma famille et mes amis. Merci à tous et voici, sans ordre particulier, un petit mot pour chacun(e);

Premièrement, merci Rosamaria et François de m'avoir donné passion, ouverture d'esprit, ambition et surtout un amour inconditionnel. Avec une vision plus mature de la vie, je réalise chaque jour la chance de vous avoir comme parents. Je vous aime.

Valérie ma splendide femme, tu me permets d'être heureux, de me sentir encourager, supporter et aimer. Je souhaite pouvoir partager avec toi une vie remplie de bonheur. Merci pour ton amour et ton support dans la réalisation de mes projets et mes rêves. Cette thèse est aussi possible grâce à toi. Je t'aime.

Karl-Frederik, tu m'as inspiré à poursuivre cette veine de recherche. Merci de toujours être là pour moi. Cédrik, tu es un petit frère magnifique, si possible ne suit pas tes frères en sciences biologiques ! il faut tout de même une diversité au sein de la fratrie.

Sylvie ma marâtre adorée, tu es un noyau essentiel de notre famille, merci pour tout ton amour, ton support et tes encouragements dans la réalisation de cette thèse.

Gilles tu as toujours été plus grand que nature pour moi. Chaque jour j'applique quelque chose que tu m'as enseigné. J'ai en moi des souvenirs indélébiles. Je t'aime mon grand-père. Jeanne, merci de m'avoir adopté, j'ai pour toi tout l'amour d'un petit-fils pour sa grand-mère.

Aleck ma chère cousine, on a partagé tant de bon moment, j'espère en partager encore de nombreux avec toi et notre belle grande famille. Je t'aime. Je pense aussi à tous mes cousins(es), tantes et oncles, vous êtes trop nombreux pour ses courtes lignes. Merci de former une famille parfois dysfonctionnelle mais tellement aimante, je ne changerai rien dans tout cela. Je t'inclus aussi Claudia dans ce groupe de personnes qui m'ont influencé de façon tellement positive. Un clin d'œil aussi à Éric, merci pour les petites corrections.

Mes amis de toujours (Jean-Philippe B, Vincent, Guillaume F, Guillaume P, Marco, Jean-Philippe H, Julien) vous avez été là avec moi dans mes meilleurs et mes mauvais moments, merci pour tout le support et encouragements. Cette thèse est aussi possible grâce à vous !

Je remercie aussi tous les membres du département de Biochimie et des laboratoires de recherche (Sylvie B, Elaine M, Luc D, Monique M, Pascal R) pour leur aide dans la réalisation de ma thèse.

Agradecimientos

Rosita y Carlos mis abuelos tan lejos. Cada abrazo de despedida, le doy como si sea por última vez. Ojalá nos abracemos de nuevo. Sepan que tengo tantos recuerdos con ustedes, aquí en Montreal o allá en Chile. Su fuerza y convicción crillaron una grande familia. Estoy orgulloso tener los como abuelos.

En el mismo tiempo agradezco a todos mis tíos, tías, primos y primas en Chile. Gracias por el cariño y el apoyo. Somos una familia junta que no hay otra cosa más linda. Le echo de menos y nos vemos pronto en Santiago como siempre. Le quiero mucho à todos.

Dédicace

À Régine, tu me manques tellement

“Podrán cortar todas las flores, pero no podrán detener la primavera.”

– Pablo Neruda

CHAPTER 1 | Introduction

Those who study life have yet no consensus on the concept of life itself [9-11]. Biologists, philosophers and theologians have argued over this topic for centuries. Some regard the cell as the material basis of life whereas others consider organic compounds as the basic units that comprise living organisms.

To push the boundaries of an Earth-centric theory of life, the National Aeronautics and Space Agency (NASA) assembled in 1994 a committee who proposed that life is a “self-sustaining chemical system capable of Darwinian evolution” [11]. I personally like this view. Although not perfect, this concept of life contains ideas, put forward by Carl Sagan and many dedicated scientists, that satisfies most requirements of the living entities that we know; from animals, to plants, to single cell bacteria or yeast, to viruses. At the molecular level, the notions of “chemical system” and “Darwinian evolution” are central to this conceptual framework, these ideas are also important to this dissertation, as highlighted below.

Chemical systems of life and their restrictions

Jacques Monod emphasized that living systems arise from interactions among molecules [12]. In other words, that no single molecule has the property of life. Life manifests itself through complex hierarchical structures that display diverse shapes, kinetics, functions, properties and interrelations with their surroundings. The chemistry behind live systems on Earth is relatively simple. If distilled to basic building blocks, the matter found in such systems is composed of water and four types of macromolecules: proteins, nucleic acids, lipids and polysaccharides [13]. The detailed chemistry of these macromolecules is beyond the scope of this dissertation and can be found in various textbooks [13]. It is the interactions among these basic

macromolecules that defines living systems; their behaviours in response to perturbations, chemical or physical, their different functions, material properties and the storage or transfer of information required to generate life. My thesis is about the interaction and assembly of macromolecules – of a group of disordered proteins in particular – and their vital mechanical function within cells.

Evolutionary and physical constraints on molecular system function

This ability to store and transmit hereditary information through a molecular genetic mechanism is a crucial process of life. Through such a mechanism, organisms acquired morphologies from an ancestral template. This simple idea, coined by Charles Darwin as “evolution”, stated that species have the potential to adapt to their environment through natural selection [14]. Individuals with favorable traits for survival in that environment are selected to the detriment of others.

Molecules that self-organize can emerge to have specific biological functions, analogous to a machine built from spare parts. Molecular “function” is a broad concept, because beyond multimolecule systems, it also encompasses the work (or tasks) performed by single molecules. For example, one protein can modify the chemistry of another molecule through a so-called enzymatic reaction. The protein in this case acts as an enzyme that catalyzes a chemical reaction on another molecule (DNA, RNA, protein or lipid), which physically interacts with the enzyme itself. One such process, protein phosphorylation, and its impact on protein function is further detailed in the phosphoproteomic section below and explored in Chapter 2.

Living things are defined by evolution and the natural selection that underlies these processes, and constrained by the physics and chemistry underlying their compositions. For example, often cited as essential to understanding the morphogenesis of living things, D’Arcy Thompson pioneered a mechanical view of the living world and considered that physical properties of living matter, such as surface

tension and elasticity, constrain biological structures, perhaps even more so than natural selection for specific physical traits [15]. In short, there are physical and mechanical limits to biological length scales and shapes. Physical constraints owing to the chemical properties and composition of biopolymers may also determine how they assemble, come in contact and influence the shapes of each other.

Spatial organization of proteins: single chains to complex networks

In this thesis, I focus on questions about proteins: how do they self-organize with each other, modify each other and perform specific functions.

Protein chemistry relies on monomeric amino acids subunits that assemble into polymeric chains. Through the folding process, each protein adopts a conformation that can confer to them specific functions. Proteins have structures as diverse as the tasks they carry out in cells [13]. Protein functions include: cell structural support, biochemical reactions catalysis, chemical signal propagation (transmission) and molecular transport (or storage) to name a few. The biological properties, interactors and function of proteins are determined by the physical interactions made with other molecules. Proteins can interact (or bind) through non-covalent bonds and favourable hydrophobic interactions to specific ions, small molecules and/or macromolecules, called ligand.

For most protein-based macromolecular complexes, shape and chemical complementarity between proteins determines affinity and specificity of binary protein-protein interactions (PPI) and is thus sensitive to conformational changes in the protein structure, as discussed in the next section. Conversely, many proteins assemble into complex-less PPI networks without any fixed stoichiometric ratio, stereospecific interactions or clear architecture. Possible molecular mechanisms that drive the formation of such protein bodies – a major theme of this dissertation – are also further detailed below.

Entropy in proteins: from chain conformation to complex systems

From single biopolymer to complexes with thousands of chains, protein structures are very dynamic and probe a wide space of conformations. These structures obey the laws of thermodynamics and based on the second law of thermodynamics, Rudolf Clausius formulated the concept of entropy, a major contribution to understand the physics behind the behaviour of biological systems [16].

In short, particles require energy to change state and organize themselves and entropy describes the tendency of matter towards the most probable state. It's important to emphasize that entropy is not a measure of disorder, but of the probability of the system to adopt a specific state [17]. If energy is more distributed in a certain state, that state is more probable.

As stochastic arrangements of proteins are more probable, such random states or structure would have larger entropy. Arrangement constraints that restrict the possible structures, of either single protein chains or complex protein networks, would thus have an entropic cost. For example, assembly of rigid protein polymers into a regular latticework has lower entropy and requires more energy to form, than a wool ball structure made of floppy and entangled polymers. Conformation flexibility also affects affinity and specificity of protein interactions [18].

Entropy is thus a major force in the arrangements of protein chains and assembly of protein bodies, as described Flory-Huggins solution theory [7, 19].

Mechanisms and consequences of macromolecular phase separation

Louis-Philippe Bergeron-Sandoval, Nozhat Safaee and Stephen W. Michnick

Note : this introductory section is part of a Perspective that was published in the journal Cell, the integral version is produced in Appendix 1.

What does the apparent lack of order in protein interactomes (Figure 1) tell us about how proteins usually behave? We have argued that many, perhaps more than fifty percent of protein-protein interactions are “noise”. By noise, we mean protein-protein interactions that serve no discernable function [20-24]. This kind of noise may also arise in protein-RNA and protein-DNA interactions [21]. Although a large proportion of protein-protein interactions may be noise, non-complex patterns of interactions that we see in protein-protein interaction networks could also represent other kinds of order created by interactions among proteins, RNA, DNA and membrane surfaces.

Over a century ago, Edmund Wilson summarized a body of work on how the protoplasm of cells appeared to be composed of phase-separated mixtures of distinct globular objects [25, 26]. What precisely accounted for these observations remained a mystery until just recently. Evidence has now emerged for alternative organizations of matter in cells that could explain some of the transient, complex-less interactions observed in protein-protein interaction networks. Notable among this body of work are the observations that proteins and protein-nucleic acid mixtures can undergo liquid-liquid phase separation (LLPS) to form liquid droplets or what have been called, “non-membranous organelles” (NMOs) [1, 27-32]. Pioneering efforts of Cliff Brangwynne, Tony Hyman and Michael Rosen established that these bodies behave like liquids and presented examples of their biological functions.

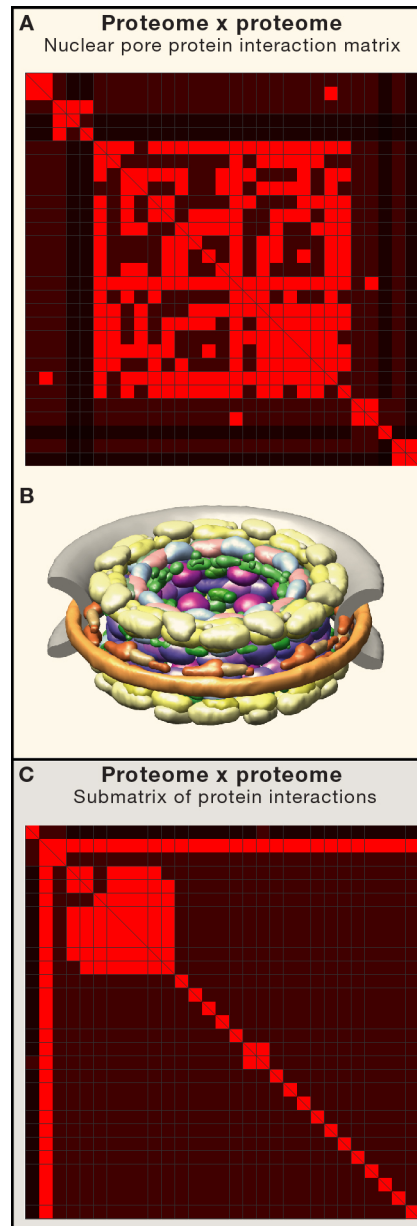


Figure 1 | Protein interactomes contain more disorder than ordered protein complexes.

(A) Clustered protein-protein interactions among the yeast *Saccharomyces cerevisiae* proteins that are subunits of the nuclear pore complex. The protein-protein interactions were retrieved from Biogrid and organized into a binary association matrix. A hierarchical agglomerative average linkage clustering with the uncentered

correlation coefficient as the distance matrix was then applied to this association matrix and the interaction were visualized with the iVici software (<http://michnick.bcm.umontreal.ca/ivici/>) [33]. (B) Architecture of the ordered assembly of the nuclear pore complex determined from biophysical and proteomic data [34]. (C) Another submatrix of the yeast protein-protein interaction network does not show multiple intersubunit protein-protein interactions that would be expected of a multiprotein complex. DSN1, a component of the MIND kineticores complex, makes a number of binary interactions; however, most make no other interactions with each other.

What we now know about liquid droplets has been extensively reviewed and it is not our intention here to cover the state of the field in detail [8, 19, 25, 27, 35-37]. Our goal with this Perspective is to focus on basic observations about the functions of and molecular mechanisms of formation of liquid droplets, and to reflect on outstanding questions that arise from recognition of their existence, including: What are the hallmarks and the distinct properties of proteins that undergo LLPS? What is the nature of the interactions among molecules that form a liquid droplet and other molecules that encounter or enter these bodies? What do molecular interactomes mean in the context of liquid droplets? Is phase separation an important and extensive form of organized matter in the cell? As our understanding of this form of organization of matter develops, the challenge then becomes figuring out how many distinct droplets exist, how they could mediate biochemical processes and (perhaps optimistically) how they may explain molecular mechanism that to date, have remained mysteries.

What are the hallmarks of liquid-liquid phase separated protein droplets?

A number of mesoscale bodies (hundreds of nanometers to micrometers), particularly in the nucleus have been described as non-membranous organelles, including nucleoli, nuclear Speckles, Cajal bodies and Promyelocytic leukemia (PML) bodies [2, 27]. More recently, these and other cellular structures have been demonstrated to behave as liquid droplets, including a number of RNA-protein assemblies such as Germline P granules, processing (P)-bodies and stress granules, as well as DNA-protein complexes such as centrosomes, mitotic spindles, and signaling and actin polymerization complex activation bodies [1, 4-6, 30, 38-41]. Across this broad swath of biology, three basic principles underlie all of these membrane-less organelles. They arise from a phase separation of proteins or proteins and nucleic acids from the surrounding milieu. They remain in a liquid state but with properties distinct from those of the surrounding matter and importantly, proteins exchange with these bodies in seconds instead of minutes, hours or longer, as occurs for subunits of stable complexes [1, 25, 28-32, 42]. Are there any common characteristics of proteins or nucleic acids that are found to form liquid droplets? As we describe next, the characteristics of amino acid sequences of droplet-forming proteins are remarkably simple.

Amino acid sequence characteristics of droplet-forming proteins

The catalog (to date) of proteins that phase separate into droplets is enriched for those having low complexity amino acid composition domains (LCD) including tandem repeats (TR) of individual amino acids or amino acid motifs, such as polyglutamine (polyQ) and polyasparagine (polyN) tracts [43]. These LCD-containing proteins belong to the general class of intrinsically disordered proteins (IDP)s that make up about a third of eukaryotic proteome peptide sequence [44-46]. We have calculated that there are over 800 such proteins in the yeast *S. cerevisiae* proteome.

One class of droplet-forming proteins have TRs contained within LCDs called prion domains (PrD) [47-61]. PrD proteins have been implicated as epigenetic agents, coding for inheritable protein complexes caused by a PrD-driven conformational change in the protein itself or other PrD-containing proteins [49, 54, 55, 62]. PrD-containing proteins have been demonstrated to underlie the molecular basis of long-term memory in eukaryotes from budding yeast to fruit flies, snails and mice [50, 54, 58, 63-68]. TR length variation has also been implicated in neutral or beneficial variations, for example in cell surface adhesion and transcription factor activities in yeast and canine skull morphology [69-71]. By contrast, mutants of PrD-containing proteins have been implicated in a number of neuro- and neuromuscular-degenerate diseases through formation of insoluble amyloid fibrils [72-76]. For example expansion of the polyQ TRs in huntingtin protein contributes to Huntington's disease. A number of other devastating inherited or acquired neurodegenerative disorders such as myotonic dystrophy and Parkinsonism may be developed through similar mechanisms [77].

We are only beginning to understand what the few known droplets do and which biochemical and physical processes drive their formation. Since proteins with LCDs represent ~30% of the eukaryotic proteome [78] and a large number of these proteins are putative droplet components, we speculate that many unique liquid droplets could exist. Microscopists have long observed numerous cellular punctate structures, revealed in fluorescence microscopy of proteins fused to fluorescent proteins. What proportion of these correspond to liquid droplets of some stripe?

Proteins containing multiple folded binding domains (to mediate interactions with other peptides or nucleic acids) separated by low complexity linkers are also proposed to phase-separate into liquid droplets. Looking at a network of the proteins Nephrin, Nck and the Wiscott-Aldrich protein (WASP) N-terminal domain, studies describe evidence, *in vivo* and *in vitro*, for tyrosine phosphorylation of the membrane-associated Nephrin as creating linear docking sites for the binding of an SH2 domain

in Nck, which in turn, organizes its three SH3 domains in space [3, 30, 38]. These reorganized SH3 domains then bind to complementary peptide motifs in N-WASP. The multivalency of these interactions generates a protein-protein interaction network as a phase-separated droplet. This phase separation was shown to induce F-actin polymerization in the presence of Arp2/3 [38]. Recently, the adaptor protein Grb2, which contains two SH3 domains, was shown to be essential to liquid phase separation of an intermediate module of T cell receptor signaling [79]. Both SH3 domains of Grb2 were necessary for phase separation. The implications from the organization of these proteins to the mechanism of phase separation are discussed below.

Does biological matter transform into distinct coalesced states?

Having considered some basic definitions for liquid droplets and the patterns of protein sequences that support their formation, it's important to bring in a more general view on phase separation that is useful for considering proteins and other biological molecules in various states of matter. Phase transitions are not uncommon. Matter can transit between many states, from gas to solid, as a function of temperature, pressure and concentration; for example, sublimation of snow to vapor on a sunny winter day.

Similarly, simple organic molecules can undergo phase transitions under the right conditions. For example, Brian Shoichet has described asymmetric aromatic compounds that are soluble in aqueous solution, but that phase-separate into liquid droplets in a concentration- and temperature-dependent manner [80]. Interestingly, the change in state of the small molecule can be used to influence biomolecules. Among these, one series of compounds was shown to spontaneously form extended amyloid-like solid fibrils that could act as scaffolds for caspases, leading to the activation of their self-cleavage; the key step in their full activation. Interestingly, beta-

amyloid peptides were shown to bind similarly to these caspases [81]. Another remarkable example is a biotinylated isoxazole molecule reported by Steven McKnight's group, which upon exposure to cell lysates concentrates RNA binding proteins into ordered arrangements. They went on to show that the LCD-containing RNA binding protein, FUS, also formed solid hydrogels that could concentrate RNAs [82, 83].

It's important to keep in mind that, liquid-liquid and liquid-solid phase separations of proteins are not unheard of nor are they specific to the LCD-containing proteins. Any stably folded, single domain protein could phase separate into a liquid droplet under the right conditions. For instance, the art of protein crystallization involves placing proteins under a number of different conditions, such as various concentrations of certain salts, buffers, detergents and crowding agents (e.g. polyethylene glycols or polyanionic polymers of different lengths). Screened under these different conditions, proteins can be driven to undergo a number of phase transitions to liquid droplets, solid precipitates, and either directly or through one of these states (if you are lucky) to ordered crystals [84]. What makes LCD-containing proteins special is that they can undergo liquid-liquid phase separation more readily, either self-coalescing at critical pH or salt concentrations, or upon binding to nucleic acids or other proteins. As we discuss later, post-translational modifications of LCD-containing proteins have also been shown to induce phase separation into liquid droplets.

Liquid droplets are not the only state that LCD-containing proteins can take on. The most well-known and extensively studied forms are amyloid fibrils. Recent *in vitro* studies show a slow transition of LCD-containing proteins from weakly associated to fibrillar arrangements, and the evolution of this process may be accelerated, *in vivo*, in the naturally occurring mutant variants of these proteins, some of which are known to be pathogenic [6, 39, 42, 85]. However, we do not know if fibrillar arrangements of LCD proteins exist *in vivo* under normal conditions. We do know that homogeneous preparations of liquid droplets *in vitro*, made of individual LCD-containing proteins,

start out as dispersed, weakly associated molecules that exchange with surrounding solutions rapidly, some of which gradually transit to a fibrillar state in which individual monomers no longer exchange rapidly with the surroundings [6, 42, 85]. Could this happen *in vivo*? We do know that protein-RNA assemblies can have a range of liquid to solid states depending on their compositions [86]. A key difference between the *in vitro* and *in vivo* settings centers on the complexity of the available protein population. It is possible that the transition of cellular liquid droplets, such as P-bodies, into fibrillar states is prevented because of their heterogeneous composition. Cellular droplets are mixtures of interacting proteins or proteins and nucleic acids. In such mixtures, competing heterogeneous interactions among the different types of molecules may somehow frustrate the formation of higher-ordered fibrillar states. The cell protein quality control machinery is also proposed to help preserve the liquid or solid states of protein and protein-RNA assemblies. For example, recent work on budding yeast showed that the action of Hsp104 disaggregase is required to maintain liquid-like P-bodies, or that the cellular disaggregation activity is needed to dissolve functional stress granule aggregates [4].

What is the nature of the interactions among molecules in a liquid droplet?

What is it about low complexity sequences that make them susceptible to forming a continuum of states? How do the various liquid droplets keep their individual compositions in the cellular milieu? Do proteins within droplets further separate into sub-phases? Very little is known and there is no all-encompassing theory for how liquid droplets form or how they have evolved. There are, however, some compelling theories, intuition and specific cases that can serve as starting points to understand liquid-liquid phase transitions of proteins.

Theories of beta-amyloid fibril formation have either explicitly or implicitly implied formation of a liquid-liquid phase separated intermediate [87]. The general idea is that

a more disordered and dynamic intermediate is needed for formation of a structured and static aggregate. A model for amyloid formation by the protein huntingtin, the pathological agent in the neurodegenerative Huntington's disease, explicitly invokes a transient coiled-coil intermediate, formed from a variable-length glutamine tract. The length of this polyQ tract determines the tendency for huntingtin to form pathological beta-amyloid structures [73-75, 88, 89]. This model has also contributed to a general model of fibrillar structural transitions of polyN/polyQ TR proteins [90]. Although a liquid-liquid phase transition, is not specifically invoked, it has inspired explanations for their potential occurrence. For instance in a recent study of the partial reconstitution of the P-body, the authors propose that the LCDs contain sequence motifs which undergo spontaneous coil to helix transitions, allowing them to serve as nucleation sites for formation of a network of intermolecular coiled-coils at a critical concentration [91]. The authors showed that disruption of helix-forming sequences could prevent formation of liquid droplets. Valency, the number of repeated or distinct binding domains or amino acid motifs in proteins can also be important to liquid-liquid phase separation. For example, phase separation SH3 domain-prolyl peptide interactions between Nck and N-WASP described above depend on the number of repeats of SH3 domains or SH3 domain binding motifs [30]. In analogy to this case, Fromm, et al. argue that phase separation depends on the number of possible intermolecular coiled-coils that the P-body proteins they studied could make [91].

The multivalent domain interaction network model described above is compelling because it explains liquid-liquid phase transitions in terms of structure and chemical complementarity [92]. It is, however, a model that is based on a limited number of examples, studied under non-physiological conditions and that cannot explain other aspects of droplet formation such as charge distribution dependencies, the fact that droplets will form from LCD-containing proteins that show no propensity or evidence of forming structured domains or are driven by simple post-translational modifications. More general theories that could account for and predict liquid droplet formations of LCD-containing proteins are needed.

Rohit Pappu has adapted a general theory to explain amyloid fibril formation from first principles of polymer theory that can also serve as a working theory for liquid-liquid phase separation of proteins [7]. In this model, IDPs with specific sequence properties do not take on extended conformations in a dilute solution, but rather, are collapsed into a compact globular form. The sequence property central to this theory is the existence of a specific length scale to intra and inter-segmental peptide interactions of 7 to 10 amino acids. These segments, referred to as “blobs”, constitute the length scale beyond which the balance of chain-chain, chain-solvent and solvent-solvent interactions is at least of the order of the thermal energy of the blob [93]. Under conditions where chain-solvent interactions are favorable (a so called “good solvent”) or above a critical temperature, the interactions between blobs are net repulsive and the chain will swell to maximize interactions of the blobs with solvent, but under the opposite conditions (in a “poor” solvent or below the critical temperature), the polypeptide chain collapses into a globular form (Figure 2A). Vitalis *et al.* have shown that this model is consistent with scattering and spectroscopic data as well as molecular dynamic simulations [94-97].

The key to understanding liquid-liquid phase transition of a peptide is the notion that when the peptide reaches a critical concentration, the intermolecular blob interactions are more attractive than the intramolecular interactions and peptide-solvent interactions, and the peptides demix from the surrounding milieu into a liquid droplet. In the liquid droplet, the peptide expands because now it can make favorable intermolecular blob interactions (Figure 2B). In a sense, the peptide is now acting as its own good solvent. The concentration of the peptides in the droplet could also influence the blob variables, including the length and volume fraction as a function of inter-chain contact distance. As the peptide volume fraction decreases, the peptide chain is predicted to undergo conformation changes from expanded globules to form flexible rods and then rigid-rod structures (Figure 2C) [98]. The rigid-rod structures could coalesce into fibrillar states of the proteins noted to occur over time in droplets *in vitro* [6, 39, 42, 85].

It is notable that this theory requires no structural transformations and blob interactions do not have to be shape complementary [25, 99]. Shape-complementary interactions can, however, also occur in liquid droplet. It is notable that the length scale of blobs is the same as that of typical secondary structure elements in folded proteins and in this theory, folded domains can be thought of as blobs themselves and phase separate with stereospecific or shape complementary interactions (Figure 2D) [30].

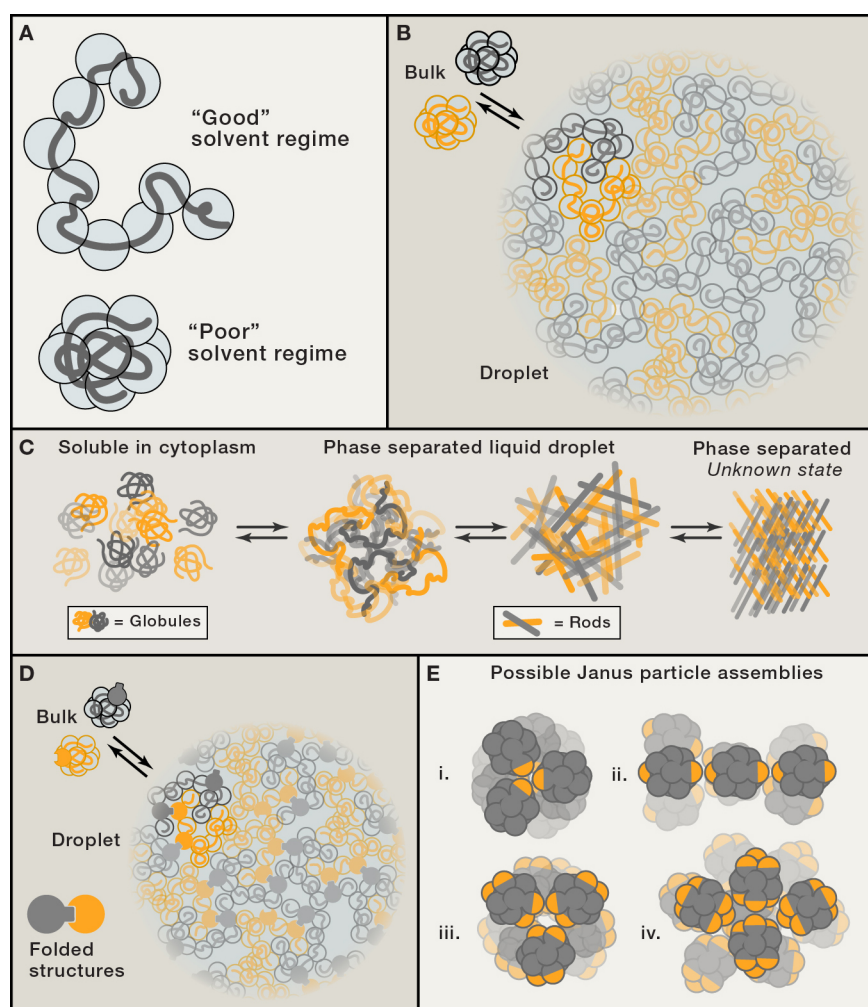


Figure 2 | Molecular structures and interactions in distinct solvent regimes.

(A) Intrinsically disordered proteins (IDPs) in dilute solution take on expanded (top) or compact globular (bottom) conformations depending on whether they are in a good or poor solvent for an individual protein. Compactness of the polypeptide chain depends

on solvent conditions and characteristics and patterns of amino acid distribution, notably of charged residues (Adapted from Pappu, *et al.* [7]). Circled peptide segments of about 7 to 10 residues are called “blobs”, segments over which the net balances of all interactions are less than or equal to thermal energy. Interactions between blobs or between blobs and solvent determine how expanded or compact the polypeptide is. (B) At critical concentrations of a protein or under specific conditions, proteins phase separate when intermolecular blob interactions overcome the intramolecular blob and blob-solvent interactions. (C) Unified theory of blob length scale in peptide solution predicts that the peptide volume fraction decreases when the phase separated peptide concentration increases. In this model, the peptide chain is predicted to undergo distinct changes from collapsed globule, to expanded globule, to flexible-rod-like and to rigid-rod-like structures. This model could account for the distinct coalesced states of proteins that result in transition from liquid droplet to fibrous aggregates. (D) Blobs can also be folded structural domains and make stereospecific and shape-complementary interactions with themselves or other proteins. (E) Proteins can have two segments with distinct properties (Janus particles) and these may interact and phase-separate in different ways and under different conditions. Different configurations can result in heterogeneous arrangements of phase-separated proteins in a liquid droplet (see Figure 3).

Patterns of amino acids in blobs may also be critical to inter- and intra-blob interactions. Furthermore, this model indirectly distinguishes between IDPs with regard to their ability to form liquid droplets. For example, as discussed below, the pattern and number of charged amino acids, lengths of TRs and presence of peptide backbone-constraining amino acids in an IDP can have a profound impact on blob interactions and their tendency to phase separate [100]. Finally, like multi-domain folded proteins, it is quite conceivable that a single polypeptide chain could form multi-globule arrangements (Figure 2E). These globules may have different properties under different conditions. Some of these conditions may lead to certain

arrangements, polarizations or interactions with other macromolecules that result in phase separation of the associated molecules into a droplet with two or more sub-compartments, or some other extended periodic arrangement [101]. In the simplest case, an entire polypeptide may collapse into a single globule, but we can also picture different regions of a protein collectively forming different interactions with itself, the rest of the protein sequence and the solvent. Such, so called “Janus” particles could, for example, be more hydrophobic in one region and more polar in another [100]. These particles are of interest in the soft matter material sciences because many interesting configurations of matter can theoretically be generated from different arrangements of the substructure of Janus particles (Figure 2E) [101]. They are interesting to us because, as discussed below, sub-compartmentalization within the droplets can occur and the possibility that they are generated from Janus protein surfaces has important functional implications [27].

Understanding the behaviors of IDPs in general, requires suspending commonly held notions of classifications of amino acids into subcategories of charged or polar “hydrophilic” and apolar aliphatic or aromatic “hydrophobic” amino acids. These notions work for most purposes in understanding, for instance, how amino acids are arranged with respect to the solvent in folded proteins or at protein-protein or protein-nucleic acid interfaces, but they fail when trying to understand the behaviors of IDPs, particularly those with LCDs. For instance, the archetypical polyQ TR-containing protein, huntingtin, forms fibrils *via* collapsing into beta-hairpins, driven by intramolecular backbone and side-chain hydrogen bonds, disrupting interactions with water. Thermodynamically, this process looks like the hydrophobic collapse of a folded protein and yet the amino acids involved are thought of as polar, hydrophilic amino acids. Thus, in the context of a tandem repeat, glutamine or asparagine prefer to interact more with themselves than with water and can therefore be viewed to behave hydrophobically. Equally paradoxical, a domain C-terminal to the polyQ tract of huntingtin that contains a preponderance of what is commonly thought to be a hydrophobic amino acid, proline, actually prevents huntingtin from collapsing into

fibrils, favoring interactions with the solvent and therefore behaving as hydrophilic agents [88]. The prolines have not magically changed chemical properties, they are as hydrophilic as other polar amino acids such as Gln and Asn. However, the barrier to cis-trans isomerization of prolyl peptides disfavors the collapse of peptide into a globule, a necessary intermediate state to fibril formation and resulting in the peptide remaining soluble. Future understanding of patterns of amino acids and the properties that favor phase separation will require empirical studies, searches for heuristic rules and ultimately, theoretical models, such as has been applied to predicting prion-forming domains or to tuning the temperature-dependent phase transition of elastin proteins [47, 102].

IDPs tend to be enriched in charged amino acids compared to folded proteins [100]. This observation might seem explainable as an obvious evolutionary adaption to these proteins being unfolded and thus requiring as many polar amino acids be exposed to solvent as possible. Though intuitively reasonable, such an argument contradicts the theory described above and evidence that IDPs can exist as compact globules, obviating the need for an enrichment of polar or charged amino acids. What could be interesting and important to the way that these proteins behave is the arrangement of charged amino acids within a protein. Again, based on first principles of polymer theory, it has been proposed that the compactness of a polypeptide will vary with the linear polarization of oppositely charged amino acids. This leads to some interesting predictions, notably that a full range of oppositely charged residues creates a phase diagram of states, in which sharply defined regions of compactness, from completely swelled to compact globules and Janus-like objects in between, can exist [100]. Secondly, given that the phase diagram predicts sharp transitions between states, one can imagine that subtle changes in charge could switch a polypeptide from one state to another. An obvious way this could be achieved is through post-translational modifications. Phosphorylation of serine, threonine and tyrosine, methylation of arginine and methylation and acetylation of lysine, among the most common of these, result in the addition of negative or reduction of positive

charge. For example, precedence for phosphorylation- or methylation-dependent liquid droplet formation has been reported [103, 104].

Formation of Nephrin-Nck-N-WASP liquid droplets described above depends on an intrinsically unstructured linker peptide between the first two SH3 domains of Nck. The linker amino acid sequence has a polarized distribution of oppositely charged amino acids with a highly conserved positively charged sequence motif at the N-terminus of the linker and negatively charged residues at the C-terminus [3]. The authors showed that this motif interacts weakly with the negatively charged second SH3 domain, but may also interact with a negative motif at the C-terminal end of the linker. These results illustrate the essentiality of charge and the notion of both regions, an intrinsically disordered motif and the folded SH3 domains as blobs, whose interactions with each other are essential to phase separation.

What do molecular interactomes mean in the context of liquid droplets?

We can now put together the principles discussed above to describe how liquid droplet interactomes are distinct from what we usually think of as protein interactomes (Figure 3A). The difference and its importance to understanding liquid phase separation in cellular biology was eloquently captured by Daniel Needleman, who wrote in a recent essay about the material nature of life that, “individual molecules of water are not wet and the individual molecules that compose glass are not brittle, the wetness of water and the brittleness of glass are collective phenomena that arise from the interactions of billions of molecules” [105].

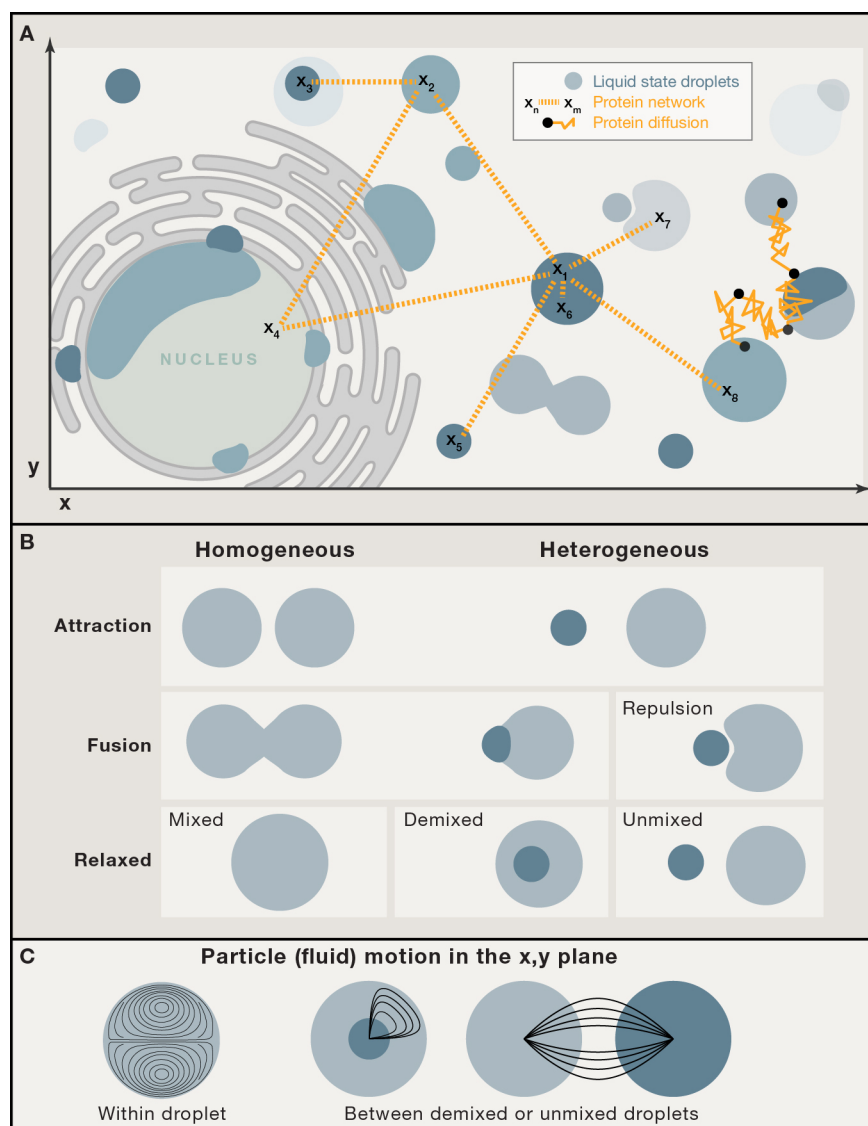


Figure 3 | A liquid droplet view of protein and protein-nucleic acid interactomes

(A) Liquid droplets of different sizes and properties may repel or attract one another, depending on the chemical properties of their interfaces and their distances from each other. Individual molecules that compose droplets can diffuse and exchange readily (black dots and gold lines) and interact with molecules in the surrounding milieu or within other droplets (black letters and dashed gold lines). In addition, droplets wet surfaces such as membranes, creating sites of high concentrations of molecules that could be involved in transport or signaling processes. (B) Attraction and/or repulsion of droplets with each other can result in mixed, demixed or unmixed

droplets, depending on the properties of each droplet. Large complexes such as ribosomes or F-actin networks may also be repelled from droplet surfaces. (C) The flow of molecules between or within droplets could partition distinct chemical reactions and generate different types of biochemical dynamics.

A first key distinction between droplets and other types of protein organization is that the macromolecules that compose a liquid droplet can exchange rapidly with the surrounding cyto-, or organelle plasms. Proteins associated with the droplets are highly dynamic, diffusing into, out of and within the droplets rapidly. There could be some drag on proteins leaving the non-membranous bodies due to the intermolecular interactions within the droplet, which may be among the steady-state conditions for maintenance of the droplet. Nonetheless, the observed exchange rates between bulk solution (reflecting the cytoplasm or other subcellular compartment milieu) and droplets have been measured to be in the range of seconds to tens of seconds [1, 30]. Exchange rates of proteins and nucleic acids determine the droplet size and could be scaled with the cellular concentration of the proteins and size of the cell [37, 106]. Thus, compared to complexes of folded proteins, the compositions of liquid droplets are transient and can dictate rapidly formation or disintegration upon slight changes in local concentrations and chemical states of components, or physical or chemical composition of the environment.

Second, the most profound difference between simple molecular interactions and those of droplets is that collective properties of these objects can result in both attractive and repulsive interactions between droplets or between droplets and other objects (Figure 3B). Depending on the physical characteristics of a droplet, it may fuse and mix with components of other droplets, demix as a result, for example, of a change in a subdroplets surface properties, or unmix, that is repel another encountered droplet. The materials within the droplet phase separate from the surroundings because the net interactions they make among each other is more

favorable than those with the surrounding milieu. Molecules at the interface are, thus, not as likely to form favorable interactions as those in the interior of the droplet. Consequently the droplet curvature will increase to minimize contact surface area with its surroundings, as a water droplet does with air. For individual small molecules, proteins and RNAs, interfacial tension of a droplet is not a barrier to their entry into the droplet, provided that they are small enough to slip between intermolecular spaces and either make favorable interactions or do not interact with the molecules composing the droplet. We speculate that contact with large complexes (e.g. ribosomes), however, causes distortion of the droplet surface increasing its surface area and therefore the interfacial tension between the droplet and its milieu [27]. One can think of the droplet as behaving like a porous balloon, in which small objects can enter while larger objects can distort the surface but cannot enter the droplet. The exclusion of large particles creates regions in the bulk that are free of such large and unfavorably interacting molecules, so-called exclusion zones. Evidence so far for such exclusion zones created by liquid droplets in cells is limited but compelling. For instance, electron micrographs of sections of P-bodies show that otherwise widespread ribosomes are excluded from the P-bodies [107]. Feric *et al.* recently demonstrated that the large nucleoli of *Xenopus* oocytes are suspended in the nucleoplasm within a network of branched actin [108]. Interestingly though, they did not see actin persistently present within the nucleoli themselves, suggesting that these dense networks of protein fibers could form extended rough surfaces that cannot penetrate the nucleoli droplets. Finally, in *C. elegans* embryos, perinuclear germ line P granules work as size-exclusion barriers that exclude dextran molecules of 70-kD and above, but are permeable to dextran molecules of 40-kD and smaller [109]. The barrier properties of these perinuclear P granules are proposed, through interacting with the Phe/Gly-rich regions, to be coupled to and could extend the nuclear pore complex.

Water and its interactions with components of a droplet, at its interior or interface, is an important factor contributing to the droplet's properties, including viscosity and

interfacial tension [110]. For example, if molecules interact more favorably with the constituents of the droplet than they do with those of the surrounding milieu, they will be drawn into the droplet, creating a sort of liquid-vapor interface. Depending on the vapor pressure at such interfaces, one droplet could repel or attract another [111, 112]. This may be one way that droplets with different compositions and functions have evolved to remain separate. One could easily imagine attractive or repulsive interactions of droplets with other structures in the cell, for example membranes and chromatin, which may serve to shape or organize these structures. We could further speculate that liquid droplets might generate force or act as a liquid couple between force-generating machines like actin filaments to distort or organize matter as part of cellular processes. We know, for instance, that liquid droplets associate with sites of damaged DNA or transcriptionally active regions and may serve essential roles in organizing chromatin, either directly or, in the case of transcriptionally active sites, through interactions with RNA [42, 43, 70, 113, 114]. It remains to be determined precisely how the droplets are organized and whether they are essential to forcing the arrangements of matter in active regions or sequestering certain molecules in a regulatory manner.

Investigate protein organization and function with mass spectrometry and micro rheology techniques

Within the paradigm of NMOs, we asked ourselves: Can protein phase separation play other basic functions besides compartmentalization of molecules and biochemical reactions [115]?

We thus began to explore the biomechanical properties of phase-separated proteins, in particular the production of energy needed to bend and shape phospholipid membranes. We hypothesized that hundreds of nanometer- to micron-scale aqueous-

aqueous phase separated viscoelastic bodies can deform the cellular environment, such as the membrane, through adhesive action.

To understand how NMOs could produce mechanical stresses, it is important to consider the material properties of both NMOs and the cellular environment. While the viscosity of NMOs has been investigated [19, 116], the elastic properties of phase separated bodies remains unexplored *in vivo*.

To test our hypothesis, we thus investigated the regulation, phase separation and function of PrD proteins that drive clathrin-mediated endocytosis (CME) in budding yeast. We summarize below; the CME process, the phosphoproteomic approach we utilized to detect functional phosphorylation events on CME proteins (detailed in Chapter 2) and the micro rheological technique we used to probe the cell material properties and deduce NMO elastic properties (detailed in Chapter 3).

Molecular system under study: clathrin-mediated endocytosis

The following is a brief summary of CME in *S. cerevisiae*. To avoid redundancy, further details of CME are highlighted in Chapters 2 and 3, respectively.

CME is a highly conserved and essential cellular process by which cells absorb or engulf extracellular and phospholipid bilayer-embedded material. CME has diverse biological functions in cell homeostasis and signaling [117]. These include: entry of nutrients, internalization of hormone-bound receptors on the plasma membrane; regulation of surface protein expression; synaptic vesicle recycling in neurons and can serve as an entry route for toxins or pathogens [118, 119].

Current electron microscopic (EM) evidence helped to elaborate a spatial model of endocytosis [120, 121]. Where a defined clathrin-coated plasma membrane surface can invaginate when it is surrounded by a complex protein network of ~200 nm diameter. Maturation of single clathrin-coated vesicles (CCV) occurs within 2 to 3

minutes in a coordinated cycle that begins with the slow emergence of a shallow membrane invagination (~25 nm), which is followed by a fast phase in the final 10 seconds of the process, in which actin polymerization drives deep membrane invagination (>100 nm) before vesicle scission [122]. Observations of the contour of membrane invaginations show that constriction to form a vesicle occurs when invaginations of about 70 nm or more are attained [120].

CME is initiated by various adaptor proteins such as Syp1 F-BAR protein, Ede1 (homolog of mammalian Eps15), Apl1, Pal1 and Yap 1801/2 (homologs of AP180) that bind to membrane lipids or membrane-associated proteins to form CME nucleation (cortical) sites [123, 124]. Clathrin heavy and light chains (Chc1 and Clc1) then interact with the adaptor proteins and assemble into a lattice on the membrane plane. Clathrin itself doesn't directly bind to the membrane or induce curvature [122, 125]. Subsequent early coat proteins such as epsins (Ent1, Ent2), Hip1R-related protein (Sla2) and CIN85/Intersectin1-related protein (Sla1) directly bind to the adaptor-clathrin lattice and form a complex protein network that extends around the cortical site. These in turn interact with late CME proteins involved in actin polymerization (Abp1, Bbc1, etc). Under normal conditions, the burst of F-actin polymerization at cortical sites is correlated with rapid invagination of the membrane and vesicle excision [126].

The presence of PrDs in CME-mediating adaptor and coat proteins – namely Sla1, Sla2, Ent1, Ent2, Pan1, Scd5, Yap1801 and Yap1802 – is a clue that these proteins may undergo phase separation (PPS) to form a droplet because other known aqueous-aqueous phase separated NMOs are composed of such PrD-containing proteins [47]. Furthermore, the presence of multiple SH3 domains in some of some of these proteins, such as Sla1 and other proteins involved in the F-actin polymerization phase of CME also suggests the existence of multivalent interactions that could drive protein phase separation as has been proposed for analogous F-actin assembly nucleation sites in animal cells [30]. These sequence characteristics are explored in

chapter 3 along with evidence that some of these proteins phase separate to form liquid droplets at CME cortical sites. It was these observations that led to the central hypothesis

In terms of energy, yeast differ from mammalian cells because they have a higher energy barrier to endocytosis [127, 128]. Contrary to their mammalian counterpart, yeast cells overcome both the membrane bending rigidity and the turgor pressure that pushes against the membrane. To alleviate this increased energy requirement, yeast cells have evolved to consistently use F-actin polymerization to bend the membrane on cortical sites [128, 129]. The observation that F-actin requirement is mitigated when turgor is relieved in both budding and fission yeast is of major interest because the mechanism that enables CME to proceed in absence of turgor and F-actin remains elusive [129, 130]. We report in Chapter 3 the details of a mechanical model to explain how phase separation of CME PrD-containing proteins produce work to ingaginate the membrane through adhesive contact.

Detection of protein phosphorylation by mass spectrometry

The regulation of CME is driven, in part by changes in the phosphorylation of a number of proteins, by protein kinases. This was demonstrated by systematically knocking down the expression of each of the 590 human kinase one-by-one by RNAi and monitoring the performance of endocytic routes [131]. The identities, however, of the proteins and specific phosphosites that are implicated in kinase regulation remain unknown, with the exception of a few. In yeast a few regulatory phosphosites have been identified, for example on the Eps15-like protein Pan1 [132, 133].

I present in Chapter 2, how we monitored real-time differential phosphorylation across the proteome during the onset of the High Osmolarity Glycerol (HOG) pathway and successfully identified functional phosphosites on CME-mediating proteins. Below is a

summary of the key mass spectrometry (MS) methodology used in these studies to facilitate understanding.

MS is a tool of choice for large-scale identification and quantitation of phosphorylation sites in proteins from a wide range of biological samples [134]. Modern MS devices consist of an ion source, a mass analyzer and a detector that measure the mass-to-charge ratio of ionized peptides and can detect chemical modifications on protein fragments [135]. The ionizer converts digested protein samples into distinct ions, where each peptide chemical species is converted into an ion with distinct properties, specifically mass-to-charge ratio (m/z).

So-called electrospray ionization (ESI), is a technique used to continuously produce ions from macromolecules in solution [136]. In the general peptide ionization mechanism of ESI, the sample is vacuum flowed into a heated capillary with a large potential differential between the ends (about 3000 V) that disperses the liquid sample into a fine aerosol. The water-based solvent of the sample travelling through the capillary, quickly evaporates to favor the formations of small liquid droplets. Droplets travelling in the capillary get smaller and eventually lose all their water (or solvent) content to form gas-phase ions. ESI prevents further fragmentation of digested protein samples and thus preserves the integrity of the peptides [136].

The ions are then accelerated and directed towards the mass analyzer and detectors of the MS device. The ionized particles moving in the device can be redirected towards different mass and charge analyzers (or detectors) with magnetic or electrostatic fields [135]. One state of the art ion analysis method, named Orbitrap, consist of injecting a group (or packet) of ionized peptides between an outer an inner barrel shaped electrode and sending the ions into a circular orbit around the inner electrode. The ions thus get trapped on complex elliptical trajectories around the central electrode [137].

A multitude of ionized peptides are sent into orbit in the Orbitrap after each injection, and these ions move and oscillate with different rotational frequencies along the inner electrode based on their mass-to-charge ratio (m/z). These m/z specific ion movements are simultaneously detected by sensors around the orbit [137]. The sensors record, for a specific period of time, the image charge induced by ions ring trajectories on the outer barrel electrode. The raw data obtained is then processed with a Fourier transform to generate mass spectra of the ions in the trap. The process is repeated either in tandem and/or for a subsequent group of ions until all of the sample is processed [135].

Prior to injection of ion packets, the Orbitrap analyzer can be interfaced to a linear ion trap (LTQ) that can efficiently store the ions and inject groups of ions in the Orbitrap when needed. LTQ technology relies on a set of quadrupole rods to confine the ions (both axially and radially) along the trap axis. LTQs are used for both ion storage and ion mass filtering [137].

To detect amino acid composition and chemical modifications of peptides, a group of precursor ions can be processed in tandem by the Orbitrap analyzer in MS/MS mode. Between the two MS detections the ions are further fragmented to obtain mass spectra of single amino acids [137]. Addition of distinct chemical groups on single amino acids can thus be measured because they alter the molecule m/z . To induce fragmentation, precursor ions are transferred from the Orbitrap analyzer into a collision-induced dissociation (CID) cell where ions are accelerated by an electrical potential and collide with neutral gas particles. Peptide bonds are broken in this collision cycle resulting in molecular ion fragmentation [135]. After the CID the fragment ions are returned into the orbitrap analyzer for mass analysis and collection of fragment spectra.

Finally, to restrict the amount and diversity of ions to process by MS, the digested peptides are loaded into the mass spectrometer in small subsets according to their physical properties by liquid chromatography (LC) on, for example cation exchange

(CE) resins. Specifically, the CE-LC separation technique uses negatively charged ion exchange resins with affinity for peptides with net positive surface charge. The peptides are then unbound from the resin with a gradient of salt concentration. The elution step separates the peptides based on their net charge, low surface charge peptides elute first from the column and go through the MS whereas high charge peptides elute last.

Peptides are identified from mass spectra with identification algorithms, such as Mascot or Andromeda [138]. These algorithms search a comprehensive database with all the amino acid sequences assumed to be present in an analyzed sample, based on predicted protease (e.g. trypsin) cleavage sites for the protease(s) used to digest the proteins in the sample. The search database is built from genomic data and creates an organism-specific list of theoretical peptide fragments along with their reverse counterparts, which accounts for peptide fragmentation from both ends. With this approach, peptide and fragment masses from MS/MS spectra are matched to a protein with a probability-based score.

Quantification of peptides and proteins observed within a sample is generally based on precursor signal intensity or spectral counting. MaxQuant, a specialized software that quantifies signal intensity from Orbitrap data, detects peptide specific peaks in each MS scan and measures the total intensity of these peaks (or hills) in the m/z -retention time three-dimensional space [139]. MS intensity profiles over sample retention time are divided into multiple 3D peaks, each one corresponding to a specific peptide, and information on the mass of single peaks is obtained through intensity integration [139].

Changes in protein PTMs occur in many cellular context and differences in PTMs can be detected by MS when cells are treated with some perturbation and compared to cells in a control condition. A reliable technique to detect difference in modified phosphoprotein abundance among samples is St_{able} Isotope Labeling with Amino acids in Cell culture (SILAC) [140]. SILAC consists of growing one sample of cells in a

medium containing amino acids composed of natural abundance isotopes (e.g. $^{12}\text{C}/^{14}\text{N}$) and a second cell sample is grown in amino acids labeled with stable heavy isotopes, such as ^{13}C - and/or ^{15}N -labeled arginine and/or lysine. For example, in cells lacking enzymes for the synthesis of these amino acids, the ^{12}C or ^{13}C - forms will be incorporated into all newly synthesized proteins. In addition, one of the samples is treated with the perturbing condition, while the other serves as a control. The ^{12}C and ^{13}C -labeled cell cultures are then combined. Proteins preparation and digestion by trypsin, which recognizes and hydrolyzes peptide bonds adjacent to arginine or lysine residues, ensures each peptide contains a labeled amino acid. Steps may then be taken to enrich for particular PTMs, such as binding and elution of peptides from TiO_4 resin, which binds to phosphopeptides, and resulting peptides are analyzed by LC-MS to obtain the abundance ratio of chemically identical peptide pairs, distinguished by a shift of the m/z of the light versus heavy isotopic versions of a peptide [141]. Although SILAC-MS is a powerful analytical tool – able to identify, quantify and compare thousands of peptides and proteins within combined samples – it is important to note that MS is not a comprehensive detection method and is blind to many peptides within the sample due to chemical composition or sample complexity.

Optical Tweezers: an active microrheology technique to probe the material properties of biological systems

A group of proteins that assemble into a large cellular body, or even a wide variety of proteins confined into a restricted cellular volume, constitutes matter with specific mechanical properties. Protein bodies are generally found to behave like viscoelastic materials [142-145]. This means that they exhibit both viscous and elastic behavior when they are forced to undergo deformation. We can deduce these properties by studying their flow and deformation under applied force, with rheological techniques.

Optical tweezers (OTs) technology is a cutting-edge active microrheology method to probe the material properties of live cells. This technique uses a focused laser to hold and oscillate beads embedded within cells and observe how the cellular matter is deformed under the applied force. Here is a summary of the theory and equipment setup used for optical tweezers (*aka* optical trap) experiments.

Arthur Ashkin was first to detect optical scattering and gradient forces on micron sized particles [146]. He observed that particles, with a refractive index higher than the surrounding medium, can be displaced by a simple light beam. The particle-trapping phenomenon can be explained by either ray optics or Rayleigh scattering, and depends on the particle size.

In the ray optics regime, if a particles dimensions are much larger than the wavelength of light, the light rays which enter and exit a transparent bead are refracted and change direction. This change in direction indicates a change in light momentum, accompanied by an equal and opposite momentum change on the particle itself. Through this mechanism light imparts net momentum change (or force) on particles [147]. The Gaussian intensity profile of lasers used in optical tweezers setups imparts more momentum at the center of the beam; particles exposed to such light profiles experience a gradient force in the spatial direction of the light intensity gradient- i.e. an off-centered particle moves laterally towards the beam center because the high intensity light at the center confers more net momentum than on the beam edges. If a particle is at the center of the beam it experiences no net lateral forces because the light rays are refracted symmetrically through the particle.

Photons that scatter on a dielectric particle can also transfer momentum in the direction of light propagation, this would result in movement of the particle away from the laser source. To overcome this scattering effect, optical tweezers systems tightly focus the laser beam into a diffraction-limited spot in the focal plane with a high numerical aperture (NA) objective [147]. The hourglass shape of the beam then creates an axial light intensity gradient which pulls the particle in this focal region with

a force that exceeds the scattering effect. On an inverted microscope setup, the balance between these gradient and scattering forces spatially traps particles in a region a bit above (away from source) the laser focal point.

Forced oscillations with optical tweezers of nanometer-sized probe particles embedded within cells can inform on the mechanical properties of biomaterials surrounding the probe particles. By oscillating the embedded particles with a known force from the optical tweezers, and tracking the time-dependent displacement, we can calculate the viscoelastic properties of the cytoplasm. First, it is essential to know the forces applied by the optical tweezers; the optical force applied to the trapped particle, usually in the piconewton range, is approximated by Hooke's law, under the assumption that the trap acts like a linear spring [148]. Effective calibration and measurement of optical force applied by the optical tweezers requires that the trap stiffness and trap force of the laser beam be determined [149]. Calibrated measurements of the optical force can be deduced from the power spectrum of bead position, which also reflects the random forces of thermal fluctuations. This calibration method uses a global fit to the particle response to forced sinusoidal oscillation, or passive response at rest. The high frequency portion of the power spectra reflects thermal motion fluctuations, whereas low frequency fluctuations of the power spectra result from optical force, active biolmechanical processes (e.g. actin polymerization) and mechanical vibrations of the microscope setup [149]. The optical trap stiffness can be calculated from the roll-off frequency and hydrodynamic drag coefficient extracted from a Lorentzian function fit to the power spectrum [150].

The particle displacements and phase shift under a forced sinusoidal laser movement can be measured with specialized optics onto a position-sensitive photodiode. The so called complex modulus (G^*) can then be obtained from a Fourier transform of the time traces of particle displacement at different frequencies and can be mathematically decomposed into the storage modulus (G'), which is related to the elasticity of a material and the loss modulus (G''), which relates to a material's

viscosity [151]. The amplitudes, slopes, minima and maxima of G' and G'' and ratio G''/G' , both as a function of frequency of forced oscillations, reveal rich details of the physical properties and arrangements and interactions among the molecules that compose an object. It is important to consider that OTs data reflects the bulk properties of the cellular matter in contact with the oscillated particle, and the effects of specific structures touching or bound to the bead cannot be uncoupled. Rigorous OTs calibration is also crucial to obtain reliable moduli magnitudes, and requires careful consideration.

Structure of this thesis

This dissertation is divided into 4 chapters; in the introductory Chapter 1, I covered our current view and ideas on the molecular mechanisms behind phase separation of NMOs, this was published in the journal *Cell* in 2016. The full version of this Perspective is found in Appendix 1.

In Chapter 2, I present the work we did on signaling networks to distinguish specific versus promiscuous phosphorylation of proteins in response to a specific stress: salt-induced osmotic shock. We achieved reliable predictions and we identified phosphosites that regulate CME-mediating proteins by combining information about the conservation of the post-translational modifications with analysis of the proportion of a protein that is dynamically phosphorylated with time. This work was published in the journal *Cell Reports* in 2015 and highlights functional phosphorylation sites on disordered proteins that mediate CME and their assembly on cortical sites.

In Chapter 3, I present evidence to support a fundamental and unforeseen mechanism by which phase separation of CME-mediating proteins can generate work and shape membranes. We demonstrate that this mechanism can drive CME to completion in specific cellular context. This manuscript is currently in preparation and will soon be submitted to a top tier journal.

I conclude my thesis with Chapter 4, where I synthesize the novel concept that I helped uncover in the context of my doctoral studies and propose future research avenues in these exciting fields.

CHAPTER 2 | A Cell Signaling Network Temporally Resolves Specific *versus* Promiscuous Phosphorylation

AUTHORS & AFFILIATIONS

Evgeny Kanshin^{1,4,*}, Louis-Philippe Bergeron-Sandoval^{1,*}, S. Sinan Isik¹, Pierre Thibault^{1, 2, 4} and Stephen W. Michnick^{1,3}

***These authors contributed equally to this work**

¹Département de Biochimie, Université de Montréal, C.P. 6128, Succursale centre-ville, Montréal, Québec, H3C 3J7, Canada.

²Département de Chimie, Université de Montréal, C.P. 6128, Succursale centre-ville, Montréal, Québec, H3C 3J7, Canada.

³Centre Robert-Cedergren, Bio-Informatique et Génomique, Université de Montréal, C.P. 6128, Succursale centre-ville, Montréal, Québec, H3C 3J7, Canada.

⁴Institute for Research in Immunology and Cancer, Université de Montréal, C.P. 6128, Succursale centre-ville, Montréal, Québec, H3C 3J7, Canada.

CONTACT

Correspondence should be addressed to S.W.M. or P.T.
(stephen.michnick@umontreal.ca or pierre.thibault@umontreal.ca).

Authors contributions

For this publication, I participated in the research conceptual design, phosphoproteomic sample collection, biological experiments (microscopy and competition assays) and data analysis. EK participated in all aspects of the conceptual design, phosphoproteomic experiments and data analysis. Specifically, EK, LPBS, PT and SWM designed research; EK and LPBS contributed equally to this work and performed research; EK, LPBS, SSI, PT and SWM analyzed data; EK, LPBS, PT and SWM wrote the paper.

Context of the research

Protein assembly and function is regulated in response to specific cues and cells have evolved the means to respond to and interpret external signals. Genetic and physical interaction studies and mass-spectroscopic analysis of phosphoproteomes suggest that kinases and phosphatases in signaling networks are highly connected and often perform redundant functions. Despite their stochastic nature, signaling networks interpret multiple signals and produce precise outputs that best reflect the response to one signal, given all other signals the cell is receiving. How are functional phosphosites distinguished from noise?

Considering the dynamic nature of phosphorylation events - phosphorylation and dephosphorylation enzymatic reaction are extremely fast - we postulated that the relevant time scale, for signaling cascades, would be within few minutes or seconds, which requires high resolution temporal studies of the phosphoproteome dynamics. We further hypothesized that complexity of the phosphorylation landscape will increase with time after activation of particular signaling pathway. If this conjecture is

correct than we would be able to dissect signaling events by studying dynamics of phosphorylation at high temporal resolution on a time scale of few seconds.

We explored this hypothesis in the context of the cellular response to salt stress in yeast. Budding yeast cells are very efficient to respond at osmotic fluctuations, to which they adapt and resume growth in about 30 minutes after exposition to 0.4 M sodium chloride [152]. Many aspects of this yeast response strategy were extensively studied; including perception, signalling and adaptation mechanisms to conquer the stressful environment before growth resumes in hyper osmotic conditions.

Fast metabolic flux adjustments, rather than *de novo* enzyme synthesis, are required for quick cell osmotic adaptation. Glycolysis and glycerol synthesis are responsible for the initial phase of adaptation, to re-establish ionic balance. Distinct processes act on different time-frame to ensure glycerol accumulation; rapid modulation of glycerol channel and metabolic enzymes activity is observed within seconds following high salt exposure whereas transcriptional activation of GPD1 and other genes necessary for glycerol accumulation is observed after 15 min or more [153].

The work presented in this chapter reveals dynamic and functional changes in protein phospho state on many major players of CME. We demonstrate that dynamic phosphosites inside some endocytic factors are partly responsible for their recruitment and function on endocytic sites.

A Cell Signaling Network Temporally Resolves Specific *versus* Promiscuous Signals

Evgeny Kanshin, Louis-Philippe Bergeron-Sandoval, S. Sinan Isik, Pierre Thibault and Stephen W. Michnick

Highlights

- A strategy for high temporal resolution phosphoproteomics with increased coverage
- The HOG signalling network implicates 25 % of the kinome and 10 % of phosphatases
- Changes in functional phosphorylation occur more rapidly than promiscuous events
- Many potentially regulatory phosphosites in cytoskeletal proteins are reported

eToc Blurb

Kanshin, Bergeron-Sandoval et al. report that conserved and putatively functional kinase- or phosphatase-substrate interactions in the High Osmolarity Glycerol (HOG) response occur more rapidly than promiscuous interactions. They provide a rich dataset of dynamic phosphosites that may be implicated in the regulation of the cell cycle, cytoskeletal dynamics and morphogenesis.

Summary

If specific and functional kinase- or phosphatase-substrate interactions are optimized for binding compared to promiscuous interactions, then changes in phosphorylation should occur faster on functional *versus* promiscuous substrates. To test this hypothesis, we designed a high temporal resolution global phosphoproteomics protocol to study the High Osmolarity Glycerol (HOG) response in the budding yeast *Saccharomyces cerevisiae*. The method provides accurate, stimulus specific measurement of phosphoproteome changes, quantitative analysis of phosphodynamics at sub-minute temporal resolution and detection of more phosphosites. Rates of evolution of dynamic phosphosites were comparable to those of known functional phosphosites and significantly lower than static or longer time-frame dynamic phosphosites. Kinetic profile analyses indicated that putatively functional kinase- or phosphatase-substrate interactions occur more rapidly, within 60 seconds, than promiscuous interactions (Figure 4). Finally, we report many changes in phosphorylation of proteins implicated in cytoskeletal and mitotic spindle dynamics that may underlie regulation of cell cycle and morphogenesis.

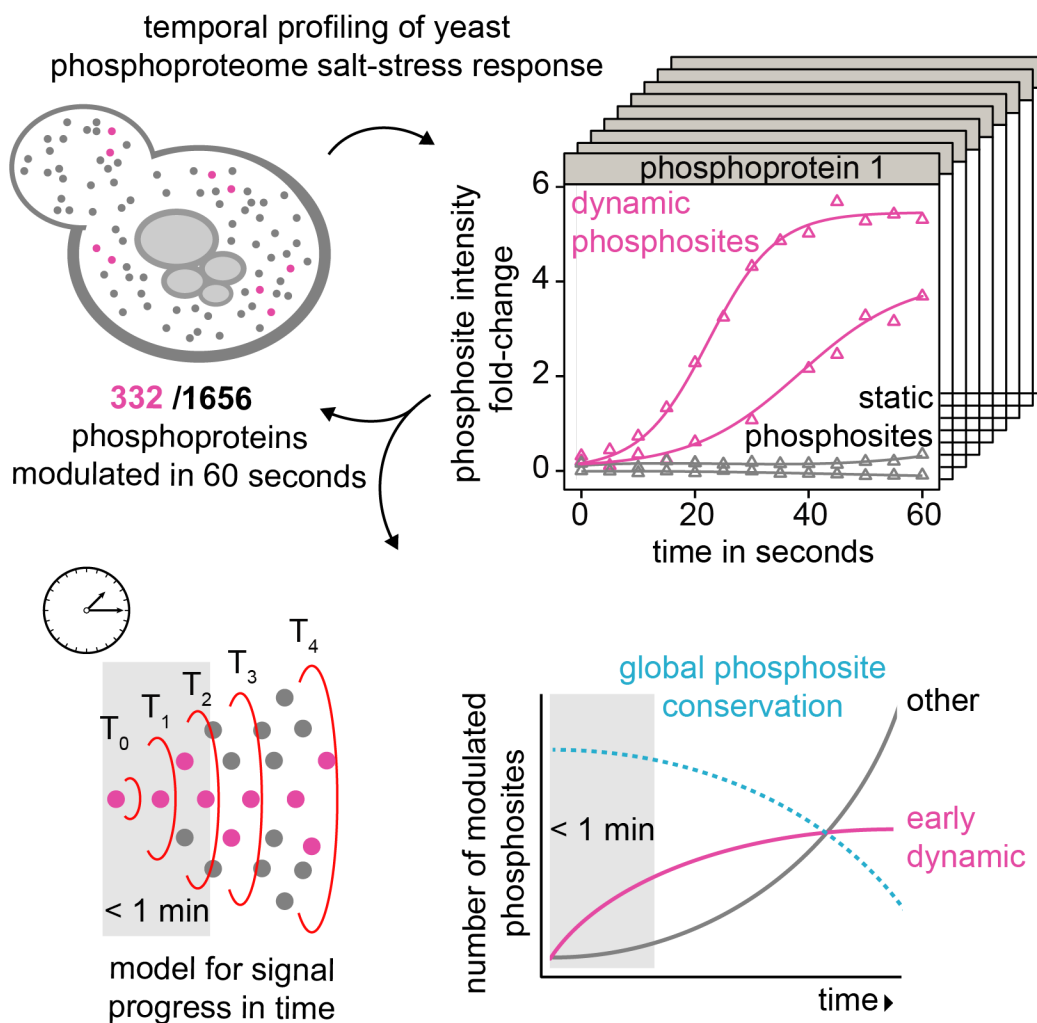


Figure 4 | Graphical abstract

To get a global view of the dynamic response of the phosphoproteome to salt stress, we measured the temporal profiles of specific phosphosites on 332 phosphoproteins in a quick time window of 60 seconds after salt treatment.

Introduction

Signaling networks have evolved to respond to distinct environmental stimuli with coherent and specific responses. Yet recent evidence suggests that protein kinases, the major signaling enzymes in the cell, form a highly connected and perhaps, irreducibly complex network [154, 155]. We have argued that complexity of the kinase network may have evolved to integrate and compare multiple signals, resulting in main and complementary responses to stimuli [156]. Such a network could also generate promiscuous phosphorylation that has no functional consequence but confounds our understanding of the signaling response (Figure 5A) [22, 23].

It is generally viewed that signaling networks have evolved so that kinase- or phosphatase-substrate interactions are made most efficient by optimization of enzyme binding and specificity for substrate recognition sequences and structural organization through domain, adaptor or scaffold protein binding [157-159]. We hypothesize that functional phosphorylation of specific substrates occurs rapidly following stimulation but that promiscuous phosphorylation takes place more slowly, following random encounters with neighboring proteins (Figure 5B). Therefore capturing early signaling (phosphorylation or dephosphorylation) immediately after cell stimuli could facilitate the detection of stimulus-specific phosphorylation.

To test this hypothesis, we chose the High Osmolarity Glycerol (HOG) response pathway of the budding yeast *Saccharomyces cerevisiae* and performed rapid (5 second resolution) phosphoproteomics analyses to yield unprecedented profiling of HOG signaling [153, 160, 161]. We chose to study this response because the signaling pathways are very well characterized and temporal responses have been studied in detail [152, 153, 162]. Upon stimulation, cell-to-cell variation is very low so that dynamics of phosphorylation likely reflect responses of all cells in the population studied.

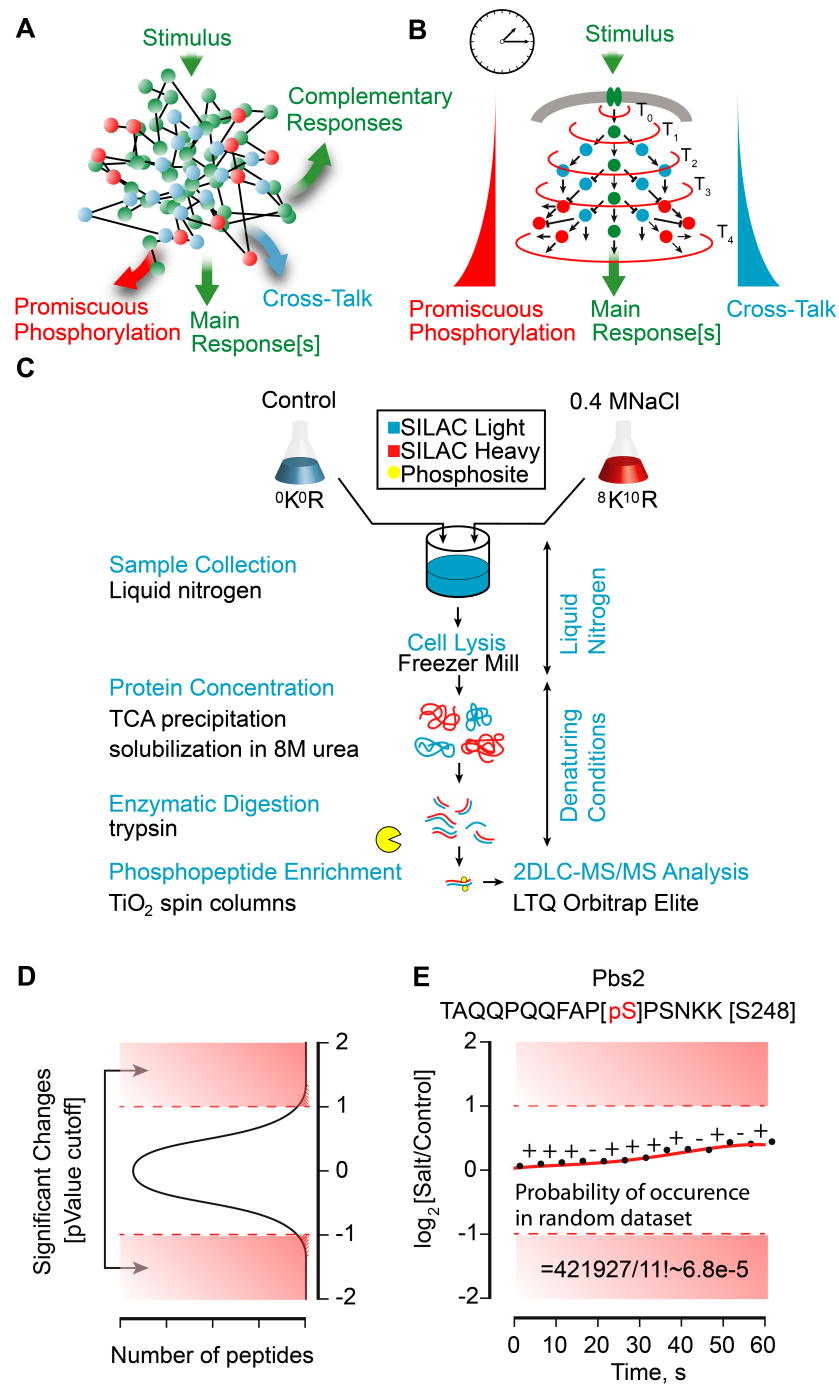


Figure 5 | The origins of complexity in signaling networks

(A) Signaling networks composed of kinases and phosphatases (green and blue dots) may be highly connected (dark lines), resulting in main and complementary responses to stimuli. Signaling that has no consequences could arise due to promiscuous phosphorylation that masks simple pathways (red dots). (B) We hypothesized that stimulus-specific signaling may occur faster than promiscuous signaling. (C) Experimental workflow to study phosphoproteome dynamics at high temporal resolution. Samples are collected by flash freezing yeast cultures in liquid nitrogen to preserve phosphorylation status. (D-E) A pattern- and FC-based analysis of high resolution phosphorylation kinetic profiles. (D) Common data analysis workflows use the distribution of fold changes (FC) for detected phosphopeptides in order to define regulated phosphosites. (E) To detect changes in phosphorylation with small FC value, such as Pbs2 Ser248, a pattern-based analyses with +/- signatures of the kinetic profiles (independent of absolute FC) was used to assign significance of individual low amplitude traces. See also Figure 6 and Table 2.

Results

Dynamic phosphoproteomics at sub-minute temporal resolution

Common sample preparation protocols used in phosphoproteomics are not generally suited to the profiling of rapid signaling events because cell harvesting typically require 5-15 minutes due to centrifugation and cell pellet washing steps. These steps can impart changes to the phosphoproteome that arise from both the stimulus of interest and the sample collection method. Thus, to assure that measured changes in the phosphoproteome are due only to the stimulus applied and to facilitate the dynamic studies at sub-minute temporal resolution, we devised a new sample collection technique (Figure 5C). Yeast cells grown in media containing either light (control) or heavy (0.4 M NaCl) isotopic forms of arginine and lysine were pooled together in liquid nitrogen to prevent any protein degradation and further activity of kinases and phosphatases. Frozen cell cultures from 13 time points ranging from 0 to

60 seconds (at 5 second intervals) were finely ground under liquid nitrogen, TCA precipitated proteins were resolubilized in denaturing urea buffer and digested with trypsin. Importantly, we could perform protein extraction with no intermediate washing steps. Consequently cells were not exposed to perturbing wash conditions that could cause changes in the phosphoproteome. Phosphopeptides were enriched on TiO_2 resin prior to offline separation on SCX spin columns and LC-MS/MS analyses (Extended Experimental Procedures) [140, 141, 163].

We collected temporal profiles for 5453 phosphopeptides on 1656 proteins with a false discovery rate (FDR) less than 1 % at both peptide and protein levels. These profiles corresponded to phosphopeptides quantified in at least 10 of 13 time points with an average phosphosite localization confidence greater than 0.75 (Figure 6A-B and Table 2). We identified 596 phosphopeptides from 332 proteins that showed distinct continuous changes in phosphorylation with time (increases or decreases) (Table 3). Abundances of the remaining phosphopeptides did not change with time (henceforth they are defined as containing “static” phosphosites). All the dynamic and static phosphosite temporal profiles can be displayed using an R script (File S1). The high temporal resolution of changes in phosphorylation obtained in this study enabled us to use a pattern-based algorithm to identify 99 additional regulated phosphosites, including for those with kinetic profiles of low amplitude that would remain undetected by conventional quantitative phosphoproteomic approaches (Extended Experimental Procedures, Figure 5D-E and Figure 6C-D-H) [164]. The reproducibility of sample processing and data analysis was confirmed through independent experiments (Figure 6E-G).

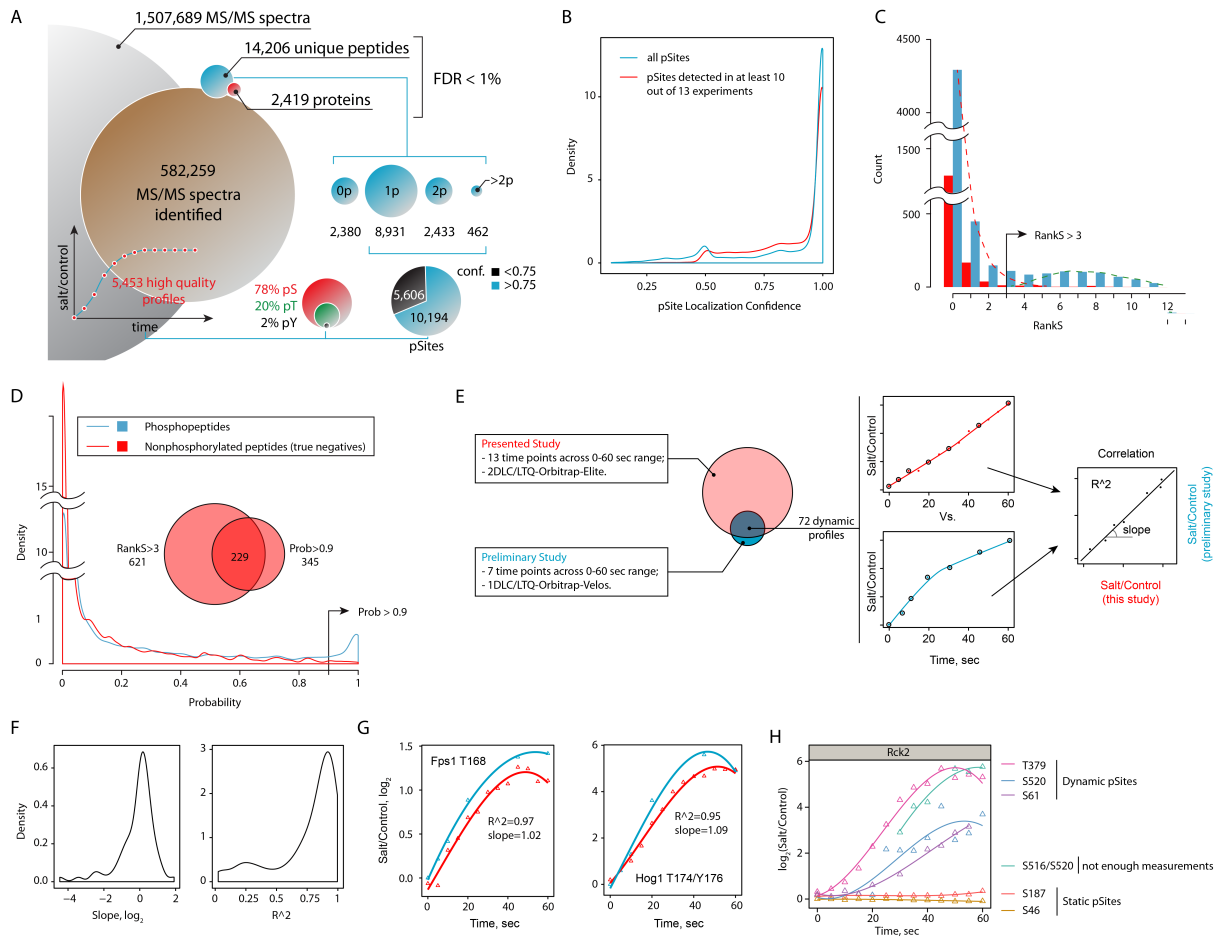


Figure 6 | Summary of phosphopeptide identification

(A) A total of 582,259 MS/MS spectra were collected, which resulted in identification of 14,206 unique peptides from 2,419 proteins at a FDR < 1%. Phosphopeptides represented 83% of all identified peptides of which 68% corresponded to phosphosite with high localization confidence (> 0.75). A total of 5,453 dynamic profiles (≥ 10 out of 13 data points/profile) were used for subsequent data analyses. (B) Density plots showing phosphosite localization confidence. Both FC-based (C) and pattern-based (D; as described in Figure 5D-E) approaches were used to define regulated phosphosite profiles. Inset shows complementarity of these methods. (E) To address reproducibility of our approach, we examined the correlations between 72 dynamic profiles that were common for both preliminary (1DLC) and final (2DLC) data sets. Basically, FC measurements from 2 separate experiments were plotted against each

other and corresponding R^2 and slope values were used to assess similarity between profiles. (F) Reproducibility of sub-minute phosphoproteomic kinetics in independent experiments were assessed with the distribution of R^2 and "slope" parameters. We observed a correlation with a median R^2 of 0.86. (G) Reproducibility between preliminary and final datasets illustrated with dynamic phosphorylation profiles of Hog1 and Fps1. (H) Profiles for all pSites on Rck2 kinase and their differentiation by our profile filtering pipeline as described in Figures 5D-E.

Recapitulation of the canonical HOG pathway

We first examined signaling within the canonical HOG signaling pathway, generally depicted as cascades of phosphorylation-activation steps (Figure 7A) [153]. The canonical HOG pathway has two branches, emanating from cell-surface osmo-receptors Sho1 and Sln1, both of which converge upon the scaffold protein-MAPKK Pbs2 and ultimately the MAPK Hog1. Early responses include cell shrinkage due to exit of water within seconds, and slower nuclear translocation of Hog1 within several minutes [152]. Simultaneously, the cell cycle arrests, channels controlling glycerol and other osmolytes are affected, and gene transcription is modulated, ultimately resulting in adaptation to changed osmolarity.

Our rapid sample preparation strategy resulted in accurate observation of dynamic phosphorylation of components of the HOG response pathway (Figure 7A). For example, we obtained distinct profiles for both monophosphorylated forms of Hog1 on its activation loop (T174/Y176) (Figure 7B), observing greater than 30-fold increase within 40 seconds following stimulation.

We did not observe changes in the Sln1 branch upstream of Ssk2. This is predictable since this branch is affected through a two-component histidine-aspartate phosphorelay (Figure 7A). The lability of these phosphosites prevents their detection under the conditions that we performed our experiments. We also did not observe

rapid changes in phosphorylation of substrates for the Sho1 branch. It is possible that these sites are phosphorylated at low stoichiometry or alternatively, that the Sho1 branch is activated on a different time scale [165]. For instance, changes in phosphorylation of both PAK-like kinases Ste20 (T203, S206 and S169) and Cla4 (S367) occurred more slowly than Hog1 phosphorylation (Table 3), suggesting that these result from later feedback phosphorylation of these proteins.

The quality of the kinetic profiles is reflected by the continuity of increasing or decreasing sequential data values between time points that we observe (Figures 2 and 3). This continuity reflects the fact that when cells are immediately frozen in liquid nitrogen, no spurious changes in phosphorylation may occur.

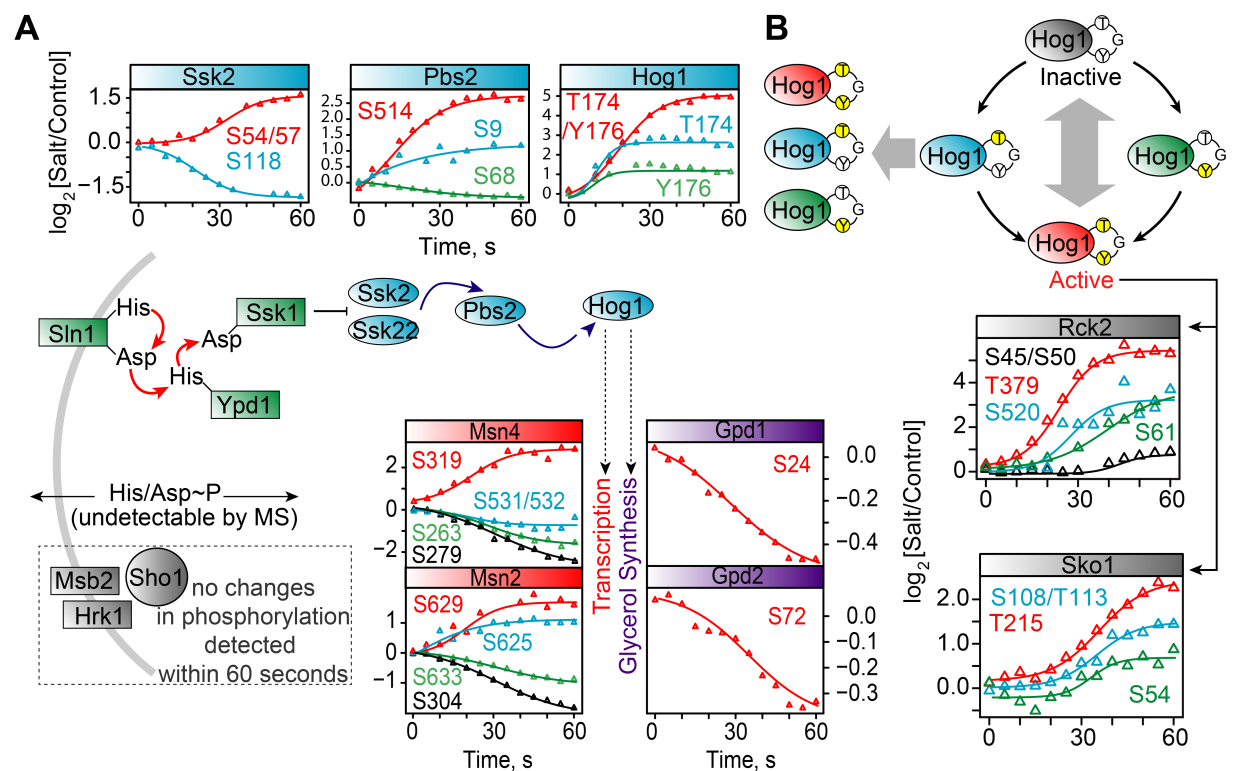


Figure 7 | Dynamic phosphorylation within the canonical HOG pathway

(A) Changes on MAPK (Hog1), MAPKK (Pbs2) and MAPKKK (Ssk2) were detected within the canonical yeast HOG pathway. We were unable to detect dynamic phosphorylation upstream of Ssk2 because of the labile nature of phosphorylation on

Asp and His residues. (B) Schematic representation of the observed dynamic double phosphorylation of Hog1 and subsequent phosphosite kinetics profiles in Hog1 substrates Rck2 and Sko1. See also Figure 8.

Anticipatory Signaling downstream of the canonical HOG pathway

We observed dynamic changes in phosphorylation for a number of reported substrates of Hog1, including transcription factors Sko1, Msn2 and Msn4, and Rck2 kinase, as well as glycerol response proteins Gpd1 and Gpd2 [166-170] (Figure 7). Surprisingly, we noted a rapid dephosphorylation of the kinase Ssk2 at residue S118 and phosphorylation on residues S54 and S57 (Figure 7A). Previous reports indicated that Ssk2 concentrates in the bud neck and forms a complex with actin during osmotic stress, where it promotes actin cytoskeleton recovery through the reestablishment of osmotic balance [171-173]. These events should, however, occur during the later adaptive period of HOG response and may involve different sites than those identified here. The dynamic phosphosites we observed may be anticipatory signals, perhaps involved in the re-localization of Ssk2 to the bud neck prior to activation during the adaptive phase.

We also observed complex phosphorylation patterns for the general stress transcription factors Msn2 and Msn4 (Figure 7A) [174]. Hyperosmotic stress was previously shown to result in a short-lived dephosphorylation of Msn2 on at least 6 serine residues (S194, S201, S288, S304, S451 and S633) two of which (S304 and S633) were observed in this study. Phosphorylation of Msn2 was also detected on PKA consensus sites (S625/S629) located in the nuclear localization sequence (NLS) and associated with the sequestration of Msn2 to the nucleus to favor its association with chromatin [174]. Early phosphorylation of these sites could be involved in the re-equilibration of active Hog1 to the nucleus as suggested previously [175-177].

Interestingly, we observed a gradual dephosphorylation of Fps1 on residues 172, 175, 181 and 185 proximal to a putative MAPK-docking site (D motif) [178] within this region (residues 176-187) (Figure 8). It was recently reported that upon osmotic shock, Hog1 is recruited to a MAPK docking site within the N-terminal domain of Fps1 and phosphorylates a redundant pair of regulators, Rgc1 and Rgc2 to induce their eviction from the C-terminal region of Fps1, which in turn causes closure of the Fps1 channel (Figure 8A) [179]. Phosphorylation/dephosphorylation of serines 172, 175, 181 and 185 could act as a regulatory switch to modulate docking of Hog1 *via* its interaction with neighboring arginine residues of the Fps1 D motif (Figure 8B). Accordingly, dephosphorylation of N-terminal residues of Fps1 would favor docking of Hog1 to the D-motif, which is used as a platform to phosphorylate Rgc1/2. Consistent with this proposal, we also observed an increase in phosphorylation of residues 21, 975, 1046, 1048 and 1059 of Rgc1 upon osmotic shock (Figure 8C).

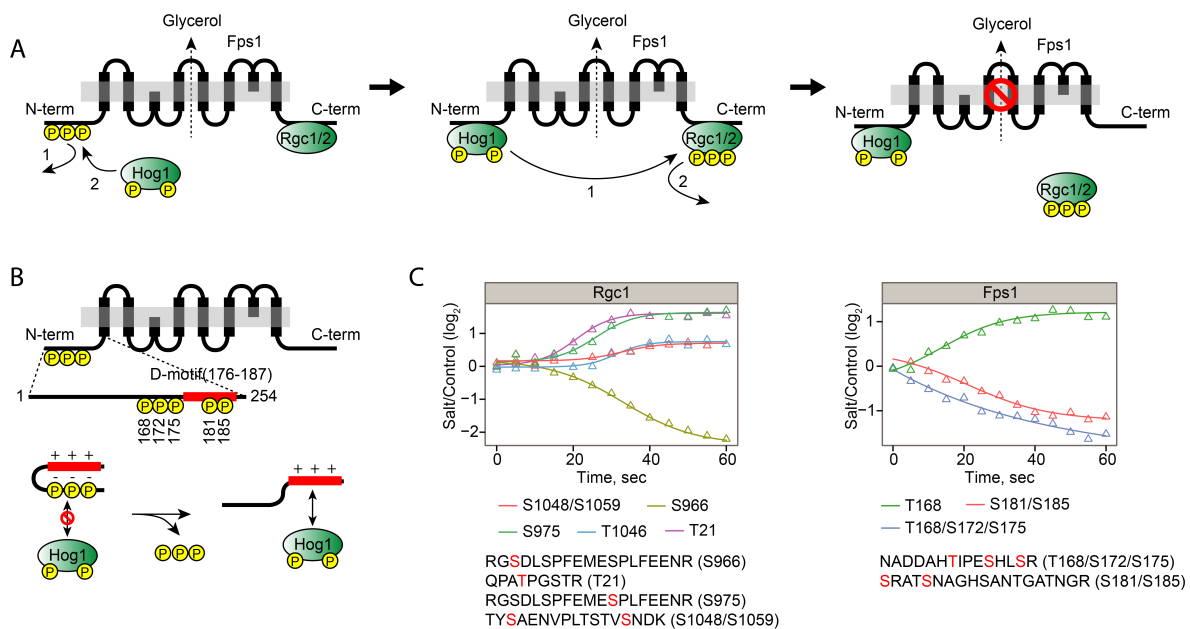


Figure 8 | Regulation of the aquaglyceroporin Fps1 in response to changes in extracellular osmolarity

(A) Model for the regulation of Fps1 by Hog1 in response to hyperosmotic shock, adapted from Lee *et al.* [179]. Under non-stress conditions, the redundant regulators Rgc1 and Rgc2 are associated with the C-terminal domain of Fps1, and maintain Fps1 channel open. Upon osmotic shock, Hog1 is activated and recruited to the N-terminal domain of Fps1 to phosphorylate Rgc1/2, resulting in the dissociation of Rgc1/2 from the C-terminus and closure of the Fps1 channel. (B) N-terminal cytoplasmic domain of Fps1 showing the location of phosphorylation sites proximal to the MAPK docking region (D-domain). Electrostatic interactions between these phosphorylated residues and neighboring basic amino acids could prevent docking of Hog1 on D-domain. (C) Dynamic phosphorylation of Rgc1 and Fps1 residues upon osmotic shock. Fps1 phosphosites phosphodynamics show a constant increase in abundance of a monophosphorylated form that is associated with actual dephosphorylation of neighbouring sites from the triple-phosphorylated form of the same peptide. Related to Figure 7.

Global dynamic properties of the HOG signaling response

We next examined global dynamic properties of the HOG signaling response. We used fuzzy c-means clustering to group our phosphosites into 6 distinct clusters according to the shape of their kinetic profiles (cluster membership > 0.5, Extended Experimental Procedures, Table 3). Analysis of the distribution of dynamic phosphosites on the corresponding proteins revealed three distinct protein groups that were either phosphorylated (200 profiles) or dephosphorylated (183 profiles) or displayed both behaviors (58 profiles) (Figure 9A). The last group, which includes the proteins Cyr1 and Sla1 (Figure 9B), is the most interesting, since it contains proteins that could interact with at least one kinase and phosphatase or be phosphorylated on multiple sites by the same kinase.

To access the temporal nature of the responses, we empirically fit profiles to a simple birth-death model and extracted two parameters: the maximum rate of fold change

(FC) corresponding to an increase or decrease in phosphorylation (dFC/dt_{\max}), and the time at which the maximum rate is observed (t_{\max}) (Extended Experimental Procedures, Figure 9C and Table 3).

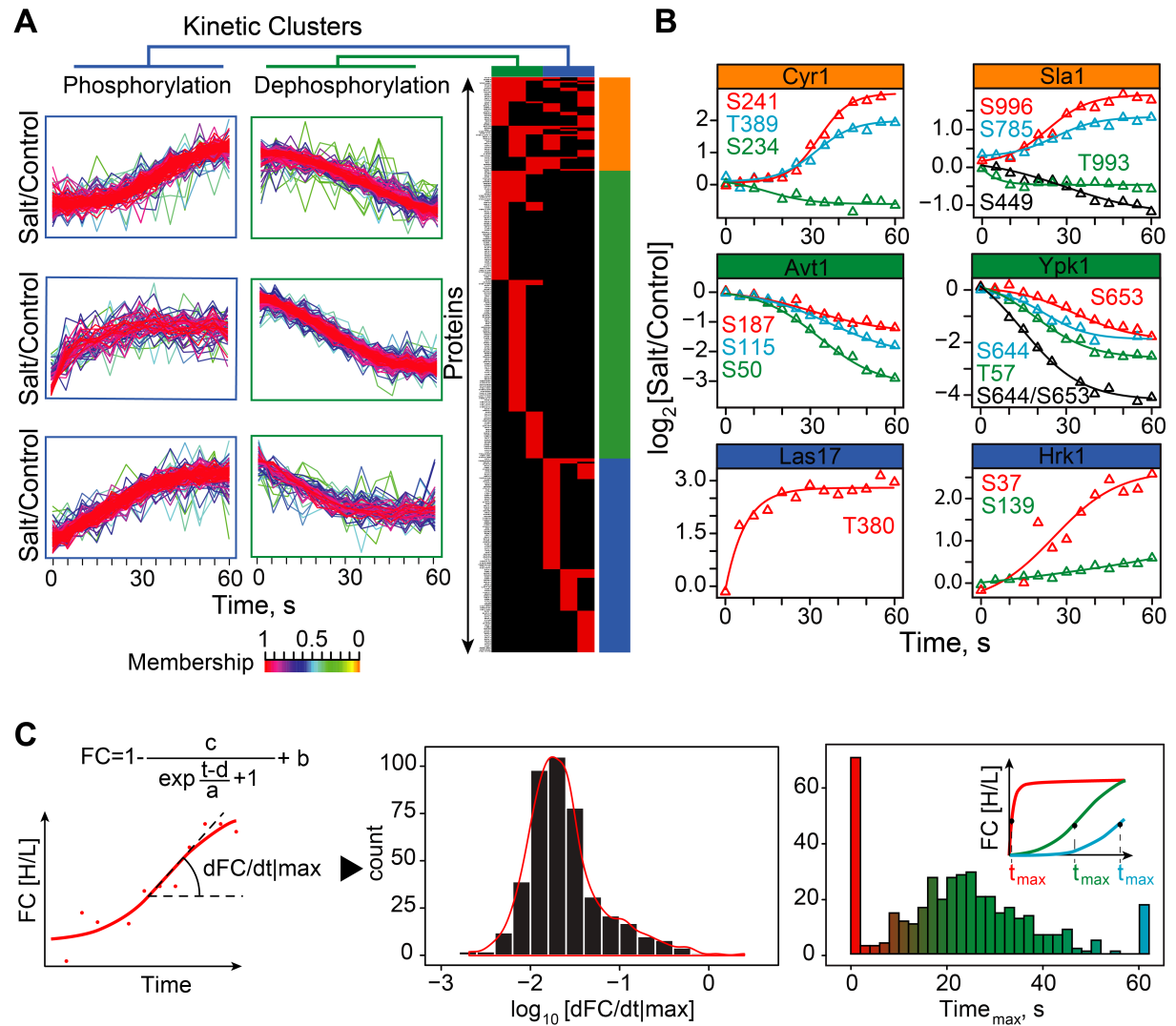


Figure 9 | Kinetic analysis of signaling response

(A) Kinetic profiles are coherent and can be clustered into 6 types (left panels). The cluster membership of the kinetic profiles is colour coded according to the scale shown below the clusters. The 596 dynamic phosphosites identified fall into 3 distinct protein groups: phosphorylated (blue box), dephosphorylated (green box) or both on

distinct sites of the same protein (orange box). These dynamic sites are contained within 332 proteins displayed in the right panel heat map according to site-associated kinetic cluster groups. (B) Examples of dynamic phosphorylation sites from each group are presented in the left panels. (C) Fitting of kinetic profiles to a birth-death model enabled the extraction of maximum rates of Fold Change (dFC/dt_{max}) (right panel) and times at which the maximum rate is achieved (t_{max}). The distribution of rates (dFC/dt_{max}) from 596 dynamic sites on a \log_{10} scale shows that sixty-eight per cent of rates (dFC/dt_{max}) fall within one order of magnitude. Profile fitting identified that 72.5% of profiles are sigmoidal in shape (see Figure 10) and reach t_{max} within a time window of 60 seconds (green bars in right panel and green trace in right panel insert). No sigmoidal-like profiles reached t_{max} at 0 or 60s (respectively represented as red and blue bars and trace in right panel) in contrast to exponential or linear-like profiles. See also Figure 10 and Table 3.

The temporal resolution we achieved in this study enabled us to discern key features of the dynamic responses. Notably, 72.5% of dynamic profiles are sigmoidal in shape (Figure 10) and most profiles approach their maxima (or minima) within 60 seconds (Figure 9C right panel). The latter suggest that either the HOG response reaches its maximum within 60 seconds or if there are later responses, they occur on a different time scale than studied here. The sigmoidal responses are interesting in that they resemble low pass filter outputs that block high frequency and random short period noise of extracellular or intracellular origins. Specifically, the delay in response of a sigmoid curve assures that any random, short duration signals will not induce a response. Furthermore, the sigmoid response assures that sequential steps in signal processing occur at rates that are optimal for the reactions in a given pathway [180]. Indeed, our results are consistent with observed responses of the HOG pathway as a function of the frequency of oscillating stimuli [152, 162].

We also observed that the range of maximum rate FC is tapered compared to a normal distribution and 68.3% of these rates fall within 1 order of magnitude (Figure 9C middle panel). This is a curious result, since one might expect reaction rates of kinases and phosphatases to have a broad distribution due to differences in intrinsic activity, substrate abundances, their subcellular localizations, structures and enzyme recognition sequences (though note that we do not measure changes in absolute rates here). Such a narrow range of rates could be favored by organization of enzymes and substrates into complexes or physical localization to specific cellular compartments [157-159].

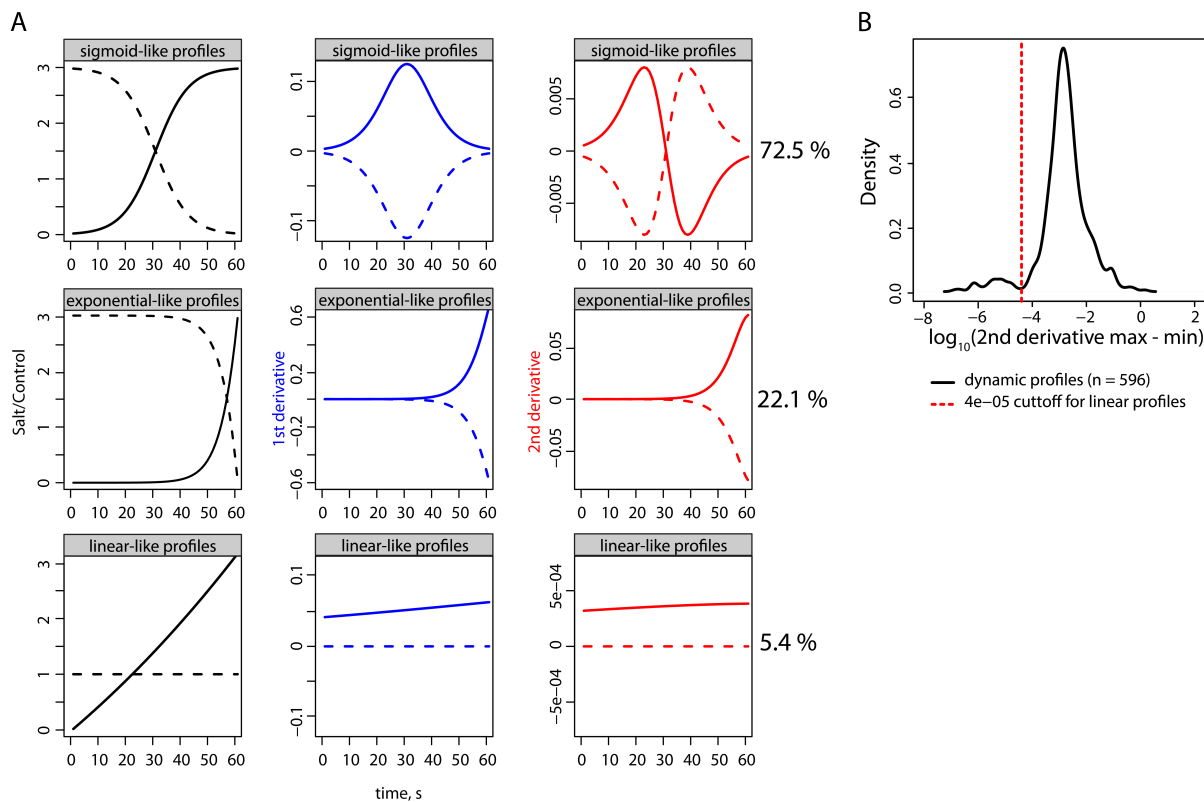


Figure 10 | Analysis of dynamic phosphorylation profiles

(A) General example of sigmoid (top), exponential (middle) and linear (bottom) shapes of fitted profiles with our birth-death model (black) along with their first derivative (blue) and second derivative (red). The shapes were sorted according to

second order local max and min values and max-min difference. The occurrence of these shapes in the dynamic profiles is indicated on the left. (B) Distribution on a \log_{10} scale of the second derivative max-min difference for the dynamic profiles. We determined a cut off of $4e-05$ for the max-min difference to sort linear-like profiles. Related to Figure 9.

Dynamic phosphorylation suggests a dense kinase-phosphatase network

At the outset we hypothesized that the complexity of signaling events could arise from the propagation of signaling through a highly connected kinase-phosphatase network resulting in main, complementary and promiscuous responses (Figure 5A). We did observe a constant increase in width of FC distributions with time (Figure 12A) and an almost 9-fold increase in the number of affected phosphosites during the first minute following osmotic shock (Figure 11A). The speed of the signal propagation is very rapid with 84 phosphosites changing in the first 5 seconds, while the complexity of the response increases concurrently. We further predict that if there is a complex kinase-phosphatase network, many of these enzymes undergo changes in phosphorylation early in response to stimulus. We observed that 25% (34/129) of all kinases and 10% (3/30) of all phosphatases had dynamic phosphosites changing within 60 seconds following stimulation, and 28 of the kinases and the 3 phosphatases are known to have at least one interaction with another kinase or phosphatase (Figure 11B and Table 3). Thus, it is possible that the combinatorial explosion of phosphorylation events we observe is due to rapid changes of enzyme activities in a highly connected kinase-phosphatase network.

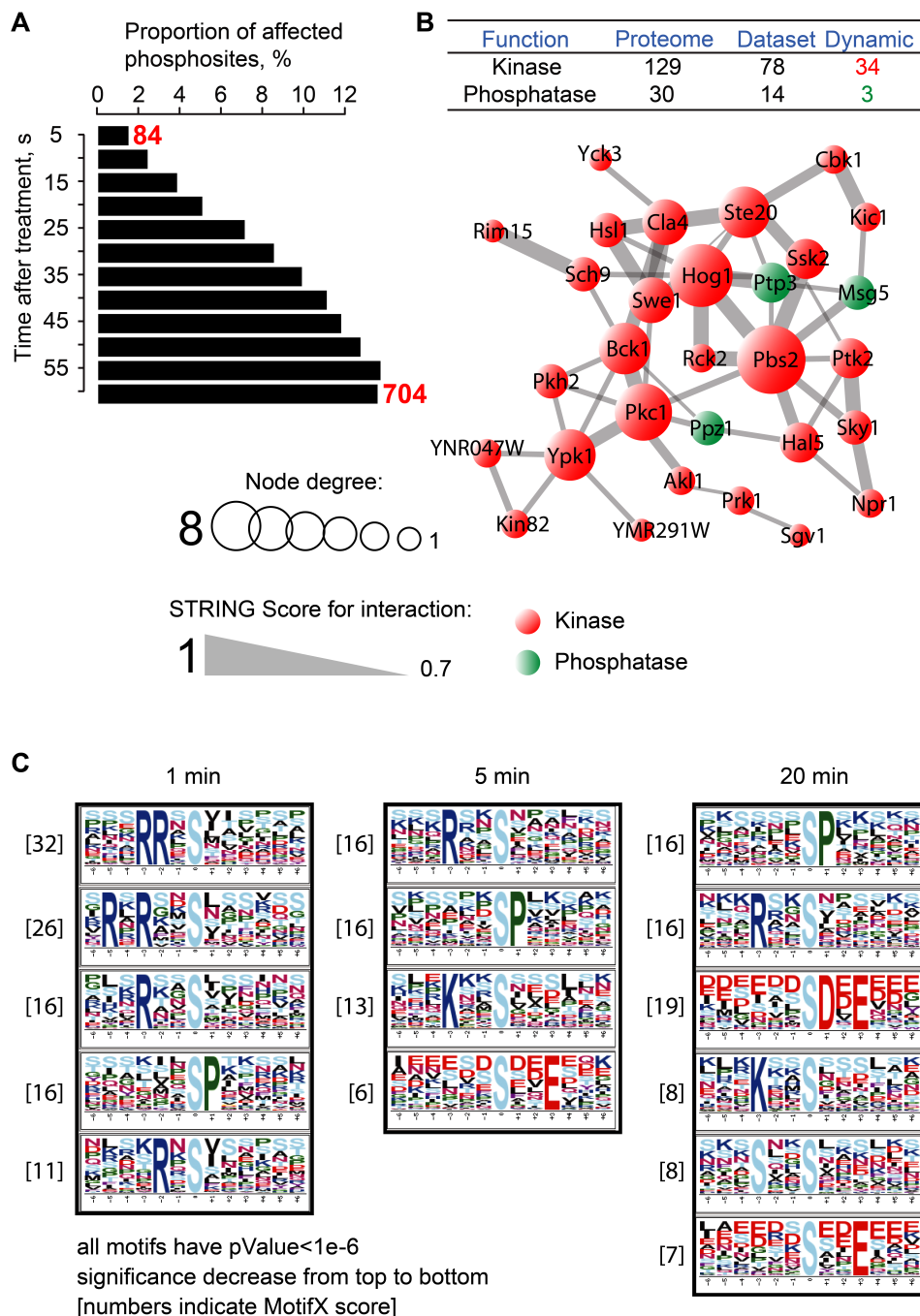


Figure 11 | Temporal complexity of the kinase-phosphatase network and relationships with dynamic substrates.

(A) The number of phosphosites that undergo a significant fold change increased with time (84 to 704 sites from 5 to 60 s after osmotic shock). (B) The HOG kinase-phosphatase network appears to be complex. Network based on known kinase-

phosphatase relationships (from STRING database <http://string-db.org/>). (C) Over-represented linear motifs in our data were detected with MotifX [181, 182]. We used default settings (min. occurrences = 20, significance = 0.000001) and SGD proteome as background. As a result we obtained different motifs among phosphosites regulated within 1, 5 and 20 min upon osmotic shock. See also Figure 12 and Table 3.

If the changes in phosphorylation of the kinases or phosphatases described above resulted in either activation or inactivation of these enzymes then we could predict that regulated phosphosites are surrounded by peptide motifs that are recognized by these enzymes. To test this hypothesis we performed two independent tests; one to predict kinases that could phosphorylate the observed phosphosites using NetworKIN (Figure 12B) and a second test for overrepresentation of linear peptide motifs surrounding dynamic phosphosites using MotifX [181-183]. We found overrepresentation of peptide motifs for those with basic residues in p-2 to p-5 positions relative to the phosphosite (Figure 11C left panel). Furthermore, 13 of the 34 kinases that showed dynamic phosphorylation changes have been experimentally demonstrated to recognize such basic peptide motifs [184]. NetworKIN showed enrichment for basophilic PKA and PAK kinases (PAKA), consistent with the MotifX search results (Figure 12B). We can also conservatively predict that at least 18 of the kinases likely recognize peptides with basic residues in the p-2 to -5 positions based on their membership to the AGC family of protein kinases (Table 3) [185].

Phosphorylation of sites with prolines at p+1 are the most expected, assuming that the canonical HOG response involves activation of MAP kinases. Such motifs are indeed enriched in our 1-minute data, though not dominant. Some phosphorylation motifs at 5 and 20 minutes [186] are acidic across the entire motif (Figure 11C middle and right panels) and could reflect the activation of acidophilic kinases of the casein kinase 2 (CK2) family at later time points.

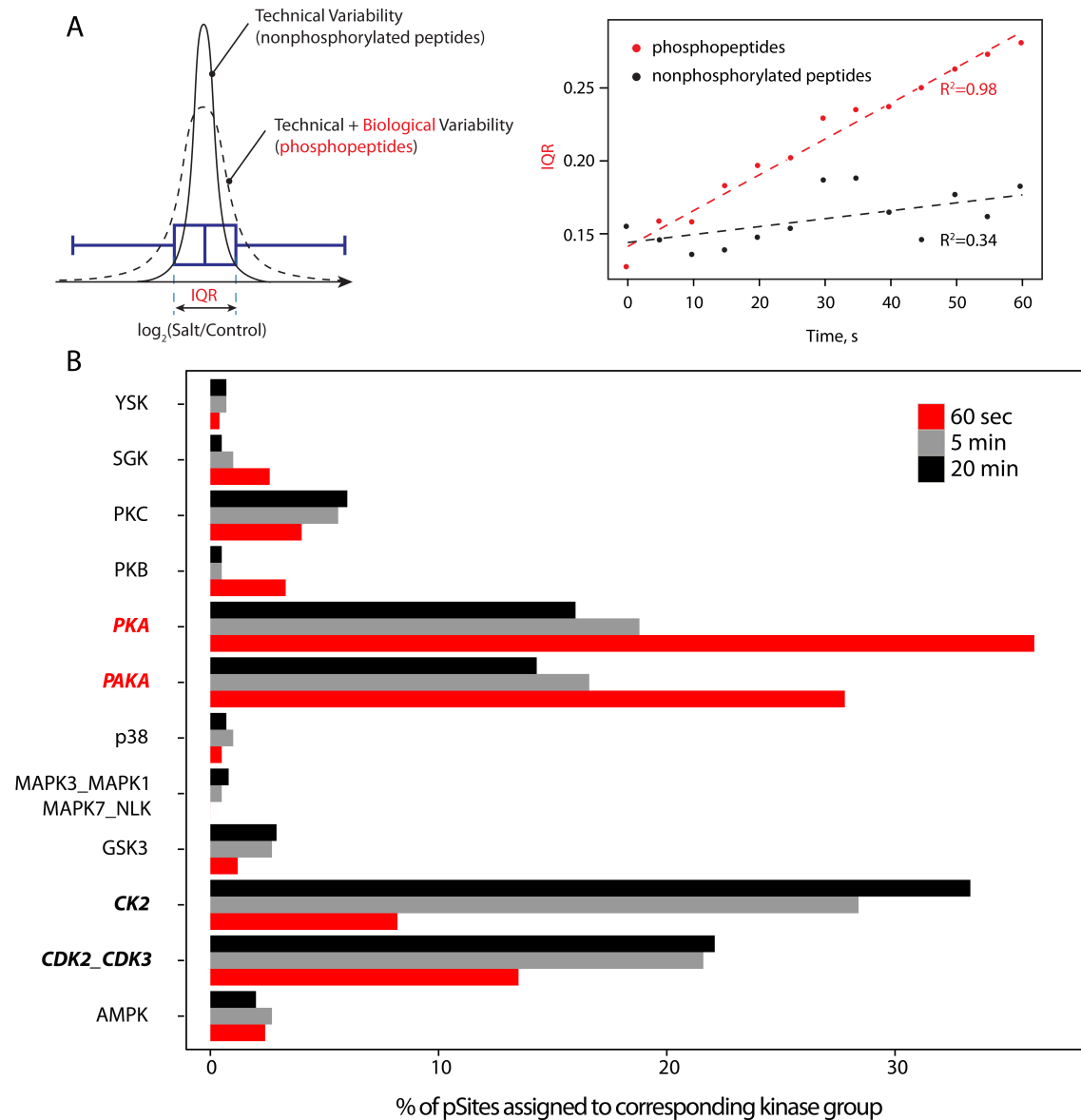


Figure 12 | Combinatorial explosion of signal complexity and kinase predictions for phosphosites

(A) Change in FC density distributions over time. We detected a constant increase in the widths of FC distribution of phosphopeptides over time, which illustrates the global effect of osmotic shock on the phosphoproteome. FC distributions of nonphosphorylated peptides remained largely unaffected and represent technical variability of our workflow (assuming protein expression is not affected within 1 minute

after osmotic shock). (B). Kinase prediction for affected phosphosites in this study (60 seconds) and at 5 and 20 minutes [186] following stimulation. Analysis was performed with PhosphoSiteAnalyzer software [187], which makes predictions of kinase substrates based on the NetworkKIN algorithm [188]. NetworkKIN applies linear motif analysis and contextual network modeling to obtain kinase-substrate associations with high accuracy and sensitivity. Related to Figure 11.

Dynamic phosphosites are more conserved than static phosphosites

We previously proposed that the apparent complexity of signaling networks could be partially due to non-functional promiscuous phosphorylation [22, 23]. We proposed here that rapidly phosphorylated phosphosites (dynamic sites) would be more likely functional and therefore more conserved than phosphosites that are phosphorylated more slowly (static sites), some of which may accumulate over very long (greater than one cell cycle) time-frames. We found that, on average, dynamic sites are significantly more conserved than static sites ($P < 0.005$) while no significant differences were observed in a study performed at 5 and 20 min following osmotic shock (Figure 13A) [186]. Furthermore, the evolutionary rates of our dynamic sites were similar to those of literature-curated functional sites ($P=0.3420$) [189]. Thus, it appears that in the initial response to osmotic shock, there is an enrichment of functional phosphosites in the dynamic compared to static phosphosites.

Conserved phosphosites of pathway-specific proteins are functional

Having compared functional to dynamic and static site conservation, we now did the reverse, selecting conserved known sites and sites we discovered for their potential functional relevance. To do this we chose proteins from two pathways, including proteins from the HOG response (Hog1, Rck2 and Gpd1) and from complementary changes observed in actin and tubulin cytoskeletal proteins (Bud6, Bim1, Syp1 and Sla1). We performed competition-growth assays to determine the fitness of dynamic and static phospho-null mutants (serine, threonine or tyrosine to alanine mutations) compared to their respective wild-type proteins (Figure 13B and Figure 14). For assessment of fitness under different conditions, we selected 13 dynamic and 5 static sites that are all conserved, with a rate of evolution below 1.8 (Figure 13C and Figure 14) [22, 23].

The mutants were all expressed from plasmids encoding the ORF of each gene flanked by native promoters and terminators [190]. Each phospho-null strain was also transformed with a plasmid coding for mCherry monomeric RFP and the wild-type strains with a plasmid coding for EYFP (Extended Experimental Procedures). Growth competition assays were performed starting from equal numbers of mutant and wild-type cells. Competition cultures were maintained in exponential growth phase for 5 days and the significant population fraction amplitude changes were determined by fluorescence spectroscopy (Figure 13B and Figure 14). Competition assays were performed in low fluorescence (LFM) medium or LFM medium plus 1 M NaCl to detect phosphosites that have impact on fitness in different cellular context.

We compared the distribution of the mutated, functional, dynamic and static sites *versus* rates of evolution (Figure 13C). Within the window of conserved sites (rate of evolution <1.8) we observed that the distribution of the phospho-null mutants was similar to those of the functional and dynamic sites, with a high proportion (0.72; binomial test $P = 0.0481$) of these sites that showed a fitness effect.

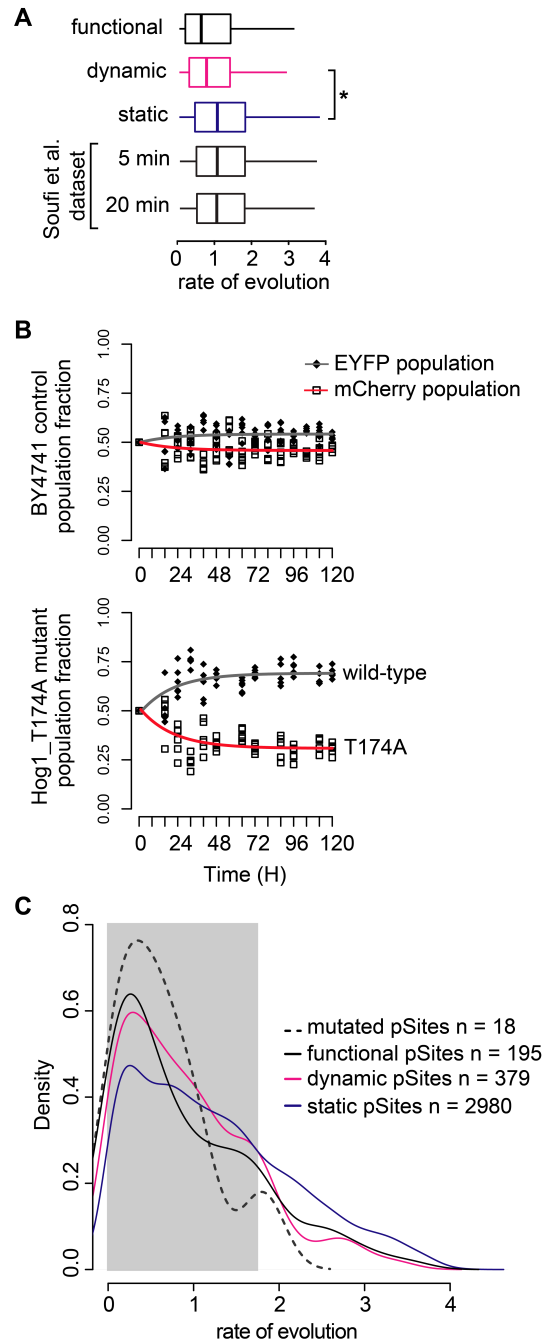


Figure 13 | Dynamic phosphosites of the HOG responses are globally more conserved than static phosphosites and conserved phosphosites affect cell fitness.

(A) The comparison of rates of evolution shows that dynamic phosphorylation sites ($n = 474$) are more conserved than static ones ($n = 3751$) ($P = 0.0014$), but do not differ from known functional phosphorylation sites ($n = 249$). Only dynamic and static sites with a single modified residue were considered for this analysis. (B) Population fractions of phospho-null Hog1 T174A mutant *versus* Hog1 wild-type strains (bottom graph) were determined in competition-growth assays using specific fluorescent reporters for the respective mutant (mCherry; empty squares and red curve) and the wild-type (EYFP; dark diamonds and grey curve) strains. Control assay was performed with strains of BY4741 expressing either mCherry or EYFP and grown in competition with each other to access normal population fluctuations (upper graph). (C) The density distribution of phospho-null mutants (dashed), functional (black), dynamic (magenta) and static (blue) phosphosites rates of evolution shows the proportion of conserved sites in the respective populations (rate of evolution cutoff = 1.8) (light grey area). Seventy-two percent of the conserved phosphosites we sampled from our dataset are functional (13/18; binomial test $P = 0.0481$) and their distribution is showed with the dashed black line. See also Figure 14.



Figure 14 | Fitness of phospho-null mutants was assessed by competition-growth under high salt and non-stressed conditions.

(A) Population fractions of phospho-null mutant *versus* wild type strains were determined in competition-growth assays using specific fluorescent reporters for the respective mutant (mCherry; empty squares and magenta curve) and the wild type (EYFP; dark diamonds and grey curve) strains. A total of 18 mutant *versus* wild type binary comparisons were performed under both 1M NaCl and normal low fluorescence medium (LFM). Each graph shows the fraction of the fluorescent readout of each population and information on mutant clone identity, growth medium, kinetic category of phosphosite (Dynamic or Static) and rate of evolution of the

mutated phosphosite. (B) Impact of phosphosite mutation on strain fitness is shown by a change in population fraction mean amplitude. Competition was assessed for cells grown in LFM (grey bars) or 1M NaCl LFM (magenta bars). Grey lines represent population standard deviation. We used a significance level cutoff of $P < 0.05$ to determine significant mean amplitude difference compared to BY4741 in competition with itself (mCherry- versus EYFP-expressing strains). We determined significant mutant amplitude differences separately for competition in LFM (grey star) or 1M NaCl LFM (magenta star). (C) From 18 phosphosites phosphonull mutant competition assays (light grey), 13 phosphonull mutants showed a fitness effect in either LFM (dark grey circle) and/or 1M NaCl LFM (yellow circle) conditions. Related to Figure 13.

HOG modulates cytoskeletal and morphogenic pathways

We predict that a complex kinase-phosphatase network will generate both main and complementary responses (Figure 5A). Gene ontology and protein-protein interaction analysis of all dynamic phosphoproteins revealed significant enrichment for main HOG responses such as membrane ion transport channels, but also complementary responses in morphogenesis and actin cytoskeleton dynamics (Figure 15A-B, Figure 8, Figure 16, File S2 and Supplemental Results). There has been a renewed interest in the relationship between hydrodynamic pressure, cytoskeletal and mitotic spindle dynamics, and cellular and subcellular morphogenesis [133, 191-194]. The observed changes of phosphorylation in our study could thus provide a unique window onto early regulation of these processes.

Actin structures and microtubule mobility are regulated by HOG

To explore effects of osmotic shock on F-actin, microtubule polymers and clathrin-mediated endocytosis (CME), we integrated fluorescent protein coding oligonucleotides 3' to reporter protein open reading frames in the genome by homologous recombination (Extended Experimental Procedures). We generated reporters to monitor *in vivo* behavior of actin cytoskeleton and cortical patches (actin-binding protein Abp1 and Abp140, cytoskeletal assembly protein Sla1 and F-Bar protein Syp1) and mitotic spindle (alpha-tubulin protein Tub1) (Figures 6C-F). Structural integrity of patches, actin cables and spindles were not affected by salt treatment, but the monitored structures remained immobile for an unusually long time (Figures 6C-F and Movie S1-S2). The treatment also perturbed the normal maturation cycles of cortical patches, where Sla1 and Abp1 markers failed to progress with time and remained associated with patches at the plasma membrane instead of entering the cell (Figure 15C). We observed extensive phosphorylation changes in a number of proteins involved in different stages of endosome maturation including regulators of F-actin assembly (actin-binding proteins Ysc84 and Abp1) and Arp2/3 dependent branching (WASP homolog Las17, WASP-binding protein Lsb3 and verprolin Vrp1) [195] (Table 3). It would be interesting to investigate whether these multi-target modifications result in complete inhibition of the endocytic cycle and block deleterious effects of cargo uptake, perhaps of the osmolytes themselves.

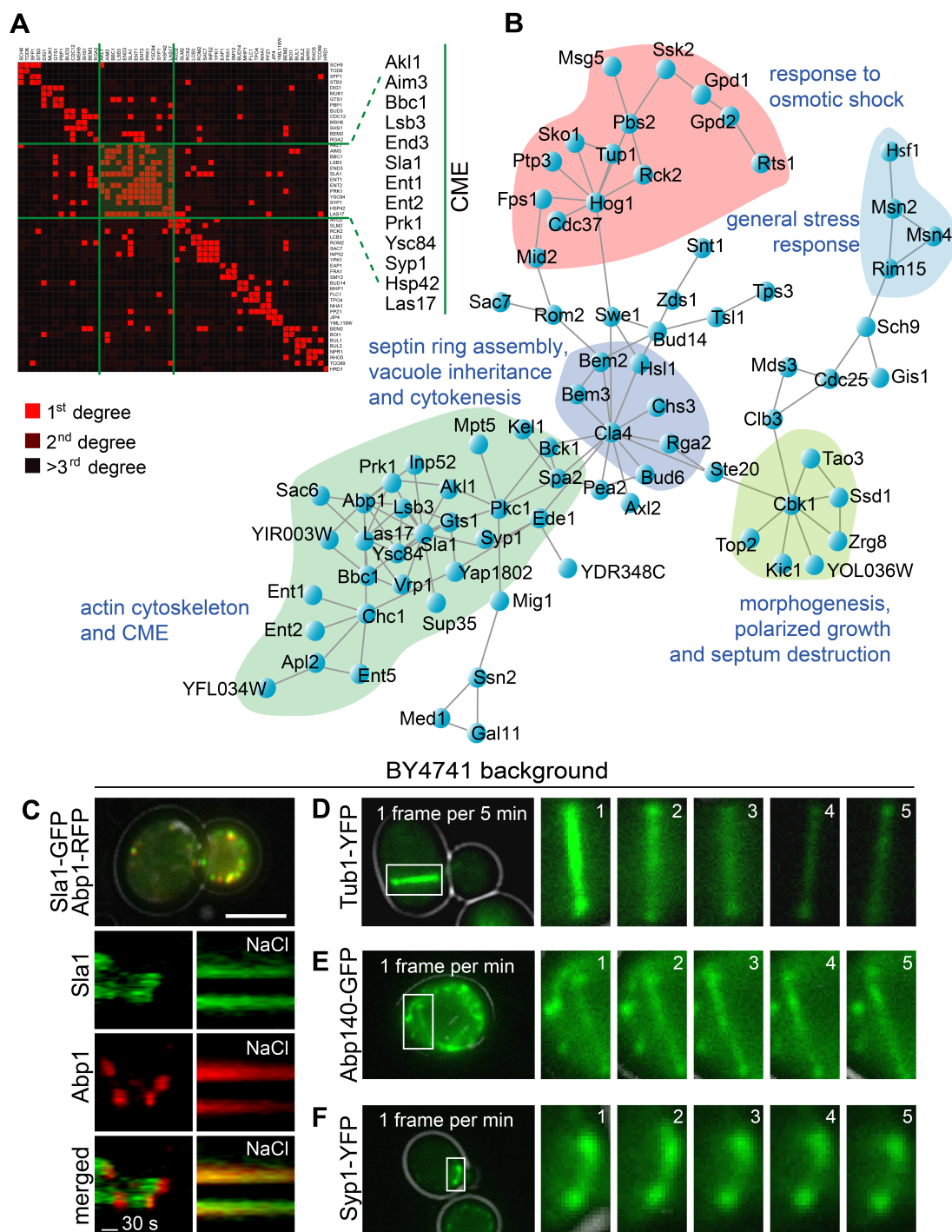


Figure 15 | Dynamic phosphosite proteins are enriched for both main HOG and complementary responses.

(A) Proteins with dynamic phosphorylation sites were used to cluster protein-protein interaction data from BioGrid. Green square shows proteins involved in Clathrin

Mediated Endocytosis (CME). (B) Protein interaction network for different GO terms (confidence >0.9 based on experimental data). (C-F) We performed time lapse fluorescence imaging of tubulin and actin structures in BY4741 cells treated with 0.4 M NaCl. (C) Cortical patches were monitored with Sla1-GFP and Abp1-mCherry at a rate of 1 frame per 5s. The impact of salt is represented with kymographs for a time period of 3 min. (D) We observed reduced mobility of spindle microtubules with Tub1-Venus YFP, (E) actin cables and patches with Abp140-GFP and (F) cortical patches and bud neck ring with Syp1-Venus YFP. Temporal changes of these structures under salt treatment are shown in right panels at distinct frame frequencies. See also Figure 16, File S2 and Movie S1-S2.

Dynamic phosphoproteomic analysis provides functional insights into polarization

To further investigate the functional predictive power of dynamic phosphoproteomics, we chose to study two regulated phosphosites on the F-Bar protein Syp1 (Figure 17A). In our competition-growth assay, only phospho-null mutants Syp1 S405A showed a fitness effect (Figure 14A-B). Both residues are located in the middle domain of Syp1. Ser405 is in a region necessary for polarized localization of Syp1 to bud tips (aa 365-565) and Ser347 is located within a region that is required for Syp1 plasma membrane (PM) localization (aa 300-365) [196]. We had previously proposed that Syp1 is central to a network linking cytoskeletal dynamics, endocytosis, monitoring of septin structure and regulation of cell polarity and morphogenesis [24, 197, 198]. To determine whether these phosphosites could be implicated in localization and function of Syp1, we created phosphomimetic (serine to glutamic acid) or phospho-null mutants of Ser347 and Ser405 as GFP fusions and integrated their coding sequences into the genome by homologous recombination or expressed them from plasmids (Extended Experimental Procedures).

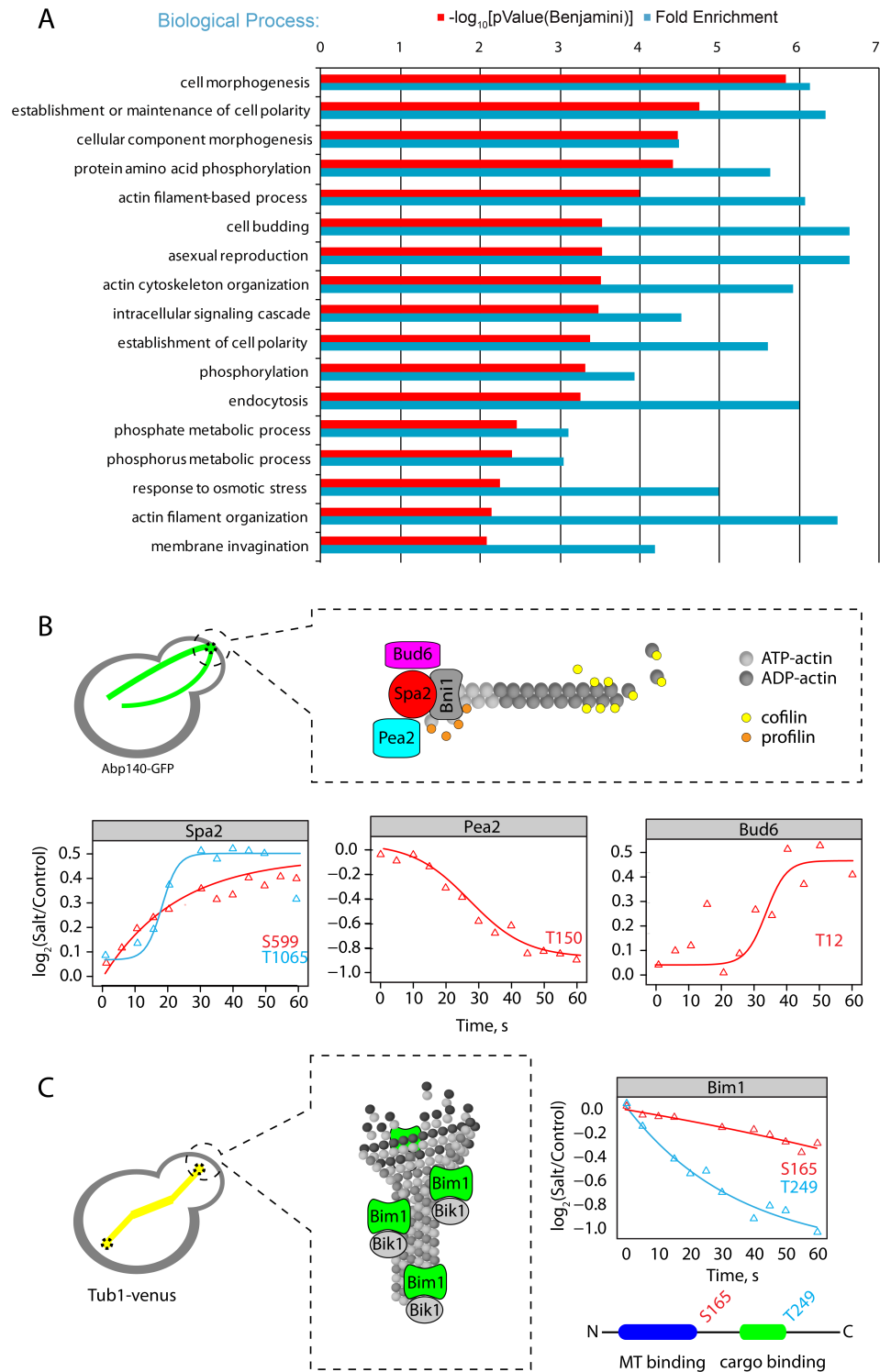


Figure 16 | GO enrichment analysis for differentially regulated phosphoproteins following osmotic shock.

(A) Significantly enriched ($P < 0.01$) GO terms among phosphoproteins containing dynamic phosphosites. Gene ontology enrichment analyses were performed with DAVID bioinformatics resources using the entire *S. cerevisiae* proteome as background. In order to eliminate biases of LC-MS/MS workflow (e.g. towards more abundant phosphoproteins) we performed parallel GO analysis of proteins with static phosphosites and removed overrepresented terms from the final figure. (B) Schematics of Abp140-marked actin cables and F-actin regulation at the bud tip by polarisome proteins Spa2, Pea2 and Bud6 with their respective dynamic phosphosites. (C) Schematic of Bim1-driven microtubule integrity following osmotic shock (assessed with Tub1-YFP reporter) and Bim1 dynamic phosphosites on its N-terminal microtubule (MT) binding domain and C-terminal cargo binding EB1 domain. Related to Figure 15.

Overexpression (OE) of both Syp1 S347A and S347E were not elongated and S347E cells were more circular than wild-type cells despite high expression levels (Figures 7B-C and Figure 18A). Fluorescently labeled Syp1 S347A displayed the normal punctate localization of Syp1 at the PM, while S347E was more diffusely distributed throughout the PM, suggesting that dephosphorylation of S347 is required for Syp1 localization to cortical patches (Figure 17B) [196]. This was in contrast to the polarized elongated phenotype caused simply by OE Syp1 [197]. OE Syp1 S405A also induced an elongated phenotype similar to OE Syp1 and appeared to be normally localized to cortical punctae (Figure 17C and Figure 18B). In contrast, the OE Syp1 S405E mutant was not elongated, but larger than wild-type cells, and appeared localized into PM-associated punctae of larger bodies (Figures 7B-C and Figures S7A-B). It is important to note that S405E was significantly less expressed than wild-type Syp1 ($P < 10^{-16}$) (Figure 18A). These results suggest that Ser347 must be dephosphorylated for Syp1 to localize to cortical patches but localization is not sufficient to induce polarization. If, however, Ser405 is also dephosphorylated,

polarization is induced (Figure 17D). Ser347 could also play a Ser405-independent role in polarization because both phosphomimetic and phospho-null OE mutants were not hyper-polarized.

Finally, since endocytic trafficking controls both symmetrical and asymmetric cell growth we examined the effects of the Syp1 mutants on CME function with our Sla1 and Abp1 markers. The most profound polarization was observed when we over expressed Syp1 S405A in wild-type cells (*SYP1* locus is intact) (Figures 7C and 7E). We also observed polarized endocytic patches at the growing tips of these cells but normal patch movement (Figure 17E). Taken together, our results suggest that dephosphorylation of Syp1 at residues Ser347 and Ser405 functions in the polarization of cell growth, in part through polarization of CME.

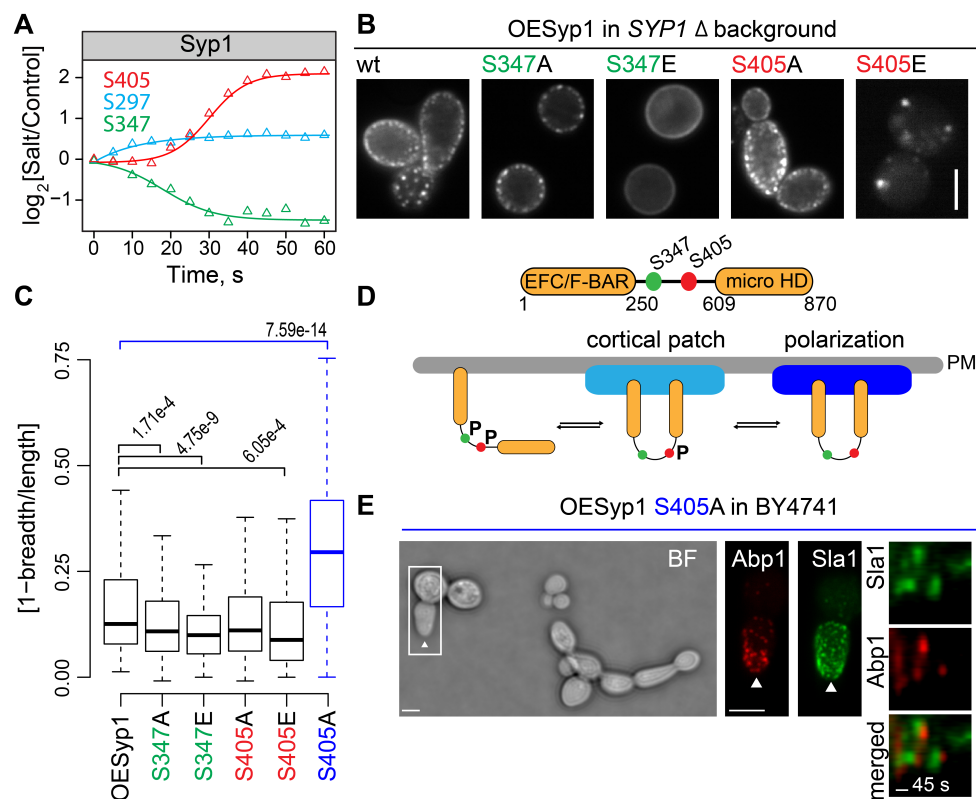


Figure 17 | Syp1 dynamic phosphosites are involved in regulation of morphogenesis.

(A) Three dynamic phosphosites on Syp1 may be implicated in control of polarization and cell growth. (B) We generated phosphomimetic or phospho-null mutants of the Ser347 and Ser405 residues and assessed cell morphology and Syp1 localization of over expressed (OE) Syp1 mutants in *SYP1* Δ deletion background. (C) We determined by morphometric analysis of segmented cells the elongation factor [1-breadth/length] for OESyp1 (n = 293 cells) and S347A (n= 463 cells), S347E (n= 264 cells), S405A (n= 493 cells), S405E (n = 209 cells) mutant strains in *SYP1* deletion background (black boxplots) and also for OESyp1 S405A (n =438 cells) in the wild-type background (blue boxplot). Student t-tests were performed to compare a sampling of 200 cells from OESyp1 to all other strains, *P*-values are indicated if < 0.05. (D) Syp1 was proposed to contain two main domains separated by a flexible middle region from residues 250 to 609. This middle region contains both dynamic phosphosites S347 and S405. *In vivo* N-terminal EFC/F-Bar domain is believed to act in Syp1 plasma membrane (PM) association and the C-terminal microHD domain is necessary for Syp1 interaction with endocytic adaptor Ede1. Syp1 is central to a network linking cytoskeletal dynamics, endocytosis, monitoring of septin structure and regulation of cell polarity. We propose that cortical patch localization of Syp1 requires S347 dephosphorylation whereas Syp1 function in cell polarization is regulated by S405 phosphorylation. (E) We assessed the OESyp1 S405A elongated cell phenotype, its impact on endocytosis by microscopy (bright field and fluorescence images) and behaviour of cortical patch fluorescent markers Sla1-GFP and Abp1-RFP in S405A mutant cells (left and middle panels). Cortical patches behaviour in the S405A strain (wild-type background) were monitored as described above and are represented with kymographs for a time period of 5 min. See also Figure 18.

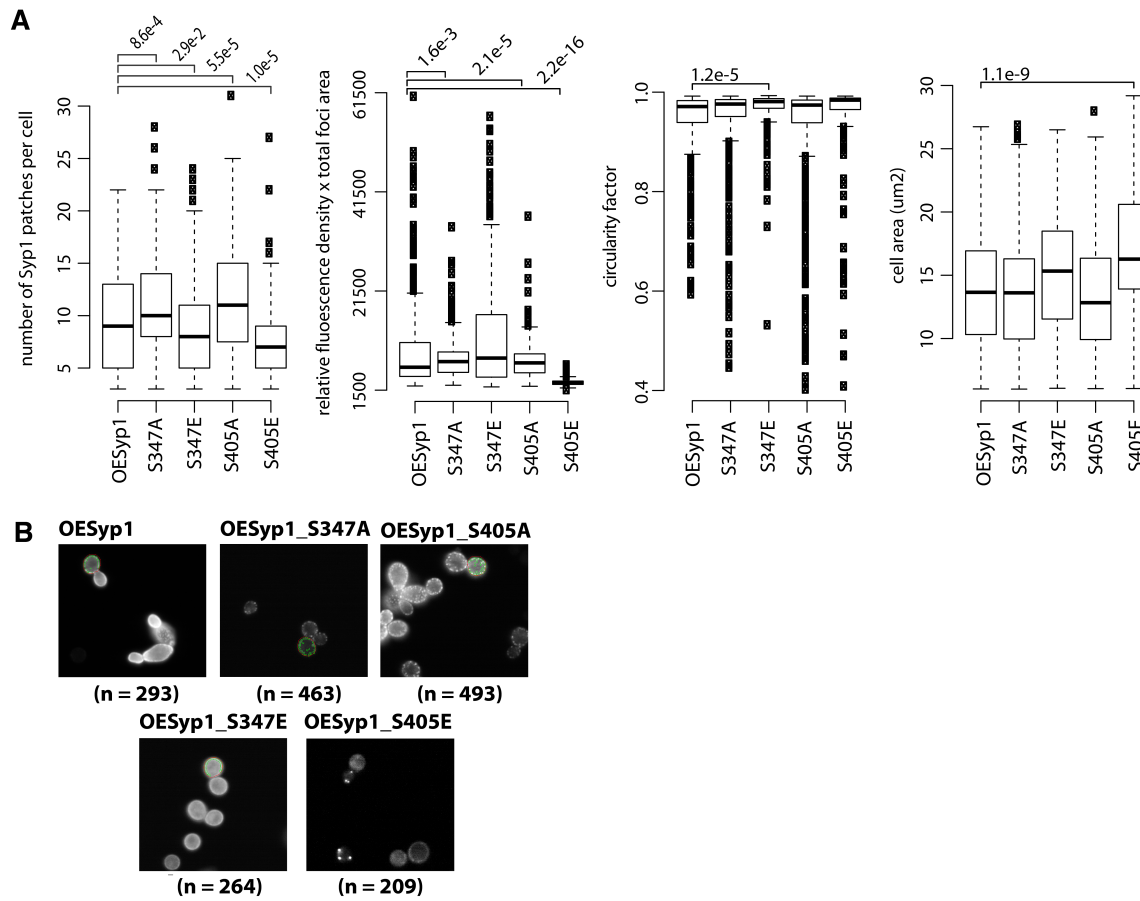


Figure 18 | Characterization of OE Syp1 and S347, S405 mutant strains.

(A) We determined the number of Syp1-GFP marked cortical patches (top left), expression levels of Syp1-GFP defined by the relative fluorescence density per μm^2 (top right), circularity factor (bottom left) and cell size in μm^2 (bottom right) by morphometric and quantitative analysis of segmented cells. T-tests were performed to compare a sampling of 200 cells from OESyp1 to all other strains, p -values are indicated if < 0.05 . (B) Bright-field and fluorescence imaging of over expressed (OE) Syp1 constructs in *SYP1* deletion strain with a segmented cell example and respective number of cells analyzed (n) per strain. Related to Figure 17.

Supplemental Results

Identification of putative phosphosites that regulate actin structures and microtubules

We identified dynamic phosphorylation in protein complexes involved in processes mediated by actin cytoskeleton, including the polarisome and clathrin-mediated endocytosis (CME) [133, 191]. The majority of the sites that we detected have not been reported previously. We did, however, detect a few that are known to have regulatory functions. For example, we detected polarisome protein phosphorylation changes, including of Bud6, which stimulates processive F-actin assembly by the formin Bni1, and the polarity scaffold protein Spa2, which is required for Bni1 localization (Figure 16B) [199]. Interestingly, we did not observe changes in proteins directly involved in actin cable assembly or degradation, including formins, cofilins or profilins, but only in regulators of F-actin assembly (actin-binding proteins Ysc84 and Abp1) and Arp2/3 dependent branching (WASP homolog Las17, WASP-binding protein Lsb3 and verprolin protein Vrp1).

We also observed dynamic phosphorylation of several proteins involved in mitotic spindle assembly, dynamics and checkpoints, including the Tid3 subunit of the kinetochore Ndc80 complex involved in microtubule attachment and spindle checkpoint activities [200], the Clb3 cyclin that regulates M phase cell cycle progression [201] and microtubule-associated proteins Mhp1, Stu2 and Bim1, all implicated in microtubule stability and spindle function [202-204]. For example, Bim1 is a microtubule plus end tracking protein (+TIP), present on astral and spindle microtubules where it promotes their assembly through the Bim1-Bik1 complex (Figure 16C) [204]. We identified two dynamic phosphosites in Bim1, S165 known to mediate binding to microtubule, and T249 a novel site located near the EB1-like domain required for interactions with Aurora protein kinase Ipl1, Stu2, Bik1 and itself. Phosphorylation of the S165 residue during anaphase by Aurora kinase unloads Bim1 from microtubules and induces microtubule depolymerization [205]. We could speculate that the dephosphorylation of S165 following osmotic shock could increase

the affinity of Bim1 for microtubules and delay their disassembly. This could contribute to preserving the spindle core structure until cells adapt and mitosis can continue following osmotic shock.

Discussion

The motivation for studying dynamics of cellular processes has always been driven by the intuitive notion that specific and functionally relevant protein interactions mediated by post-translational modifications should be dynamic in response to external or internal changes of state [206]. This notion has motivated and driven the analysis of dynamic phosphoproteomes [140, 141, 207, 208]. However, we still do not know why only such a small proportion of observed phosphosites are dynamic and whether dynamic phosphosites are more likely functional.

We started from the general assumption that signaling networks have evolved so that kinase- or phosphatase-substrate interactions are made most efficient by the optimization of enzyme binding and specificity for substrate recognition sequences [157-159]. We argued that with such an organization, we would predict that early signaling events (phosphorylation or dephosphorylation) are most likely functional, but slower phosphorylated sites could represent promiscuous phosphorylation that have no functional consequences [22, 23].

We found the HOG response to be complex, integrating a large proportion of the kinases and phosphatases in the cell, and initiating a large number of changes in protein phosphorylation. Based on the conservation of these dynamically modulated sites, they are likely enriched in specific and functional sites but promiscuous phosphorylation must also be occurring over longer time scales, reflected in the lower average conservation of static phosphosites. Static sites are not necessarily non-functional. They may be dynamic and have functions under other conditions or in different time frames following osmotic shock.

Thus, the HOG signaling network appears to have evolved so that promiscuous phosphorylation is slower to appear than functional phosphorylation. The lower conservation of static phosphosites, suggest that they may be the result of promiscuous phosphorylation that may accumulate and persist over more than one cell cycle. While putative functional phosphosites represent a small subset of the phosphoproteome, optimizing specificity in signaling networks may come at a higher cost to the cell than the occurrence of some promiscuous phosphorylation. There may also be a tradeoff between the rate at which kinases and phosphatases act on their substrates and the specificity of kinase- and phosphatase-substrate interactions. Optimization of either could reduce the other and thus, cells may have evolved to achieve the best possible specificity at limited cost [22, 209].

Two final points must be stressed about the interpretation of phosphosite conservation. First, dynamic or static phosphosites that are weakly conserved are not necessarily non-functional but may simply reflect functional sites that have been evolving rapidly. Second, the evolution of transcriptional regulatory networks can be both rapid and extensive and so can protein regulatory networks, such as kinase-phosphatase networks. The evolution of such networks can contribute to both intra- and inter-species diversification and promiscuous phosphorylation may be one mechanism by which signaling networks evolved [210].

We observed a narrow range of kinetic rates for dynamic profiles that may reflect the physical organization of signaling networks and relative abundances of enzymes and their substrates. One condition under which homogeneous rates might be observed would be if the kinase or phosphatase reactions occur at saturation due to their high abundances compared to substrates. It has in fact been noted recently that kinases or phosphatases are indeed often more abundant than their substrates [211]. In addition, kinases and phosphatases can form complexes with their substrates, either directly or through scaffold or adaptor proteins [157-159]. In both cases, maximum efficiency of reactions can be achieved.

Finally, the accurate prediction of functional *versus* non-functional post-translational modifications remains a significant challenge. The strategy we describe here is based on the general idea that good predictions of functionality could be derived based on chemical principles of molecular interactions [21, 212]. The strategy can be applied to other signaling responses and post-translational modifications and may reveal a deeper understanding of the evolution and organization of signaling machineries. In addition, combining information about the conservation of the post-translational modifications with careful analysis of the proportion of a protein that is dynamically phosphorylated may provide the best possible predictions of phosphosite functionality [22, 213].

Extended Experimental Procedures

Cell culture

To allow for quantitative SILAC mass spectrometry we used an S288 strain in which genes encoding de novo arginine or lysine synthetic enzymes Argininosuccinate lyase (ARG4) and Saccharopine dehydrogenase (LYS1) are deleted (S288C LYS1 Δ ::kanMX; ARG4 Δ ::kanMX strain - a generous gift of Ole Jensen, University of Southern Denmark). Cells were then grown in Synthetic Dextrose (SD) supplemented with either ^{12}C -, ^{14}N - (light) or ^{13}C -, ^{15}N - (heavy) lysine and arginine (Cambridge Isotope Laboratories). Cells were inoculated into and grown in SD medium (0.17% yeast nitrogen base without amino acids, 0.5% ammonium sulfate, 2% glucose, appropriate amino acids) supplemented with light or heavy arginine (20 mg/L) and lysine (30 mg/L). In order to prevent arginine to proline metabolic conversion, media were also supplemented with L-Proline (20 mg/l). Typically, after 7-9 doublings, heavy culture incorporated almost 100% of heavy arginine and lysine. Cells were grown until late-exponential phase ($\text{OD}_{600}=0.8-1$).

Cell stimulations

All treatments were performed with cultures at $OD_{600}=1$. Light and heavy cultures were split into 25 mL portions. Heavy cultures were treated with 4 M NaCl dissolved in the culture medium (preheated to 30°C) to a final concentration of 0.4 M NaCl. Light cultures were used as controls and were treated with the corresponding volume of culture medium without NaCl. In order to stop all metabolic activity at specific times, individual light and heavy cultures were combined at fixed interval following treatment (0-60 seconds at 5 second intervals) in ~ 500 ml of liquid nitrogen and stored at -80°C.

Cell lysis

Cells were lysed by mechanical grinding under liquid nitrogen using a Freezer Mill apparatus (BioSpec). Efficiency of the lysis was monitored by microscopy. Lysis efficiency depends on cell concentration and in our case in order to lyse > 90% of cells, frozen cultures had to be ground for 32 cycles consisting of 2 minute grind at maximum intensity with 2 min cool down periods in between. Frozen culture powders were stored at -80°C.

Protein extraction

In order to concentrate and purify proteins from other components of culture media, they were precipitated with TCA. Frozen culture powders were mixed with equal volume of 30% TCA solution and incubated on ice for 2 hours. Then samples were centrifuged at 20,000 x g for 20 minutes at 4°C. Supernatants were discarded and protein pellets were washed in 10 mL of cold 10% TCA and centrifuged one more time. Then pellets were washed in cold acetone and proteins were resolubilized in 8 M urea buffer (8 M urea, 100 mM Tris pH 8.0, supplemented with HALT phosphatase

inhibitor cocktail (Pierce)). Samples were cleared by centrifugation at 40,000 x g for 10 min, the supernatants were transferred into clean tubes and the protein concentrations were measured by BCA assay (Thermo Fisher Scientific).

Enzymatic digestion

Disulfide bridges were reduced by adding dithiothreitol to a final concentration of 5 mM and incubating at 56 °C for 30 minutes. The samples were allowed to cool down to room temperature and the reduced cysteines were alkylated by adding iodoacetamide to 15 mM and incubating for 30 minutes in the dark at room temperature. Alkylation was quenched with 5 mM dithiothreitol and incubation for an additional 15 minutes. Samples were diluted 6 times with 20 mM TRIS pH 8 containing 1 mM CaCl₂ and trypsin was added to an enzyme to substrate mass ratio of 1:50. Proteins were digested overnight at 37°C. Because trypsin cleaves after arginine or lysine, heavy and light versions of every peptide (except the very C-terminal peptide of each protein) should be distinguishable based upon the mass difference between the heavy and light versions of at least one lysine or arginine. After digestion peptide mixtures were acidified by addition of FA to a final concentration of 1%, clarified by centrifugation (20,000 x g 10 min) and desalted on Oasis HLB cartridges (Waters) according to the manufacturer instructions. Peptide eluates were snap-frozen in liquid nitrogen, lyophilized in a speedvac and stored at -80°C.

Phosphopeptide isolation

Tryptic digests were subjected to the TiO₂ enrichment protocol as described previously [214]. Briefly, sample loading, washing, and elution steps were performed in homemade spin columns assembled following the StageTip extraction [215, 216]

and comprised of 200 μ L pipette tip with frit made of SDB-XC membrane (3M) and filled with TiO_2 beads. SDB-XC material has similar hydrophobic properties as C18 and allows for combining phosphopeptide enrichment and desalting steps. Centrifugation speed was set to 2,000 x g. Before peptide loading, columns were equilibrated with 100 μ l of loading buffer (250 mM lactic acid in 70% ACN 3% TFA). Peptides were solubilized in 100 μ L of loading buffer and applied on a TiO_2 column. Each column was washed with 100 μ L of loading buffer followed by 2 x 100 μ l of 125 mM asparagine and glutamine in 70% ACN 3% TFA and 100 μ l of 70% ACN 3% TFA. Subsequent washing with 50 μ l of 1% FA was used to equilibrate SDB-XC frit material. Phosphopeptides were eluted from TiO_2 with 2 x 50 μ L portions of 500 mM Na_2HPO_4 pH 7 and retained on SDB-XC. Peptides were desalted in 50 μ L of 1% FA and subsequently eluted from SDB-XC in 50 μ l of 50% ACN 0.5% FA. Eluates were dried on a speedvac and stored at -80°C .

Off-line fractionation of phosphopeptides

In order to increase phosphoproteome coverage prior to MS analysis, phosphopeptides were fractionated offline by SCX chromatography. Peptides were solubilized in 100 μ L of loading buffer (0.2% FA 15% ACN) and loaded onto StageTips containing 6 mg of Poly-sulfoethyl-A SCX phase. Then columns were washed with an additional 50 μ l of the loading buffer and peptides were eluted in 100 μ L salt steps with 40, 70, 100, 150 and 500 mM NaCl dissolved in loading buffer. Flow-through and salt fractions were dried on a speedvac, resuspended in 15 μ L of 4% FA and analyzed by nanoLC-MS/MS.

nanoLC- MS/MS

SCX fractions obtained after offline fractionation were analyzed by online reverse phase chromatography coupled with an electrospray ionization interface to acquire MS (measuring intensity and m/z ratio for peptides) and MS/MS (fragmentation spectra of peptides) scans. A nanoflow HPLC system (Eksigent, Thermo Fisher Scientific) was used for online reversed-phase chromatographic separation; peptides were concentrated on 5 mm long trap columns (inner diameter 300 μ m) and separated on 18 mm long fused silica capillary analytical columns (inner diameter 150 μ m), both packed with 3 μ m 200A Magic AQ C18 reverse-phase material. Peptides were eluted by an increasing concentration of buffer B (5-40% in 100 min). Following the gradient elution, the column was washed with 80% buffer B and re-equilibrated with 5% buffer B. The HPLC solvent A was 0.2% FA and the solvent B was ACN/0.2% FA. Peptides were eluted into the mass spectrometer at a flow rate of 600 nL/min. The total run time was approximately 125 min, including sample loading and column conditioning. Peptides were analyzed using an automated data-dependent acquisition on a LTQ-Orbitrap Elite mass spectrometer. Each MS scan was acquired at a resolution of 240,000 full width half maximum (at 400 m/z) for mass range m/z 300-2,000 with the lock mass option enabled (m/z: 445.120025) and was followed by up to 12 MS/MS data dependent scans on the most intense ions using collision induced dissociation (CID). AGC target values for MS and MS/MS scans were set to 1e6 (max fill time 500 ms) and 1e5 (max fill time 50 ms) respectively. The precursor isolation window was set to 2 m/z with CID normalized collision energy of 35, the dynamic exclusion time was set to 60 s.

MS Data processing and analysis

MS data were analyzed using MaxQuant [139, 217] software version 1.3.0.3 and searched against the SGD database (<http://www.yeastgenome.org/>) containing 5,904

entries. A list of 248 common laboratory contaminants included in MaxQuant were also added to the database as well as reversed versions of all sequences. For searching, the enzyme specificity was set to trypsin with the maximum number of missed cleavages set to 2. The precursor mass tolerance was set to 20 ppm for the first search (used for non-linear mass re-calibration [217]) and then to 6 ppm for the main search. Phosphorylation of serine, threonine and tyrosine residues was searched as variable modification; carbamidomethylation of cysteines was searched as a fixed modification. The false discovery rate (FDR) for peptide, protein, and site identification was set to 1%, the minimum peptide length was set to 6, and the filter 'labeled amino acid', and 'peptide requantification' functions were enabled. To match identifications across different conditions, the 'match between runs' option in MaxQuant was enabled with a retention time window of one minute. MaxQuant parameters.txt and experimentalDesign.txt files used in this study are listed in Table 4.

Data quality filtering

In addition to FDR, which was set to a maximum of 1% for peptide, protein and phosphosite identification levels, we used some additional criteria to increase data quality. First we considered only peptides for which isotopic abundance ratios ($FC = \text{Salt/Control}$) were measured in at least 10 time points (out of 13). Thus all kinetic profiles are represented by at least 10 points. Then we set a cut-off for phosphosite localization confidence across experiments (time points) to 0.75. Based on these criteria we obtained 5453 high confidence phosphosite kinetic profiles (Table 2). To demonstrate the reproducibility of the results we included preliminary data obtained at a lower temporal resolution and with fewer identified pSites due to LC-MS/MS setup (1DLC and short gradients) (Figure 6E). pSites detected in both studies showed qualitatively similar temporal profiles (Figure 6G). We plotted FC ratios

obtained in 2 studies against each other for each pSite and calculated the slope and R^2 of the corresponding correlation as measures of similarity (Figure 6E-F).

Assessing significance of phosphosites

As in any large-scale phosphoproteomics experiment, the majority of detected phosphopeptides are not affected by the treatment. It is thus required to choose regulated phosphosites prior to subsequent analysis. The standard approach to define regulated sites is based on the value of the fold change (FC) ratio between conditions, e.g. it is often considered that peptides that are either up-regulated ($FC=2$) or down-regulated ($FC=1/2$) by 2 fold have undergone significant changes. Since phosphopeptide enrichment selectivity in our experiment was lower than 100%, we also had kinetic profiles for non-phosphorylated peptides (Table 4) that were not supposed to be affected by any short treatments (we assume that there are no significant changes in protein abundance taking place within 1 min). We used these FC ratios as a true-negative distribution in order to estimate what are significant FC ratios for phosphopeptides ($P < 0.05$ with correction for multiple hypothesis testing). The major limitation of this approach is that phosphosites with low FC ratios can be eliminated. The dynamic nature of our dataset allowed us to apply a complementary method that does not consider values of FC but rather relies on the continuity of consecutive data points in a dynamic trace. The approach has been applied to the analysis of gene expression profiles [164] but is applicable to any kind of temporal data analysis with a sufficient number of measurements (>10). In our case, a kinetic profile was transformed into a pattern signature based on the difference between adjacent FC values (Figure 5E). We identified non-random time traces by using the correlation between random data and the probability $P(\sigma)$ of a trace up-down signature (Figure 5E). By assumption, most profiles are not correlated with the independent time variable and hence will exhibit random fluctuations. The small number of profiles that are correlated will tend to exhibit more regular behavior.

Briefly, the equivalence between up–down properties of random data and the up–down properties of random permutations allowed us to calculate the probability $P(\sigma)$ that a random trace has signature σ of length N .

The probability $P(\sigma)$ that $N + 1$ random time points has a signature σ is :

$$P(\sigma) = \frac{C(\sigma)}{(N + 1)!}$$

Thus a dynamic profile with signature σ is correlated with the independent time variable by the probability $A(\sigma, M)$. The probability that all of M random signatures have frequency greater than $C(\sigma)$ is given by:

$$A(\sigma, M) = F(\sigma) \cdot M$$

We decided to use an $A(\sigma, M)$ cutoff of 0.9, in which $1/[1-A(\sigma, M)]$ represents the number of times one has to repeat a random experiment to find a profile with signature as unlikely as σ . We used both FC-based and pattern-based analyses to obtain a list of regulated profiles. A kinetic profile was considered to be regulated if it had either more than 3 significant FC ratios (621 profile) or if the probability of getting even a single profile in the dataset by chance was lower than 0.1 (345 profiles) (Figures S1C-D). Interestingly pattern-based analysis allowed us to identify 116 significant kinetic profiles, of which 99 were uniquely discovered in pattern-based analysis, some having very low FC ratios that would have remained undetected by standard FC-based approach (Table 3).

Fitting of dynamic profiles

We modeled the phosphosite kinetic profiles with non-linear regression using the Matlab fit type function with the following birth-death model:

$$FC(t) = \left(1 - \frac{c}{\exp\left(\frac{t-d}{a}\right) + 1} \right) + b$$

where t is time, $FC(t)$ is the fold change ratio between conditions ($FC = \text{Salt}/\text{Control}$) and the kinetic profile-specific constants starting values were set to $a = 0.219$, $b = 0.308$, $c = 0.711$ and $d = 0.571$.

We performed a first derivative test to determine the local maximum or minimum rate of change (dFC/dt) of the phosphosite kinetic profiles (Figure 9C and Figure 10A) and also extracted the time at which the maximum absolute rate is observed (dFC/dt_{\max}) (Figure 9C). Fits and values extracted from first derivative are available in Table 3. We applied simple statistics to determine the mean, standard deviation and excess kurtosis ($\mu^4/\sigma^4 - 3$) of the distribution on a \log_{10} scale of dFC/dt for the dynamic profiles. This analysis confirmed that the distribution of dFC/dt_{\max} of dynamic profiles is leptokurtic (kurtosis value of 1.03) compared to the normal distribution with a more acute peak around the mean and fatter tails. This observation is complemented by the fact that 98.5% of the dynamic profile rates are distributed within 2 orders of magnitude (± 2 SD from the mean) or 68.3% within about 1 order of magnitude (± 1 SD).

Next, we interpreted the shapes of the fitted profiles by calculating the second derivative of the birth-death model (Figure 9C). The values and difference between local max and min of the second derivative within the time range of measurements (0 to 60 seconds) allowed us to classify dynamic profiles into: (i) sigmoid-like traces with a positive max and negative min, (ii) exponential-like traces displaying max and min values in the same Cartesian quadrant and (iii), linear-like traces having a difference between max and min smaller than $4e-05$ (Figure 10B). The max and min difference cutoff for linear-like shape classification was determined with the distribution of the second derivative difference of all of the dynamic profiles (Figure 10B).

Clustering of kinetic profiles, GO and PPI network analysis

All regulated kinetic profiles were used for "soft" clustering [218] which offers several advantages compared to "hard" clustering methods. First, it indicates how well corresponding clusters represent temporal profiles. Second, the overall relation between clusters, and thus a global clustering structure, can be defined. Additionally, soft clustering is more robust to noise. We used fuzzy C-means algorithm [219]. Analysis and visualization were performed in the R environment (<http://www.r-project.org/>) with the Mfuzz package [220]. Optimal setting of the "fuzzifier" parameter was 1.242 as estimated with the mestimate function. In order to find the optimal number of clusters, we performed repeated soft clustering for a range of cluster numbers from 2 to 20 and calculated the minimum centroid distance (minimum distance between two cluster centers produced by c-means clustering) [221]. Based on this analysis we chose to use 6 clusters. All regulated (both pattern and FC-based analysis) profiles (737) were used for clustering which resulted in 596 profiles belonging to 332 proteins being assigned to one of the clusters with membership value higher than 0.5. These sites were considered "dynamic" (Table 3). It has to be noted that there still could be biologically regulated phosphosites that were not selected by our filtering procedure. Particularly it could be low-abundance phosphosites for which precise quantification is more difficult due to low intensity of the signal. Thus corresponding kinetic profiles could be masked by technical MS noise.

Gene ontology enrichment analyses were performed in DAVID bioinformatics resources [222, 223] for proteins containing dynamic phosphosites against whole *S. cerevisiae* proteome as background. In order to eliminate GO terms that could be enriched due to the nature of our experiment (e.g. MS detection can be biased towards high abundant proteins) we performed parallel GO analysis for proteins containing only static phosphosites and then subtracted the results from our initial analysis. We thus treat enrichment in the static data set as background.

A protein-protein interaction network was built in STRING for all proteins containing dynamic phosphosites [224]. All interaction predictions were based on experimental methods with the minimal confidence score of 0.9. Results were visualized in Cytoscape network visualization and analysis [225-227]. Alternatively, we clustered the dynamic phosphoproteins using an association matrix based on the number of links that connect two proteins, described in [24]. This approach also allows visualizing non-direct interactions between proteins that belong to the same complex. Briefly, the interaction network was retrieved from Biogrid [228, 229] and organized into an association matrix with entries for pairs of dynamic phosphoproteins that range between 0 and 1. Values were calculated as $1/d^2$, where d is the shortest path in the network between these two proteins. A hierarchical agglomerative average linkage clustering with the uncentered correlation coefficient as the distance matrix was then applied to the association matrix. We visualized these interactions using iVici (<http://michnick.bcm.umontreal.ca/ivici/>) [24].

We performed kinase prediction for our dynamic phosphosites (60 sec) as well as those affected after 5 and 20 min upon osmotic stress using PhosphoSiteAnalyzer Software [187] based on NetworKIN algorithm [188] and we used MotifX [181, 182] to look for over represented linear motifs in our data. We used default settings (min. occurrences = 20, significance = 0.000001) and whole yeast proteome as background.

Rates of evolution of phosphosites

Rates of evolution were determined for all phosphosites as described previously by Landry *et al.* [23]. The analysis was performed on the subset of peptides that were monophosphorylated. We considered phosphosites in both ordered and disordered protein regions. We determined a significant difference in distribution of rates of evolution (p -value = 0.0014) with a Kolmogorov-Smirnov test between the dynamic

and static sites. No significant difference in rates of evolution (P-value = 0.3420) was observed between a literature-curated set of functional phosphosites [230] and our dynamic set of phosphosites.

Site-directed mutagenesis

To examine the fitness effects of dynamic and static phosphosites on Hog1, Rck2, Gpd1, Bud6, Bim1, Syp1 and Sla1 and the potential functions of Syp1 dynamic phosphosites Ser347 and Ser405, we created phosphomimetic (Ser-Glu) and/or phospho-null (Ser-Ala; Thr-Ala; Tyr-Ala) mutants of these residues. Disruption of dynamic phosphosites was achieved using a standard site-directed mutagenesis protocol with the high fidelity AccuPrime DNA polymerase (Invitrogen) and DpnI restriction enzyme (NEB). Gene-specific primers for site-directed mutagenesis were designed using Primer-BLAST online software [231] and mutations were performed on either MoBY-ORF plasmids for Hog1, Rck2, Gpd1, Bud6, Bim1, Syp1 and Sla1 genes [190] or the budding yeast ORF collection BG1805 vector (Open Biosystems) containing the Syp1 gene. We used distinct mutagenic primer pairs to generate the mutants listed below. All ORF mutations were confirmed by sequencing.

Phospho-null mutants of MoBY-ORF plasmids were used as is with their wild type counterparts in the competition growth assays (see below). Mutated Syp1 sequences in BG1805 were then cloned into the Gateway destination vectors pAG406GPD-ccdB and/or pAG416GPD-ccdB-EGFP using Gateway cloning technology (Invitrogen). These Syp1-encoding plasmids were transformed into the BY4741 cellular background and integrants were selected in uracil-depleted medium and final clones were confirmed by sequencing. Constructs in pAG406GPD vector allowed genome integrated expression of coding sequences in BY4741 Sla1-GFP Abp1-mCherry cells whereas constructs in pAG416GPD-EGFP were expressed from plasmids in BY4741 SYP1 Δ cells.

Assessment of phospho-null mutant fitness through competition-growth

Target phosphosites were selected amongst dynamic proteins involved in the main HOG response and complementary actin and tubulin cytoskeletal responses. We successfully generated 18 phospho-null mutants on 7 proteins that showed a fitness defect under salt conditions when deleted. Our set of phospho-null mutant phosphosites consisted of 13 dynamic and 5 static pSites. Phospho-null mutants were expressed from MoBY-ORF p5472 plasmids and we measured their performance to complement their respective deletion strains. We considered only dynamic and static phosphosites with rates of evolution below 1.8 [23].

Each phospho-null mutant strain was also transformed with a p413 plasmid coding for mCherry monomeric RFP and the wild type strains with a p413 plasmid coding for EYFP. Both fluorescent reporters were expressed under the control of a constitutive ADH1 promoter. Competent cells of respective deletion strains were co-transformed with the specific mutant or wild type ORF and fluorescent marker expression plasmid combinations and co-integrants were selected in uracil-histidine-depleted medium supplemented with geneticin.

To assess fitness of phospho-null mutants in competition growth, the mutants and their corresponding wild type protein-expressing strains were cultured together starting from OD₆₀₀ of 0.5 and mixed in equal quantities, diluted 1:100 and grown in competition at 30°C for 5 days in normal LFM or LFM supplemented with 1M NaCl. Cells were diluted 1:50 once or twice per day to keep them in exponential growth. OD₆₀₀ of cultures were monitored with an automated Spectra MAX 190 microplate spectrophotometer (Molecular Devices). Fluorescence of each population in competition was monitored every 8 to 16 hours with a SpectraMax Gemini XS microplate reader spectrophotometer (Molecular Devices). Absorbance and fluorescence emissions were acquired on samples dispensed in special optics 96-well

plates (Corning Costar 3614). Fluorescence acquisitions for the EYFP channel were conducted with excitation fixed at 485 nm and emission at 535 nm, whereas acquisitions on the RFP channel were conducted with excitation at 570 nm and emission at 620 nm.

Analyses were performed in the R environment, respective mCherry and EYFP relative fluorescent units were normalized and trends in population fraction changes were fitted to a bounded exponential equation (Figure 14). To determine the amplitude of single population fraction changes, we subtracted the initial value (0.5) from the respective time-point values. To determine a change in population fraction we calculated the respective amplitude mean for the concatenated time points 24 hours to 120 hours ($n = 72$) and we used control strain BY4741 mixed in competition with itself to perform a Welch's t-test with a significance level cutoff of $P < 0.05$ (Figure 14B-C). With this approach we calculated that a proportion of 0.72 (13 out of 18) phospho-null mutants showed a fitness effect with a statistical significance of $P = 0.0481$ (binomial test).

Fluorescent protein-tagged reporter strains

All strains for visualizing actin cortical patches, actin cables and microtubules contained cellular coding sequences for fluorescent proteins integrated into the genome 3' to reporter protein ORFs. The fluorescent tags were integrated by homologous recombination as described previously [24]. GFP constructs (Sla1-GFP and Abp140-GFP) were a generous gift from J Vogel at McGill University. Abp1-mCherry, Tub1-Venus and Syp1-Venus were tagged via homologous recombination by amplifying the HPH resistance cassette from pAG32-mCherry or pAG32-Venus YFP (yellow fluorescent protein variant) [232] with primer tails with homology to flanking sequences to the ABP1, TUB1 or SYP1 loci respectively. BY4741 strain was

transformed with the respective PCR cassettes, selected for HPH resistance and confirmed by diagnostic PCR.

Microscopy

For experiments in Figures 6C-F, 7E (left panels) and Movies S1-S2 we used the microfluidic ONIX platform with Y04C plates (Cellasic). Cells were grown in low fluorescence medium (LFM) [233] to an OD₆₀₀ of 0.6 and were diluted 1:3 before loading into the chambers. Salt treatment was performed in LFM with 0.4 M NaCl under continuous stable pressure of 5 psi. Fluorescence images were acquired with a Cool SNAP HQ camera on a Nikon TE2000 inverted microscope equipped with a 100X/1.45 plan APO lambda oil objective (Nikon) and respective FITC (Chroma 41001HQ), EYFP (Chroma 49003ET) and mCH/TR (Chroma 49008ET) dichroic cubes. Time course images were acquired for 5-30 min with a continuous flow of LFM or LFM plus 0.4 M NaCl into the immobilization chambers. Two color images were collected sequentially from a single focal plane at frames rates of 5s for Abp140-GFP, Sla1-GFP and Abp1-mCherry, 30s for Syp1-venus YFP and 60s for Tub1-venus YFP. Image analysis and processing of movies and kymographs was performed with NIS elements (Nikon).

Alternatively, for experiments in Figures 7B, 7C, 7E and Figure 18 concanavalin A (Sigma-Aldrich ConA # C-2631) was used as a binding agent for imaging on glass bottom 96 well plates (Matrical Bioscience MGB096-1-2-LG-L). Each well was loaded with 0.1% of ConA solution at room temperature for 15 minutes. ConA was removed and wells were washed with sterile water. ConA was activated with 20 mM CaCl₂ and 20 mM MnSO₄ solution and incubated for 15 min at room temperature and washed once again with sterile water. Cells were grown in complete LFM to an OD₆₀₀ of 0.6, diluted 1:5 into wells and incubated for 10 min at room temperature allowing for cells attachment. Images were collected on an InCell 6000 automated confocal microscope

configured with a 100x/0.9 Plan FLUOR objective (Nikon) and 488 nm laser diode and FITC 525/20 emission filter for GFP fluorescence (Syp1-EGFP and Sla1-GFP) or 561 nm DPSS laser and dsRed 605/52 emission filter (GE healthcare life sciences) for Abp1-mCherry. Two color images were collected sequentially on a single focal plane with an exposure time of 100 ms and a confocal slit of 2AU. The temperature was maintained at 30 °C.

Image analysis was performed with InCell Developer (GE healthcare life sciences). We used automated cell and Syp1 vesicle top-hat segmentation on phase-contrast and GFP images respectively to define objects for morphometric measurements and quantification of fluorescence. For each strain we concatenated the segmented cells and their linked vesicles from 9 fields of view. Sample cell counts for each mutant strain were as follows: OESyp1 (n = 293 cells), S347A (n= 463 cells), S347E (n= 264 cells), S405A (n= 493 cells) and S405E (n = 209 cells) mutant strains in SYP1 Δ background and OESyp1 S405A (n =438 cells) in the wild type (SYP1 locus intact) background. From these objects, we extracted the Syp1 vesicle count per cell, the cell and vesicle area (μm^2), the cell form factor which estimates circularity, and length (μm) of the cell longer and shorter perpendicular axes of symmetry to calculate the cell elongation factor. As the GFP signal was limited to Syp1 patches and membrane considered as segmented vesicles, we extracted the integrated density in each vesicle and calculated the level of relative fluorescence per cell. Specifically, for each cell we determined the total integrated density multiplied by vesicle area and corrected for background by subtracting mean fluorescence of background multiplied by total vesicle area. We performed a two-sample t-test to determine if the extracted measurements differed between the Syp1 and all other mutant strains. A random sampling of 200 cells from each strain allowed the pairwise analysis with a significance level cutoff of $P < 0.05$

Supplementary information

Supplemental information (SI) includes seven figures, supplemental results and extended experimental procedures which are inserted in Chapter 2 above. The three tables in excel format, two supplemental files and two movies are produced in Appendix 2.

Acknowledgements

The authors thank Jacqueline Kowarzyk for invaluable assistance and advice for growth-competition assays. The authors acknowledge support from CIHR grants MOP-GMX-152556 (SWM), MOP-GMX-231013 (SWM, PT), and NSERC grant 311598 (PT). The Institute for Research in Immunology and Cancer (IRIC) receives infrastructure support from the Canadian Center of Excellence in Commercialization and Research, the Canadian Foundation for Innovation, and the Fonds de recherche du Québec - Santé (FRQS).

CHAPTER 3 | Endocytosis caused by liquid-liquid phase separation of proteins

AUTHORS & AFFILIATIONS

Louis-Philippe Bergeron-Sandoval¹, Hossein Khadivi Heiris², Adam Hendricks², Allen Ehrlicher², Paul François³, Rohit V. Pappu⁴ and Stephen W. Michnick^{1,5*}

¹Département de Biochimie, Université de Montréal, C.P. 6128, Succursale centre-ville, Montréal, Québec, H3C 3J7, Canada.

²Department of Bioengineering, McGill University, Montreal, Quebec, H3A0C3, Canada.

³Ernest Rutherford Physics Building, 3600 rue University, McGill University, Montreal, Québec, H3A2T8, Canada.

⁴Department of Biomedical Engineering and Center for Biological Systems Engineering, Washington University in St. Louis, One Brookings Drive, Campus Box 1097, St. Louis, Missouri 63130, United States.

⁵Centre Robert-Cedergren, Bio-Informatique et Génomique, Université de Montréal, C.P. 6128, Succursale centre-ville, Montréal, Québec, H3C 3J7, Canada.

CONTACT

Correspondence should be addressed to S.W.M. (stephen.michnick@umontreal.ca)

Authors contributions

For this publication, I participated in the research conceptual design, performed all biological experiments and optical tweezers data collection. HHK participated in OTs data collection and performed OTs data analysis. I also developed the adhesive mechanical model under supervision of HHK and PF. Specifically, L.P.S.B. and S.W.M. designed all of the research and R.V.P. helped in designing part of the research; L.P.S.B. performed biological research; L.P.S.B. and H.K.H. performed micro rheology experiments; L.P.B.S., H.K.H., A.J.E. and A.G.H analyzed micro rheology data; L.P.S.B., A.J.E. and S.W.M. analyzed biological data; L.P.B.S., H.K.H. and P.F. developed physical droplet model; L.P.S.B., R.V.P., and S.W.M. combined physical models with data analysis; all authors wrote the paper.

Context of the research

Beyond fine tuning of protein function and recruitment through post-translational modifications, we believe that key protein domains participate in the assembly of endocytic proteins through phase separation. What common feature drives the Sla1, Sla2, Ent1, Ent2, Yap1801 and Yap1802 proteins to coalesce together and readily transit from single to binary aqueous phases?

Sequence encoded information, shown by the meta-predictor PONDR-FIT [234], suggest that these proteins are in fact intrinsically disordered proteins (IDPs) with defined disordered (*low complexity*) domains (Figure 19). These domains perfectly match with previous predictions for prion domains (PrDs) [47] also made for Sla1, Sla2, Ent1, Ent2, Yap1801 and Yap1802. PrDs could mediate multiple interactions within single or multiple binding partners and aggregate proteins together. Furthermore, detailed analysis of prion-like proteins in yeast revealed a strong

enrichment in QN-rich proteins that are associated with the cortical actin network and endocytosis [56].

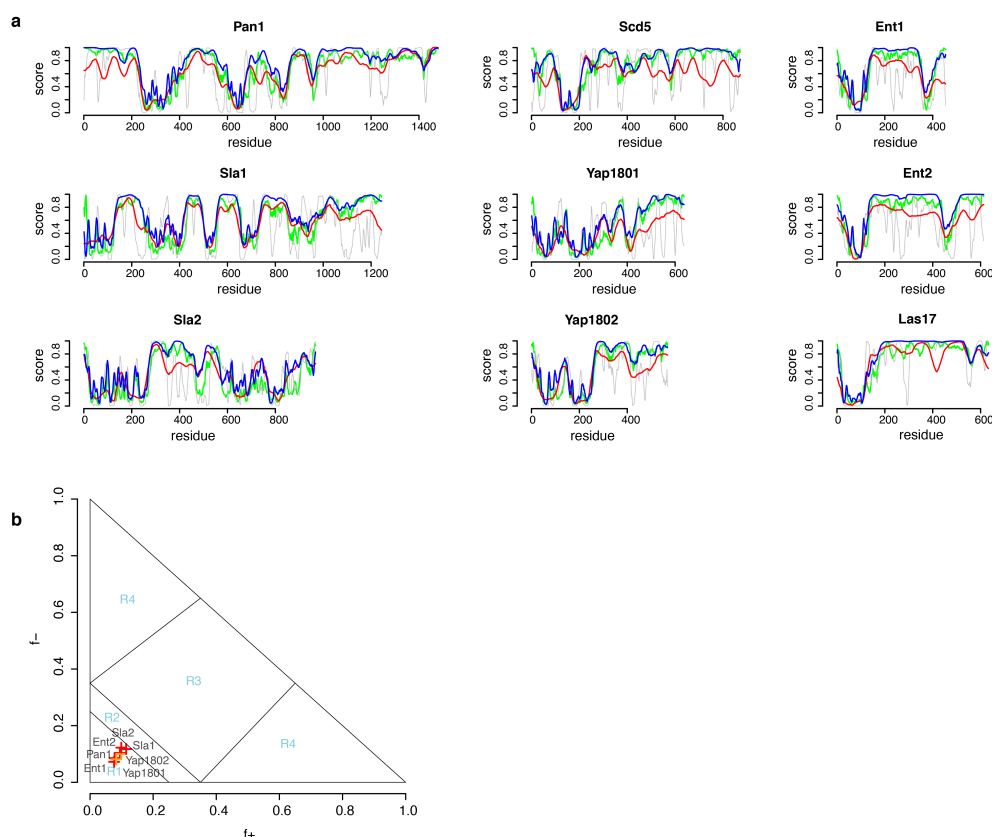


Figure 19 | Adaptor-coat endocytic proteins predicted to be intrinsically disordered and behave as globules in poor solvent regime.

(a) We investigated the disorder of key CME coat components with the online algorithm DisCons. Respective Fasta sequences were inputted into the online service and we extracted four distinct computational predictions for protein disorder; VL3, VSL2, VLXT and P-FIT. These were plotted together in protein respective panels. (b) To further assess the possible state that CME disordered coat protein can adopt, we analyzed our sequences with the localCider algorithm. Fraction of negative and positive residues for each protein was plotted on a Das-Pappu diagram of states.

From an exhaustive catalog of 93 proteins obtained from SGD [235] with the search words CME, 10 proteins have SH3 interaction domains and 13 contain PrD domains of low complexity. Hypergeometric enrichment analysis of these subpopulations confirms a significant enrichment of both SH3 proteins ($P = 4.6 \times 10^{-16}$) and PrD proteins in CME ($P = 3.0 \times 10^{-5}$).

The presence of both type of domains could play a key role in aqueous-aqueous phase separation of these protein. Proteins with multiple SH3 domains (Sla1 contains 3 SH3 domains) can make multivalent interactions and are sometimes shown to phase separate, as the Nck-WASP system [3]. Whereas proteins with PrDs are predicted to form prionic aggregates or assemble through phase separation [56], consistent with our hypothesis.

For 5 out of 13 of these proteins, the PrD domain is located at the C-terminal region. They correspond to our IDPs of interest Sla1, Ent1, Ent2, Yap1801 and Yap1802. Analysis of the spatio temporal behavior of these proteins, with fluorescent tags encoded into their open reading frame, reveals a coordinated process with low variability in both time and space [236], indicative of phase separation.

We further confirmed with the CIDER computational tool [237] that these IDPs have the potential to coalesce together. The analysis of the fraction of positive (+) and negative (-) residues reliably predicts the conformation of IDPs and is mapped onto the Das-Pappu diagram of state [100]. For all the analyzed protein sequences, we obtained +/- fractions of 0.13 (or less) and a kappa value of 0.22 (or less), kappa informs on the charge mixing along the sequence [100] (Figure 19). These values indicate a collapsed globule conformation in aqueous solution (*poor solvent regime*) for Sla1, Sla2, Ent1, Ent2, Yap1801 and Yap1802 (Figure 19). Phase separation of these globules into a condensed phase would favor more extended protein states and intermolecular interactions (*cohesive energy*) required for their mutual assembly [7].

Based on these molecular clues, we propose that the intrinsically disordered coat elements with PrD domains Sla1, Ent1, Ent2, Yap1801 and Yap1802 phase separate into an aqueous droplet at the cortical site of CME. Presence of SH3 domains, proline rich motifs (PRMs) and also PrDs on many other proteins involved in CME suggest phase separation could be a common strategy to organize matter on cortical sites. The segregation observed in space and time of subgroups of these proteins could reflect the coalescence of immiscible bodies, with distinct material properties and functions.

I present in this chapter an alternative and more comprehensive mechanism for CME-mediating disordered proteins to coalesce on cortical site and provide energy to bend the membrane to drive endocytosis.

Endocytosis caused by liquid-liquid phase separation of proteins

Louis-Philippe Bergeron-Sandoval, Hossein Khadivi Heiris, Adam Hendricks, Allen Ehrlicher, Paul François, Rohit V. Pappu and Stephen W. Michnick

Summary

Clathrin-mediated endocytosis (CME) underlies intra- and extracellular material trafficking in eukaryotes, and is essential to protein metabolism, intercellular signaling, membrane remodeling and other cell regulatory processes. Although CME is usually driven by F-actin polymerization, membrane invagination can also occur through unknown actin independent mechanisms. Here, we present evidence that CME is driven by the accumulation of proteins at sites of endocytosis initiation that undergo liquid-liquid phase separation to form viscoelastic droplets. The surfaces of these droplets, bind to the membrane and surrounding cytosol and generate the work required to drive membrane invagination. The proposed mechanism expands the repertoire of functions of membraneless organelles that form via liquid-liquid phase separation to include their ability to do work due to soft interfaces that shape and organize cellular matter.

Introduction

Evolution has resulted in numerous innovations by which morphogenesis of organisms occurs within limits imposed by physical and chemical constraints on the underlying biochemical processes [14, 15]. At the cellular level these biochemical processes include active polymerization of cytoskeletal proteins [238], motor protein regulation of polymerization [239] and cytoplasmic transport [143, 149], the generation and maintenance of osmotic gradients [240] and peptidoglycan cell walls [241]. However, the mechanical forces that drive some subcellular mechanics remain a mystery. This includes the membrane invagination and vesicle formation process called clathrin-mediated endocytosis (CME) [129, 242, 243]. In the baker's yeast *Saccharomyces cerevisiae* CME is preceded by the spatially focused accumulation of a number of proteins on the plasma membrane, among which are those that encode low amino acid sequence complexity and structurally disordered "prion-like domains" (PLD) (Figure 20a) [56, 120, 123, 124, 236, 244]. Here, we demonstrate that membrane invagination can arise from liquid-liquid phase separation (demixing) of PLD-containing proteins from the cytosol. Demixing of these proteins results in formation of a droplet, which, by virtue of its viscoelastic properties, binds to and deforms plasma membrane and cytosol to which it binds. Demonstration that phase separated droplets can perform mechanical work expands the repertoire of known protein droplet functions to include the ability to do work at the droplet surfaces and their interfaces. Similar mechanisms may govern or contribute to other membrane shaping, invagination and budding processes that are involved in the cellular material uptake, secretion, and cell shape remodeling.

In *S. cerevisiae*, the dominant force for vesicle generation in CME is branched actin assembly, which is required to compete against intracellular turgor pressure and membrane tension to drive the invagination of the plasma membrane [127, 128, 243, 245]. If, however, turgor pressure is eliminated, CME in *S. cerevisiae* cells can also occur independent of actin polymerization [129].

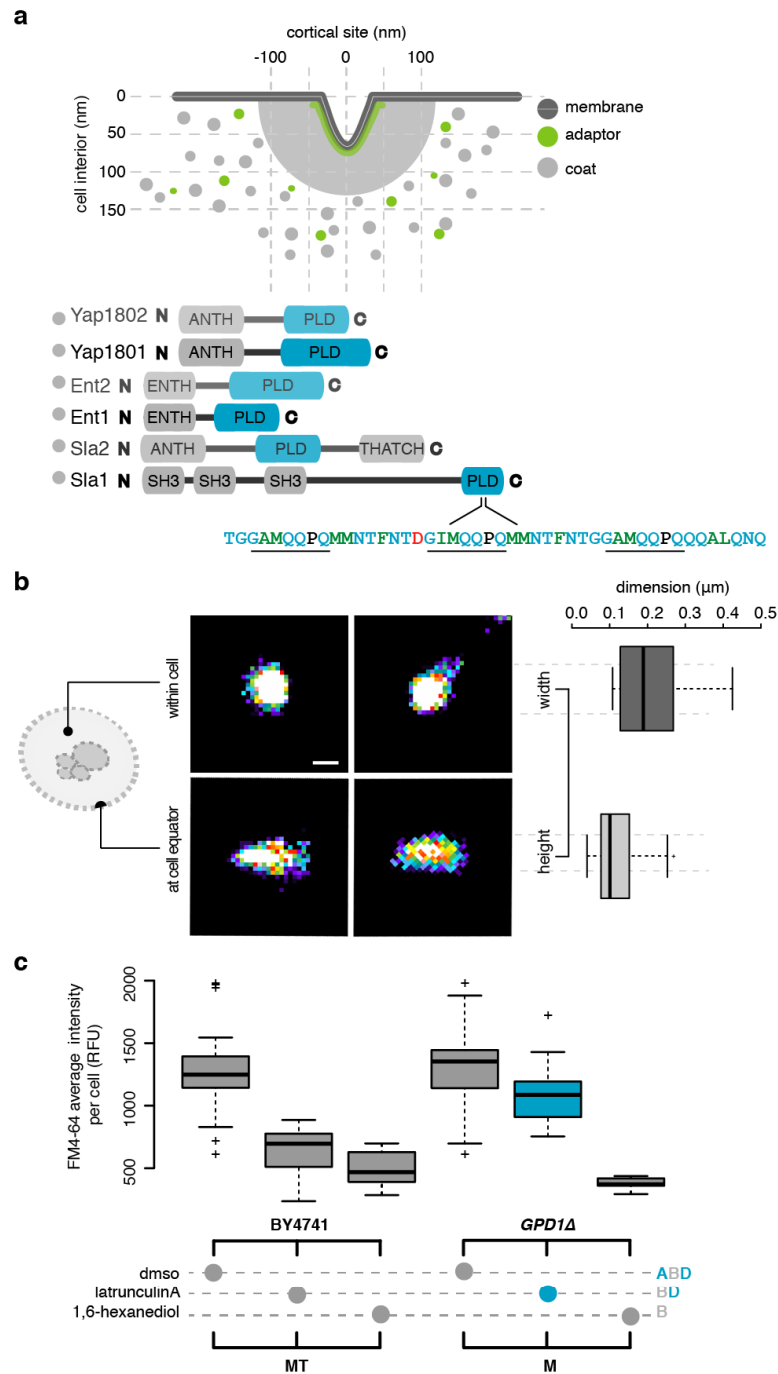


Figure 20 | Assembly of proteins into a cortical droplet drive clathrin-mediated endocytosis.

(a) (Upper panel) Illustration of the geometry of a plasma membrane (dark grey) invagination into the cell during clathrin-mediated endocytosis (CME). 70 nm

invagination is required for vesicle scission to occur. Electron microscopic data suggest that clathrin-coated plasma membrane patches are surrounded by a cortical body of ~200 nm diameter (light grey) before appearance of actin structures. Clathrin heavy and light chains (Chc1 and Clc1) interact with adaptor proteins (Ede1 and Syp1) to form a lattice on the membrane (in green). Subsequently, early coat proteins (light grey), such as Sla1/2, Ent1/2, and Yap1801/2, directly bind to the adaptor-clathrin lattice and form the cortical body (in grey). (lower panel) Coat proteins contain “Prion-like domains” (PLD, in blue) that include tandem repeats of asparagine and glutamine. (b) Geometry and size distribution of coat protein Sla1-GFP at cortical sites measured using super-resolution microscopy (dSTORM). Lateral x, y resolution was ~10 nm. Pseudo-color reconstructed images show circular structures (left panels) when viewed from the top, or within cells (left, upper), but form narrow ellipses when imaged at the equator of cells (left, lower). Automatic segmentation and morphological analysis (right) were performed on these reconstructed images to determine the width (209 ± 10 nm) and height (118 ± 6 nm) of cortical bodies (mean \pm sd; n = 250), consistent with other electron and light micrographic evidence. (c) Lipophilic cargo membrane-labelling dye FM4-64 is taken up into vesicles by CME in wild type (left) and *GPD1* Δ cells (eliminates turgor pressure; right) treated with either DMSO, latrunculin A (prevents F-actin polymerization) or 1,6-hexanediol (disrupts liquid-liquid phase separated protein droplets). Each boxplot shows the relative fluorescence units of n = 50 cells. Note that *GPD1* Δ cells can undergo CME in the absence of F-actin polymerization (blue) because there is no turgor pressure in these cells (Figure 22-23).

Alternative mechanisms to explain actin-independent membrane invagination in CME include intrinsic twisting of the membrane by the clathrin matrix, binding of curved BAR (Bin/Amphiphysin/Rvs) domain-containing proteins, protein domain insertion in the membrane bilayer, or steric repulsion of coat and adaptor proteins due to their crowding at cortical CME nucleation sites. Although these models are physically

plausible, as demonstrated in model systems, their importance *in vivo* remain controversial (detailed in Material and Methods) [122, 127, 246]. For instance, deletion of the only F-BAR domain-containing protein that accumulates on cortical sites prior to excision, Syp1, does not affect membrane invagination (Figure 21) [247].

A potential mechanism that could drive actin-independent CME in yeast was suggested to us by the observation that there is a common amino acid sequence pattern found among coat and adapter proteins. Several of these proteins have PLDs (Figure 20a) [47, 56]. Such proteins are known to phase separate *in vitro* and in cells to form spherical condensates or droplets that are hundreds of nanometers to micrometers in size and having a range of viscoelastic properties [1-8, 85, 142]. We postulate that such droplets exist at CME initiation sites and that, owing to their viscoelastic properties and interfacial tension bind to the plasma membrane adaptors and generate a force that drives invagination of the membrane [248-251].

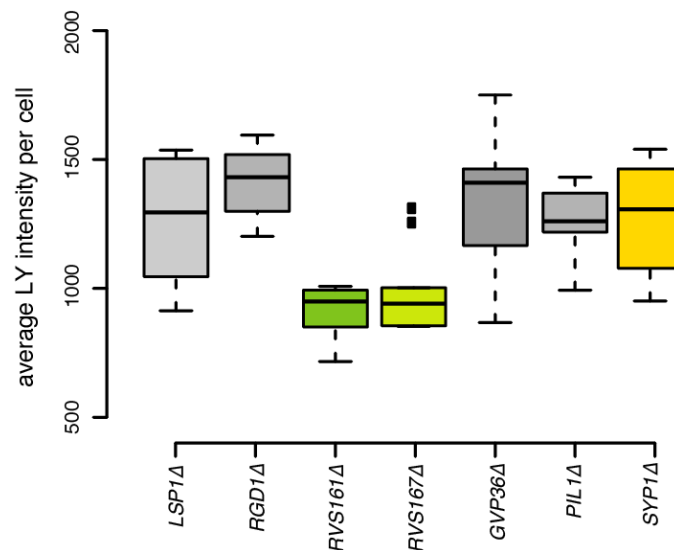


Figure 21 | Syp1 protein is the only BAR domain protein recruited to CME nucleation sites prior to F-actin polymerization and is not required for CME.

F-BAR protein Syp1-mCherry and N-BAR proteins Rvs161-mCherry and Rvs167-mCherry (scission phase) were colocalized with both Sla1-GFP (early phase marker)

and Sac6-GFP (late actin phase marker). Line scan analyses on 2-channel images were performed across the Sla1-GFP or Sac6-GFP puncta and plotted on 8-bit intensity range. LY uptake was assessed for each strain by fluorescence intensity (n = 100 cells).

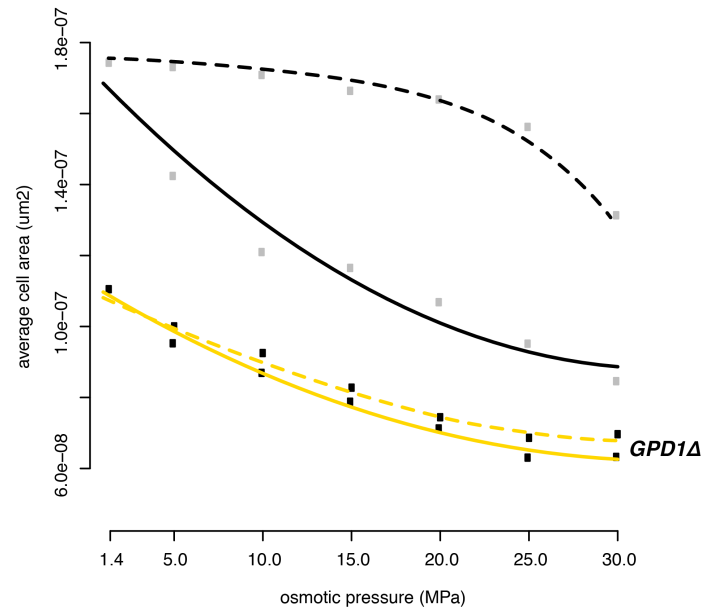


Figure 22 | *GPD1Δ* cells cannot maintain turgor.

To detect turgor pressure and cell size adaptation to osmotic shock in wild type (black) and *GPD1Δ* strain (yellow), we monitored by fluorescent microscopy the cross-sectional area (μm^2) of shocked cells (solid lines) and adapted cells (dashed lines) in water-glycerol binary solutions from 1.4 MPa to 30 MPa. Points represent mean area values (n=200 cells).

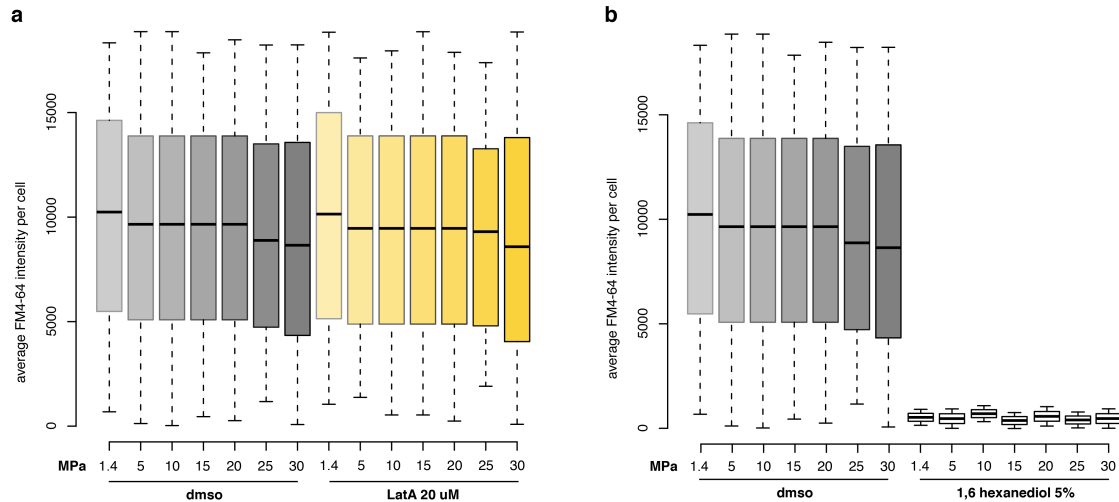


Figure 23 | Membrane-associated probe (FM4-64) uptake.

was quantitatively assessed by fluorescence imaging. (a) *GPD1Δ* strains undergo normal CME in the absence of actin polymerization (Latrunculin A-treated), (b) but not when treated with 1,6-hexanediol, $n = 900$ cells for each condition.

Results and discussion

PLD-containing CME proteins accumulate and phase separate at cortical sites

Evidence that a protein droplet (henceforth called the cortical droplet) could form at CME sites include first, electron and light microscopic studies that reveal a region surrounding CME membrane invaginations and mature vesicles of ~200 nm diameter that is devoid of ribosomes [121, 126]. This “exclusion zone” thus appears to present a physical barrier to large molecular complexes at least as large as ribosomes (> 10 nm) [121]. Furthermore, we and as others have observed an object at cortical sites of ~200 nm diameter by super-resolution imaging of Sla1 in cells treated with Latrunculin A (LatA), an inhibitor of actin polymerization. The exclusion zone cannot, thus, be attributed only to F-actin bundles (Figure 20b, Figure 24) [126]. Our results agree with quantitative immuno-EM data which show that many endocytic coat proteins (including Sla1/2 and Ent1/2) assemble into a hemisphere of similar dimensions,

consistent with a protein droplet that associates with membrane on cortical sites [120, 252].

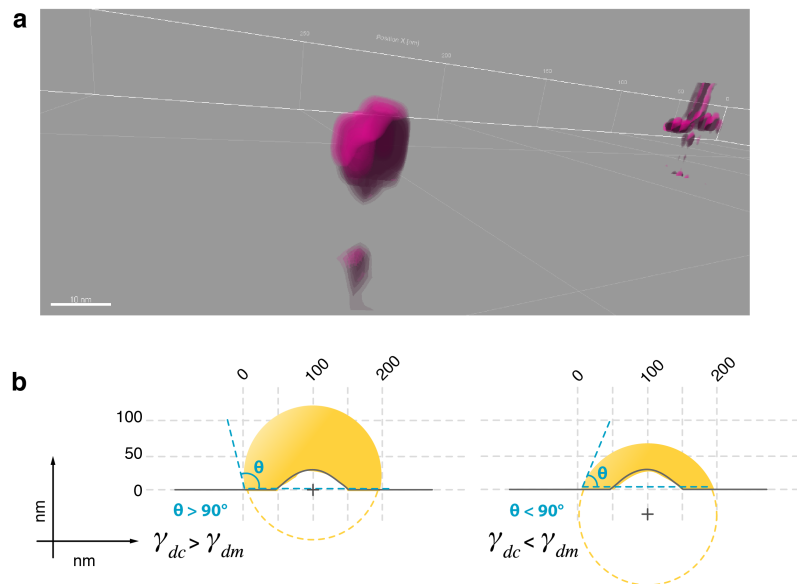


Figure 24 | Geometry of coat protein distribution at cortical sites with super-resolution (dSTORM) fluorescence imaging of Alexa647-labeled Sla1-GFP.

Reconstructed images for these proteins show circular structures when viewed from top but are narrow ellipses when imaged at the equator of cells. (a) 3D dSTORM acquisition was achieved with an astigmatic lens. We gated single fluorophore emission events with a 16-bit intensity above 250. z location was determined based on a calibration curve made with TetraSpeck beads (Supplementary methods). We exported the (x,y,z) coordinates from Wave Tracer to Imaris Software to build 3D reconstructions of droplets, consistent with hemispherical domes, as suggested by the asymmetrical 2D projections (Fig 2a). (b) Cortical droplet width ($209 \pm 10\text{nm}$) and height ($118 \pm 6\text{nm}$) give a contact angle (θ) of $\sim 97^\circ$. θ above 90° is indicative of poor wettability whereas a θ below 90° would wet the membrane. θ also informs on the relationships between the surface tensions (γ_x) at the interfaces.

The simple alcohol 1,6-hexanediol (HD) has been demonstrated to prevent liquid-liquid phase separation of proteins to form droplets *in vivo* and *in vitro* [4, 6, 109, 253, 254]. CME, as measured by cell uptake of a lipophilic membrane-bound fluorescent dye (FM4-64), was inhibited by HD, whether or not turgor pressure and actin polymerization were present (Figure 20c, left *versus* right panels, respectively). Furthermore, an HD dose-response of uptake of the fluorescent dye (Lucifer Yellow) into vacuoles and formation of puncta monitored as Sla1-GFP fluorescence at cortical sites were prevented, but not in cells treated with the related alcohol 1,2,3-Hexanetriol that does not disrupt droplets (Figure 25a, Figure 26). The other PLD-containing proteins, including Sla2, Ent1, Ent2, Yap1801 and Yap1802, all failed to form puncta in cells treated with HD (Figure 26). Pulse-chase experiments showed that HD-dependent dissolution of Sla1 puncta was reversible (Figure 27 and Movie S3).

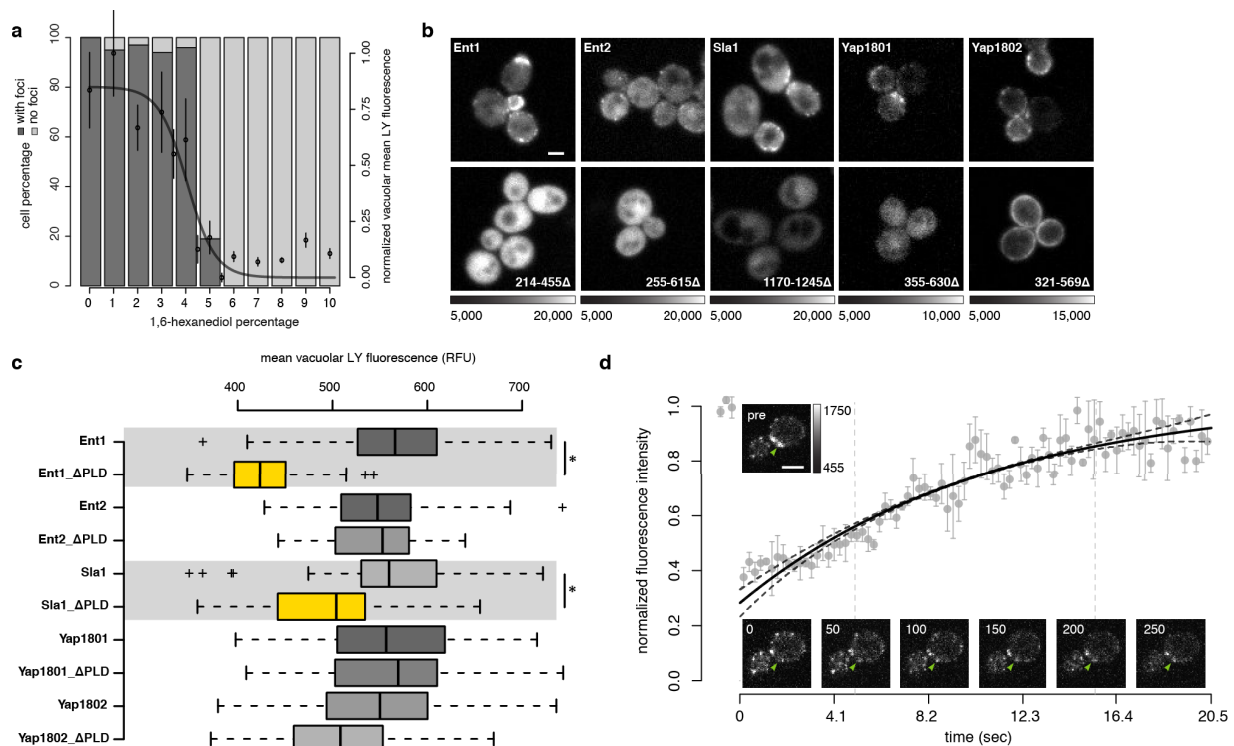


Figure 25 | CME adaptor and coat proteins phase separate to form droplets

(a) 1,6-hexanediol (HD), disrupts cortical droplets in an all-or-none manner. Barplot shows percentage of cells that contain Sla1-GFP foci (dark grey), or not (light grey),

as a function of HD concentration monitored by counting fluorescent puncta containing Sla1-GFP at cortical sites 5 minutes after HD treatment ($n = 150$ cells). Plot overlay (in black) shows quantification of lucifer yellow fluorescent dye uptake in CME vesicles (mean \pm sd; $n = 25$; logistic fit) (b) Prion-like domains (PLDs) are essential for localization of proteins to the cortical sites. Fluorescence images of cortical localization of Ent1, Ent2, Sla1, Yap1801 and Yap1802 fused to Venus YFP. Localization of full-length (upper panels) *versus* C-terminal PLD truncation mutants of the proteins (lower panels). Amino acid positions of the deleted PLDs are indicated for respective images. Grayscale dynamic range for image pairs are indicated below. Scale bar, 2 μ m. (c) Quantification by fluorescence microscopy of lucifer yellow dye uptake for strains that express either full-length or PLD-truncated Ent1, Ent2, Yap1801, Yap1802 and Sla1 (as detailed in panel b). We observed a significant decrease in CME for PLD truncation mutants of Sla1 and Ent1 (two-sided t-test; star indicates $P < 0.001$; $n = 100$ cells). (d) Coat proteins exchange with cortical droplets at rates typical of those observed for proteins that compose other protein droplets. Fluorescence recovery after photo bleaching (FRAP) of Sla2-GFP, GFP signal recovery was measured within a segmented Sla1-mCherry region of interest to ensure that FRAP was acquired within the cortical droplet (mean \pm sd; $n = 5$); photo bleached Sla1-mCherry region identified arrows in image inserts. Data was fitted to a single term recovery equation (full line) and corrected for the known rate of molecule accumulation and depletion that occurs during the droplet lifecycle (dashed lines) (Material and Methods). Incomplete fluorescence recovery suggests that cortical droplets are viscoelastic. Representative cell images before bleaching, upon bleaching, and after recovery are shown in inserts; frame numbers are indicated in the upper left of each image. Grayscale values, 455 to 1750. Scale bar, 2 μ m.

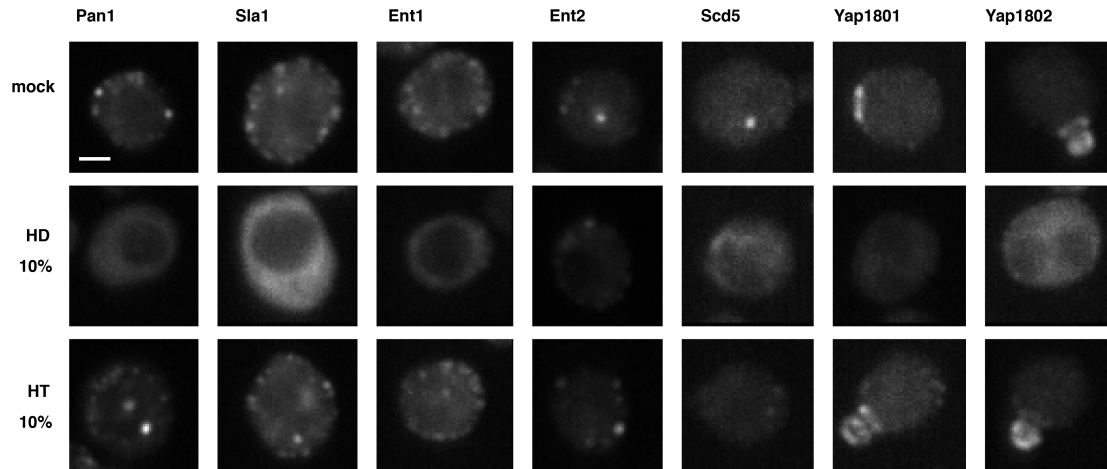


Figure 26 | Cortical patch-associated PLD-containing proteins fail to form puncta in cells treated with 1,6-hexanediol (HD)

, but behave normally upon 1,2,3-hexanetriol (HT) treatment. Fluorescence images of GFP-tagged Pan1, Sla1, Sla2, Ent1, Ent2, Scd5, Yap1801 and Yap1082 puncta 5 min after treatment with either DMSO, 1,6-hexanediol or 1,2,3-hexanetriol, images where acquired with InCell6000 confocal microscope. Scale bar 2 μ m.

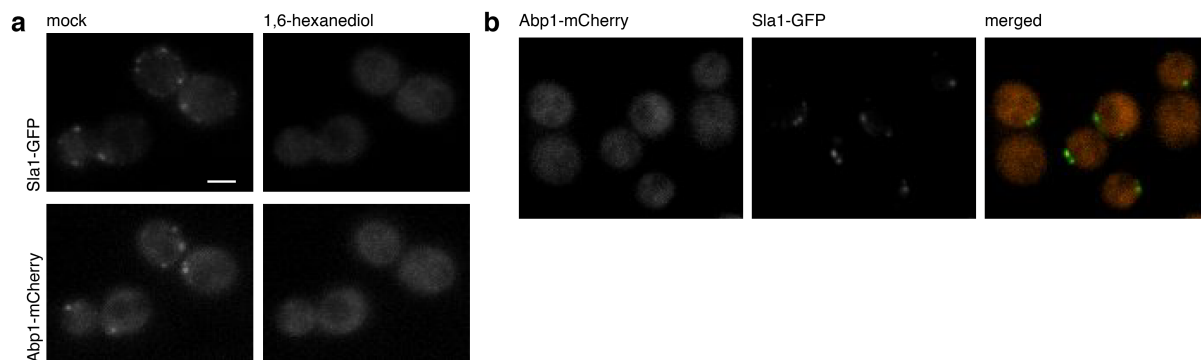


Figure 27 | Pulse-chase experiments with HD show that HD-dependent dissolution of Sla1 puncta is reversible.

(a) Pulse-chase experiments with HD show that HD-dependent dissolution of Sla1 puncta is reversible. Images from fluorescent monitoring through time of Sla1-GFP and Abp1-mCherry under a pulse-chase cycle of 10% HD. Low Fluorescence Medium (LFM) was replaced with 10% HD LFM at 10 min and replaced with fresh LFM at 15

min. Maximal intensity projections of Z-stacks are shown before HD treatment (left), 2.5 min incubation with HD (middle) and 3.5 min after HD removal (right). Scale bar 2 μm . See also Supplementary Movie S3. (b) F-actin polymerization is also disrupted by Latrunculin A. Assessment of Abp1-mCherry actin structures by fluorescence microscopy in presence of 5-20 μM LatA for 5 min. Maximal intensity projections of Z-stacks of cells before (left) and after (right) treatment are shown. Scale bar 2 μm .

Finally, PLD-containing proteins can also form amyloid aggregates, which can be diagnosed by binding and co-localization of Thioflavin T (ThT) to the aggregates [255]. We observed no colocalization of ThT with Sla1-mCherry-labelled puncta (Figure 28).

The PLDs of cortical CME proteins were essential to their localization to cortical sites (Figure 25b). Furthermore, CME was significantly reduced in cells where the PLDs of Sla1 and Ent1 were deleted and with substitutions of proline for other residues in the Sla1 PLD, which weakens the driving force for phase separation (Figure 25c, Figure 29) [60, 88]. Our results supports evidence that there is a functional redundancy among most of the PLD-containing proteins with the two that are more essential, perhaps required for specific functions mediated by other domains within their sequences [256, 257].

The interactions among proteins in liquid-liquid phase separated droplets are expected to be weak and this is assessed by their rapid exchange within and between droplets and their surroundings [1, 39, 116, 258]. In fluorescence recovery after photobleaching (FRAP) experiments we measured both mobile (0.7 ± 0.2) and immobile (0.3 ± 0.2) fractions for the coat protein Sla2 and rapid recovery time (7.5 seconds), similar to other protein and nucleic acid droplets including the dense internal fibrillar component of *X. laevis* nucleoli (Figure 25d) [258]. Taken together, these results support the hypothesis that the cortical bodies are phase separated viscoelastic droplets. We next set out to determine the material properties of the

cortical droplets and to test our postulate that their binding to the plasma membrane generates the force that drives invagination of the membrane.

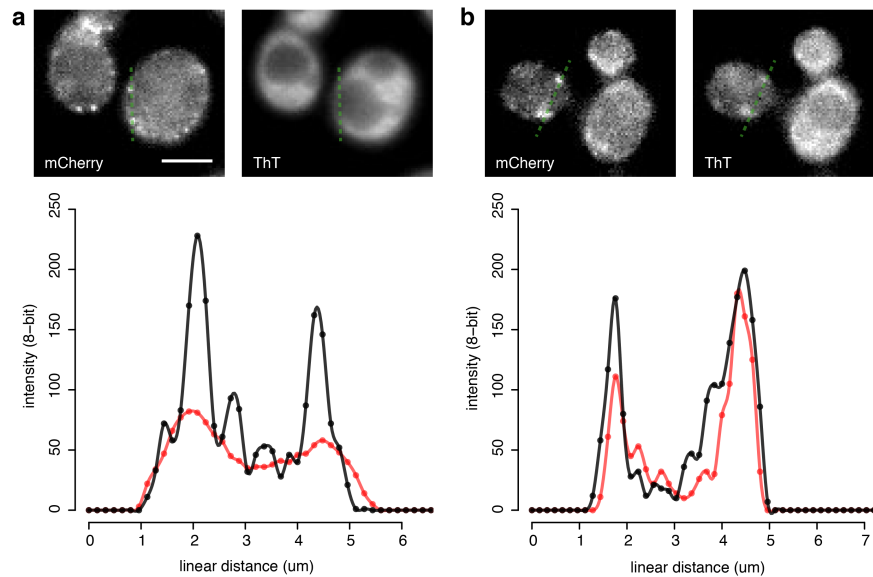


Figure 28 | We observed no colocalization of Thioflavin T (ThT) to Sla1-mCherry puncta.

(a) Fluorescence microscopy of Sla1-mCherry (upper left), ThT stain (upper right) and line scan analysis (lower panel) for the dashed line in green. Scale bar, 2 μm (b) Fluorescence microscopy of Sup35-mCherry (upper left), ThT stain (upper right) and line scan analysis (lower panel) for the dashed line in green. Scale bar, 2 μm.

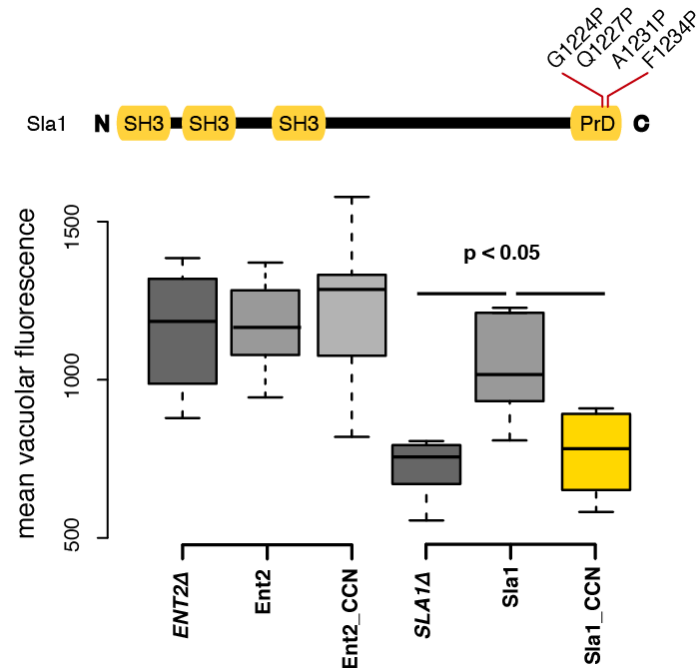


Figure 29 | Mutations of PLDs that prevent phase separation of proteins also disrupt CME.

Proline mutations were introduced near or within the C-terminal PLD domains of Sla1 and Ent2 mutant strains and CME measured by fluorescence of lucifer yellow dye uptake. Positions of the mutation are shown on the schematic representation of the proteins. Introduction of such mutations into the PLDs of Ent1 and Sla1 resulted in equivalent effects of complete PLD deletion on CME-mediated lucifer yellow dye uptake. Boxplots with $n > 100$ cells and a t-test used to determine P -values.

Cortical droplets can mechanically deform both cytosol and membrane

We hypothesized that free energy released by cortical droplet phase separation is converted into mechanical work to deform the membrane and the cytosol. Simply stated, we posit that binding of the droplet to cytosol draws the droplet inward as it grows, while the membrane follows, mediated by its own binding to the droplet and the requirement that the volume of the droplet be conserved. This idea is captured by the well-known Johnson-Kendall-Roberts (JKR) theory, which describes how non-flat

material surfaces stick to and conform to one another in order to minimize their interfacial energy [259-261]. When they stick to one another, soft and compliant materials such as the membrane and cytoplasm are deformed to a degree limited by their elasticity. Style, *et al.* adapted the JKR theory of contact mechanics to describe the contact surface geometry between a microscopic rigid particle and a soft substrate [250]. We followed a similar approach in a simple phenomenological model expressed as the sum of mechanical strain energy (ϕ term) and work (ψ term), respectively;

$$U \sim \phi \cdot \delta^{1+\varepsilon} - \psi \cdot \delta ; \quad (1)$$

Here, U is the mean-field energy, δ is the invagination depth of both the membrane and cytosol (which we assume to be coupled to each other by virtue of conservation of volume of the droplet) and the exponent $\varepsilon > 0$ reflects the deformation geometry (Material and Methods) [248, 249]. Close to equilibrium (as $\partial U / \partial \delta$ approaches 0) we expect invagination to balance the two contributions so that δ^* minimizes energy in (1) resulting in,

$$\delta^* = \left(\frac{\psi}{\phi (1 + \varepsilon)} \right)^{\frac{1}{\varepsilon}} ; \quad (2)$$

Equation (2) shows that the invagination depth δ is determined by the ratio ψ/ϕ and the deformation geometry ε . Values of ϕ and ψ can be determined as functions of individual geometries, elasticities, and viscosities of cytosol, droplet and membrane and interfacial tensions among them (Material and Methods). These in turn can be determined by super-resolution imaging (geometries) and elastic and viscous moduli, taken from the literature or determined by active micro-rheology experiments as described next.

We used active rheology to determine the material properties of the cytosol in which cortical droplets are embedded and then, because the droplets are too small to probe directly, we calculated their properties through well-understood relationships between

the properties of materials in contact and their resulting geometries, as described below. Specifically, we used optical tweezers to examine the frequency-dependent amplitude and phase responses of polystyrene beads that are embedded in cells (Figure 30a, Material and Methods). 200 nm diameter polystyrene beads were integrated into cells by osmoporation (Figure 31) [262]. Measurements of passive diffusion of the beads showed mean square displacements (MSD) close to that of random mechanical noise caused by vibration of the microscope (Figure 31). Furthermore, we established that the osmoporation procedure did not affect rheological properties of cells by measuring the MSD of expressed viral capsid microNS particles labeled with GFP in untreated or osmoporated cells and showing that their diffusion behaviors were identical (Figure 32) [145].

For active rheology experiments, we used an acousto-optic device to oscillate the position of the optical trap in the specimen plane at frequencies over four orders of magnitude and measured the displacement of trapped beads from the trap center using back focal plane interferometry (Figure 30b). We could thus measure the viscoelastic properties of the cytosol surrounding the beads by measuring their phase and amplitude response to the oscillations of the optical tweezers. Then by calculating the power spectrum of unforced fluctuations of the bead we obtained storage (G') and loss (G'') moduli as a function of frequency (Figure 30c-d, Figure 33, Material and Methods) [149, 263, 264].

In addition to obtaining quantities essential to calculate material properties of the cytoplasm and droplet, active rheology combined with spatiotemporal dynamics of interacting materials can inform of their structures. The mechanical properties of living cells can be compared to that of the popular children's toy "Silly Putty" [265]. Like this material, cells and underlying structures show different mechanical properties depending on the rates at which forces are applied to them [143, 149, 266]. Thus if a force is applied at a low velocity, the cell behaves like a viscous fluid; taking on whatever shape it is forced into. When a force is applied at higher velocity, however,

the material behaves like an elastic object, bouncing back to its original shape. As we discuss below, these behaviors reflect the manner and strengths with which the molecules that make up a material interact with each other and their environment.

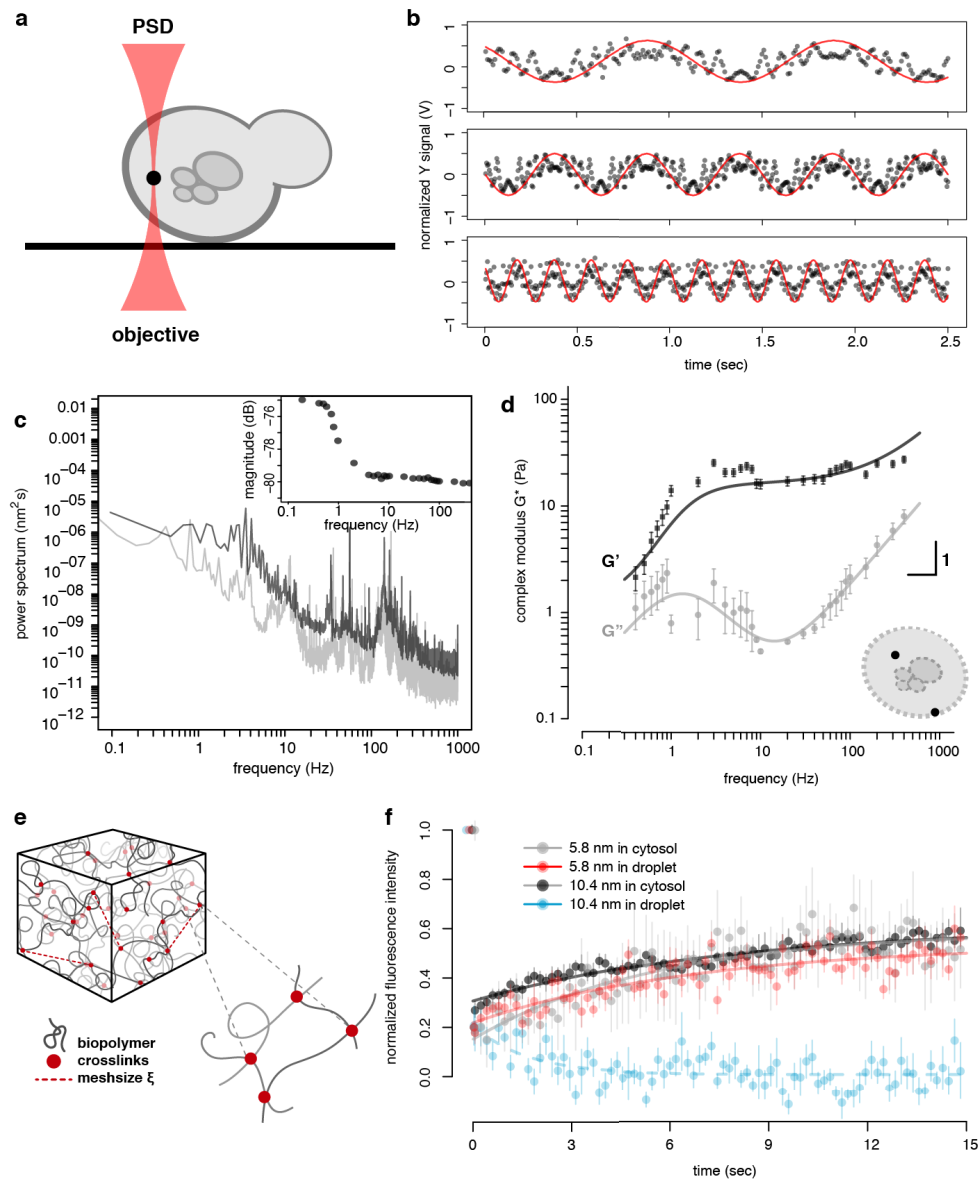


Figure 30 | Cytosol and cortical droplets are composed of a viscoelastic amorphous network of interacting proteins

(a) We used optical tweezers (red beam between the microscope objective and a position sensitive detector (PSD) coupled to an acousto-optic device (AOD) to

oscillate polystyrene beads in cells. Two pulses of osmotic shock were used to osmoporate 200 nm polystyrene beads (black) into latA-treated haploid yeast *GPD1Δ* cells. (b) PSD output signal in volts (V) as a function of time for acquisitions made at 1 Hz (top), 2 Hz (middle) and 5 Hz (bottom). A bead, located in the cell periphery, was oscillated with the AOD in the Y-axis of the specimen plane with fixed tweezer movement amplitude (normalized red curve) at different frequencies. The recorded PSD raw traces (black points) were also normalized to a corresponding magnitude range (coherence cutoff of 0.9). (c) Power spectrum of the oscillated bead (black) with magnitude of response as a function of frequency (insert). (d) Decomposition of G^* as a function of frequency into G' (storage modulus; darker squares) and G'' (loss modulus; light shade circles) for beads distributed at both the cell periphery and interior (see schematic insert; mean \pm sd; $n = 17$) with an average trap stiffness k_{trap} (mean \pm se; $8.0 \times 10^{-5} \pm 2.7 \times 10^{-5} \text{ N m}^{-1}$) and photodiode sensitivity factor β (mean \pm se; $10.7 \times 10^3 \pm 2.3 \times 10^3 \text{ nm V}^{-1}$). Data was fitted to a model of an entangled and crosslinked network of flexible polymers (Material and Methods; Eq. 2.9-2.10). (e) 3D illustration and zoom-in of the latticework composed of amorphous protein chains (grey filaments) with the binding sites (red dots) through which they are non-covalently associate and the mesh size (dashed red line). (f) Fluorescence recovery after photo bleaching (FRAP) of fluorescent dye (FITC)-conjugated dextran of different size (see legend) within a Sla1-mCherry focus (red and blue) or neighbouring cytosolic regions without Sla1 signal (grey and black) in latA-treated *GPD1Δ* cells. Data points represent normalized fluorescence recovery (mean \pm sd; $n=3$). Values for distinct dextran-FITC sizes and cell region were fitted to a single term recovery equation (Material and Methods).

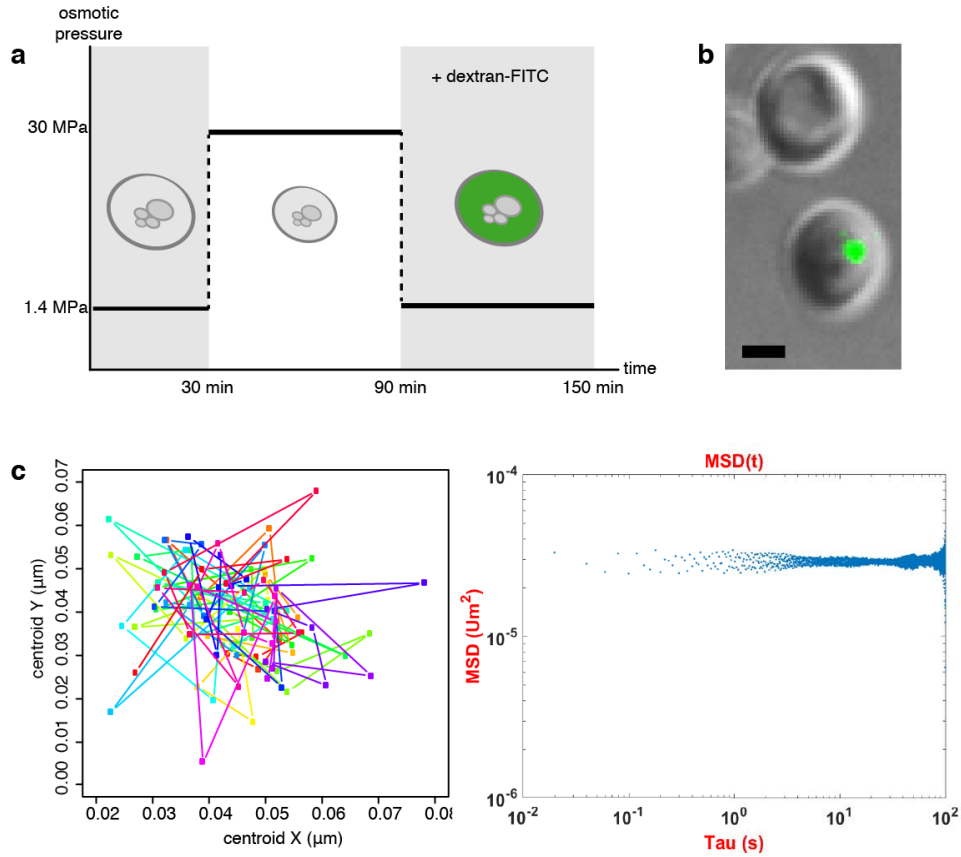


Figure 31 | Osmoporation of polystyrene beads and micro-rheology.

(a) Schematic representation of the two-cycle osmotic shock used to osmoporate 200 nm polystyrene beads into haploid yeast cells. The osmoporation treatment induces a senescent-like state in most cells, but we could rescue a small fraction of cells that continue to divide in rich YPD medium. (b) Images of Sla2-Dronpa3 (green foci) cells with osmoporated beads (left panel). Scale bar is 2 μm . (c) Passive 2D displacement in x and y of 200 nm polystyrene beads measured based on centroid tracking. We observed the movement of beads by centroid tracking (middle panel) and also determined the mean square displacement (right panel). The polystyrene beads we incorporated into cells were confined within the cytosol with a MSD close to that of technical noise.

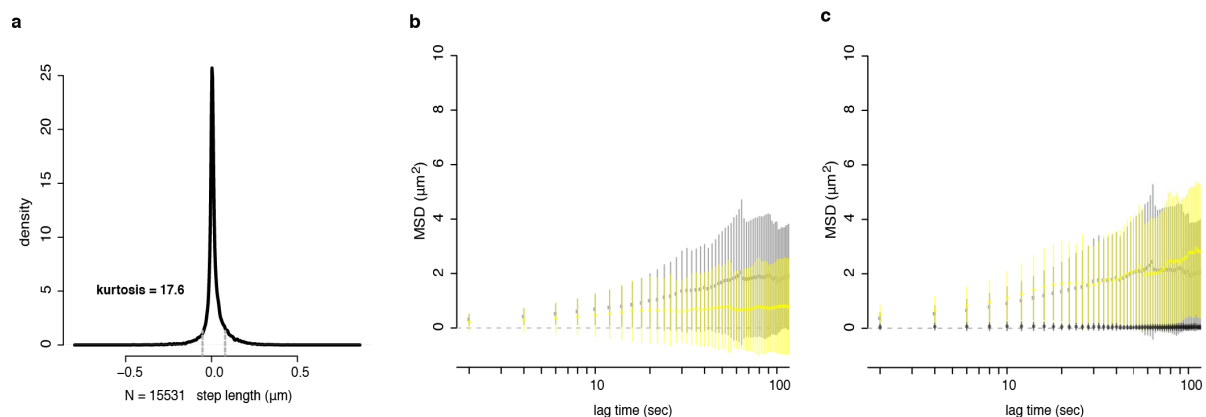


Figure 32 | We measured displacement of expressed viral capsid microNS particles labeled with GFP in both untreated and osmoporated cells.

(a) Distribution of step length of expressed microNS-GFP particles determined by centroid tracking in untreated cells. (b-c) MSD of microNS particles in untreated (grey) and osmoporated (yellow) cells as a function of lag time (seconds). Data points represent mean \pm standard deviation of 300 traces in untreated *versus* osmoporated cells, panel b shows raw data and panel c shows data filtered for caged particles with $\text{MSD} < 1$ represented in black.

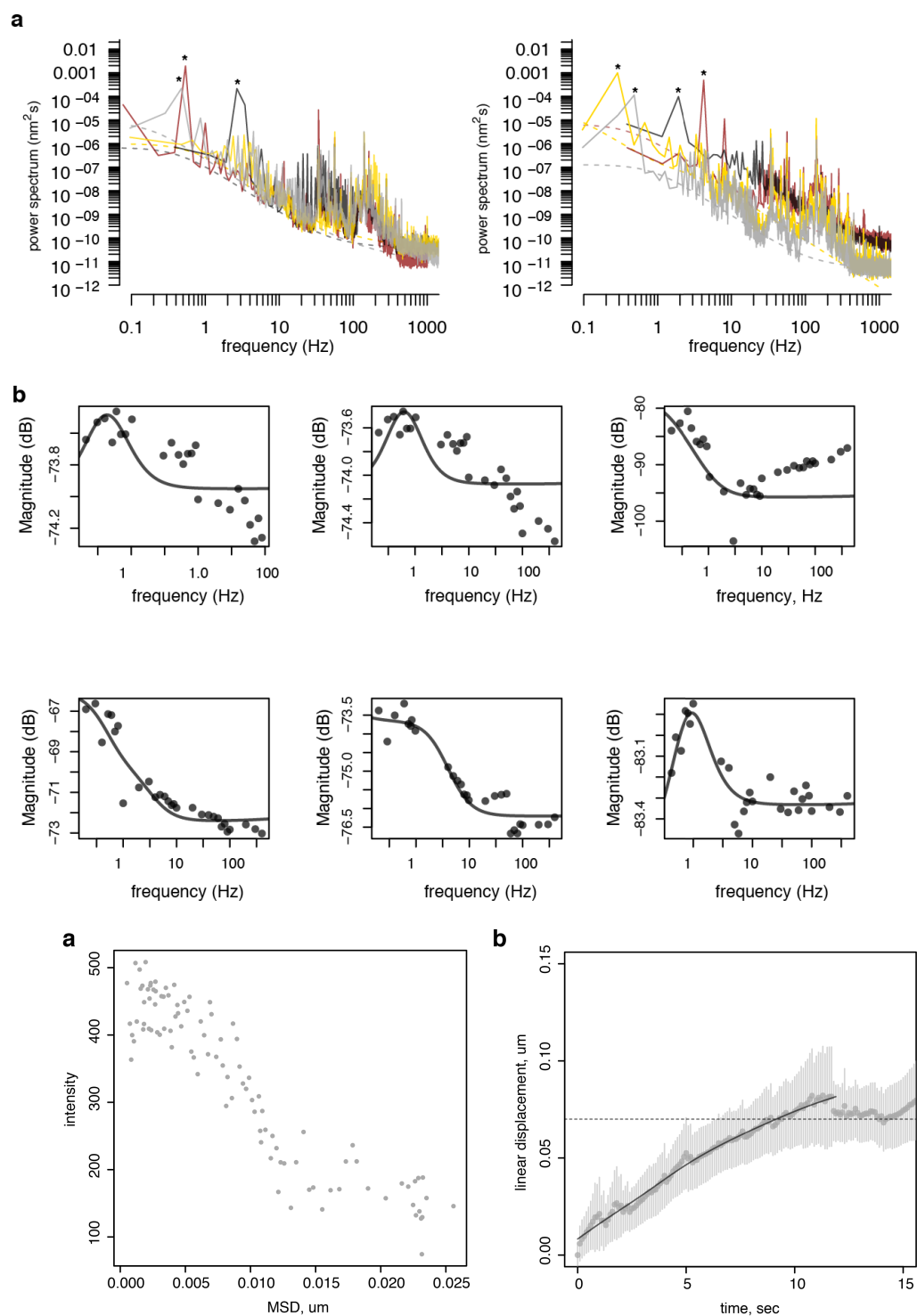


Figure 33 | Dynamic mechanical analysis of cytosol with optical tweezers.

We measured the viscoelastic properties of the cytosol using the response of 200 nm polystyrene beads to sinusoidal oscillations of the tweezers and the high frequency domain of the power spectrum associated with thermal motions of the bead. (a) Power spectra of samples coded with distinct colors. Below frequencies of 500 Hz, the power spectra show fluctuations from tweezer oscillations (marked *), cellular processes and sample vibration. (b) Magnitude of the response (dB) of the bead displacement to sinusoidal oscillations of the optical trap position. Lines indicate global fits of the power spectra and response magnitudes to a model that describes the viscoelasticity of a crosslinked polymer network (Supplementary methods).

In specific terms, the material properties of the yeast cytoplasm and its interactions with the cortical droplet could be interpreted from the complex modulus versus frequency plot as follows (Figure 30d): The inflection of the G' modulus at 2 Hz results in similar G' and G'' values at low frequencies, which indicates that the cytosol is more viscous near rest. When deformed by the droplet growth (at a velocity of growth $=2360 \pm 120 \text{ nm s}^{-1}$; corresponding to a stress at $\sim 30 \pm 2 \text{ Hz}$) the cytosol is more elastic, whereas membrane invagination occurs at a rate at which the cytoplasm is more viscous (a velocity of $7.4 \pm 2.5 \text{ nm s}^{-1}$; corresponding to $0.1 \pm 0.04 \text{ Hz}$) (Figure 20b, 3d, Figure 34). The G' and G'' we measured are similar to the cytoplasm of adherent mammalian cells and indicate that the beads are confined within a dense network of interacting molecules [143, 149, 266]. We observed that the cytosol has a more malleable behavior at high frequencies than expected for an exclusively crosslinked network of flexible polymers; this may be attributed to an entangled, rather than crosslinked, network or due to compliant polymers that act more like entropic springs (Figure 30d-e) [267-272].

We could now determine the mechanical properties of the cortical droplet as follows. First, our micro-rheological data is consistent with both cortical droplets and cytosol behaving as elastic materials at rates above 1 Hz (Figure 30d). Classic Hertz theory relates contact geometries of elastic materials to their mechanical properties. We

could thus, use the geometry of the cortical droplets determined in our super-resolution imaging experiments and elasticity of the cytosol in which they are embedded to estimate the cortical droplet elastic modulus as 59 Pa (Figure 20b, 3d, Material and Methods; Eq. 3.7-3.10) [248]. These results suggest that the cortical droplets have similar material properties as the surrounding cytosol, which as an elastic (or Young's) modulus of 45 Pa at 1 Hz (Material and Methods). We estimated the mesh size of the cortical droplets by probing them with fluorophore-conjugated dextran molecules of 2.4, 5.8, and 10.4 nm in size and measured FRAP and colocalization of dextrans with Sla1-mCherry puncta (Figure 30g-h, Figure 35, FIGURE 36). Both 2.4 nm and 5.8 nm dextran-FITC recovered equally in the Sla1 droplet and cytosolic zones, with a mobile fraction of 0.37 ± 0.1 and recovery rate constant of 12.7 ± 1.1 s. In contrast, the 10.4 nm dextran-FITC molecules cannot be replaced once the PLD-rich protein network in the droplet is formed whereas they recover in the neighbour cytosol. These results are consistent with an exclusion zone for ribosomes as discussed above and with exclusion of dextrans of 5.8 nm and more by known protein-RNA phase separated droplets called P bodies [109, 121].

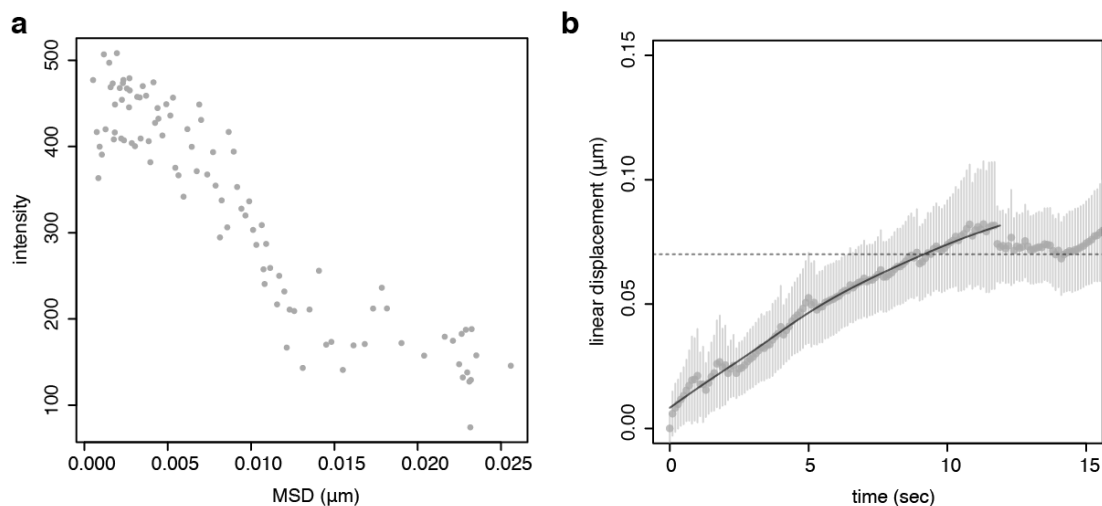


Figure 34 | Centroid tracking within a confocal volume of Sla1-GFP foci in *GPD1Δ* mutant strains treated with LataA.

(a) Single Sla1-GFP focus fluorescence intensity as a function of mean square displacement in a confocal volume as determined by spinning disk pinhole size. Images were acquired at 10 frames per second. Only foci with a decreasing fluorescence bleaching were selected to measure their displacement. (b) Linear displacement of Sla1 foci within a confocal volume as a function of time. Mean \pm sd of displacement is shown for $n > 50$ per time point. Total traces $n = 275$; note that traces do not have the same length. The average displacement is about 7.4 nm per second from polynomial fit (black curve). Horizontal dashed line indicates an invagination of 70 nm, depth required for the scission step.

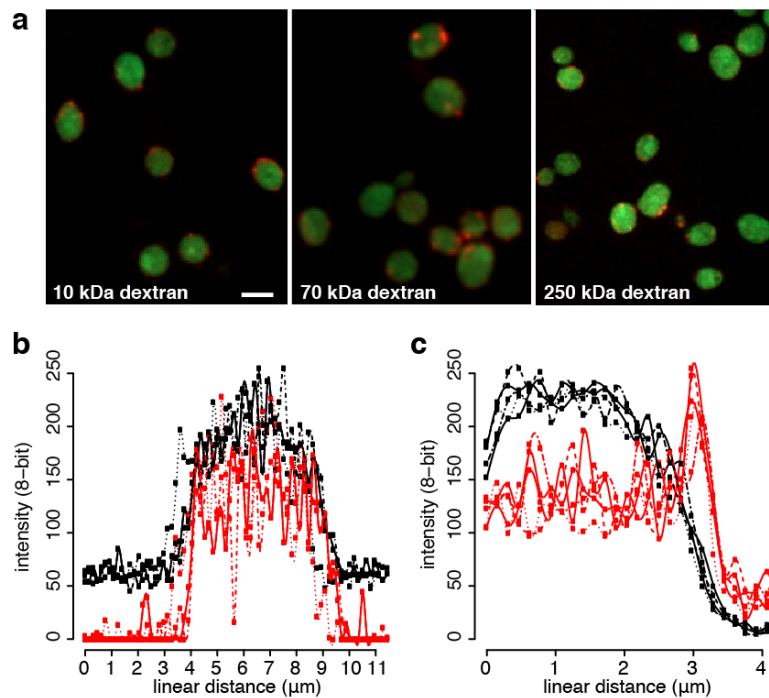


Figure 35 | Colocalization of different sized dextran-FITC revealed that cortical droplets exclude objects of diameters > 5.8 nm.

(a) 2-color fluorescent images of osmoporated dextran-FITC of different sizes in a Sla1-mCherry strain, Scale bar is 4 μ m. (b) Multiple line scans of osmoporated 70 kDa (5.8 nm) dextran-FITC fluorescent signal (back traces) outside Sla1-mCherry cortical regions (red traces). Fluorescence intensity patterns thus show the

fluorescence of a line across the cytoplasm that doesn't include any concentrated foci of Sla1-mCherry. (c) Multiple line scans of osmoporated 70 kDa (5.8 nm) dextran-FITC fluorescent signal (back traces) within Sla1-mCherry cortical regions (red traces).

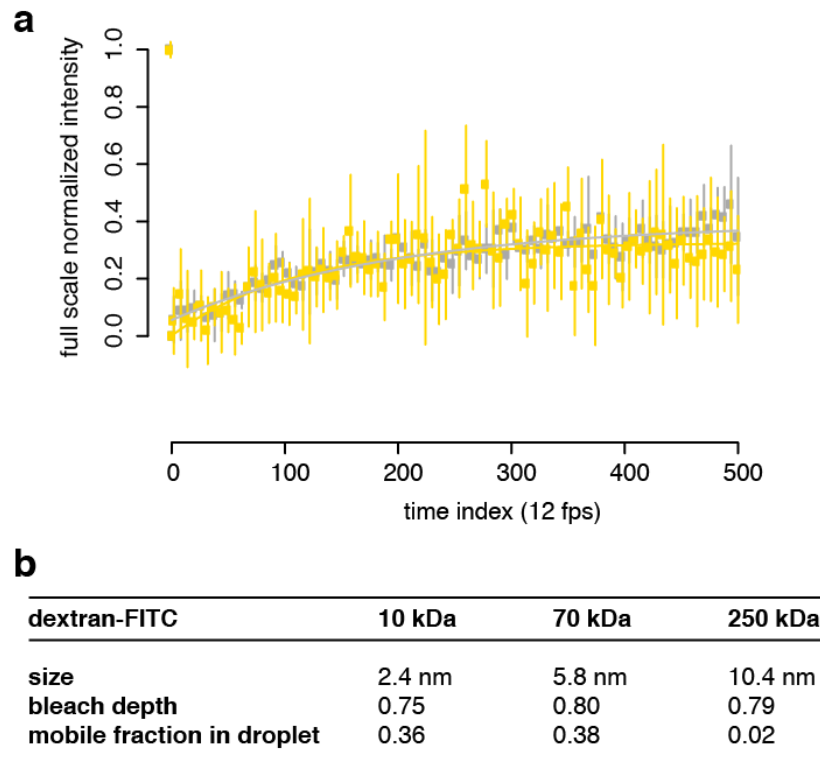


Figure 36 | Fluorescence recovery after photobleaching (FRAP) of dextran within cortical droplets or cytosol regions of interest.

(a) FRAP of the bleached 2.4 nm (10 kDa) dextran-FITC within the Sla1 foci (yellow) and neighbouring cytosol regions (grey) without Sla1 signal. Images before and after FRAP. Data points represent mean normalized fluorescence of 3 independent samples. (b) Summary of FRAP analyzed for 2.4 nm, 5.8 nm and 10.4 nm dextran-FITC in the cortical droplet Sla1-mCherry region. Data shows absence of mobile fraction for the 10.4 nm dextran-FITC.

Cortical droplet binding to cytosol provides energy to drive membrane invagination

The deformation of the membrane in response to contact of a soft viscoelastic object depends on the geometries and mechanical properties of the object and the vessel it is in (in our case the cytosol of a cell) and the membrane (Figure 37a). From all electron and super-resolution fluorescence microscopic evidence, we know that the favored geometry of the membrane is flat with invagination centered in the middle of the droplet (Figure 37a, lower). Such geometries could be explained by a local radial stress-gradient generated by the droplet adhesion to both the membrane and cytosol. Simply stated, as the droplet grows the binding to the cytosol draws it inward and the membrane follows, mediated by its own binding to the droplet and the requirement that the volume of the droplet be conserved.

We could now quantify the work performed by the droplet to invaginate the membrane using the storage and loss moduli obtained from the micro-rheology experiments, geometric data obtained from super-resolution imaging and other data available from the literature, to solve the explicit form of the ϕ and ψ terms (mechanical strain and work, respectively) in Equation (1) as functions of membrane and cytosol invagination δ (Material and Methods; Eq. 4.25-4.26). We first estimated with the Young-Laplace equation an interfacial tension for the droplet-cytosol interface, γ_{dc} , of $7 \times 10^{-5} \text{ N}\cdot\text{m}^{-1}$, from the pressure difference across the cytosolic interface and the droplet mean curvature (Material and Methods; Eq. 4.6). This value falls within the range of $10^{-5} \text{ N}\cdot\text{m}^{-1}$ to $10^{-4} \text{ N}\cdot\text{m}^{-1}$ that has been reported for other protein droplets, including nucleoli and P granules (Materials and Methods; Eq. 4.9) [32, 116].

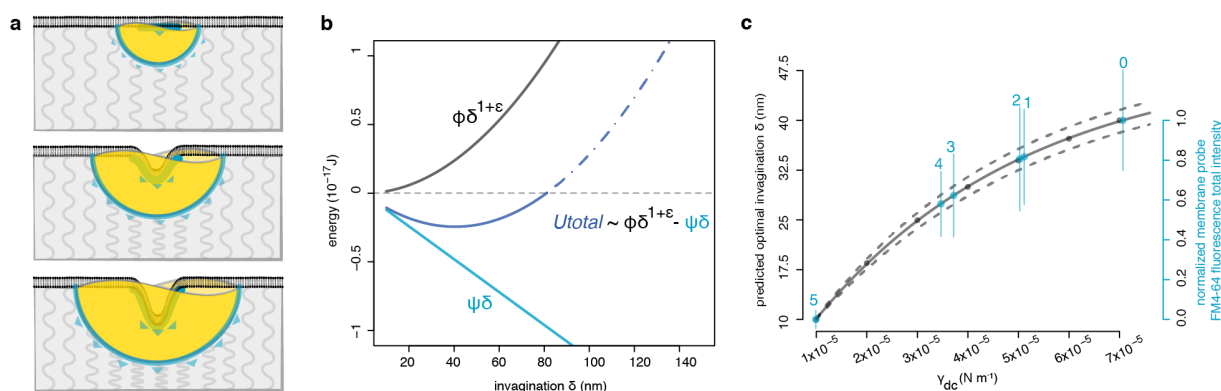


Figure 37 | Cortical droplets do mechanical work to deform the membrane and cytosol

(a) Illustration of a cortical droplet (gold) that binds to (wets) a bilayer membrane (black) and drives membrane invagination (top to bottom). Resultant membrane deformations reflect how forces balance under a Young-Dupré adhesion gradient (blue lines and arrows). Resistance to deformation is represented by grey curved lines. (b) Equation (1) (insert) was used to calculate the energy penalties (ϕ) and contributions (ψ) at the cytosol and membrane interfaces with the cortical droplet. Total energy of the system (dark blue), energy penalties (black) and energy contributions (light blue) are presented as a function of membrane invagination (δ). The energy of membrane invagination is favourable for δ between about 15-80 nm (solid blue line) and unfavourable above 80 nm (dashed blue line). Quantities used to calculate energies are detailed in Figure 38 and Tables 9-10. (c) Our model predicts that vesicle size is proportional to the strength of droplet intermolecular protein-protein interactions that are proportional to γ_{dc} , the droplet-to-cytosol interfacial tension. Predicted membrane invagination δ as a function of γ_{dc} (left axis and black points). Data points were fitted to an exponential decay function (full line) with 95% confidence interval (dashed lines). Titration of 1,6-hexanediol was used to reduce intermolecular cohesion and therefore γ_{dc} resulting in reduced vesicle size as measured by uptake of the lipophilic membrane probe FM4-64 into cells (Right axis, red) *versus* % HD (blue numbers, $n = 25$, mean \pm sd) expressed as a function of the droplet-cytosol interfacial tension γ_{dc} (Material and Methods).

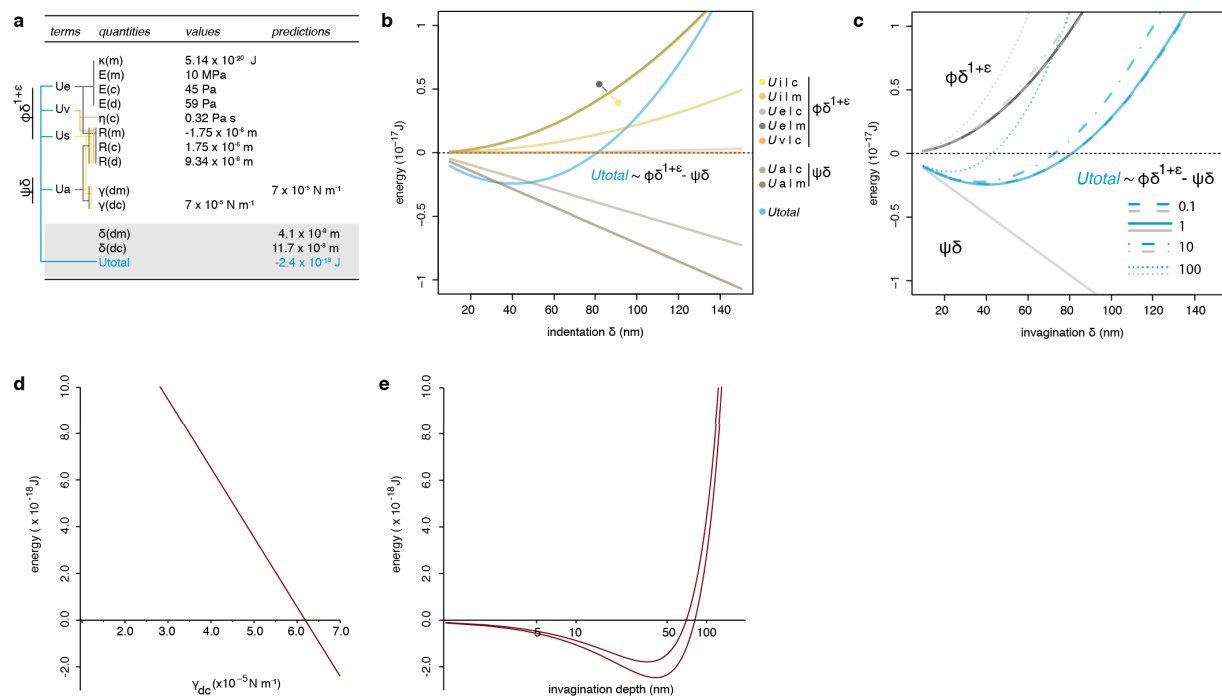


Figure 38 | Cortical droplets apply mechanical stress that deform the membrane.

(a) Values of bending, elastic, viscosity, surface tension and geometry quantities used in the calculation are recapitulated. Colour coded lines indicate which quantities were used to calculate the respective energies U_x , that in turn compose the ϕ and ψ terms of Equation 1. (b) Equation (1) (insert) was used to calculate the energy penalties and contributions at the cytosol and membrane interfaces with the cortical droplet. Total energy of the system (blue), energy penalties (yellow, orange and grey) and energy contributions (brown) are presented as a function of membrane invagination (δ). Colour legend (right) specifies energy traces U_{xly} , where $x = (e)$, elasticity or (v) , viscosity of either the cytosol (c) or membrane (m) and (i) is interfacial tension and (a) is adhesion of cytosol or membrane with the cortical droplet. Quantities used to calculate energies are detailed in Tables 9 and 10. (c) Plot of total energy (y axis) as a function of droplet-cytosol surface tension (x axis) shows that the energy favorable values of γ_{dc} range between $6.2 \times 10^{-5} \text{ N} \cdot \text{m}^{-1}$ to $7 \times 10^{-5} \text{ N} \cdot \text{m}^{-1}$. (d) 2D representation of the energy and depth accessible to a successful invagination. With the minimal (top

curve) and maximal (lower curve) values of γ_{dm} our model predicts precise range of favorable δ (x axis) that minimizes total energy (y axis).

With estimates of γ_{dc} we also determined the work of adhesion that is released when the droplet surfaces are created, as described by the Young-Dupré equation (Materials and Methods; Eq. 4.11). Again, we assumed a radial adhesion gradient around the invagination peak in the middle of the cortical droplet (Figure 37a). We calculated an adhesion energy (ψ) of 4.9×10^{-18} J from interactions between the cortical droplet and both the membrane and cytosol (Figure 37b, Figure 38, Materials and Methods; Eq. 4.26). Our results suggest that the most significant contribution of the mechanical energy comes from the droplet-cytosol interface, where the adhesion energy of 2.9×10^{-18} J is enough to overcome energy penalty of 2.4×10^{-18} J to deform both membrane and cytosol. This energy cost includes the elastic, viscous, and interfacial stress penalties (Figure 37b, Figure 38, Table 10). We also calculated an average adhesion energy of $1.3 \text{ kJ}\cdot\text{mol}^{-1}$ at the droplet-cytosol interface (Material and Methods), which is consistent with the free energies expected of non-covalent interactions [273].

Our model provides a physical framework to explain how cortical droplets do the mechanical work needed to induce invagination of membranes in CME. The interface between droplets, formed, by phase separation of disordered proteins into cortical bodies, and the cytosol- membrane interface deforms the surrounding materials through adhesive interactions. Invagination occurs when ψ dominates ϕ and this is favored within the observed δ interval of 40 nm to 80 nm (Figure 38). Notably, this predicted δ interval is within the range of plasma membrane invagination of ~70 nm at which point a membrane scission mechanism is activated and vesicle generation is completed [120].

We propose that cortical droplets store and dissipate mechanical energy in the form of surface tension, whereby the composition of the droplets determines their

interfacial interactions and provides the energy for adhesion and invagination of membranes. Accordingly, the underlying energy stored within the droplets and the balance of interactions amongst droplet components and solvent governs the nature of the interface. The potential energy ψ of droplets, which by the work-energy theorem should be equivalent to the total work of adhesion, should be dictated by the density and strengths of physical interactions amongst proteins within the droplet (the droplet cohesion and interfacial tensions). We tested this assumption by weakening the favorable free energies of the protein-protein interactions that hold droplet components together using 1,6-hexanediol (HD). These are the interactions that drive the phase separation of cortical droplets, and so would correspond to a decrease of the droplet surface tension (γ_{dc} or ψ). Our model predicts that invagination depth should continuously vary with ψ from Equation (2). We titrated HD below the effective concentration that prevents protein phase separation and quantified individual membrane excision events by quantifying uptake of the lipophilic membrane probe FM4-64 into cells by fluorescence microscopy (Figure 25a, Material and Methods). In LatA treated *GPD1Δ* cells, this measures the amount of labeled membrane taken up into cells under the action of cortical droplets alone. By increasing subcritical HD concentration (corresponding to a decrease in ψ), the average fluorescence-labeled membrane per vesicle (a proxy for invagination δ) was continuously reduced over one order of magnitude in the value of γ_{dc} (Figure 37c, Material and Methods; Eq. 2.8). This observation fits with the reduced membrane invagination that we predicted at the outset (*i.e.*, that δ scales with the ψ/ϕ ratio) when the droplet cohesion (γ_{dc} or ψ) is also reduced (Figure 37c, Material and Methods; Eq. 4.2).

Conclusion

Our results provide a framework for answering many questions regarding CME and other membrane budding processes. Given our observations, how is CME coupled to multiple signaling pathways that integrate to regulate vesicle formation? For instance, the PLD-containing CME proteins we investigated are enriched for multiple phosphorylation sites, which undergo changes in response to activation of a CME-regulating signaling pathway [20]. Since the amount and distribution of charge in disordered regions of proteins regulate their interactions and conformations [100], such post-translational modifications may be important to regulating CME. Our fluorescence microscopy and electron micrographic evidence from the literature suggests that the cortical droplet remains associated temporarily with mature vesicles [121]. Does the droplet play any role in trafficking and fusing with, for instance, plasma membrane (protein recycling) or lysosome (protein degradation)? CME underlies several fundamental mechanisms of vesicle trafficking and attendant membrane and vesicle protein cargo transport, including late secretory pathways, endocytosis and neuronal synaptic vesicle recycling. Yeast and human proteins implicated in clathrin-mediated vesicle trafficking are enriched for long disordered protein domains (47/23% of proteins with long consecutive disordered regions of 30 residues and more for humans and yeast, respectively) whereas those involved in two other vesicle trafficking systems are not (COPI: 8/5%; COPII: 8/5%) [274, 275]. These observations argue for investigating the generality and conservation of protein droplet adhesion-driven membrane invagination as the basis of clathrin-mediated vesicle trafficking in the absence of actin polymerization.

It is possible that other liquid-liquid phase separated protein and protein nucleic acid droplets may influence cellular sub-structural dynamics and shape thus contributing to cell, tissue, and organism morphology [115]. More broadly, interfacial contact potentials between different biological materials could represent a vastly underestimated source of complex pattern formation in biology, such as has been observed in embryonic tissue layers [276] or recently in a model of growing brain convolutions [277] or in protein stabilization [278].

Materials and Methods

Cell culture, gene manipulations and fluorescent reporters

We performed *in vivo* experiments in the *Saccharomyces cerevisiae* BY4741 *MATa his3Δ1 leu2Δ0 met15Δ0 ura3Δ0* background. Cells were normally grown to exponential phase (OD₆₀₀ 0.1 to 0.6) in either rich medium (YPD) or low fluorescence medium (LFM) [233]. Liquid media or solid-agar cultures were incubated at 30°C. To decouple the effects of turgor pressure on clathrin-mediated endocytosis (CME) we performed many experiments in a yeast strain with the gene for glycerol-3-phosphate dehydrogenase deleted, *GPD1Δ*. We acquired the *GPD1Δ* and other deletion strains from the Yeast Knock-out (YKO) deletion collection and GFP fluorescent strains from the Yeast GFP Clone Collection [279], were generous gifts from J Vogel at McGill University.

For 2-color imaging and other specific needs, the coding sequences for different fluorescent proteins were integrated into the genome, 3' to reporter protein open reading frames (ORFs) by homologous recombination [24]. In short, mCherry, Dronpa3 and Venus tags were integrated *via* homologous recombination by amplifying the HPH or NAT resistance cassettes from the respective pAG32 or pAG25 vectors with primer tails homologous to flanking sequences to the respective loci. BY4741, *GPD1Δ* or other YKO strains were then transformed with the respective PCR cassettes, selected for HPH or NAT resistance in YPD medium and confirmed by diagnostic PCR.

Truncation and site-directed mutagenesis within ORFs

Integration of the coding sequence for fluorescent protein Venus YFP by homologous recombination into the genome was also used to truncate the prion-like domains (PLDs) sequences in the ORFs of Sla1, Ent1, Ent2, Yap1801 and Yap1802. In order

to truncate the required gene fragments, the Venus YFP coding sequence was integrated at precise locations prior to the STOP codon. The amino acid sequences that are deleted in each PLD truncation mutant are; Sla1 (1170-1245 Δ), Ent1 (214-455 Δ), Ent2 (255-615 Δ), Yap1801 (355-630 Δ) and Yap1802 (321-569 Δ).

To generate proline substitution point mutations within or near PLDs of Sla1 and Ent2; we cloned synthetic gene fragments (GenScript) that coded for the mutations into the respective MoBy-ORF p5472 plasmids of our target genes [190]. The respective position of proline mutations, gene fragment size and restriction enzymes are; Sla1 G1224P, Q1227P, A1231P, F1234P (842 bp, NarI and XmaI); Ent2 R359P, Q362P, H366P, L369P, L385P, L388P, K401P, E404P, L408P, Q411P, L415P, Q418P (1395 bp, XhoI and AflII). Standard cloning procedures with matching restriction enzymes were used to build the constructs and we confirmed final constructs by sequencing. Respective deletion strains were then complemented with either the proline-mutated or original p5472 plasmids.

Diffraction-limited fluorescence microscopy

For most experiments, cells were grown in LFM to an OD₆₀₀ of ~0.1 to 0.6 and plated on either Nunc glass bottom 96-well plates (Thermo Scientific; 164588), glass bottom 8-well plates (ibidi) or glass bottom 35 mm round dishes (MatTek). We used concanavalin A (Sigma-Aldrich ConA # C-7275) as a cell surface binding agent. Each well was loaded with 1mg/ml final concentration of ConA solution at room temperature for 15 minutes. ConA was then removed and wells were completely air dried before cells were added. Fluorescence images were acquired with distinct imaging platforms;

For the assessment of PLD truncations, we imaged cells on a Nikon TE2000 inverted microscope equipped with a 100X/1.45 plan APO lambda oil objective (Nikon), X-Cite lamp source (Excelitas), respective FITC (Chroma 41001HQ), EYFP (Chroma

49003ET) and mCH/TR (Chroma 49008ET) dichroic cubes and a Cool SNAP HQ camera. Z-stacks were acquired through a micron deep region with 5 planes and presented by maximal Z-projection.

For the measurements of fluorescent probe uptake and cell sizes under different osmotic pressures, fluorescence images were collected on an InCell 6000 automated confocal microscope configured with a 100x/0.9 Plan FLUOR objective (Nikon) and 488 nm laser diode and FITC 525/20 emission filter for GFP fluorescence or 561 nm DPSS laser and dsRed 605/52 emission filter (GE healthcare life sciences). Single or two color images were collected sequentially on a single focal plane with an exposure time of 100 msec. and a confocal slit of 2 AU. Image analysis and signal automated segmentation was performed with the InCell Developer software (GE healthcare life sciences) and the data was further analyzed and plotted in the R environment.

For other imaging data, the Quorum Diskovery platform was used in open aperture, confocal and super-resolution imaging modes. Our Quorum Diskovery platform consists of a Leica DMI6000 inverted microscope equipped with a Diskovery multi-modal imaging system (Spectral) attached to either a Hamamatsu EM X2 camera or ORCA FLASH 4.0 V2 digital CMOS camera. Wide field or confocal excitation are achieved with a Spectral laser merge module with mounted 405 nm, 440 nm, 488 nm, 561 nm, and 640 nm diode pumped solid state laser sources linked to a Borealis beam conditioning unit. Images were acquired with a HCX PL APO 63x /1.47 NA oil corrected TIRF objective (Leica). This platform was remote controlled by the Metamorph software (Molecular Devices) and images were acquired and analyzed through distinct pipelines. For particle tracking and mean squared displacement analyses, we used the Wave Tracer plugin to localize fluorescent foci centroid position through a wavelet algorithm and tracks particles in times stacks to calculate particles movement.

Finally, a Axio Imager Z2 spinning disk confocal microscope with a DirectFRAP module (Carl Zeiss) was used for all the FRAP assays. Complete details of FRAP

experiments are included below. This imaging platform is equipped with a AxioCam mRM charged-coupled device camera (Carl Zeiss), a DirectFRAP module (Carl Zeiss) and filter sets 49002 ET-GFP and 49008 ET-mCherry from Chroma Technology.

Fluorescent probes to quantify endocytosis or detect amyloid structures

Lucifer yellow (LY; Molecular Probes) assays to quantify endocytosis were performed at a final concentration of 1 mg/ml in YPD medium. Cells were incubated with the LY for 20 min or more. We then centrifuged at 3000 x g and washed cells 3 times in phosphate buffered saline (PBS; 137 mM sodium chloride, 10 mM phosphate, 2.7mM potassium chloride) before imaging in either PBS or LFM with excitation wavelength (λ_{ex}) of 428 nm and emission wavelength (λ_{em}) of 536 nm.

The lipophilic styryl dye FM4-64 (*N*-(3-Triethylammoniumpropyl)-4-(6-(4-(Diethylamino) Phenyl) Hexatrienyl) Pyridinium Dibromide) (Molecular Probes) was used to monitor plasma membrane uptake and staining of vacuolar membranes. Plasma membrane was labeled with 10 to 20 μ M FM4-64 in YPD media and cells were incubated for 5 to 120 min. Cells were washed once in PBS and resuspended in LFM for imaging. FM4-64 stained cells were quantified by fluorescence microscopy (λ_{ex} of 510 nm, λ_{em} of 750 nm) on our Quorum platform or if specifically indicated on the InCell6000 (see Diffraction-limited fluorescence microscopy section). When cell populations (or conditions) were compared, we applied a Welch's two-sided t-test with sample sizes to achieve a power greater than 0.9 with a 95% confidence level.

We determined whether Sla1-mCherry puncta were also labeled with the amyloid binding dye thioflavin T (ThT) in both live and fixed cells. Live cell ThT staining was performed as described by Kroschwald and collaborators [4]. Cells grown to OD₆₀₀ ~0.6 were harvested and resuspended in 30 μ M ThT, 10 mM Tris/EDTA buffer (pH 7) for 20 min. Cells were then washed 3 times in PBS and resuspended in LFM media

for imaging. Fluorescence microscopy (λ_{ex} of 405nm, λ_{em} of 450/50 nm) or (λ_{ex} of 488 nm, λ_{em} of 525/50 nm) were performed on the Quorum platform (see Diffraction-limited fluorescence microscopy section). BY4741 cells transformed with the plasmid pRS416-GAL-Sup35NM-RFP and induced for 2 hours in 2% galactose LFM were used as positive ThT stain controls. Alternatively, we confirmed ThT *in vivo* results with ThT staining of fixed cells. Cells were fixed with 4% paraformaldehyde 2% sucrose PBS for 20 min and washed once in PBS. Cells were then permeabilized with 0.1% Triton-X phosphate buffered (pH 7.5) detergent solution, and treated with 0.001% ThT for 10 min at room temperature. ThT stained cells were washed at 3–4 times with PBS and imaged on the Quorum platform (λ_{ex} of 488 nm, λ_{em} of 525/50 nm) (see Diffraction-limited fluorescence microscopy section).

Cell treatment with water-glycerol solutions, 1,6 hexanediol and latrunculin-A

Water and glycerol binary combinations were mixed to obtain solutions with precise osmotic pressures ranging from 1.4 MPa to 30 MPa. Cells were grown to log phase, centrifuged for 2 minutes at 3000 x g and resuspended in the different water-glycerol binary solutions in Nunc 96-well glass bottom imaging plates (Thermo Scientific; 164588). Fluorescence images of cells, that express EGFP from a pAG416-GPD plasmid, were then captured immediately after resuspension and at 1 hour intervals with the confocal InCell6000 (see Diffraction-limited fluorescence microscopy section). Intensity thresholding of the GFP channel allowed us to segment the cells and obtain cell area values. These area values were used as a proxy for cell size at the different osmotic pressures.

We utilized 1,6-hexanediol (HD) to differentiate phase separated intracellular bodies from stable solid or fibrillar protein aggregates or to modulate the interactions among proteins that compose the cortical droplet. HD is thought to change the solvent quality inside cells resulting in disruption of the interactions favorable to liquid-liquid phase

separation. 1,2,3-hexanetriol (HT) was used as a negative control in all the HD assays. We treated cells grown to mid-log phase (OD_{600} 0.6) with HD or HT from 0 to 10 % wt/v and we measured both the uptake of fluorescent probes and progression of CME protein accumulation at cortical foci by fluorescence microscopy. Lifetime of Sla1-GFP at cortical sites in the presence of HD was assessed on the Quorum platform (see Diffraction-limited fluorescence microscopy section) and kymographs were generated with the Metamorph image analysis software (Molecular Devices).

Inhibition of F-actin synthesis was achieved using Latrunculin A (LatA) at concentrations determined by titrating LatA from 0 to 50 μ M. Cells were treated for 20 minutes prior to measurements of the uptake of membrane (FM6-64 dye) and bulk fluorescent reporter uptake (LY dye) and of Abp1-mCherry accumulation at cortical foci described above for the HD assays. The dose-response curve indicated that a concentration of 20 μ M LatA was sufficient to impair actin nucleation at cortical sites and we used this concentration of LatA in all our experiments unless mentioned otherwise.

Direct stochastic optical reconstruction microscopy (dSTORM)

Direct stochastic optical reconstruction data was acquired with the custom-imaging platform built by Quorum Technologies (see Diffraction-limited fluorescence microscopy section). Sample preparation for dSTORM was performed according to Reiter, *et al.* with minor modifications [133]. Cells were grown to an OD_{600} = 0.1 and plated on ConA coated glass bottom 35 mm round dishes for 10 minutes. Cells were then fixed with 4 % paraformaldehyde 2% sucrose PBS for 15 min. Fixation was stopped with two sequential incubations of 10 minutes in 50 mM NH_4Cl PBS and cells were further permeabilized and blocked in 0.25 % Triton X-100, 5 % BSA, 0.004 % NaN_3 PBS for another 30 minutes. We used GFP-trap nanobodies (Chromotek) to label Sla1-GFP at a concentration of 10 μ M in 0.25 % Triton X-100, 1% BSA, 0.004 %

NaN₃ PBS for 60 minutes. Cells were washed extensively in PBS before imaging in blinking buffer 30 mM β -mercaptoethylamine (MEA), 0.5 % glucose, 0.25 mg/ml glucose oxidase and 20 μ M catalase. We acquired streams of 10,000 to 20,000 frames at 30 msec. exposures and we used Wave Tracer plugin (Molecular Devices) to detect and gate events with a 16-bit intensity threshold of 1,000. When possible we didn't use gain on the EMCCD camera to better calculate resolution; the camera has a conversion factor of 6e⁻/count when no gain is used. Based on photon counts, we estimate an x, y-resolution of \approx 10 nm with the 647 nm wavelength Alexa-647 fluorophore and a z-resolution of \approx 50 nm with the astigmatic lens in 3D configuration calibrated on TetraSpeck beads (ThermoFisher). Center of mass for each event was calculated and we reconstructed images in Wave Tracer before further analysis in Metamorph (Molecular Devices). Sla1 structures were separated in circular and narrow elliptical shapes that correspond respectively to structure within or at the equator of cells.

Fluorescence recovery after photobleaching

Fluorescence recovery after photobleaching (FRAP) experiments (for recovery of Sla2-GFP and dextran-FITC) were performed on a Axio Imager Z2 spinning disk confocal microscope (Carl Zeiss). Images were acquired with a 100x NA 1.3 oil objective and a circular FRAP ROI-size of 1.5 μ m of diameter selected from the DirectFRAP diaphragm wheel. A photobleaching 488 nm 100 mW laser unit was pulsed for 1 second on samples, followed by acquisition of fluorescence recovery with time resolution from 50 msec. to 2 seconds depending on samples. Analysis of the images intensity (I) fluctuations and segmentation of regions of interest (ROI) were performed on Zen imaging software (Carl Zeiss). We analyzed the data as follows:

We first determined bleach depth with the equation:

$$bleach\ depth = \frac{\left(\frac{1}{n_{pre}} \cdot \sum_{t=1}^{n_{pre}} I(t)_{ROI\ 1'}\right) - I(t)_{ROI\ 1'}}{\frac{1}{n_{pre}} \cdot \sum_{t=1}^{n_{pre}} I(t)_{ROI\ 1'}}; \quad (1.1)$$

, and then applied a double normalization on bleached ROI1:

$$I(t)_{dbl\ norm} = \left(\frac{\frac{1}{n_{pre}} \cdot \sum_{t=1}^{n_{pre}} I(t)_{ROI\ 2'}}{I(t)_{ROI\ 2'}}\right) \cdot \left(\frac{I(t)_{ROI\ 1'}}{\frac{1}{n_{pre}} \cdot \sum_{t=1}^{n_{pre}} I(t)_{ROI\ 1'}}\right); \quad (1.2)$$

, where ROI2 is a non-bleached region and n_{pre} is the number of pre-bleached images. We finally fitted each normalized trace with a non-least square function to best fit the single term equation:

$$f(I) = I_0 - a \cdot e^{-\omega t}; \quad (1.3)$$

from which we extracted half recovery times for the Sla2-GFP and dextran-FITC samples. We selected the Sla2 protein because the apparent number of molecule in the fluorescent foci remains relatively constant during vesicle budding [126]. We nonetheless corrected for possible accumulation or reduction of the total number of molecules in the foci with a rate of 4 molecules per second in the initial or the last 5

seconds of the acquired recovery window. Analyses were performed using subroutines of the R package.

Centroid tracking of Sla1 foci

We measured the mean square displacement (MSD) of single Sla1-GFP fluorescent foci within a confocal volume on the Quorum platform (see Diffraction-limited fluorescence microscopy section). Images were acquired at 20 fps for 30 seconds with a 50 μm pinhole spinning disk and we performed particle centroid tracking with the Wave Tracer plugin in the Metamorph software (Molecular Devices). We included only foci that remained in the confocal volume throughout the acquisition and which showed decreasing fluorescence intensity as a function of MSD (Figure 34a). We next determined the linear displacement of the Sla1 foci towards the cell interior with the particle coordinates plotted as a function of elapsed time (Figure 34b).

Quantification of membrane in nascent vesicles under HD titration

We quantified the amount of membrane in single nascent CME vesicles by fluorescence emitted from FM6-64 labelled membrane. Overnight Sla1-YFP cell cultures were diluted 1:40 in fresh LFM with HD concentrations from 0 to 5%. Cells were incubated in the HD solutions for 5 minutes and then labelled with 5 μM FM4-64 for another 5 minutes before direct fluorescence image acquisition on the Quorum platform (see Diffraction-limited fluorescence microscopy section). Single vesicles were segmented with an intensity threshold in both YFP and FM4-64 channels to quantify the membrane fluorescence that co-localizes with Sla1 signal. Average intensity measurements per nascent vesicle were normalized to values between 0 and 1 for the whole HD treatment concentration range. As a reference point to compare with membrane invagination predictions, we extracted mean and standard

deviation values from data for HD concentration below 2 %; mean and standard deviation were also determined for each HD concentration.

Effect of 1,6-hexanediol (HD) titration on droplet stability

Formation of a cortical droplet results in an interface between the droplet and the cytosol and we can treat the droplet and the dispersed cytosol as two phases defined by an interface between them. In a mean field description, the cohesive interactions that drive the formation of the droplet derive from the balance of interactions amongst the droplet and cytosolic components. This will determine the stability of the droplet. In addition, the interface between the droplet and cytosol will be governed by an interfacial tension. A simple adaptation of the Flory-Huggins model for binary mixtures can be used to quantify the interfacial tension [280].

The model is as follows: We shall define two condensed phases *viz.*, the droplet phase (D) and the cytosolic phase (C). The interfacial tension γ_{DC} defines the free energy penalty associated with increasing the interfacial area between the two phases. If $\gamma_{DC} > 0$, then the interfacial area will be minimized, thus resulting in spherical droplets. From the vantage point of the droplet, reducing the interfacial tension decreases the number of droplet components that are “sacrificed” to be at the interface and thus lose favorable intra-droplet interactions.

If the total free energy of the two bulk phases D and C and the interface between the phases is F , then the interfacial tension associated with changing the interfacial area A is defined as:

$$\gamma_{DC} = \left(\frac{\partial F}{\partial A} \right)_{n_D, n_C, T}; \quad (2.1)$$

For simplicity, we shall use a mean-field model with the two phases defined on a lattice with coordination number z . The molecules of D and C will be assumed to be of

similar size and the translational entropy will be set to zero. If a is the area per molecular unit that is exposed to the interface, then equation (2.1) becomes:

$$\gamma_{\text{DC}} = \left(\frac{\partial F}{\partial A} \right)_{n_D, n_C, T} = \left(\frac{\partial U}{\partial A} \right)_{n_D, n_C, T} = \frac{1}{a} \left(w_{\text{DC}} - \frac{w_{\text{DD}} + w_{\text{CC}}}{2} \right); \quad (2.2)$$

Here, the w terms are the effective mean-field energies associated with interactions between components of the droplet (w_{DD}), the cytosol (w_{CC}) and the components of the droplet and the cytosol (w_{DC}). These energies are in units of $k_B T$ and the convention is that the energies are negative if they are favorable and positive if they are unfavorable. Accordingly, it follows that:

$$\begin{aligned} \gamma_{\text{DC}} &> 0 \text{ if } |w_{\text{DC}}| < \left| \frac{w_{\text{DD}} + w_{\text{CC}}}{2} \right| \\ \gamma_{\text{DC}} &= 0 \text{ if } |w_{\text{DC}}| = \left| \frac{w_{\text{DD}} + w_{\text{CC}}}{2} \right|; \quad (2.3) \\ \gamma_{\text{DC}} &< 0 \text{ if } |w_{\text{DC}}| > \left| \frac{w_{\text{DD}} + w_{\text{CC}}}{2} \right| \end{aligned}$$

Importantly, equation (2.2) can be rewritten in terms of the Flory-Huggins interaction coefficient using the relationship:

$$\chi_{\text{DC}} = \frac{z}{k_B T} \left[w_{\text{DC}} - \left(\frac{w_{\text{DD}} + w_{\text{CC}}}{2} \right) \right] = \left(\frac{c_E}{k_B T} \right); \quad (2.4)$$

Here, c_E is cohesive energy that holds the droplet together and represents the balance of droplet-cytosol, intra-droplet and intra-cytosol interactions. Accordingly,

$$\begin{aligned} \gamma_{\text{DC}} &= \frac{1}{a} \left(w_{\text{DC}} - \frac{w_{\text{DD}} + w_{\text{CC}}}{2} \right) = \left(\frac{k_B T}{za} \right) \chi_{\text{DC}}; \quad (2.5) \\ za\gamma_{\text{DC}} &= k_B T \chi_{\text{DC}} \end{aligned}$$

Alternatively,

$$\chi_{DC} = \left(\frac{za}{k_B T} \right) \gamma_{DC} = \left(\frac{c_E}{k_B T} \right); \quad (2.6)$$

$$za = \left(\frac{c_E}{\gamma_{DC}} \right)_{HD=0\%}; \quad (2.7)$$

Note that the values of z and a are fixed by the lattice and components of the droplet. Through measurements combined with the Young-Laplace theory, we have estimates of the interfacial tension and c_E in the absence of HD – as shown in equation (2.7). These estimates can be used as shown in equation (2.7) to estimate the value of za . Since this value of za is independent of HD concentration, one can fix za and use the estimate of cohesive energy c_E at different HD concentrations to estimate the change in interfacial tension as a function of HD concentration using equation (2.8) below:

$$\gamma_{DC}(\%HD) = \left[\frac{c_E(\%HD)}{za} \right]; \quad (2.8)$$

Polystyrene beads and Dextran-FITC osmoporation

To incorporate dextran-FITC of different chain length inside haploid yeast cells, we used an osmoporation technique similar to that described by da Silva Pedrini *et al.* [262]. Cells were centrifuged for 2 minutes at 3000 x g and resuspended in a water-glycerol binary solution at 1.4 MPa for 30 minutes, then in a 30 MPa solution for 1 hour. Osmoporation of dextran-FITC is performed after these steps, by centrifuging cells at 3000 x g and resuspending the pellet in the 1.4 MPa water-glycerol solution with the dextran-FITC at 10 mg/ml for 1h. After this incubation period, cells were put on ice and washed 3 times with cold PBS. Cells were preserved on ice until they were plated on ConA treated 35 mm imaging dishes for 10 minutes and imaged on either

the Quorum or Zeiss platforms (see Diffraction-limited fluorescence microscopy section).

We also incorporated 200 nm orange (540/560) FluoSpheres carboxylate-modified polystyrene beads (ThermoFisher) with this technique. Beads were either coated with 10 mg/ml BSA or directly incorporated in strains with Sla2-Dronpa3 fluorescent protein. After osmoporation, cells were preserved on ice until they were plated on ConA treated coverslips and mounted on glass imaging slides for subsequent image acquisition and optical tweezers experiments.

microNS-GFP micro-rheology

To determine the effect of *osmoporation* on the cell rheological properties, we measured displacement of expressed viral capsid microNS particles labeled with GFP in both normal and osmoporated cells (Figure 31). Cells were transformed with the microNS-GFP pRS expression plasmid, a generous gift of S. Alberti at Max Planck Institute of Molecular Cell Biology and Genetics (MPI-CBG). microNS movement was recorded on the Quorum platform (see Diffraction-limited fluorescence microscopy section) within a 2 micron thick Z-stack of 5 confocal planes (50 μ m pinholes) acquired at 5 frames per second (fps). Image analysis was performed with Metamorph and Wave Tracer plugin (Molecular Devices), to track particles displacement with centroid localization on maximum intensity projections. We further filtered the mean square displacement (MSD) data for particles that are confined and showed that they have MSD similar to the technical noise of our apparatus setup.

Optical tweezers measurements and calibration

Dynamic mechanical analysis of yeast cytoplasm was performed with a custom optical tweezers (OT) platform. Our OT system is an inverted microscope (Nikon Ti-E)

equipped with a CFI APO SR TIRF 100x / 1.49 NA oil immersion objective (Nikon), a 1,064 nm Nd:YVO₄ 10 W infrared laser (IPG Photonics), an X-cite lamp source (Excelitas) and a nano-positioning stage (Mad City Labs). Oscillation of the tweezers on the specimen plane from 0.1 Hz to 2000 Hz was achieved with an acousto-optic deflector (AOD, AA Optoelectronics) coupled to a digital frequency synthesizer that we controlled with in house Labview routines. Light transmitted through the specimen was collected with a condenser lens and reflected onto a position-sensitive detector (PSD) (Thorlabs, PDP90A) to perform back focal plane interferometry. Before acquisitions we adjusted the microscope for Köhler illumination and ensured that all the optics were conjugate to the respective specimen plane or back focal plane. At each frequency of excitation we recorded the signals (120,000 samples at 1000 Hz to 2,000,000 samples at 0.1 Hz at 20 kHz) and performed Fourier analysis. Measurement time for each frequency sweep was about 15 minutes. For each sample, we covered the frequency domain from high-to-low frequencies, then we repeated the procedure from low-to-high to ensure consistent frequency response with prolonged laser exposure.

Calibration of the optical tweezers measures was performed as previously described with minor modifications [149]. Data analysis was conducted with in-house Matlab code. Data quality was first confirmed by assessment of the sinusoidal shape of the response to the applied stress. Traces with a coherence of 0.95 or greater were included in the analysis. We averaged 17 traces in distinct cellular locations and determined their trap stiffness k_{trap} (mean \pm standard error; $8.0 \times 10^{-5} \pm 2.7 \times 10^{-5} \text{ N}\cdot\text{m}^{-1}$), photodiode sensitivity factor β (mean \pm standard error $10.7 \times 10^3 \pm 2.3 \times 10^3 \text{ nm}\cdot\text{V}^{-1}$) and frequency-dependent viscoelastic moduli G' (storage) and G'' (loss) (see Figure 30).

To account for the relaxation dynamics observed, we performed a fit on the forced response to sinusoidal oscillations and the power spectra of the spontaneous

fluctuations of the bead to a model of a crosslinked network of flexible polymers [269]

$$G' = G_0 - a \cdot \frac{Nk_{off}}{\frac{k_{off}^2}{4\pi^2} + f^2} + b \cdot \left(\frac{f}{f_0}\right)^\alpha ; \quad (2.9)$$

$$G'' = c \cdot \frac{Nf}{\frac{k_{off}^2}{4\pi^2} + f^2} + d \cdot \left(\frac{f}{f_0}\right)^\alpha ; \quad (2.10)$$

From these fits, we extracted the average parameters (G_0 ; 16.53), (f_0 ; 37.44), number of crosslinks (N ; 3×10^{14}), crosslink off-rate (k_{off} ; 8.28), power law (α ; 0.98) and constants ratios (a/b ; $1.06 \times 10^{-14}/2.19$), (c/d ; $1.33 \times 10^{-14}/0.72$). Deviation of α above a value 0.75 indicates that retraction or extension of entangled protein filaments ends could contribute to the relaxation mechanism [272].

Dimensions and geometry of membrane contour and cortical droplets

From published EM data, we considered that the optimal membrane U-shaped geometry before vesicle excision is about 70 nm high and 60 nm wide [121, 252]. To approximate the area and volume, the U-shape was decomposed into a hemispherical cap of 30 nm radius over a cylinder of 30 nm radius and 40 nm high. We then calculated, with these dimensions, an invaginated membrane area of $1.32 \times 10^{-14} \text{ m}^2$ and volume of $1.70 \times 10^{-22} \text{ m}^3$.

We also defined for the membrane bending energy, the invagination height profile as a function of position around the invagination peak and middle of the droplet;

$$h(x, y) = h_0 \cdot \exp\left(\frac{-(x^2 + y^2)}{2R_0^2}\right); \quad (3.1)$$

where h_0 is the invagination depth and R_0 is the radius of invagination.

To calculate the area and volume occupied by the cortical droplet and thus the amount of displaced cytosol material, we used our dSTORM measurements. The hemispherical cortical droplet volume was calculated to be $2.43 \times 10^{-21} \text{ m}^3$ for a radius of 105 nm. The same hemispheric droplet has an area of $6.93 \times 10^{-14} \text{ m}^2$. These dimensions agree with the size of ribosome exclusion zones observed surrounding invaginated clathrin patches observed by EM [121].

Calculation of the energies that counteract membrane invagination

Our observation of cortical droplets coupled to endocytosis suggests that membrane deformation in actin-independent CME results from a droplet-dependent stress. It has been proposed that some contribution to the energy needed for membrane invagination in CME could be provided by the clathrin lattice, by membrane-curving convex-shaped BAR domains (for Bin, Amphiphysin and Rvs) in BAR domain-containing proteins, insertion of amphipathic protein helix into membrane layers [281], lipid composition or simply by steric exclusion or crowding of proteins at cortical sites. It's also possible that alternative mechanisms have an additive effect *in vivo*, but the mechanism we introduce here is essential to actin-independent membrane invagination. We examined each of these arguments in turn.

Although clathrin forms a cage structure around mature endosomes it was recently demonstrated that it assembles into a flat lattice on cortical sites [244]. Furthermore, studies have showed that clathrin doesn't produce work or curve the membrane itself [120]. Deletion of clathrin heavy chain gene (*CHC1Δ*) does not change the morphology or the rate of formation of CME vesicles [122]. Clathrin, thus, may provide a scaffold for binding of other proteins involved in CME, be essential to site selection, and participate in vesicle size and scission [122].

Second, proteins containing BAR domains, that have a curved structure, have been implicated in membrane remodeling, including in the scission step of CME that requires the BAR domain-containing proteins Rvs161 and Rvs167 [282]. The only protein, however, that contains a BAR domain that is recruited to CME nucleation site prior to actin synthesis is Syp1. As previously reported deletion of the BAR domain of Syp1 had no effect on CME. Our results exclude a role of Syp1 F-BAR domain in inducing membrane curvature but not in other functions including to act as a sensor of membrane curvature [247], forming membrane microdomains [283] or polarizing CME cortical sites in the cell [20].

Third, simple steric repulsion of proteins bound to and concentrated at confined membrane surfaces were proposed to cause invaginations of membranes *in vivo* and *in vitro*, including proteins implicated in CME. The disordered C-terminal domains (CTDs) of Ent1/2 and Yap1801/1802 proteins can crowd membranes and induce tubulation of giant unilamellar vesicles (GUVs). They further propose an *in vivo* model, where Epsin1 and Ap180 disordered CTDs create *steric pressure* at the intracellular surface that increases the membrane curvature. Furthermore, Gleisner and collaborators recently demonstrated the ability of these ENTH proteins to effectively reduce membrane tension of GUVs, thus facilitating deformation and curvature of the membrane [274, 284]. The precise physical mechanisms by which Epsins and protein crowding in general drives membrane invagination *in vivo* is unclear. As we describe in our work, however, the geometries of the hemispherical

body composed of CME coat proteins and that of the membrane invagination are not consistent with those expected to be caused by protein crowding. In addition, there is no evidence of a mechanism that confines proteins at a sufficient concentration to generate steric hindrance between proteins enough to drive membrane invagination. Unlike the crowding effect, our model doesn't rely on lateral confinement and restrictions of diffusion in the membrane [285]. Furthermore, calculations of the entropic gain and pressure produced in the crowded protein layer, obtained with the Carnahan-Starling equation, assumes proteins are non-attracting (non-interacting) disks, not compatible with protein based structures.

Energy penalties for bending of the membrane | We calculated the membrane bending energy with the standard Helfrich model for the membrane profile obtained by equation (3.1) and considered a membrane bending modulus κ_m of $12.5 \cdot K_B T$ [127, 286, 287]:

$$U_{em} = 11 \sqrt{\left(\frac{\pi^3}{32}\right)} \left(\frac{h_0}{R_0}\right)^2 \kappa_m; \quad (3.2)$$

We determined the energy required to generate a 70 nm deep invagination to be 3×10^{-18} J.

Energy penalties for elastic and viscous deformation of the cytosol | We assumed that the viscoelastic cytosol behaves as a Kelvin-Voigt material and that the total stress is equal to the sum of the elastic and viscous stresses, such that:

$$\sigma = \varepsilon E_i + \dot{\varepsilon} \eta; \quad (3.3)$$

, where η is the cytosol viscosity at a specific frequency f_x obtained with:

$$\eta = \frac{G''}{2\pi f_x}; \quad (3.4)$$

For stringency, we used a Young's (or elastic) modulus (E) for the cytosol of 45 Pa (see Eq. 3.6 below) and calculated the deformation with the droplet radius (1.18×10^{-7} m) over the cell radius (2×10^{-6} m). We obtained an elastic stress of 3 Pa.

We next determined η at 0.5 Hz to be 0.35 Pa•s. and the deformation rate of 0.004 s^{-1} , for a droplet velocity v of $7.4 \times 10^{-9} \text{ m}\cdot\text{s}^{-1}$ (Figure 34).

$$\dot{\epsilon} = \frac{v}{6\pi R_{drop}}; \quad (3.5)$$

, which gives a negligible viscous stress of 0.0014 Pa. With a volume of $2.42 \times 10^{-21} \text{ m}^3$, the total stress of 3.0014 Pa corresponds to an energy cost of $7.26 \times 10^{-21} \text{ J}$ to displace the viscoelastic cytosol.

Cortical droplet material properties and contact angle

We determined the values of the elastic modulus of the cytosol under the assumption that compressible biological materials have a Poisson's ratio (ν), which relates all material moduli to each other, of 0.45 (or between 0.3 and 0.5) [288]. We then used the relationship between shear modulus (G) and Young's (or elastic) modulus (E):

$$E_i = 2(1 + \nu_i)G_i; \quad (3.6)$$

to calculate an approximate elastic modulus of 45 Pa for the cytosol from the G' of 15 Pa at 1 Hz. This strain rate was used to consider a G' near the elastic plateau of the material response. With the volume of displaced cytosol and this modulus value, we could determine the mechanical stress imposed on the cytosol to be ~ 3 Pa (see Eq. 3.3-3.5). This corresponds to a compression force (F) of $\approx 1.4 \times 10^{-13}$ N. We then isolated the equivalent modulus (E') from Hertz elastic contact equation

$$F = \frac{4}{3}E'_{ij}R'_{ij}^{\frac{1}{2}}\delta_{ij}^{\frac{3}{2}}; \quad (3.7)$$

into

$$E'_{ij} = \frac{4F}{3R'_{ij}^{\frac{1}{2}}\delta_{ij}^{\frac{3}{2}}}; \quad (3.8)$$

, where δ_{ij} is the interface indentation (or invagination depth), to estimate the respective elastic moduli of the cytosol and the droplet, again under the assumption that both materials have a Poisson's ratio of 0.45. The equivalent modulus is determined by:

$$\frac{1}{E'_{ij}} = \frac{(1 + \nu_i)^2}{E_i} + \frac{(1 + \nu_j)^2}{E_j}; \quad (3.9)$$

where E_i and E_j are the respective elastic moduli of the objects in contact and

$$\frac{1}{R'_{ij}} = \frac{1}{R_i} + \frac{1}{R_j}; \quad (3.10)$$

for contact between two spheres of radii R_i and R_j . These relationships gave us a cortical droplet elastic modulus of 59 Pa.

Assuming that gravity is negligible, the droplet can be treated as a sectional arc of a sphere or hemispherical cap alone (Figure 24b) and we can estimate the droplet contact angle;

$$\theta = 2 \cdot \tan^{-1} \left(\frac{h}{d} \right) \quad (3.11)$$

, where d is droplet radius and h is droplet height. Based on our 2D dSTORM measures we obtained a contact angle of about 97° . Note that at the hundred nanometer scale, droplet wetting geometries are also affected by evaporation and line tension at the three-phase contact line.

Theoretical model based on elastic and adhesive contact mechanics

To explain how phase separation of disordered proteins into a 100 nm-scale viscoelastic body can invaginate the membrane (in the absence of turgor, F-actin polymerization and steric effects), we propose a model in which elastic and adhesive

contact mechanics can generate enough energy (estimated from membrane bending to be $\approx 3 \times 10^{-18}$ J) to drive local invagination of the membrane.

We explored the idea that when cortical droplets are nucleated between the membrane and cytoplasm, new interfaces are created and the free energy available on the droplet interfaces can produce work to deform both surrounding substrates (membrane and cytosol). We thus assume that free energy is released upon phase separation and adhesion of the cortical droplet to neighbor structures, which is converted into mechanical work.

Calculations and graphics of the elastic, viscous, surface and adhesive energies in our model were performed in either Maple or the R software environment. The parameters, variables and relationships we used in the calculation are listed in Tables S1 and S2. A summary of the invagination and energy results we obtained with these specific parameters are in Table 9. We describe below the details of the model.

General mechanic model to bend the membrane | We first propose a general model where the energy penalties to create interfaces around the droplet and deform the cytosol and the membrane follow a super-linear growth as a function of invagination depths δ (of both cytosol and membrane), whereas the free energy released by droplet phase separation is linear. We expressed the relationship between these two general energy terms and the total energy U with the power-law function:

$$U \sim \phi \cdot \delta^{1+\varepsilon} - \psi \cdot \delta; \quad (4.1)$$

, where ϕ is the energy penalty term, ψ is the available work and the exponent $\varepsilon > 0$. When δ is isolated from the partial derivative of equation (4.0), such as:

$$\begin{aligned}\frac{\partial U}{\partial \delta} &= \phi(1 + \varepsilon) \cdot \delta^\varepsilon - \psi; \\ \delta^* &= \left(\frac{\psi}{\phi(1 + \varepsilon)} \right)^{\frac{1}{\varepsilon}};\end{aligned}\tag{4.2}$$

, we observe that our model predicts that δ scales with ϕ and ψ :

$$\delta^* \sim \frac{\psi}{\phi};\tag{4.3}$$

We provide below a proof for this model, where ϕ is decomposed into individual elastic, viscous friction and surface stress terms and ψ is fragmented in the work of adhesion from the respective droplets interfaces. We also describe the quantities contained within these individual terms; either directly measured, calculated or estimated.

Interfaces at equilibrium on cortical droplets | Parallel to the membrane plane, surface energies formed by the droplet (d), cytosol (c) and membrane (m) come to equilibrium as described by Young's equation:

$$\gamma_{cm} = \gamma_{dm} + \gamma_{dc} \cdot \cos \theta;\tag{4.4}$$

With a contact angle of about 97° , the cytosol-membrane surface tension (γ_{cm}) is predicted to be approximately equal to the droplet-membrane surface tension (γ_{dm}). We determined the values of γ_{dc} and γ_{dm} next.

Surface tension at cortical droplet interfaces | We assumed an apparent Young's modulus (E_{cell}) of 1 kPa, determined from atomic force microscopy on haploid yeast spheroblast [145]. We assumed that this modulus represents the bulk material properties of both membrane and cytosol when deformed towards the cell interior, as for a CME-driven invagination. We then calculated the overall mechanical stress in the system with Hooke's law:

$$\sigma = \varepsilon E_i ; \quad (4.5)$$

to create the U-shape membrane geometry observed by EM. The deformation ε of the membrane was decomposed to represent stretching of an elastic band, where deformation equals length difference over original length. For our U-shaped deformation the linear contour was established at 174.2 nm, whereas the same membrane line measured ≈ 80 nm before invagination. This gives us a deformation of 1.18 (dimensionless) and a stress of 1178 Pa.

This mechanical stress corresponds to the pressure difference ΔP experienced by the cytoplasm and the membrane due to the presence of the cortical droplet. This pressure difference arises from adhesive, hydrostatic and elastic stress energies. We then used the Young-Laplace equation:

$$\Delta P = 2\gamma_{dc} \cdot H ; \quad (4.6)$$

, where H is the mean curvature of the interface and is equal to $1/R_d$, to calculate γ_{dc} at the cytosol interface under the assumption that the droplet is circular in shape. Equation (4.6) determines the pressure difference across the droplet-cytosol curved interface as a function of surface energy, and gives a droplet/cytosol interfacial tension γ_{dc} of $7 \times 10^{-5} \text{ N}\cdot\text{m}^{-1}$.

Based on Young's equation (4.4) and the cortical droplet-membrane contact angle θ value, the relationships between interfacial tensions is:

$$\begin{aligned}\gamma_{cm} &= \gamma_{dm} + \gamma_{dc} \cdot \cos \theta \\ \gamma_{cm} &= \gamma_{dm} - (8 \cdot 10^{-6});\end{aligned}\tag{4.7}$$

and

$$\gamma_{dc} > \gamma_{dm};\tag{4.8}$$

where the droplet-membrane surface tension γ_{dm} can range between about 1.8 to 7 x 10⁻⁵ N•m⁻¹. The γ_{dm} limits also arise from equation (4.9) below.

Biopolymeric constraints on interfacial tension values | The interfacial tension γ of a fluid droplet is inversely proportional to the square of the length ξ of its discrete elements (i.e. the individual biopolymers), we used this relationship to estimate maximal and minimal γ values:

$$\gamma = \frac{k_B T}{\xi^2};\tag{4.9}$$

, where k_B is the Boltzmann constant and T is temperature in kelvin [32]. The interfacial tension values for protein based biological droplets (in which protein radii range from 1 to 10 nm) should be on the order of 1 x 10⁻⁵ N•m⁻¹ to 1 x 10⁻⁴ N•m⁻¹.

Work of adhesion at cortical droplet interfaces | To directly estimate the work of adhesion at the cortical droplet interfaces, we used the Young-Dupré equation:

$$W_{dm} = \gamma_{dc} \cdot (1 + \cos \theta); \quad (4.10)$$

that implies a direct relationship between work of adhesion of an interface (W_{ij}), the droplet contact angle and the surface tension γ_{dc} . We could determine the work of adhesion at the membrane interface W_{dm} to be $6 \times 10^{-5} \text{ N}\cdot\text{m}^{-1}$.

We also combined the Young's equation (4.1) and the Dupré relationship:

$$W_{dc} = \gamma_{dm} + \gamma_{cm} - \gamma_{dc}; \quad (4.11)$$

to express the work of adhesion at the cortical droplet-cytosol interface W_{dc} :

$$W_{dc} = 2\gamma_{dm} + \gamma_{dc} \cdot (\cos \theta - 1); \quad (4.12)$$

in terms of interfacial tension at cortical droplet interfaces with both membrane and cytosol. We could thus estimate the maximal W_{dc} value to be $6 \times 10^{-5} \text{ N}\cdot\text{m}^{-1}$, under the assumption that $\gamma_{dm} \approx \gamma_{dc}$.

Young-Dupré regime dominates nanoscopic viscoelastic bodies | We determined in parallel whether adhesion dominates the mechanical potential of cortical droplets, as opposed to capillary effects. Under so called elasto-capillary action, droplet interfacial tension (γ) can deform an elastic sheet as a function of either droplet radius (R) or the thickness (h) and elastic modulus (E) of the slender material in contact with the droplet; in our case, the plasma membrane [289]. We can assume that the phospholipid bilayer membrane is about 10 nm thick and the cell has a bulk elastic

modulus E of 1 kPa [145]. With a surface tension γ_{dc} of $7 \times 10^{-5} \text{ N}\cdot\text{m}^{-1}$, we determined that R is larger and h is about equal to the elasto-capillary length:

$$\frac{\gamma}{E}; \quad (4.13)$$

, and the membrane sheet should remain undeformed at the 3-line contact point by interfacial tension alone (Figure 37a). This prediction is also consistent with EM data where the membrane doesn't bulge out under the Laplace pressure within droplets on cortical sites [252]. In this scenario our system should obey the Young-Dupré equation and deformation can only come from work of adhesion.

Elastic-adhesive model to deform membrane and cytosol under action of cortical droplet phase separation | Johnson-Kendall-Roberts (JKR) theory describes how non-flat surfaces stick together and conform to one another to minimize their interfacial energy. When they adhere to one another, soft and compliant materials such as the membrane and cytoplasm are subject to a deformation limited by elastic strain. Style, *et al.* adapted the JKR theory of contact mechanics to describe the contact surface geometry between a microscopic rigid particle and a soft substrate [250]; we followed a similar approach to estimate model 4.1 parameters and test our hypothesis.

If we consider the two droplet interfaces where deformation occurs, both membrane and cytoplasm, the energy penalty to create these curved surfaces (or interfaces) are equal to the sum of elastic, viscous and surface energies.

To build a complete energy model, the elastic energy penalties were determined with the JKR theory. Since the geometry of the contact surface corresponds to the cortical droplet geometry itself, we calculated the elastic penalties U_{ely} to deform both interfaces as a function of invagination depth δ_{ij} :

$$U_{el,y}(\delta_{ij}, E'_{ij}, R'_{ij}) = c E'_{ij} R'_{ij}{}^{\frac{1}{2}} \cdot \delta_{ij}{}^{\frac{5}{2}}; \quad (4.14)$$

where E'_{ij} and R'_{ij} are calculated with (3.5) and (3.6) respectively and c is a constant.

$$c = \frac{8}{15} \cdot \sqrt{3}; \quad (4.15)$$

We incorporated a correction for the membrane elastic penalty to compensate for the reduced JKR accuracy at the hundred nanometer scale and for soft materials [250] by addition of the Helfrich Hamiltonian of membrane bending at individual δ_{ij} values. We substituted h_0 in equation (3.2.0) for δ_{ij} and assumed a fixed radius of invagination R_{ij} to get the relationship:

$$U_{em.corr}(\delta_{ij}) = 11 \sqrt{\left(\frac{\pi^3}{32}\right)} \left(\frac{\delta_{ij}}{R_{ij}}\right)^2 \kappa_m; \quad (4.16)$$

We calculated a corrected energy cost of $\approx 1 \times 10^{-18}$ J to deform the membrane (Table S3). The cytoplasm elastic energy barrier did not require correction and we assumed no elastic nor viscous droplet deformation in our model.

JKR theory is also less accurate for very soft materials and small particles because the model neglects surface stresses [250]. Inclusion of energy penalties to increase surface length at the interfaces was proposed by Style *et al.* to compensate for this reduced accuracy [250]. We incorporated the surface penalties (U_{ly}) for the formation of the new interfaces into our model with the function;

$$U_{i|y}(\delta_{ij}, \gamma_{ij}) = \pi \gamma_{ij} \cdot \delta_{ij}^2 \quad (4.17)$$

, where the respective interfacial tensions γ_{dc} and γ_{dm} determine the energy cost to increase the interfacial areas. The energy to form the droplet/cytosol interface is $\approx 1 \times 10^{-18}$ J and is equivalent to the combined elastic penalties. These energy values confirm that at the hundreds of nanometers scale, surface stress can dominate (or equate) elasticity in material responses to deformation. With this approach, we propose a more comprehensive model of the energy required to deform the membrane on cortical sites, that also takes into account creation of new surfaces and deformation of the cytosol.

We also incorporated an additional energy penalties $U_{v|y}$ to displace the viscous cytosol with the equation:

$$U_{v|y}(\delta_{ij}, R'_{ij}, \eta, \dot{x}) = \eta \dot{x} \delta_{ij} \cdot 6\pi R'_{ij}; \quad (4.18)$$

, where the displacement rate is the droplet maximum velocity of $7.4 \times 10^{-9} \text{ m}\cdot\text{s}^{-1}$ (Figure 34).

If the conversion of the energy released by adhesive contact into mechanical energy is above the total energy barrier, the droplet should drive membrane invagination. The extent of membrane invagination will be limited by the free energy available. For the purpose of our model, we calculated the energy of adhesion ($U_{a|y}$) with the JKR term:

$$U_{a|y}(\delta_{ij}, W_{ij}, R'_{ij}) = W_{ij} R'_{ij} \cdot \delta_{ij}; \quad (4.19)$$

where W_{ij} is the work of adhesion at each interface, as determined by equations (4.10) and (4.12), respectively. The work of adhesion refers to the energy released in the wetting process of the cortical droplet on the membrane, it equals the work needed to separate the two adjacent phases and is given by the Dupré equation (4.11).

We then integrated the elastic (4.14, 4.16), interfacial (4.17), viscous (4.18) and adhesion (4.19) terms into a complete energy equation for i,j interfaces, where:

$$\begin{aligned} i &= \{droplet\}; \\ j &= \{membrane, cortex\}; \end{aligned} \quad (4.20)$$

into

$$\begin{aligned} U_{total}(\delta_{dm}, \delta_{dc}, \gamma_{dm}, \gamma_{dc}, W_{dm}, W_{dc}) = \\ cE'_{dm}R'_{dm}{}^{\frac{1}{2}} \cdot \delta_{dm}^{\frac{5}{2}} + 11 \sqrt{\left(\frac{\pi^3}{32}\right)} \left(\frac{\delta_{dm}}{R_{dm}}\right)^2 \kappa_m + \pi\gamma_{dm} \cdot \delta_{dm}^2 - W_{dm}R'_{dm} \cdot \delta_{dm} \\ + cE'_{dc}R'_{dc}{}^{\frac{1}{2}} \cdot \delta_{dc}^{\frac{5}{2}} + \pi\gamma_{dc} \cdot \delta_{dc}^2 + \eta\dot{x}6\pi R'_{dc} \cdot \delta_{dc} - W_{dc}R'_{dc} \cdot \delta_{dc}; \end{aligned} \quad (4.21)$$

To reduce the number of free fitting parameters, we first defined the values of the variables that were measured (or calculated) and expressed the work of adhesion of each interface W_{ij} , as determined by (4.10) and (4.12) respectively:

$$\begin{aligned} U_{total}(\delta_{dm}, \delta_{dc}, \gamma_{dm}) = \\ cE'_{dm}R'_{dm}{}^{\frac{1}{2}} \cdot \delta_{dm}^{\frac{5}{2}} + 11 \sqrt{\left(\frac{\pi^3}{32}\right)} \left(\frac{\delta_{dm}}{R_{dm}}\right)^2 \kappa_m + \pi\gamma_{dm} \cdot \delta_{dm}^2 - \frac{7\pi R'_{dm}\gamma_{dc} \cdot \delta_{dm}}{4} \\ + cE'_{dc}R'_{dc}{}^{\frac{1}{2}} \cdot \delta_{dc}^{\frac{5}{2}} + \pi\gamma_{dc} \cdot \delta_{dc}^2 + \eta\dot{x}6\pi R'_{dc} \cdot \delta_{dc} \\ - \left(4\pi R'_{dc}\gamma_{dm} - \frac{9\pi R'_{dc}\gamma_{dc}}{4}\right) \cdot \delta_{dc}; \end{aligned} \quad (4.22)$$

Finally, we coupled the membrane and cytosol invagination or penetration depth δ_{ij} with a simple function:

$$\delta_{dc} \rightarrow f(\delta_{dm}) = \mu \cdot \delta_{dm} + k; \quad (4.23)$$

, that reflects a mechanical coupling assumption, where μ and k are constants that were solved for the $(\delta_{dm}, \delta_{dc})$ coordinates $(0,0)$ and $(7 \times 10^{-8}, 1.2 \times 10^{-7})$ to 1.7 and 0 respectively. This linear relationship between δ_{dm} and δ_{dc} ensures that a critical droplet volume is conserved and that invagination values are consistent with the distribution of droplet size and membrane invagination from imaging and EM data [120]. This single δ_{ij} variable was henceforth referred to as δ (without any index).

We ended with a total energy function with 2 independent variables:

$$\begin{aligned} U_{total}(\delta, \gamma_{dm}) = & cE'_{dm}R'_{dm}{}^{\frac{1}{2}} \cdot \delta^{\frac{5}{2}} + 11 \sqrt{\left(\frac{\pi^3}{32}\right)} \left(\frac{\delta}{R_{dm}}\right)^2 \kappa_m + \pi\gamma_{dm} \cdot \delta^2 - \frac{7\pi R'_{dm}\gamma_{dc} \cdot \delta}{4} \\ & + cE'_{dc}R'_{dc}{}^{\frac{1}{2}} \cdot (\mu\delta)^{\frac{5}{2}} + \pi\gamma_{dc} \cdot (\mu\delta)^2 + \eta\dot{x}6\pi R'_{dc} \cdot (\mu\delta) \\ & - \left(4\pi R'_{dc}\gamma_{dm} - \frac{9\pi R'_{dc}\gamma_{dc}}{4}\right) \cdot (\mu\delta); \end{aligned} \quad (4.24)$$

that expresses the total energy as a function of membrane invagination and interfacial tension of the cortical droplet-membrane interface.

We explicitly defined the mechanical strain term of the model (4.1):

$$\phi \cdot \delta^{1+\varepsilon} = \left(cE'_{dm} R'_{dm} \frac{1}{2} + 11 \sqrt{\left(\frac{\pi^3}{32}\right)} \left(\frac{\delta^{-\frac{1}{2}}}{R_{dm}^2}\right) \kappa_m + \pi \gamma_{dm} \cdot \delta^{-\frac{1}{2}} + cE'_{dc} R'_{dc} \frac{1}{2} \mu^{\frac{5}{2}} \right) \cdot \delta^{\frac{5}{2}}; \quad (4.25)$$

$$+ \pi \gamma_{dc} \cdot (\mu \delta)^{-\frac{1}{2}} + \eta \dot{x} 6 \pi R'_{dc} \cdot (\mu \delta)^{-\frac{3}{2}}$$

, where the power law variable ε of 1.5 reflects the energy penalties for parabolic shaped cytosol and membrane deformations, and the mechanical work term of (4.1):

$$\psi \cdot \delta = \left(\frac{7\pi R'_{dm} \gamma_{dc}}{4} + \mu \left(4\pi R'_{dc} \gamma_{dm} - \frac{9\pi R'_{dc} \gamma_{dc}}{4} \right) \right) \cdot \delta; \quad (4.26)$$

We minimized the function (4.24) on the δ_{dm} (1×10^{-9} m to 7×10^{-9} m) and γ_{dm} interval (1.8×10^{-5} N·m⁻¹ to 7×10^{-5} N·m⁻¹) and obtained an energy minimum. This corresponds to an energy optimal invagination of 41 nm with a maximal γ_{dm} of 7×10^{-5} N·m⁻¹. For the γ_{dm} value of membrane invagination is favorable up to a depth of 80 nm (Figure 38). We also determined that to achieve an energy favorable membrane invagination of 70 nm (total energy U_{total} equal or less than 0 J) the system requires a minimal γ_{dm} of 6×10^{-5} N·m⁻¹ (Figure 38d). With this lower γ_{dm} value, the system would reach a minimum energy with a membrane invagination of 35 nm (Figure 38e).

With the geometric data and estimates of γ_{dc} , we determined the energy required to create new interfaces U_i around the droplet and the adhesive energy U_a at these interfaces (Figure 37b, Figure 38, Supplementary method; Eq. 4.17,4.19). At a δ value of 41 nm (corresponds to energy minimum), we summed the energy penalties (ϕ term) and estimated a total energy barrier of 2.4×10^{-18} J to deform the membrane and cytosol in contact with the cortical droplet. This energy cost includes the elastic,

viscous, and interfacial stress penalties (Figure 37b, Eq. 4.25, Table 10). The interfacial stress penalty to form the droplet/cytosol interface is 1.0×10^{-18} J and is equivalent to the membrane elastic penalties. These results are consistent with studies of artificial materials where at the 100 nm scale, surface stress can dominate elasticity in material responses to deformation [250]. When we consider the energy favourable domain, our model correctly predicts the magnitude of invagination (about 40 nm to 80 nm) that is accessible for a successful invagination that leads to vesicle excision (Figure 38e).

Calculation of adhesive energy on the droplet interfaces | To relate the free energy on the cortical droplet interface to density of molecular interaction on the droplet surface, we divided the adhesion energy of 3×10^{-18} J at the cytosol interface by the protein density on the droplet surface. We estimated, based on our dextran exclusion experiment, that proteins on the droplet surface are arranged in a matrix with mesh size of 10 nm (or less). If we assume an average protein filament width of 2 nm, for a droplet area of 6.93×10^{-14} m², we obtain a minimum of 1.4×10^3 protein segments on the droplet surface, based on the assumption that single proteins maximize their interactions with the cytosol elements, which is not likely given that these proteins phase separate from the bulk and favour intermolecular interactions. To maximize the adhesive energy per protein exposed on the interface, we determined the minimum amount of protein that the droplet could be composed of to be about 2×10^{-21} moles on its surface and a maximal adhesive energy density of 1.3 kJ•mol⁻¹. Conversely, this approach gives a maximum of 2.8×10^{10} molecules on the surface, or 4.7×10^{-14} moles of proteins, and a minimal adhesive energy of 6.3×10^{-5} J•mol⁻¹. To be stringent, we considered the former.

Supplementary information

Supplementary Information (SI) includes 15 figures inserted in Chapter 3 above. The 4 tables and 1 supplemental movie are produced in Appendix 2.

Acknowledgments

The authors acknowledge support from CIHR grants MOP-GMX-152556 (SWM) and the US National Institutes of Health grant R01NS056114 (RVP). We thank Simon Alberti for insightful discussions and microNS plasmid, Jackie Vogel for strains, Jacqueline Kowarzyk for technical assistance, Susan Liebman for the Sup35 plasmids, Daniel Zenklussen and Pascal Raymond for help with FRAP experiments.

CHAPTER 4 | Discussion

CME is a highly studied process in budding yeast, in which the proteins involved have been extensively catalogued and the chronology of their recruitment to the membrane have been studied in detail [236]. I identified functional phosphosites on CME-mediating proteins and discovered that these are enriched for proteins with PrDs that phase separate into viscoelastic droplets on cortical sites. I further demonstrated that condensation of cortical droplets generates mechanical work to cause invagination of the membrane through adhesive contact, enough to drive CME to completion when yeast turgor pressure is relieved.

The mechanisms and strategy I have laid out in this dissertation could help to better understand functional phosphorylation events, regulation of CME, evolution of NMOs and, importantly, length scales available to NMOs with mechanical properties. Below, I discuss these implications and propose future research avenues that stem from my work.

Detection of functional phosphosites on CME-mediating proteins

Our SILAC-based approach allows for unprecedented, time-lapse phosphoproteomic analysis of flash frozen cell cultures, seconds after initiation of osmotic shock. At each time point, sample collection was performed without any washing steps, and thus with no further impact on cellular environment and signalling events. Our phosphoproteomic method could be used to further understand how signaling networks have evolved to ensure specificity and timing of cellular responses to different types of or combinations of stimuli and thus, in the future provide deeper insight into how signal integration and processing occurs in living cells.

We revealed key functional PTMs in CME-mediating proteins by monitoring real-time differential phosphorylation across the proteome during the onset of the HOG-response. We further established a connection between osmotic response and CME regulation, proposed before with the modulation of Pan1 phospho states and higher osmosensitivity of diploid yeast that contained just one allele of ACT1 [133, 191]. We demonstrate that post-translational modification of proteins in response to salt increase affects CME and other morphogenic pathways. We also show that PTMs have an impact on the kinetics and/or assembly of CME-mediating proteins on cortical sites.

Could the phosphosites we identified be involved in modulation of protein chemical states that favor phase separation? Further investigation of single proteins and their respective dynamic phosphosites could yield rich information on the phospho regulation of cortical droplet phase separation.

Are heat shock proteins required to regulate phase separation of cortical droplet?

We identified dynamic phosphosites within the chaperone protein Hsp42, which shares many PPI with CME-mediating proteins (Figure 10A) and there is compelling evidence that other chaperones have an important role in CME. Could chaperones directly regulate the phase separation of CME-proteins? Protein chaperones are crucial elements of the proteome quality control system and they are viewed as important factors to prevent protein misfolding and aggregation [4]. Specifically, in the context of CME, the heat shock cognate 70 (Hsc70) protein is believed to be involved in the endosome uncoating process; by which the proteins involved with CME are removed from mature endosomes [290]. Furthermore, it was shown that diverse disease-associated protein aggregates can sequester Hsc70 and completely block progression of CME compartments [291]. Chaperone availability is thus essential to CME and association of CME-mediating PrD proteins with chaperones could favor

unsuspected and surprising molecular conformations that help to determine cortical droplet organization, size and lifetime.

Aberrant phase separation of endocytic proteins in neurodegenerative pathologies?

If an homologous CME phase separation mechanism occurs in mammalian cells, it could prove to be an important therapeutic target for neurodegenerative pathologies; including Huntington's disease, Alzheimer's, myotonic dystrophy and Parkinsonism. Because, as briefly mentioned in Chapters 1 and 3, erroneous self-assembly and aggregation of QN-rich and/or PrD-containing proteins are potentially a root cause of these pathologies and it is conceivable that these proteins interact with those of CME and disrupt endocytosis [72-77].

For example the etiology of Huntington's chorea in neural cells involves defects in polyglutamine domain expansions of Huntingtin protein (Htt) which induces aberrant aggregation – possibly through phase separation – of Htt and other IDPs, such as the Htt-interacting protein (HIP1R) [292]. HIP1R, an endocytic protein orthologous to yeast Sla2, further interacts with clathrin light and heavy chains, AP180 and Epsins through a central predicted PrD domain [47, 292]. Defects in the phase separation of endocytic proteins could also be involved in other neurodegenerative diseases, such as Alzheimer's, with elusive relationships to inadequate endocytic mechanisms [293]. The potential role of aberrant phase separation of endocytic proteins in these neuronal disease merits testing, and conserved functional phosphosites identified in this dissertation on CME proteins could be effective targets to regulate such anomaly.

Implications of cortical droplets in regulation and function of CME

Phase separation of CME adaptor and coat proteins – Sla1, Sla2, Ent1, Ent2, Yap1801 and Yap1802 – into a cortical droplet with mechanical properties could

constitute a fail-safe mechanism that ensures coordinated condensation of key proteins and completion of CME in distinct energy requirement scenarios. This mechanism could also account for the robust nature of CME and its progression with heterogeneous protein composition within cortical droplets, as observed by Brach *et al.* [124]. We can hypothesize that droplet material and mechanical properties are theoretically less affected by protein composition as opposed to protein-specific functions.

Presence of SH3 domains and proline rich motifs (PRMs) on many proteins involved in CME further suggests that phase separation could be a common strategy to organize matter on cortical sites. The segregation observed in space and time of subgroups of CME proteins – coat and actin phases – could reflect the coalescence of immiscible bodies, with distinct material properties and functions. This model could explain how yeast have evolved a two-phase design for CME and how early coat and late actin endocytic phases can be physically uncoupled, by depletion of Pan1 and End3 proteins, to create the so-called “actin comet tail” phenotype [294, 295]. These distinct cortical phases of matter are currently being explored in the Michnick lab.

Proteins that coalesce on cortical sites could be further involved in recruitment of other proteins that don't phase separate per se, through stereospecific interactions between folded domains for example. Distinct classes of PPI domains could coordinate the phases of CME, with initial phase separation of the adaptor-coat proteins followed by recruitment of proteins that regulate F-actin polymerization (WASP/MYO module) or vesicle scission (AMPHIPHYSIN module) through multivalent SH3 interactions and other types of interactions.

At the mechanical level, the implications of cortical droplets go beyond providing additional mechanical force to bend the membrane. Cortical droplets could help to harness and/or ensure a mechanical coupling between the membrane and forces provided by F-actin polymerization. The work presented here thus serves as a basis to investigate such questions and better understand how CME phases are regulated.

Evolution of phase separated NMOs and specific length scales

The cortical NMOs we investigated are small, they nucleate synergistically with membrane contact and their formation drives membrane invagination. With a simple F-actin and turgor pressure-free yeast model, we demonstrated that phase separation of specific disordered proteins is necessary and sufficient to drive CME.

The intermolecular cohesive energy that drives phase separation of cortical droplets counteracts both the entropy that would tend to maintain a homogeneous mixture of proteins against phase separation and the mechanical energy penalties to deform the membrane and cell cortex. To achieve these energy requirements, cortical droplet phase separation is probably mediated, at least indirectly, by active, ATP-driven processes, including post-translational modifications, such as phosphorylation, as I described in Chapter 2.

Our mechanical model shows that the energy available to phase separate cortical droplets is limited by penalties to deform the surrounding milieu. If correct, this conjecture suggests that dimensions of the contact surface, membrane invagination and the droplet size itself, are determined by the cytoplasm and membrane material properties. This mechanism to set the length scale of sub-microscopic phase separated bodies complements the inverse concentration-dependent size scaling observed for nucleoli [106]. More importantly, cells have evolved cortical droplets of a specific size, which allow for an energy favorable – but limited – invagination of the membrane.

This basic source of mechanical energy has implications to how cellular shape and morphology are physically constrained and to the origins of life. Simple phase separated bodies could have generated work, imposed specific shapes and mediated interaction within the ancestral protocells. How phase separated NMOs have evolved

and specialized themselves into sensors, reservoirs or machines is a fascinating new field, which remain to be explored.

APPENDIX 1 | Mechanisms and consequences of macromolecular phase separation

AUTHORS & AFFILIATIONS

Louis-Philippe Bergeron-Sandoval^{1,*}, Nozhat Safaee¹, and Stephen W. Michnick^{1,2}

¹Département de Biochimie, Université de Montréal, C.P. 6128, Succursale centre-ville, Montréal, Québec, H3C 3J7, Canada.

²Centre Robert-Cedergren, Bio-Informatique et Génomique, Université de Montréal, C.P. 6128, Succursale centre-ville, Montréal, Québec, H3C 3J7, Canada.

CONTACT

Correspondence should be addressed to S.W.M. (stephen.michnick@umontreal.ca)

Mechanisms and consequences of macromolecular phase separation

Louis-Philippe Bergeron-Sandoval, Nozhat Safaee and Stephen W. Michnick

Summary

Over a century ago colloidal phase-separation of matter into non-membranous bodies was recognized as a fundamental organizing principal of cell “protoplasm”. Recent insights into the molecular properties of such phase-separated bodies present challenges to our understanding of cellular protein interaction networks, as well as opportunities for interpreting and understanding of native and pathological genetic and molecular interactions. Here we briefly review examples of and discuss physical principles of phase-separated cellular bodies and then reflect on how knowledge of these principles may direct future research on their functions.

Introduction

Just prior to the beginning of this century, Bruce Alberts eloquently described how the next generation of molecular biologists would need to be trained in order to meet the challenges of studying the organization of matter in living cells [296]. He argued that students would need an appreciation of physico-chemical principles and techniques for them to perform the future research necessary to understand the structures and dynamics of well-organized protein complexes, or “protein machines” and how they are spatially and temporally arranged to perform distinct cellular functions. More recently, Alberts has emphasized that important challenges in molecular biology also include understanding other types of cellular molecular organizations, including what he referred to as “subcompartments that are not membrane-enclosed” [13, 297].

To begin to understand these machines and their subcompartments, it's important to understand their constituent components. What has emerged from extensive large scale protein-protein interaction network studies is that few of the proteins in these networks form stable complexes with fixed stoichiometry (of equal or nearly equivalent numbers of each subunits) that one would expect of protein machines [24, 298-303]. For example, *in vivo* and *in vitro* proteome-wide protein-protein interaction mapping resulted in successful detection of stable complexes such as the nuclear pore complex (Figure 1A, B), but large regions of protein interactomes are not composed of stable, defined complexes (Figure 1C). In addition, in a recent large-scale study of human protein-protein interactions, the investigators observed few examples of complexes with high subunit stoichiometry [301].

What does the apparent lack of order in protein interactomes (Figure 1) tell us about how proteins usually behave? We have argued that many, perhaps more than fifty percent of protein-protein interactions are “noise”. By noise, we mean protein-protein interactions that serve no discernable function [20-24]. This kind of noise may also arise in protein-RNA and protein-DNA interactions [21]. Although a large proportion of protein-protein interactions may be noise, non-complex patterns of interactions that we see in protein-protein interaction networks could also represent other kinds of order created by interactions among proteins, RNA, DNA and membrane surfaces.

Over a century ago, Edmund Wilson summarized a body of work on how the protoplasm of cells appeared to be composed of phase-separated mixtures of distinct globular objects [25, 26]. What precisely accounted for these observations remained a mystery until just recently. Evidence has now emerged for alternative organizations of matter in cells that could explain some of the transient, complex-less interactions observed in protein-protein interaction networks. Notable among this body of work are the observations that proteins and protein-nucleic acid mixtures can undergo liquid-liquid phase separation (LLPS) to form liquid droplets or what have been called, “non-membranous organelles” (NMOs) [1, 27-32]. Pioneering efforts of Cliff Brangwynne,

Tony Hyman and Michael Rosen established that these bodies behave like liquids and presented examples of their biological functions.

What we now know about liquid droplets has been extensively reviewed and it is not our intention here to cover the state of the field in detail [8, 19, 25, 27, 35-37]. Our goal with this Perspective is to focus on basic observations about the functions of and molecular mechanisms of formation of liquid droplets, and to reflect on outstanding questions that arise from recognition of their existence, including: What are the hallmarks and the distinct properties of proteins that undergo LLPS? What is the nature of the interactions among molecules that form a liquid droplet and other molecules that encounter or enter these bodies? What do molecular interactomes mean in the context of liquid droplets? Is phase separation an important and extensive form of organized matter in the cell? As our understanding of this form of organization of matter develops, the challenge then becomes figuring out how many distinct droplets exist, how they could mediate biochemical processes and (perhaps optimistically) how they may explain molecular mechanism that to date, have remained mysteries.

What are the hallmarks of liquid-liquid phase separated protein droplets?

A number of mesoscale bodies (hundreds of nanometers to micrometers), particularly in the nucleus have been described as non-membranous organelles, including nucleoli, nuclear Speckles, Cajal bodies and Promyelocytic leukemia (PML) bodies [2, 27]. More recently, these and other cellular structures have been demonstrated to behave as liquid droplets, including a number of RNA-protein assemblies such as Germline P granules, processing (P)-bodies and stress granules, as well as DNA-protein complexes such as centrosomes, mitotic spindles, and signaling and actin polymerization complex activation bodies [1, 4-6, 30, 38-41]. Across this broad swath of biology, three basic principles underlie all of these membrane-less organelles.

They arise from a phase separation of proteins or proteins and nucleic acids from the surrounding milieu. They remain in a liquid state but with properties distinct from those of the surrounding matter and importantly, proteins exchange with these bodies in seconds instead of minutes, hours or longer, as occurs for subunits of stable complexes [1, 25, 28-32, 42]. Are there any common characteristics of proteins or nucleic acids that are found to form liquid droplets? As we describe next, the characteristics of amino acid sequences of droplet-forming proteins are remarkably simple.

Amino acid sequence characteristics of droplet-forming proteins

The catalog (to date) of proteins that phase separate into droplets is enriched for those having low complexity amino acid composition domains (LCD) including tandem repeats (TR) of individual amino acids or amino acid motifs, such as polyglutamine (polyQ) and polyasparagine (polyN) tracts [43]. These LCD-containing proteins belong to the general class of intrinsically disordered proteins (IDP)s that make up about a third of eukaryotic proteome peptide sequence [44-46]. We have calculated that there are over 800 such proteins in the yeast *S. cerevisiae* proteome.

One class of droplet-forming proteins have TRs contained within LCDs called prion domains (PrD) [47-61]. PrD proteins have been implicated as epigenetic agents, coding for inheritable protein complexes caused by a PrD-driven conformational change in the protein itself or other PrD-containing proteins [49, 54, 55, 62]. PrD-containing proteins have been demonstrated to underlie the molecular basis of long-term memory in eukaryotes from budding yeast to fruit flies, snails and mice [50, 54, 58, 63-68]. TR length variation has also been implicated in neutral or beneficial variations, for example in cell surface adhesion and transcription factor activities in yeast and canine skull morphology [69-71]. By contrast, mutants of PrD-containing proteins have been implicated in a number of neuro- and neuromuscular-degenerate

diseases through formation of insoluble amyloid fibrils [72-76]. For example expansion of the polyQ TRs in huntingtin protein contributes to Huntington's disease. A number of other devastating inherited or acquired neurodegenerative disorders such as myotonic dystrophy and Parkinsonism may be developed through similar mechanisms [77].

We are only beginning to understand what the few known droplets do and which biochemical and physical processes drive their formation. Since proteins with LCDs represent ~30% of the eukaryotic proteome [78] and a large number of these proteins are putative droplet components, we speculate that many unique liquid droplets could exist. Microscopists have long observed numerous cellular punctate structures, revealed in fluorescence microscopy of proteins fused to fluorescent proteins. What proportion of these correspond to liquid droplets of some stripe?

Proteins containing multiple folded binding domains (to mediate interactions with other peptides or nucleic acids) separated by low complexity linkers are also proposed to phase-separate into liquid droplets. Looking at a network of the proteins Nephrin, Nck and the Wiscott-Aldrich protein (WASP) N-terminal domain, studies describe evidence, *in vivo* and *in vitro*, for tyrosine phosphorylation of the membrane-associated Nephrin as creating linear docking sites for the binding of an SH2 domain in Nck, which in turn, organizes its three SH3 domains in space [3, 30, 38]. These reorganized SH3 domains then bind to complementary peptide motifs in N-WASP. The multivalency of these interactions generates a protein-protein interaction network as a phase-separated droplet. This phase separation was shown to induce F-actin polymerization in the presence of Arp2/3 [38]. Recently, the adaptor protein Grb2, which contains two SH3 domains, was shown to be essential to liquid phase separation of an intermediate module of T cell receptor signaling [79]. Both SH3 domains of Grb2 were necessary for phase separation. The implications from the organization of these proteins to the mechanism of phase separation are discussed below.

Does biological matter transform into distinct coalesced states?

Having considered some basic definitions for liquid droplets and the patterns of protein sequences that support their formation, it's important to bring in a more general view on phase separation that is useful for considering proteins and other biological molecules in various states of matter. Phase transitions are not uncommon. Matter can transit between many states, from gas to solid, as a function of temperature, pressure and concentration; for example, sublimation of snow to vapor on a sunny winter day.

Similarly, simple organic molecules can undergo phase transitions under the right conditions. For example, Brian Shoichet has described asymmetric aromatic compounds that are soluble in aqueous solution, but that phase-separate into liquid droplets in a concentration- and temperature-dependent manner [80]. Interestingly, the change in state of the small molecule can be used to influence biomolecules. Among these, one series of compounds was shown to spontaneously form extended amyloid-like solid fibrils that could act as scaffolds for caspases, leading to the activation of their self-cleavage; the key step in their full activation. Interestingly, beta-amyloid peptides were shown to bind similarly to these caspases [81]. Another remarkable example is a biotinylated isoxazole molecule reported by Steven McKnight's group, which upon exposure to cell lysates concentrates RNA binding proteins into ordered arrangements. They went on to show that the LCD-containing RNA binding protein, FUS, also formed solid hydrogels that could concentrate RNAs [82, 83].

It's important to keep in mind that, liquid-liquid and liquid-solid phase separations of proteins are not unheard of nor are they specific to the LCD-containing proteins. Any stably folded, single domain protein could phase separate into a liquid droplet under the right conditions. For instance, the art of protein crystallization involves placing

proteins under a number of different conditions, such as various concentrations of certain salts, buffers, detergents and crowding agents (e.g. polyethylene glycols or polyanionic polymers of different lengths). Screened under these different conditions, proteins can be driven to undergo a number of phase transitions to liquid droplets, solid precipitates, and either directly or through one of these states (if you are lucky) to ordered crystals [84]. What makes LCD-containing proteins special is that they can undergo liquid-liquid phase separation more readily, either self-coalescing at critical pH or salt concentrations, or upon binding to nucleic acids or other proteins. As we discuss later, post-translational modifications of LCD-containing proteins have also been shown to induce phase separation into liquid droplets.

Liquid droplets are not the only state that LCD-containing proteins can take on. The most well-known and extensively studied forms are amyloid fibrils. Recent *in vitro* studies show a slow transition of LCD-containing proteins from weakly associated to fibrillar arrangements, and the evolution of this process may be accelerated, *in vivo*, in the naturally occurring mutant variants of these proteins, some of which are known to be pathogenic [6, 39, 42, 85]. However, we do not know if fibrillar arrangements of LCD proteins exist *in vivo* under normal conditions. We do know that homogeneous preparations of liquid droplets *in vitro*, made of individual LCD-containing proteins, start out as dispersed, weakly associated molecules that exchange with surrounding solutions rapidly, some of which gradually transit to a fibrillar state in which individual monomers no longer exchange rapidly with the surroundings [6, 42, 85]. Could this happen *in vivo*? We do know that protein-RNA assemblies can have a range of liquid to solid states depending on their compositions [86]. A key difference between the *in vitro* and *in vivo* settings centers on the complexity of the available protein population. It is possible that the transition of cellular liquid droplets, such as P-bodies, into fibrillar states is prevented because of their heterogeneous composition. Cellular droplets are mixtures of interacting proteins or proteins and nucleic acids. In such mixtures, competing heterogeneous interactions among the different types of molecules may somehow frustrate the formation of higher-ordered fibrillar states. The

cell protein quality control machinery is also proposed to help preserve the liquid or solid states of protein and protein-RNA assemblies. For example, recent work on budding yeast showed that the action of Hsp104 disaggregase is required to maintain liquid-like P-bodies, or that the cellular disaggregation activity is needed to dissolve functional stress granule aggregates [4].

What is the nature of the interactions among molecules in a liquid droplet?

What is it about low complexity sequences that make them susceptible to forming a continuum of states? How do the various liquid droplets keep their individual compositions in the cellular milieu? Do proteins within droplets further separate into sub-phases? Very little is known and there is no all-encompassing theory for how liquid droplets form or how they have evolved. There are, however, some compelling theories, intuition and specific cases that can serve as starting points to understand liquid-liquid phase transitions of proteins.

Theories of beta-amyloid fibril formation have either explicitly or implicitly implied formation of a liquid-liquid phase separated intermediate [87]. The general idea is that a more disordered and dynamic intermediate is needed for formation of a structured and static aggregate. A model for amyloid formation by the protein huntingtin, the pathological agent in the neurodegenerative Huntington's disease, explicitly invokes a transient coiled-coil intermediate, formed from a variable-length glutamine tract. The length of this polyQ tract determines the tendency for huntingtin to form pathological beta-amyloid structures [73-75, 88, 89]. This model has also contributed to a general model of fibrillar structural transitions of polyN/polyQ TR proteins [90]. Although a liquid-liquid phase transition, is not specifically invoked, it has inspired explanations for their potential occurrence. For instance in a recent study of the partial reconstitution of the P-body, the authors propose that the LCDs contain sequence motifs which undergo spontaneous coil to helix transitions, allowing them to serve as

nucleation sites for formation of a network of intermolecular coiled-coils at a critical concentration [91]. The authors showed that disruption of helix-forming sequences could prevent formation of liquid droplets. Valency, the number of repeated or distinct binding domains or amino acid motifs in proteins can also be important to liquid-liquid phase separation. For example, phase separation SH3 domain-prolyl peptide interactions between Nck and N-WASP described above depend on the number of repeats of SH3 domains or SH3 domain binding motifs [30]. In analogy to this case, Fromm, et al. argue that phase separation depends on the number of possible intermolecular coiled-coils that the P-body proteins they studied could make [91].

The multivalent domain interaction network model described above is compelling because it explains liquid-liquid phase transitions in terms of structure and chemical complementarity [92]. It is, however, a model that is based on a limited number of examples, studied under non-physiological conditions and that cannot explain other aspects of droplet formation such as charge distribution dependencies, the fact that droplets will form from LCD-containing proteins that show no propensity or evidence of forming structured domains or are driven by simple post-translational modifications. More general theories that could account for and predict liquid droplet formations of LCD-containing proteins are needed.

Rohit Pappu has adapted a general theory to explain amyloid fibril formation from first principles of polymer theory that can also serve as a working theory for liquid-liquid phase separation of proteins [7]. In this model, IDPs with specific sequence properties do not take on extended conformations in a dilute solution, but rather, are collapsed into a compact globular form. The sequence property central to this theory is the existence of a specific length scale to intra and inter-segmental peptide interactions of 7 to 10 amino acids. These segments, referred to as “blobs”, constitute the length scale beyond which the balance of chain-chain, chain-solvent and solvent-solvent interactions is at least of the order of the thermal energy of the blob [93]. Under conditions where chain-solvent interactions are favorable (a so called “good solvent”)

or above a critical temperature, the interactions between blobs are net repulsive and the chain will swell to maximize interactions of the blobs with solvent, but under the opposite conditions (in a “poor” solvent or below the critical temperature), the polypeptide chain collapses into a globular form (Figure 2A). Vitalis *et al.* have shown that this model is consistent with scattering and spectroscopic data as well as molecular dynamic simulations [94-97].

The key to understanding liquid-liquid phase transition of a peptide is the notion that when the peptide reaches a critical concentration, the intermolecular blob interactions are more attractive than the intramolecular interactions and peptide-solvent interactions, and the peptides demix from the surrounding milieu into a liquid droplet. In the liquid droplet, the peptide expands because now it can make favorable intermolecular blob interactions (Figure 2B). In a sense, the peptide is now acting as its own good solvent. The concentration of the peptides in the droplet could also influence the blob variables, including the length and volume fraction as a function of inter-chain contact distance. As the peptide volume fraction decreases, the peptide chain is predicted to undergo conformation changes from expanded globules to form flexible rods and then rigid-rod structures (Figure 2C) [98]. The rigid-rod structures could coalesce into fibrillar states of the proteins noted to occur over time in droplets *in vitro* [6, 39, 42, 85].

It is notable that this theory requires no structural transformations and blob interactions do not have to be shape complementary [25, 99]. Shape-complementary interactions can, however, also occur in liquid droplet. It is notable that the length scale of blobs is the same as that of typical secondary structure elements in folded proteins and in this theory, folded domains can be thought of as blobs themselves and phase separate with stereospecific or shape complementary interactions (Figure 2D) [30].

Patterns of amino acids in blobs may also be critical to inter- and intra-blob interactions. Furthermore, this model indirectly distinguishes between IDPs with

regard to their ability to form liquid droplets. For example, as discussed below, the pattern and number of charged amino acids, lengths of TRs and presence of peptide backbone-constraining amino acids in an IDP can have a profound impact on blob interactions and their tendency to phase separate [100]. Finally, like multi-domain folded proteins, it is quite conceivable that a single polypeptide chain could form multi-globule arrangements (Figure 2E). These globules may have different properties under different conditions. Some of these conditions may lead to certain arrangements, polarizations or interactions with other macromolecules that result in phase separation of the associated molecules into a droplet with two or more sub-compartments, or some other extended periodic arrangement [101]. In the simplest case, an entire polypeptide may collapse into a single globule, but we can also picture different regions of a protein collectively forming different interactions with itself, the rest of the protein sequence and the solvent. Such, so called “Janus” particles could, for example, be more hydrophobic in one region and more polar in another [100]. These particles are of interest in the soft matter material sciences because many interesting configurations of matter can theoretically be generated from different arrangements of the substructure of Janus particles (Figure 2E) [101]. They are interesting to us because, as discussed below, sub-compartmentalization within the droplets can occur and the possibility that they are generated from Janus protein surfaces has important functional implications [27].

Understanding the behaviors of IDPs in general, requires suspending commonly held notions of classifications of amino acids into subcategories of charged or polar “hydrophilic” and apolar aliphatic or aromatic “hydrophobic” amino acids. These notions work for most purposes in understanding, for instance, how amino acids are arranged with respect to the solvent in folded proteins or at protein-protein or protein-nucleic acid interfaces, but they fail when trying to understand the behaviors of IDPs, particularly those with LCDs. For instance, the archetypical polyQ TR-containing protein, huntingtin, forms fibrils *via* collapsing into beta-hairpins, driven by intramolecular backbone and side-chain hydrogen bonds, disrupting interactions with

water. Thermodynamically, this process looks like the hydrophobic collapse of a folded protein and yet the amino acids involved are thought of as polar, hydrophilic amino acids. Thus, in the context of a tandem repeat, glutamine or asparagine prefer to interact more with themselves than with water and can therefore be viewed to behave hydrophobically. Equally paradoxical, a domain C-terminal to the polyQ tract of huntingtin that contains a preponderance of what is commonly thought to be a hydrophobic amino acid, proline, actually prevents huntingtin from collapsing into fibrils, favoring interactions with the solvent and therefore behaving as hydrophilic agents [88]. The prolines have not magically changed chemical properties, they are as hydrophilic as other polar amino acids such as Gln and Asn. However, the barrier to cis-trans isomerization of prolyl peptides disfavors the collapse of peptide into a globule, a necessary intermediate state to fibril formation and resulting in the peptide remaining soluble. Future understanding of patterns of amino acids and the properties that favor phase separation will require empirical studies, searches for heuristic rules and ultimately, theoretical models, such as has been applied to predicting prion-forming domains or to tuning the temperature-dependent phase transition of elastin proteins [47, 102].

IDPs tend to be enriched in charged amino acids compared to folded proteins [100]. This observation might seem explainable as an obvious evolutionary adaption to these proteins being unfolded and thus requiring as many polar amino acids be exposed to solvent as possible. Though intuitively reasonable, such an argument contradicts the theory described above and evidence that IDPs can exist as compact globules, obviating the need for an enrichment of polar or charged amino acids. What could be interesting and important to the way that these proteins behave is the arrangement of charged amino acids within a protein. Again, based on first principles of polymer theory, it has been proposed that the compactness of a polypeptide will vary with the linear polarization of oppositely charged amino acids. This leads to some interesting predictions, notably that a full range of oppositely charged residues creates a phase diagram of states, in which sharply defined regions of compactness,

from completely swelled to compact globules and Janus-like objects in between, can exist [100]. Secondly, given that the phase diagram predicts sharp transitions between states, one can imagine that subtle changes in charge could switch a polypeptide from one state to another. An obvious way this could be achieved is through post-translational modifications. Phosphorylation of serine, threonine and tyrosine, methylation of arginine and methylation and acetylation of lysine, among the most common of these, result in the addition of negative or reduction of positive charge. For example, precedence for phosphorylation- or methylation-dependent liquid droplet formation has been reported [103, 104].

Formation of Nephrin-Nck-N-WASP liquid droplets described above depends on an intrinsically unstructured linker peptide between the first two SH3 domains of Nck. The linker amino acid sequence has a polarized distribution of oppositely charged amino acids with a highly conserved positively charged sequence motif at the N-terminus of the linker and negatively charged residues at the C-terminus [3]. The authors showed that this motif interacts weakly with the negatively charged second SH3 domain, but may also interact with a negative motif at the C-terminal end of the linker. These results illustrate the essentiality of charge and the notion of both regions, an intrinsically disordered motif and the folded SH3 domains as blobs, whose interactions with each other are essential to phase separation.

What do molecular interactomes mean in the context of liquid droplets?

We can now put together the principles discussed above to describe how liquid droplet interactomes are distinct from what we usually think of as protein interactomes (Figure 3A). The difference and its importance to understanding liquid phase separation in cellular biology was eloquently captured by Daniel Needleman, who wrote in a recent essay about the material nature of life that, “individual molecules of water are not wet and the individual molecules that compose glass are not brittle, the

wetness of water and the brittleness of glass are collective phenomena that arise from the interactions of billions of molecules” [105].

A first key distinction between droplets and other types of protein organization is that the macromolecules that compose a liquid droplet can exchange rapidly with the surrounding cyto-, or organelle plasms. Proteins associated with the droplets are highly dynamic, diffusing into, out of and within the droplets rapidly. There could be some drag on proteins leaving the non-membranous bodies due to the intermolecular interactions within the droplet, which may be among the steady-state conditions for maintenance of the droplet. Nonetheless, the observed exchange rates between bulk solution (reflecting the cytoplasm or other subcellular compartment milieu) and droplets have been measured to be in the range of seconds to tens of seconds [1, 30]. Exchange rates of proteins and nucleic acids determine the droplet size and could be scaled with the cellular concentration of the proteins and size of the cell [37, 106]. Thus, compared to complexes of folded proteins, the compositions of liquid droplets are transient and can dictate rapidly formation or disintegration upon slight changes in local concentrations and chemical states of components, or physical or chemical composition of the environment.

Second, the most profound difference between simple molecular interactions and those of droplets is that collective properties of these objects can result in both attractive and repulsive interactions between droplets or between droplets and other objects (Figure 3B). Depending on the physical characteristics of a droplet, it may fuse and mix with components of other droplets, demix as a result, for example, of a change in a subdroplets surface properties, or unmix, that is repel another encountered droplet. The materials within the droplet phase separate from the surroundings because the net interactions they make among each other is more favorable than those with the surrounding milieu. Molecules at the interface are, thus, not as likely to form favorable interactions as those in the interior of the droplet. Consequently the droplet curvature will increase to minimize contact surface area

with its surroundings, as a water droplet does with air. For individual small molecules, proteins and RNAs, interfacial tension of a droplet is not a barrier to their entry into the droplet, provided that they are small enough to slip between intermolecular spaces and either make favorable interactions or do not interact with the molecules composing the droplet. We speculate that contact with large complexes (e.g. ribosomes), however, causes distortion of the droplet surface increasing its surface area and therefore the interfacial tension between the droplet and its milieu [27]. One can think of the droplet as behaving like a porous balloon, in which small objects can enter while larger objects can distort the surface but cannot enter the droplet. The exclusion of large particles creates regions in the bulk that are free of such large and unfavorably interacting molecules, so-called exclusion zones. Evidence so far for such exclusion zones created by liquid droplets in cells is limited but compelling. For instance, electron micrographs of sections of P-bodies show that otherwise widespread ribosomes are excluded from the P-bodies [107]. Feric *et al.* recently demonstrated that the large nucleoli of *Xenopus* oocytes are suspended in the nucleoplasm within a network of branched actin [108]. Interestingly though, they did not see actin persistently present within the nucleoli themselves, suggesting that these dense networks of protein fibers could form extended rough surfaces that cannot penetrate the nucleoli droplets. Finally, in *C. elegans* embryos, perinuclear germ line P granules work as size-exclusion barriers that exclude dextran molecules of 70-kD and above, but are permeable to dextran molecules of 40-kD and smaller [109]. The barrier properties of these perinuclear P granules are proposed, through interacting with the Phe/Gly-rich regions, to be coupled to and could extend the nuclear pore complex.

Water and its interactions with components of a droplet, at its interior or interface, is an important factor contributing to the droplet's properties, including viscosity and interfacial tension [110]. For example, if molecules interact more favorably with the constituents of the droplet than they do with those of the surrounding milieu, they will be drawn into the droplet, creating a sort of liquid-vapor interface. Depending on the

vapor pressure at such interfaces, one droplet could repel or attract another [111, 112]. This may be one way that droplets with different compositions and functions have evolved to remain separate. One could easily imagine attractive or repulsive interactions of droplets with other structures in the cell, for example membranes and chromatin, which may serve to shape or organize these structures. We could further speculate that liquid droplets might generate force or act as a liquid couple between force-generating machines like actin filaments to distort or organize matter as part of cellular processes. We know, for instance, that liquid droplets associate with sites of damaged DNA or transcriptionally active regions and may serve essential roles in organizing chromatin, either directly or, in the case of transcriptionally active sites, through interactions with RNA [42, 43, 70, 113, 114]. It remains to be determined precisely how the droplets are organized and whether they are essential to forcing the arrangements of matter in active regions or sequestering certain molecules in a regulatory manner.

Finally, as discussed above, phase separation of matter could further occur inside of the already phase-separated droplets and several examples of sub-compartmentalization of droplets have been reported [27, 104, 107]. Nucleoli suborganization can be recapitulated *in vitro*, due to the distinct interfacial tension generated by the distinct phase-separated proteins that make up the different subcompartments of the nucleoli [258]. Specifically, they observed that a droplet with a relatively high surface tension could be enveloped by a droplet with relatively lower surface tension. It should also be noted that the high surface tension enveloped droplet has other distinct properties including being not liquid but viscoelastic, a property anyone who has played with silly putty will understand: Such materials will take on any shape depending on the forces applied to them but if a force is applied rapidly, they will bounce back to their original shape. Regardless of their nature, such sub-compartmentalization creates a strategy to isolate catalytic processes and could also generate gradients and therefore chemical potentials (Figure 3C). For example, frog oocyte nucleolus organization described above is thought to partition the

sequential steps of ribosome biogenesis into the distinct nucleolar subcompartments [258]. P-bodies have been shown to separate into at least two regions, a core, where proteins responsible for 5' mRNA decapping activity (such as Dcp1) are found and a mantle where the proteins involved in translational repression (including Dhh1) accumulate [107]. What the functional significance of this layered organization is remains a subject of investigation, but the results point to the possibility that such arrangements may be common. Sub-compartments of stable complexes within a droplet have been described for mammalian and yeast stress granules. In this study, the authors referred to a stable “core” structure that was demonstrated to form in an ATP-dependent manner within stress granules [304]. In summary, liquid droplets we have described, like other subcellular compartments and the cell itself, may not be just simple concentrators of molecules, they may organize matter and chemical reactions in very specific ways.

Are droplets (and other alternative organizations of matter) important?

The discovery of liquid properties among known non-membranous organelles will remain subjects of research in and of themselves, but whether phase separation is more generally important to our understanding of the organization of matter in the cell will depend on whether it is a very interesting but rare phenomenon, or it is more common and can explain known or reveal novel biological phenomena. There are reasons to hope that the latter may be the case. First of all, there are hundreds, perhaps thousands of proteins that have been localized into puncta or “granules” in cells of different origins. It is conceivable that many of these bodies are liquid droplets and that the cell might be sub-compartmentalized into many such structures. For instance, some objects that to date have been referred to as granules, implying some kind of solid aggregates, have turned out to have liquid properties, including so-called stress and axonal mRNA transport granules and other local RNA translation regulatory bodies [305-307]. Second, about one-third of eukaryotic proteomes consist

of intrinsically unstructured peptide sequences and at least half of these contain low complexity sequences [45, 46]. It is conceivable that some or all of these proteins phase separate under some circumstances.

In some organisms the proportion of low complexity sequences is unusually high. For instance the slime mold *Dictyostelium discoideum* has a high proportion of LCD-containing proteins and, interestingly, pathological LCD-containing proteins, that form aggregates in yeast and mammals, are soluble when expressed in this organism [308]. What purpose it may serve that some organisms have more LCD-containing proteins than others remains to be explored, but it will be interesting to see if one consequence is simply more utilization of non-membranous organelles to partition biochemical processes.

Finally, there are many genetic interactions that cannot be explained through any obvious functional or structural interactions. It is possible that a proportion of such interactions could be explained by the phase separation of the encoded proteins into a droplet to perform cellular functions [51]. In the past, if you knew that proteins A, B and C were important to a function, likely you'd seek to show that they interact physically with each other or are somehow functionally linked in consecutive or parallel pathways. If they were not, you would just scratch your head and move on. Now, you might be able to explain their genetic interaction by the fact that they phase separate together.

Different non-membranous organelles may have similar functions in organizing cellular material. For example, the first clear example of liquid droplets, the germ cell P granules of *C. elegans* embryos polarize the distribution of mRNA along the embryo polar axis through a protein concentration-dependent mechanism [1]. The rate of P granules condensation, and consequently mRNA, was shown to increase with PGL-1 concentration. This could be a more general mechanism for polarization of cellular material. In another example, an essential step in assembly of functional spliceosomal small nuclear ribonucleoproteins (snRNPs) requires a protein coilin that

concentrates the snRNP components in Cajal bodies [309]. The authors propose that coilin may phase separate into a droplet with other components of Cajal bodies, concentrating the snRNP components so that they assemble into an active complex. Detailed evidence that phase separation drives this process remains to be demonstrated

The all-or-none nature of phase separation may also provide explanations for some abrupt cellular processes. For example, Richard Sear proposed that the Wnt pathway effector protein Dishevelled (Dvl) undergoes a liquid phase transition upon phosphorylation and that this transition is the mechanism underlying switch-like cell fate decisions that are driven by Dvl in this pathway during embryogenesis [40]. It is possible that other switch-like activation/deactivation of cellular processes are driven by phase separation.

Another example of all-or-none phase separation of signal transduction machinery has recently emerged that explains a well known and curious phenomenon of clustering of activated cell surface membrane receptors for a wide variety of hormones and other signaling molecules [79]. They showed that intermediate signaling modules phase separated into liquid like clusters upon T cell receptor phosphorylation. This central module included the adaptor and effector binding proteins Grb2 and SOS, respectively; canonical components of many cell surface receptors. They also showed that these clusters partitioned distinct enzyme activities, allowing protein kinases that catalyze phase separation to segregate with the clusters but repelling a protein phosphatase. They also result in activation of the canonical MAP kinase signaling cascade and recruit actin regulators, catalyzing actin filament assembly.

While the number of cellular droplet types appears to be growing and we are beginning to understand some fundamental facts about them, many questions remain. Concerning droplet origins – how many are there? What is it about proteins

and nucleic acids that cause them to phase separate with some, but not with other molecules?

Concerning function – what do the droplets actually do and how do their organizations or sub-organizations determine what they do and how cellular processes involving them work?

Concerning evolution - how did droplets evolve and, if they are evolvable, what is it about them that evolves? Is the evolution and selection of some, for example LCD-containing, proteins associated with the evolution of droplets? Finally, assuming that droplets are evolved objects, it is reasonable to ask then, how the existence of droplets could contribute to theories of the origins of life since phase transitions are an obvious and simple way to organize matter [26].

One question that needs close attention is whether droplets have unique compositions or do they share components and what makes one distinct from another, seem within reach. For example, two mRNA processing bodies, P-bodies and stress granules, share a number of common components, but also have distinct protein species [310-312]. How such partitioning occurs will have to be determined empirically through analysis of the sequences and properties of proteins that make up individual droplets as has been done, as mentioned above, to determine proteins that tend to form prions or undergo temperature-dependent soluble aggregate transformations [47, 56, 102].

Since the same proteins that form droplets are also those implicated in protein homeostasis pathologies, could their behavior in droplets provide new insights into diseases, (e.g. neuromuscular disorders) and could these behaviors be “druggable”?

Conclusions

Liquid droplets can be individually appreciated as interesting biological phenomena. From the perspective of molecular interaction networks, the discovery of liquid droplets presents fresh challenges and quandaries, which we've endeavored to explore. Furthermore, although the most obvious and cited functional significance of droplets is their ability to store molecules or concentrate chemical processes in space in an efficient way, we believe that droplets may serve more subtle and interesting functions. Here we've attempted to provide possibilities that we could imagine but doubtless, nature may have many surprises in store. Only time will tell.

Acknowledgements

We are grateful to Cliff Brangwynne, Rohit Pappu and Simon Alberti for many stimulating discussions and for reading the manuscript. We also thank Andrej Sali for providing us with a figure of his yeast nuclear pore model. SWM holds the Canada Research Chair in Cell Architecture.

Table 1 | Definition of terms related to protein phase separation

<i>term</i>	<i>definition</i>
Liquid-liquid phase separation (LLPS)	Demixing of two liquid phases with identical chemical potentials, but distinct molecular composition
Low complexity domains (LCDs)	Amino acid sequence regions composed of unusually few distinct types of amino acids.
Prion-like domains (PrDs)	LCDs predicted to cause a protein to form prionic aggregates
Tandem repeat (TR)	Amino acid sequence region of a protein in which each amino acid is identical.
Janus particles	Particles with two or more different properties on different regions of the particle surface
Blobs	Typical length of amino acids (typically 7-10) within proteins over which there is a net balance of all intra- and inter-peptide and peptide-solvent interactions <i>versus</i> thermal energy of the same peptide. Blobs will be found in globules or, above a critical concentration, phase-separate from solvent, if the intra- and inter-peptide interactions are greater than blob-solvent interactions.
Globules	Compact multi-blob arrangements within a single polypeptide chain
Droplet	Fluid body formed by condensation of elements (small molecules or macromolecules) in space and time
Colloid	Homogeneous suspension of large molecules or particles of 1 to 1000 nanometer dispersed in a second material that do not sediment
Hydrogel	Rigid network of hydrophilic polymer chains
amyloid	Insoluble solid protein fibrillar aggregates
Surface tension	Property of a fluid surface that resists external forces due to the cohesive force between liquid molecules

APPENDIX 2

Supplemental Movies

Movie S1. **Chapter 2.** Time-lapse dynamics and integrity of actin cortical patches under normal condition. We performed time-lapse fluorescent imaging of cortical patches in BY4741 cells grown in regular low fluorescence. Related to Figure 15. See [hyperlink: www.cell.com/cms/attachment/2078329092/2071029852/mmc5.mp4](http://www.cell.com/cms/attachment/2078329092/2071029852/mmc5.mp4).

Movie S2. **Chapter 2.** Time-lapse dynamics and integrity of actin cortical patches under salt condition. We performed time-lapse fluorescent imaging of cortical patches in BY4741 cells grown in regular low fluorescence medium (LFM) with 0.4 M NaCl. Related to Figure 15. See [hyperlink: www.cell.com/cms/attachment/2078329092/2071029853/mmc6.mp4](http://www.cell.com/cms/attachment/2078329092/2071029853/mmc6.mp4).

Movie S3. **Chapter 3.** Pulse-chase experiments with HD showed that HD-dependent dissolution of Sla1 puncta is reversible. See [hyperlink: www.dropbox.com/s/ez8smtkaze1x5tm/extended_movie_1.AVI?dl=0](http://www.dropbox.com/s/ez8smtkaze1x5tm/extended_movie_1.AVI?dl=0).

Supplemental Files

File S1. **Chapter 2.** R environment script and step-by-step instructions to interact with the data and access all dynamic and static temporal profiles. Supplemental file is provided in .zip format. See [hyperlink: www.cell.com/cms/attachment/2078329092/2071029848/mmc7.zip](http://www.cell.com/cms/attachment/2078329092/2071029848/mmc7.zip).

File S2. **Chapter 2.** Clustered protein-protein association matrix to visualize multiple degrees of interactions between dynamic phosphoproteins. Related to Figure 15. See [hyperlink: www.cell.com/cms/attachment/2078329092/2071029849/mmc8.zip](http://www.cell.com/cms/attachment/2078329092/2071029849/mmc8.zip).

Supplemental Tables

Table 2 | Temporal profiles of 5453 phosphopeptides on 1656 proteins with a false discovery rate (FDR) less than 1 % at both peptide and protein levels. These profiles correspond to phosphopeptides quantified in at least 10 of 13 time points with a phosphosite localization confidence greater than 0.75. Related to Figure 5. See [hyperlink: www.cell.com/cms/attachment/2078329092/2071029854/mmc2.xlsx](http://www.cell.com/cms/attachment/2078329092/2071029854/mmc2.xlsx).

Table 3 | We identified 596 dynamic phosphopeptides from 332 proteins that showed distinct continuous changes in phosphorylation with time after salt treatment. We separately listed the kinases and phosphatases that display a dynamic change in phosphorylation within 60 seconds following salt stimulation. Also all dynamic and static profiles were empirically fitted to a birth-extinction model. The maximum rate of fold change in depletion or enrichment (dFC/dt_{max}), and the time at which the maximum rate is observed (t_{max}) were extracted. Related to Figure 9 and Figure 11. See [hyperlink: www.cell.com/cms/attachment/2078329092/2071029855/mmc3.xlsx](http://www.cell.com/cms/attachment/2078329092/2071029855/mmc3.xlsx).

Table 4 | MaxQuant “parameters.txt” and “experimentalDesign.txt” files used in Chapter 2 and kinetic profiles for non-phosphorylated peptides used to model experimental variability in order to estimate thresholds for significant FC ratios of phosphopeptides. Related to Extended experimental procedures. See [hyperlink: www.cell.com/cms/attachment/2078329092/2071029856/mmc4.xlsx](http://www.cell.com/cms/attachment/2078329092/2071029856/mmc4.xlsx).

Table 5 | Yeast strains and mutagenic primer pairs to generate all phosphosite mutants used in Chapter 2

Strain	ORF	vector	mutation	primer pair used for site-directed mutagenesis	background	co-vector
YPH499	NA	NA	NA	NA	S288C LYS1Δ::kanMX; ARG4Δ::kanMX	NA
BY4741 ABP1- mCherry SLA1- GFP	NA	NA	NA	NA	BY4741 ABP1- mCherry::NAT1 SLA1-GFP::HPt	NA
BY4741 TUB1- YFP	NA	NA	NA	NA	BY4741 TUB1- YFP::HPt	NA
BY4741 ABP140-GFP	NA	NA	NA	NA	BY4741 ABP140- GFP::HPt	NA
BY4741 SYP1- YFP	NA	NA	NA	NA	BY4741 SYP1- YFP::HPt	NA
BY4741 EYFP	NA	NA	NA	NA	MATa his3Δ1 leu2Δ0 met15Δ0 ura3Δ0	p413ADH1- EYFP
BY4741 mCHERRY	NA	NA	NA	NA	MATa his3Δ1 leu2Δ0 met15Δ0 ura3Δ0	p413ADH1- mCherry
HOG1 wildtype	HOG1	p5472	NA	NA	BY4741 HOG1Δ::kanMX	p413ADH1- EYFP
RCK2 wildtype	RCK2	p5472	NA	NA	BY4741 RCK2Δ::kanMX	p413ADH1- EYFP
GPD1 wildtype	GPD1	p5472	NA	NA	BY4741 GPD1Δ::kanMX	p413ADH1- EYFP
SYP1 wildtype	SYP1	p5472	NA	NA	BY4741 SYP1Δ::kanMX	p413ADH1- EYFP
BIM1 wildtype	BIM1	p5472	NA	NA	BY4741 BIM1Δ::kanMX	p413ADH1- EYFP
SLA1 wildtype	SLA1	p5472	NA	NA	BY4741 SLA1Δ::kanMX	p413ADH1- EYFP

BUD6 wildtype	BUD6	p5473	NA	NA		BY4741 BUD6Δ::kanMX	p413ADH1- EYFP
HOG1_T174A	HOG1	p5472	T174A	GAATTCAAGACCCCTCAAATGGCTGGCTATGTTCCACTAGATAC GTATCTAGTGGAACATAGCCAGCCATTGAGGGTCTTGAATTC		BY4741 SYP1Δ::kanMX	p413ADH1- mCherry
HOG1_Y176A	HOG1	p5472	Y176A	CAAGACCTCAAATGACAGGCGCTGTTCCACTAGATACTACAG CTGTAGTATCTAGTGGAACAGCGCCTGTCATTGAGGGTCTTG		BY4741 SYP1Δ::kanMX	p413ADH1- mCherry
RCK2_T379A	RCK2	p5472	T379A	CCAAGAACCAAGGCTCTTGTGGTACAG CTGTACCACAAGGAGCCTTGGTGTCTTGG		BY4741 SYP1Δ::kanMX	p413ADH1- mCherry
GPD1_S24A	GPD1	p5472	S24A	GGTAGAAAGAGAAGTTCGCTTCTGTTCTTTGAAGGC GCCTTCAAAGAAACAGAAAGCGGAAGCTTCTCTTTCTACC		BY4741 SYP1Δ::kanMX	p413ADH1- mCherry
GPD1_S27A	GPD1	p5472	S27A	GAGAAGTTCCTCTTCTGTTGCTTTGAAGGCTGCCGAAAAG CTTTTCGGCAGCCTTCAAAGCAACAGAAAGAGGAAGCTTCTC		BY4741 SYP1Δ::kanMX	p413ADH1- mCherry
Strain	ORF	vector	mutation	primer pair used for site-directed mutagenesis		background	co-vector
SYP1_S297A	SYP1	p5472	S297A	CCACAAAAGGATAAGCGTAAGGCTGCATTGGAAACATTGGAC GTCCAATGTTTCCAAATGCAGCCTTACGCTTATCCTTTTGTGG		BY4741 SYP1Δ::kanMX	p413ADH1- mCherry
SYP1_S577A	SYP1	p5472	S577A	CACACTCTCTCTCAGATTGCTGGCGAGCTAAGAGAAC GTTCTCTTAGCTCGCCAGCAATCTGAGAGGAGAGTGTG		BY4741 SYP1Δ::kanMX	p413ADH1- mCherry
SYP1_S347A	SYP1	p5472	S347A	CCCTAAGATCTAAAGTGGGCGCTATTTTCGGTAGAAATAAGACC GGTCTTATTCTACCGAAAATAGCGCCCACTTTAGATCTTAGGG		BY4741 SYP1Δ::kanMX	p413ADH1- mCherry
SYP1_S405A	SYP1	p5472	S405A	CCACCTATTCATCATCAAAAGCTAACAATTGGACCCCGGTG CACCCGGGGTCCAATTGTTAGCTTTTGATGATGAATAGGTGG		BY4741 SYP1Δ::kanMX	p413ADH1- mCherry
BIM1_S165A	BIM1	p5472	S165A	GAGGATTAGCAACAAGACATGCTTCGCTGGGAATAAACGG CCGTTTATCCCAGCGAAGCATGTCTTGTGCTAATCCTC		BY4741 SYP1Δ::kanMX	p413ADH1- mCherry
BIM1_T249A	BIM1	p5472	T249A	GAAGGTGTTTATAAATTTAATGATGAGGCTATCACCGCCATGGTAATGGAAATGGGG CCCCATTTCATTACCATGGCCGGTGATAGCCTCATCAATAATTTATAAACACCTTC		BY4741 SYP1Δ::kanMX	p413ADH1- mCherry
SLA1_S996A	SLA1	p5472	S996A	GGATTAATTCAGCTAATACTGGTGTGCTATGCCAACTGTACAAGAACAGGCGGC GCCGCCTGTCTTTGTACAGTTGGCATAGCGACACCACTATTAGCTGAAATTAATCC		BY4741 SYP1Δ::kanMX	p413ADH1- mCherry
SLA1_T993A	SLA1	p5472	T993A	GGATTAATTCAGCTAATGCTGGTGTCTCAATGCCAAC GTTGGCATTGAGACACCAAGCATTAGCTGAAATTAATCC		BY4741 SYP1Δ::kanMX	p413ADH1- mCherry
SLA1_S340A	SLA1	p5472	S340A	GGTGAATATAAAGGTGCTGCTCGTGATCCTGGGTTGAGAG		BY4741	p413ADH1-

				CTCTCAACCCAGGATCACGAGCAGCACCTTTATATTACC	SYPIΔ::kanMX	mCherry
SLA1_S437A	SLA1	p5472	S437A	CAAGAAAACTTCACCAAAGCTCCATCTAGGTCGAGATC GATCTCGACCTAGATGGAGCTTTGGTGAAGTTTTTCTTG	BY4741 SYPIΔ::kanMX	p413ADH1- mCherry
SLA1_T818A	SLA1	p5472	T818A	CTAAAAAGGCAGCTGCCTCGGCTCCTGAACCAAACCTAAAAG CTTTTAGGTTTGGTTTCAGGAGCCGAGGCAGCTGCCTTTTAG	BY4741 SYPIΔ::kanMX	p413ADH1- mCherry
BUD6_T12A	BUD6	p5472	T12A	GTGGATGACCTACGTATGGCGCTCCAAGATTAAAGAAGTGC GCAGTTCTTTAATCTTTGGAGCGCCATACGTAGGGTCATCCAC	BY4741 SYPIΔ::kanMX	p413ADH1- mCherry
BUD6_S233A	BUD6	p5472	S233A	CAATGCTCCAAACGCAGCTGATGATGATGATGC GCATCATCATCATCAGCTGCGTTTGGAGCATTG	BY4741 SYPIΔ::kanMX	p413ADH1- mCherry
OESYP1-EGFP	SYP1	pAG416GPD- EGFP	NA	NA	BY4741 SYPIΔ::kanMX	NA
OESYP1_S347A- EGFP	SYP1	pAG416GPD- EGFP	S347A	CCCTAAGATCTAAAGTGGGCGCTATTTTCGGTAGAAATAAGACC GGTCTTATTTCTACCGAAAAATAGCGCCCACTTTAGATCTTAGGG	BY4741 SYPIΔ::kanMX	NA
OESYP1_S347E- EGFP	SYP1	pAG416GPD- EGFP	S347E	CCCTAAGATCTAAAGTGGGCGAAATTTTCGGTAGAAATAAGAC GTCTTATTTCTACCGAAAAATTCGCCCACTTTAGATCTTAGGG	BY4741 SYPIΔ::kanMX	NA
OESYP1_S405A- EGFP	SYP1	pAG416GPD- EGFP	S405A	CCACCTATTCATCATCAAAAGCTAACAATTGGACCCCGGGTG CACCCGGGGTCCAATTGTTAGCTTTTGATGATGAATAGGTGG	BY4741 SYPIΔ::kanMX	NA
OESYP1_S405E- EGFP	SYP1	pAG416GPD- EGFP	S405E	CCCACCTATTCATCATCAAAAGAAAACAATTGGACCCCGGGTG CACCCGGGGTCCAATTGTTTCTTTTGATGATGAATAGGTGGG	BY4741 SYPIΔ::kanMX	NA
OESYP1	SYP1	pAG406GPD	NA	NA	BY4741 SYPIΔ::kanMX	NA
OESYP1_S405E	SYP1	pAG406GPD	S405E	CCCACCTATTCATCATCAAAAGAAAACAATTGGACCCCGGGTG CACCCGGGGTCCAATTGTTTCTTTTGATGATGAATAGGTGGG	BY4741 mCherry::NAT1 SLA1-GFP::HPt	ABP1- NA

Table 6 | Terminology. **Chapter 2.**

Term	Definition
FC	Fold change in abundance of the corresponding peptide (phosphopeptide) between control and treated (0.4 M NaCl) conditions.
Kinetic profile	Represents phosphorylation dynamics on particular phosphopeptide represented by corresponding FC values measured at all time points.
Amplitude of response	Maximum deviation of the $\log_2(\text{FC})$ from 0. Could be used in the context of individual measurements (single time point) or over the whole kinetic profile.
Regulated phosphosites	Phosphosites with statistically significant amplitude of response at particular time point.
Regulated profile	Kinetic profile showing statistically significant changes in phosphorylation (as defined by FC-based or pattern-based analysis, see below).
Dynamic profile	Regulated profile that was assigned (membership > 0.5) to one of the clusters after c-means clustering.
Dynamic phosphosite	Phosphosite represented by a dynamic profile.
Dynamic protein	Protein that contains at least one dynamic phosphosite.
Static profile	Kinetic profile that is not considered dynamic.
Static phosphosite	Phosphosites represented by a static profile.

Table 7 | Table S1. **Chapter 3.** strains used in this study

<i>name</i>	<i>genotype</i>	<i>source</i>
BY4741	MATa his3Δ1 leu2Δ0 met15Δ0 ura3Δ0	this study
GPD1Δ	4741 gpd1Δ::KanMX	YKO
SLA1Δ	4741 sla1Δ::KanMX	YKO
ENT1Δ	4741 ent1Δ::KanMX	YKO
ENT2Δ	4741 ent2Δ::KanMX	YKO
LPS1Δ	4741 lps1Δ::KanMX	YKO
RGD1Δ	4741 rgd1Δ::KanMX	YKO
RVS161Δ	4741 rvs161Δ::KanMX	YKO
RVS167Δ	4741 rvs167Δ::KanMX	YKO
GVP36 Δ	4741 gvp36Δ::KanMX	YKO
PIL1Δ	4741 pli1Δ::KanMX	YKO
SYP1Δ	4741 syp1Δ::KanMX	YKO
Sla1-PLDΔ	4741 sla1-PLDΔ-Venus::HygMX	this study
Ent1-PLDΔ	4741 ent1-PLDΔ-Venus::HygMX	this study
Ent2-PLDΔ	4741 ent2-PLDΔ-Venus::HygMX	this study
Yap1801-PLDΔ	4741 yap1801f-PLDΔ-Venus::HygMX	this study
Yap1802-PLDΔ	4741 yap1802-PLDΔ-Venus::HygMX	this study
Sla1-GFP	4741 sla1-GFP::His3MX	GFP
Sla1-venus	4741 sla1-Venus::HygMX	this study
Sla1-mCherry	4741 sla1-mCherry::HygMX	this study
Sla1-Dronpa	4741 sla1-Dronpa3::NatMX	this study
Sla2-GFP	4741 sla2-GFP::His3MX	GFP
Ent1-venus	4741 ent1-Venus::HygMX	this study
Ent2-venus	4741 ent2-Venus::HygMX	this study
Yap1801-venus	4741 yap1801-Venus::HygMX	this study
Yap1802-venus	4741 yap1802-Venus::HygMX	this study
Sla1-mCherry Sla2-GFP	4741 sla2-GFP::His3MX sla1-mCherry::HygMX	this study
Sla1-GFP Sla2- mCherry	4741 sla1-GFP::His3MX sla2-mCherry::HygMX	this study
Lps1-GFP Sla1-mCherry	4741 lps1-GFP::His3MX sla1-mCherry::HygMX	this study

<i>name</i>	<i>genotype</i>	<i>source</i>
Rgd1-GFP Sla1-mCherry	4741 rgd1-GFP::His3MX sla1-mCherry::HygMX	this study
Rvs161-GFP Sla1-mCherry	4741 rvs161-GFP::His3MX sla1-mCherry::HygMX	this study
Rvs167-GFP Sla1-mCherry	4741 rvs167-GFP::His3MX sla1-mCherry::HygMX	this study
Gvp36-GFP Sla1-mCherry	4741 gvp36-GFP::His3MX sla1-mCherry::HygMX	this study
Pil1-GFP Sla1-mCherry	4741 pil1-GFP::His3MX sla1-mCherry::HygMX	this study
Syp1-GFP Sla1-mCherry	4741 syp1-GFP::His3MX sla1-mCherry::HygMX	this study
Lps1-GFP Sac6-mCherry	4741 lps1-GFP::His3MX sac6-mCherry::HygMX	this study
Rgd1-GFP Sac61-mCherry	4741 rgd1-GFP::His3MX sac6-mCherry::HygMX	this study
Rvs161-GFP Sac6-mCherry	4741 rvs161-GFP::His3MX sac6-mCherry::HygMX	this study
Rvs167-GFP Sac6-mCherry	4741 rvs167-GFP::His3MX sac6-mCherry::HygMX	this study
Gvp36-GFP Sac6-mCherry	4741 gvp36-GFP::His3MX sac6-mCherry::HygMX	this study
Pil1-GFP Sac6-mCherry	4741 pil1-GFP::His3MX sac6-mCherry::HygMX	this study
Syp1-GFP Sac6-mCherry	4741 syp1-GFP::His3MX sac6-mCherry::HygMX	this study

Table 8 | Table S2. **Chapter 3.** parameters and variables used in our theoretical framework were either measured in this study or obtained from the literature

<i>parameters</i>	<i>definition</i>	<i>value</i>	<i>note</i>	<i>source</i>
E_m	membrane elastic modulus	$1 \times 10^7 \text{ Pa}$	<i>estimate</i>	Landau 1986
κ_m	membrane bending modulus	$12.5 \cdot K_B T$		Harmandaris 2006
ν_m	membrane poisson's ratio	0.45	<i>from 0.1 to 0.5</i>	Zhang 2013
δ_m	membrane indentation	$5 \times 10^{-8} \text{ m}$	from 2.5×10^{-8} to $5 \times 10^{-8} \text{ m}$	EM
R_m	membrane radius	$-1.75 \times 10^{-6} \text{ m}$	<i>negative curvature</i>	<i>this study</i>
E_c	cytosol elastic modulus	45 Pa	at 1 Hz	<i>this study</i>
η	cytosol viscosity	$0.35 \text{ Pa} \cdot \text{s}^{-1}$	at 0.5 Hz	<i>this study</i>
ν_c	cytoplasm poisson's ratio	0.45	<i>from 0.1 to 0.5</i>	Zhang 2013
δ_c	indentation cytosol	$1.18 \times 10^{-7} \text{ m}$	$\pm 6 \times 10^{-9} \text{ m}$	<i>this study</i>
R_c	membrane radius	$1.75 \times 10^{-6} \text{ m}$		<i>this study</i>
E_{drop}	droplet elastic modulus	59 Pa		<i>this study</i>
$2a_{\text{drop}}$	droplet contact diameter	$2.09 \times 10^{-7} \text{ m}$	$\pm 1 \times 10^{-8} \text{ m}$	<i>this study</i>
δ_{drop}	indentation droplet	$1.18 \times 10^{-7} \text{ m}$	$\pm 6 \times 10^{-9} \text{ m}$	<i>this study</i>
R_{drop}	droplet radius	$9.3 \times 10^{-7} \text{ m}$	$\sim a^2/R$	<i>Hertz</i>
θ	droplet contact angle	96.7°	$\theta = 2 \arctan(\delta_{\text{drop}}/a_{\text{drop}})$	Young

* EM refers to electron microscopy data from [122] and Hertz refers to Hertz contact theory [248]. Landau 1986 refers to estimation of membrane elastic modulus from the bending modulus and Poisson's ratio [313], Harmandaris 2006 [287] and Zhang 2013 [288].

Table 9 | Table S3. **Chapter 3.** Constants and equations used in the elasto-adhesion model for the deformation of the membrane by protein droplets on cortical sites

<i>variables</i>	<i>definition</i>	<i>value</i>	<i>note</i>	<i>source</i>
<i>mechanical stress method</i>				
$\dot{\varepsilon}$	cytosol deformation rate	0.004 s ⁻¹		
E _{cell}	cell apparent elastic modulus	1000 Pa		AFM
σ	mechanical stress	1181 Pa	$\sigma = \varepsilon E + \varepsilon \eta$	Kelvin-Voigt
ΔP	pressure difference	1181 Pa	$\Delta P = \sigma$	Laplace
H	interface mean curvature	8.5 x10 ⁶ m ⁻¹	1/R	Laplace
γ_{dc}	droplet-cytoplasm surface tension	7 x10 ⁻⁵ N•m ⁻¹	$\gamma = \Delta P / (2H)$	Young-Laplace
<i>elasto-adhesive contact method</i>				
c	constant	0.92	8/ (5 ^{1/3})	JKR
E _{dc} [*]	cytoplasmic interface equivalent elastic modulus	32 Pa	$1/E_c^* = (1-\nu_c^2)/E_c + (1-\nu_m^2)/E_m$	Hertz
E _{dm} [*]	membrane interface equivalent elastic modulus	75 Pa		Hertz
R _{dm}	equivalent radius	1.27 x10 ⁻⁷ m	$1/R = 1/R_m + 1/R_d$	Hertz
R _{dc}	equivalent radius	1.11 x10 ⁻⁷ m	$1/R = 1/R_c + 1/R_d$	Hertz
δ_c	cytoplasm indentation	see table 9	$f(\delta_m) = \mu + \omega \delta_m$	this study
μ	constant	1.65		this study
k	constant	0		this study
W _{dm}	droplet-membrane work of adhesion	6.15 x10 ⁻⁵ N•m ⁻¹	$W_{dm} = \gamma_{dc} (1 + \cos\theta)$	Young-Dupré
W _{dc}	droplet-cytosol work of adhesion	6.15 x10 ⁻⁵ N•m ⁻¹	$= \gamma_{cm} + \gamma_{dm} - \gamma_{dc}$ predicted from model (1 x 10 ⁻⁵ to 7 x10 ⁻⁵ N•m ⁻¹)	this study
γ_{dm}	droplet-membrane surface tension	6.15 x10 ⁻⁵ N•m ⁻¹	$\gamma_{dm} < \gamma_{dc}$ (<i>hydrophobic</i>) $\gamma_{dm} \sim (W_{dc} + \gamma_{dc})/2$	Young-Dupré
γ_{cm}	cytosol-membrane surface tension	5.75 x10 ⁻⁵ N•m ⁻¹	$\gamma_{cm} = \gamma_{dm} + (\gamma_{dc} \cos\theta)$	Young

* not determined (nd). AFM refers to atomic force microscopy data from [145].

Table 10 | Table S4. **Chapter 3.** Summary of the indentations and energies predicted with our elasto-adhesive contact model

<i>variable</i>	<i>definition</i>	<i>value</i>	<i>in kT</i>	<i>source</i>
δ_m	membrane indentation	$4.06 \times 10^{-8} \text{ m}$	<i>nd</i>	<i>this study</i>
δ_c	cytoplasm indentation	$1.17 \times 10^{-7} \text{ m}$	<i>nd</i>	<i>this study</i>
U_{total}	total energy of system	$-2.4 \times 10^{-18} \text{ J}$	$-590 \cdot kT$	<i>this study</i>
U_{penal}	total energy penalties	$2.4 \times 10^{-18} \text{ J}$	$590 \cdot kT$	<i>this study</i>
U_{em}	corrected elastic energy at membrane interface	$1 \times 10^{-18} \text{ J}$	$250 \cdot kT$	<i>this study</i>
U_{ec}	elastic energy at cytoplasm interface	$1.2 \times 10^{-20} \text{ J}$	$3 \cdot kT$	<i>this study</i>
U_{ym}	surface energy at membrane interface	$3.6 \times 10^{-19} \text{ J}$	$88 \cdot kT$	<i>this study</i>
U_{yc}	surface energy at cytoplasm interface	$1 \times 10^{-18} \text{ J}$	$249 \cdot kT$	<i>this study</i>
U_{vc}	viscous friction energy	$2.5 \times 10^{-21} \text{ J}$	$1 \cdot kT$	<i>this study</i>
U_{adh}	total adhesion energy	$4.9 \times 10^{-18} \text{ J}$	$1180 \cdot kT$	<i>this study</i>
U_{am}	adhesion energy at membrane interface	$2 \times 10^{-18} \text{ J}$	$477 \cdot kT$	<i>this study</i>
U_{ac}	adhesion energy at cytoplasm interface	$2.9 \times 10^{-18} \text{ J}$	$703 \cdot kT$	<i>this study</i>

BIBLIOGRAPHY

1. Brangwynne, C.P., et al., *Germline P granules are liquid droplets that localize by controlled dissolution/condensation*. Science, 2009. **324**(5935): p. 1729-32.
2. Nott, T.J., et al., *Phase transition of a disordered nuage protein generates environmentally responsive membraneless organelles*. Mol Cell, 2015. **57**(5): p. 936-47.
3. Banjade, S., et al., *Conserved interdomain linker promotes phase separation of the multivalent adaptor protein Nck*. Proc Natl Acad Sci U S A, 2015. **112**(47): p. E6426-35.
4. Kroschwald, S., et al., *Promiscuous interactions and protein disaggregases determine the material state of stress-inducible RNP granules*. Elife, 2015. **4**: p. e06807.
5. Jiang, H., et al., *Phase transition of spindle-associated protein regulate spindle apparatus assembly*. Cell, 2015. **163**(1): p. 108-22.
6. Molliex, A., et al., *Phase separation by low complexity domains promotes stress granule assembly and drives pathological fibrillization*. Cell, 2015. **163**(1): p. 123-33.
7. Pappu, R.V., et al., *A polymer physics perspective on driving forces and mechanisms for protein aggregation*. Arch Biochem Biophys, 2008. **469**(1): p. 132-41.
8. Hyman, A.A., C.A. Weber, and F. Julicher, *Liquid-liquid phase separation in biology*. Annu Rev Cell Dev Biol, 2014. **30**: p. 39-58.
9. Koshland, D.E., Jr., *Special essay. The seven pillars of life*. Science, 2002. **295**(5563): p. 2215-6.
10. Cleland, C.E. and C.F. Chyba, *Defining 'life'*. Orig Life Evol Biosph, 2002. **32**(4): p. 387-93.
11. Benner, S.A., *Defining life*. Astrobiology, 2010. **10**(10): p. 1021-30.
12. Monod, J., *Chance and necessity; an essay on the natural philosophy of modern biology*. 1st American ed. 1971, New York,: Knopf. xiv, 198 p.
13. Alberts, B., et al., *Molecular Biology of the Cell*. 5 ed. 2007, New York: Garland Science.
14. Darwin, C., *On the origin of species by means of natural selection, or, The preservation of favoured races in the struggle for life*. 1859, London: J. Murray. ix, 502 p., 1 folded leaf of plates.
15. Thompson, D.A.W., *On growth and form*. 1917, Cambridge Eng.: University press. xv, 793 p.
16. Clausius, R. and T.A. Hirst, *The mechanical theory of heat with its applications to the steam-engine and to the physical properties of bodies*. 1867, London: J. van Voorst. xvi, 376 p.
17. Lambert, F.L., *The Misinterpretation of Entropy as "Disorder"*. J Chem Educ, 2012. **89**(3): p. 310–310.
18. Eaton, B.E., L. Gold, and D.A. Zichi, *Let's get specific: the relationship between*

- specificity and affinity*. Chem Biol, 1995. **2**(10): p. 633-8.
19. Brangwynne, C.P.T., P.;Pappu, R. V., *Polymer physics of intracellular phase transitions*. Nature Physics, 2015. **11**: p. 899-904.
 20. Kanshin, E., et al., *A cell-signaling network temporally resolves specific versus promiscuous phosphorylation*. Cell Rep, 2015. **10**(7): p. 1202-14.
 21. Landry, C.R., et al., *Extracting insight from noisy cellular networks*. Cell, 2013. **155**(5): p. 983-9.
 22. Levy, E.D., S.W. Michnick, and C.R. Landry, *Protein abundance is key to distinguish promiscuous from functional phosphorylation based on evolutionary information*. Philos Trans R Soc Lond B Biol Sci, 2012. **367**(1602): p. 2594-606.
 23. Landry, C.R., E.D. Levy, and S.W. Michnick, *Weak functional constraints on phosphoproteomes*. Trends Genet, 2009. **25**(5): p. 193-7.
 24. Tarassov, K., et al., *An in vivo map of the yeast protein interactome*. Science, 2008. **320**(5882): p. 1465-70.
 25. Hyman, A.A. and C.P. Brangwynne, *Beyond stereospecificity: liquids and mesoscale organization of cytoplasm*. Developmental Cell, 2011. **21**(1): p. 14-16.
 26. Wilson, E.B., *THE STRUCTURE OF PROTOPLASM*. Science (New York, NY), 1899. **10**(237): p. 33-45.
 27. Brangwynne, C.P., *Soft active aggregates: mechanics, dynamics and self-assembly of liquid-like intracellular protein bodies*. Soft Matter, 2011. **7**(7): p. 3052-3059.
 28. Brangwynne, C.P., *Phase transitions and size scaling of membrane-less organelles*. The Journal of cell biology, 2013. **203**(6): p. 875-881.
 29. Lee, C.F., et al., *Spatial organization of the cell cytoplasm by position-dependent phase separation*. Physical review letters, 2013. **111**(8): p. 088101.
 30. Li, P., et al., *Phase transitions in the assembly of multivalent signalling proteins*. Nature, 2012. **483**(7389): p. 336-340.
 31. Weber, S.C. and C.P. Brangwynne, *Getting RNA and protein in phase*. Cell, 2012. **149**(6): p. 1188-1191.
 32. Brangwynne, C.P., T.J. Mitchison, and A.A. Hyman, *Active liquid-like behavior of nucleoli determines their size and shape in Xenopus laevis oocytes*. Proc Natl Acad Sci U S A, 2011. **108**(11): p. 4334-9.
 33. Tarassov, K. and S.W. Michnick, *iVici: Interrelational Visualization and Correlation Interface*. Genome Biol, 2005. **6**(13): p. R115.
 34. Alber, F., et al., *The molecular architecture of the nuclear pore complex*. Nature, 2007. **450**(7170): p. 695-701.
 35. Hyman, A.A. and K. Simons, *Cell biology. Beyond oil and water--phase transitions in cells*. Science (New York, NY), 2012. **337**(6098): p. 1047-1049.
 36. Sear, R.P., I. Pagonabarraga, and A. Flaus, *Life at the mesoscale: the self-organised cytoplasm and nucleoplasm*. BMC biophysics, 2015. **8**: p. 4.
 37. Zhu, L. and C.P. Brangwynne, *Nuclear bodies: the emerging biophysics of nucleoplasmic phases*. Current opinion in cell biology, 2015. **34**: p. 23-30.
 38. Banjade, S. and M.K. Rosen, *Phase transitions of multivalent proteins can promote clustering of membrane receptors*. Elife, 2014. **3**.

39. Lin, Y., et al., *Formation and Maturation of Phase-Separated Liquid Droplets by RNA-Binding Proteins*. Molecular Cell, 2015. **60**(2): p. 208-219.
40. Sear, R.P., *Dishevelled: a protein that functions in living cells by phase separating*. Soft Matter, 2007. **3**(6): p. 680.
41. Zwicker, D., et al., *Centrosomes are autocatalytic droplets of pericentriolar material organized by centrioles*. Proceedings of the National Academy of Sciences of the United States of America, 2014.
42. Patel, A., et al., *A Liquid-to-Solid Phase Transition of the ALS Protein FUS Accelerated by Disease Mutation*. Cell, 2015. **162**(5): p. 1066-77.
43. Altmeyer, M., et al., *Liquid demixing of intrinsically disordered proteins is seeded by poly(ADP-ribose)*. Nature communications, 2015. **6**: p. 8088.
44. Dunker, A.K., et al., *Intrinsically disordered proteins and multicellular organisms*. Semin Cell Dev Biol, 2015. **37**: p. 44-55.
45. Toretsky, J.A. and P.E. Wright, *Assemblages: functional units formed by cellular phase separation*. The Journal of cell biology, 2014. **206**(5): p. 579-588.
46. van der Lee, R., et al., *Intrinsically Disordered Segments Affect Protein Half-Life in the Cell and during Evolution*. CellReports, 2014. **8**(6): p. 1832-1844.
47. Alberti, S., et al., *A systematic survey identifies prions and illuminates sequence features of prionogenic proteins*. Cell, 2009. **137**(1): p. 146-58.
48. Alexandrov, A.I. and M.D. Ter-Avanesyan, *Could yeast prion domains originate from polyQ/N tracts?* Prion, 2013. **7**(3): p. 209-214.
49. Brown, J.C.S. and S. Lindquist, *A heritable switch in carbon source utilization driven by an unusual yeast prion*. Genes & Development, 2009. **23**(19): p. 2320-2332.
50. Caudron, F. and Y. Barral, *A Super-Assembly of Whi3 Encodes Memory of Deceptive Encounters by Single Cells during Yeast Courtship*. Cell, 2013. **155**(6): p. 1244-1257.
51. Costanzo, M., et al., *The genetic landscape of a cell*. Science, 2010. **327**(5964): p. 425-31.
52. Decker, C.J., D. Teixeira, and R. Parker, *Edc3p and a glutamine/asparagine-rich domain of Lsm4p function in processing body assembly in Saccharomyces cerevisiae*. The Journal of cell biology, 2007. **179**(3): p. 437-449.
53. Duennwald, M.L., A. Echeverria, and J. Shorter, *Small Heat Shock Proteins Potentiate Amyloid Dissolution by Protein Disaggregases from Yeast and Humans*. PLoS Biology, 2012. **10**(6): p. e1001346-23.
54. Heinrich, S.U. and S. Lindquist, *Protein-only mechanism induces self-perpetuating changes in the activity of neuronal Aplysia cytoplasmic polyadenylation element binding protein (CPEB)*. Proceedings of the National Academy of Sciences, 2011. **108**(7): p. 2999-3004.
55. Holmes, D.L., et al., *Heritable remodeling of yeast multicellularity by an environmentally responsive prion*. Cell, 2013. **153**(1): p. 153-165.
56. Malinovska, L., S. Kroschwald, and S. Alberti, *Protein disorder, prion propensities, and self-organizing macromolecular collectives*. Biochim Biophys Acta, 2013. **1834**(5): p. 918-31.
57. Patel, B.K., J. Gavin-Smyth, and S.W. Liebman, *The yeast global*

- transcriptional co-repressor protein Cyc8 can propagate as a prion*. Nature Cell Biology, 2009. **11**(3): p. 344-349.
58. Raveendra, B.L., et al., *Characterization of prion-like conformational changes of the neuronal isoform of Aplysia CPEB*. Nature Structural & Molecular Biology, 2013. **20**(4): p. 495-501.
 59. Sabate, R., et al., *What Makes a Protein Sequence a Prion?* PLoS Computational Biology, 2015. **11**(1): p. e1004013.
 60. Toombs, J.A., B.R. McCarty, and E.D. Ross, *Compositional Determinants of Prion Formation in Yeast*. Molecular and Cellular Biology, 2009. **30**(1): p. 319-332.
 61. Webb, S., et al., *PAR-CLIP data indicate that Nrd1-Nab3-dependent transcription termination regulates expression of hundreds of protein coding genes in yeast*. Genome Biol, 2014. **15**(1): p. R8.
 62. Chung, C.Y., et al., *Identification and rescue of α -synuclein toxicity in Parkinson patient-derived neurons*. Science (New York, NY), 2013. **342**(6161): p. 983-987.
 63. Drisaldi, B., et al., *SUMOylation Is an Inhibitory Constraint that Regulates the Prion-like Aggregation and Activity of CPEB3*. CellReports, 2015. **11**(11): p. 1694-1702.
 64. Fioriti, L., et al., *The Persistence of Hippocampal-Based Memory Requires Protein Synthesis Mediated by the Prion-like Protein CPEB3*. Neuron, 2015. **86**(6): p. 1433-1448.
 65. Keleman, K., et al., *Function of the Drosophila CPEB protein Orb2 in long-term courtship memory*. Nature neuroscience, 2007. **10**(12): p. 1587-1593.
 66. Si, K., et al., *Aplysia CPEB can form prion-like multimers in sensory neurons that contribute to long-term facilitation*. Cell, 2010. **140**(3): p. 421-435.
 67. Si, K., et al., *A Neuronal Isoform of CPEB Regulates Local Protein Synthesis and Stabilizes Synapse-Specific Long-Term Facilitation in Aplysia*. Cell, 2003.
 68. Stephan, J.S., et al., *The CPEB3 Protein Is a Functional Prion that Interacts with the Actin Cytoskeleton*. CellReports, 2015. **11**(11): p. 1772-1785.
 69. Fondon, J.W., 3rd and H.R. Garner, *Molecular origins of rapid and continuous morphological evolution*. Proc Natl Acad Sci U S A, 2004. **101**(52): p. 18058-63.
 70. Gemayel, R., et al., *Variable Glutamine-Rich Repeats Modulate Transcription Factor Activity*. Molecular Cell, 2015: p. 1-14.
 71. Verstrepen, K.J., et al., *Intragenic tandem repeats generate functional variability*. Nat Genet, 2005. **37**(9): p. 986-90.
 72. Duim, W.C., et al., *Sub-Diffraction Imaging of Huntingtin Protein Aggregates by Fluorescence Blink-Microscopy and Atomic Force Microscopy*. ChemPhysChem, 2011. **12**(13): p. 2387-2390.
 73. Jayaraman, M., et al., *Slow Amyloid Nucleation via α -Helix-Rich Oligomeric Intermediates in Short Polyglutamine-Containing Huntingtin Fragments*. Journal of molecular biology, 2012. **415**(5): p. 881-899.
 74. Kim, M.W., et al., *Secondary Structure of Huntingtin Amino-Terminal Region*. Structure/Folding and Design, 2009. **17**(9): p. 1205-1212.
 75. Liebman, S.W. and S.C. Meredith, *Protein folding: Sticky N17 speeds*

- huntingtin pile-up*. Nature Publishing Group, 2010. **6**(1): p. 7-8.
76. Mishra, R., et al., *Inhibiting the Nucleation of Amyloid Structure in a Huntingtin Fragment by Targeting α -Helix-Rich Oligomeric Intermediates*. Journal of molecular biology, 2012. **415**(5): p. 900-917.
 77. La Spada, A.R. and J.P. Taylor, *Repeat expansion disease: progress and puzzles in disease pathogenesis*. Nat Rev Genet, 2010. **11**(4): p. 247-258.
 78. Sim, K.L. and T.P. Creamer, *Abundance and distributions of eukaryote protein simple sequences*. Mol Cell Proteomics, 2002. **1**(12): p. 983-95.
 79. Su, X., et al., *Phase separation of signaling molecules promotes T cell receptor signal transduction*. Science, 2016.
 80. Sassano, M.F., et al., *Colloidal aggregation causes inhibition of G protein-coupled receptors*. J Med Chem, 2013. **56**(6): p. 2406-14.
 81. Zorn, J.A., et al., *Self-Assembling Small Molecules Form Nanofibrils That Bind Procaspase-3 To Promote Activation*. Journal of the American Chemical Society, 2011. **133**(49): p. 19630-19633.
 82. Han, T.W., et al., *Cell-free Formation of RNA Granules: Bound RNAs Identify Features and Components of Cellular Assemblies*. Cell, 2012. **149**(4): p. 768-779.
 83. Kato, M., et al., *Cell-free Formation of RNA Granules: Low Complexity Sequence Domains Form Dynamic Fibers within Hydrogels*. Cell, 2012. **149**(4): p. 753-767.
 84. Zhang, F., et al., *Charge-controlled metastable liquid-liquid phase separation in protein solutions as a universal pathway towards crystallization* Soft Matter, 2012. **8**(5): p. 1313-1316.
 85. Zhang, H., et al., *RNA Controls PolyQ Protein Phase Transitions*. Molecular Cell, 2015. **60**(2): p. 220-230.
 86. Hubstenberger, A., et al., *Modifiers of solid RNP granules control normal RNP dynamics and mRNA activity in early development*. J Cell Biol, 2015. **211**(3): p. 703-16.
 87. Padrick, S.B. and A.D. Miranker, *Islet Amyloid: Phase Partitioning and Secondary Nucleation Are Central to the Mechanism of Fibrillogenesis †*. Biochemistry, 2002. **41**(14): p. 4694-4703.
 88. Crick, S.L., et al., *Unmasking the roles of N-and C-terminal flanking sequences from exon 1 of huntingtin as modulators of polyglutamine aggregation*. Proceedings of the National Academy of Sciences, 2013. **110**(50): p. 20075-20080.
 89. Williamson, T.E., et al., *Modulation of polyglutamine conformations and dimer formation by the N-terminus of huntingtin*. Journal of molecular biology, 2010. **396**(5): p. 1295-1309.
 90. Fiumara, F., et al., *Essential role of coiled coils for aggregation and activity of Q/N-rich prions and PolyQ proteins*. Cell, 2010. **143**(7).
 91. Fromm, S.A., et al., *In Vitro Reconstitution of a Cellular Phase-Transition Process that Involves the mRNA Decapping Machinery*. Angewandte Chemie International Edition, 2014. **53**(28): p. 7354-7359.
 92. Falkenberg, C.V., M.L. Blinov, and L.M. Loew, *Pleomorphic Ensembles: Formation of Large Clusters Composed of Weakly Interacting Multivalent*

- Molecules*. Biophysj, 2013. **105**(11): p. 2451-2460.
93. Tran, H.T. and R.V. Pappu, *Toward an Accurate Theoretical Framework for Describing Ensembles for Proteins under Strongly Denaturing Conditions*. Biophysj, 2006. **91**(5): p. 1868-1886.
 94. Vitalis, A., N. Lyle, and R.V. Pappu, *Thermodynamics of beta-sheet formation in polyglutamine*. Biophysical journal, 2009. **97**(1): p. 303-311.
 95. Vitalis, A. and R.V. Pappu, *Assessing the contribution of heterogeneous distributions of oligomers to aggregation mechanisms of polyglutamine peptides*. Biophysical chemistry, 2011. **159**(1): p. 14-23.
 96. Vitalis, A., X. Wang, and R.V. Pappu, *Atomistic simulations of the effects of polyglutamine chain length and solvent quality on conformational equilibria and spontaneous homodimerization*. Journal of molecular biology, 2008. **384**(1): p. 279-297.
 97. Vitalis, A., X. Wang, and R.V. Pappu, *Quantitative characterization of intrinsic disorder in polyglutamine: insights from analysis based on polymer theories*. Biophysj, 2007. **93**(6): p. 1923-1937.
 98. Uematsu, T., C. Svanberg, and P. Jacobsson, *A Unified Picture of Static and Dynamic Length Scales in Polymer Solutions*. Macromolecules, 2005. **38**(14): p. 6227-6230.
 99. Burke, K.A., et al., *Residue-by-Residue View of In Vitro FUS Granules that Bind the C-Terminal Domain of RNA Polymerase II*. Molecular Cell, 2015. **60**(2): p. 231-241.
 100. Das, R.K. and R.V. Pappu, *Conformations of intrinsically disordered proteins are influenced by linear sequence distributions of oppositely charged residues*. Proc Natl Acad Sci U S A, 2013. **110**(33): p. 13392-7.
 101. Li, Z.-W., et al., *Model, self-assembly structures, and phase diagram of soft Janus particles* Soft Matter, 2012. **8**(25): p. 6693-6697.
 102. Quiroz, F.G. and A. Chilkoti, *Sequence heuristics to encode phase behaviour in intrinsically disordered protein polymers*. Nature Materials, 2015.
 103. Scaramuzzino, C., et al., *Protein arginine methyltransferase 6 enhances polyglutamine-expanded androgen receptor function and toxicity in spinal and bulbar muscular atrophy*. Neuron, 2015. **85**(1): p. 88-100.
 104. Wang, J.T., et al., *Regulation of RNA granule dynamics by phosphorylation of serine-rich, intrinsically-disordered proteins in C. elegans*. eLife, 2014. **3**.
 105. Needleman, D., *The Material Basis of Life*. Trends Cell Biol, 2015. **25**(12): p. 713-6.
 106. Weber, S.C. and C.P. Brangwynne, *Inverse size scaling of the nucleolus by a concentration-dependent phase transition*. Curr Biol, 2015. **25**(5): p. 641-6.
 107. Cougot, N., et al., *The Dual Organization of P-bodies Revealed by Immunoelectron Microscopy and Electron Tomography*. Journal of molecular biology, 2012. **420**(1-2): p. 17-28.
 108. Feric, M. and C.P. Brangwynne, *A nuclear F-actin scaffold stabilizes ribonucleoprotein droplets against gravity in large cells*. Nature Cell Biology, 2013. **15**(10): p. 1253-1259.
 109. Updike, D.L., et al., *P granules extend the nuclear pore complex environment in the C. elegans germ line*. J Cell Biol, 2011. **192**(6): p. 939-48.

110. Chandler, D., *Hydrophobicity: two faces of water*. Nature, 2002. **417**(6888): p. 491.
111. Cira, N.J., A. Benusiglio, and M. Prakash, *Vapour-mediated sensing and motility in two-component droplets*. Nature, 2015. **519**(7544): p. 446-450.
112. Zwicker, D., A.A. Hyman, and F. Jülicher, *Suppression of Ostwald ripening in active emulsions*. Physical Review E, 2015. **92**(1): p. 012317.
113. Pennisi, E., *Long Noncoding RNAs May Alter Chromosome's 3D Structure*. Science (New York, NY), 2013. **340**(6135): p. 910-910.
114. Weber, S.C., N. Vaidya, and M. Haataja, *RNA transcription modulates phase transition-driven nuclear body assembly*, in *Proceedings of the* 2015.
115. Bergeron-Sandoval, L.P., N. Safaee, and S.W. Michnick, *Mechanisms and Consequences of Macromolecular Phase Separation*. Cell, 2016. **165**(5): p. 1067-79.
116. Elbaum-Garfinkle, S., et al., *The disordered P granule protein LAF-1 drives phase separation into droplets with tunable viscosity and dynamics*. Proc Natl Acad Sci U S A, 2015. **112**(23): p. 7189-94.
117. Conner, S.D. and S.L. Schmid, *Regulated portals of entry into the cell*. Nature, 2003. **422**(6927): p. 37-44.
118. Abrami, L., et al., *Endocytosis of the anthrax toxin is mediated by clathrin, actin and unconventional adaptors*. PLoS Pathog, 2010. **6**(3): p. e1000792.
119. Krzyzaniak, M.A., et al., *Host cell entry of respiratory syncytial virus involves macropinocytosis followed by proteolytic activation of the F protein*. PLoS Pathog, 2013. **9**(4): p. e1003309.
120. Idrissi, F.Z., et al., *Ultrastructural dynamics of proteins involved in endocytic budding*. Proc Natl Acad Sci U S A, 2012. **109**(39): p. E2587-94.
121. Kukulski, W., et al., *Plasma membrane reshaping during endocytosis is revealed by time-resolved electron tomography*. Cell, 2012. **150**(3): p. 508-20.
122. Kukulski, W., et al., *Clathrin modulates vesicle scission, but not invagination shape, in yeast endocytosis*. Elife, 2016. **5**.
123. Hom, R.A., et al., *pH-dependent binding of the Epsin ENTH domain and the AP180 ANTH domain to PI(4,5)P2-containing bilayers*. J Mol Biol, 2007. **373**(2): p. 412-23.
124. Brach, T., et al., *The initiation of clathrin-mediated endocytosis is mechanistically highly flexible*. Curr Biol, 2014. **24**(5): p. 548-54.
125. Maldonado-Baez, L. and B. Wendland, *Endocytic adaptors: recruiters, coordinators and regulators*. Trends Cell Biol, 2006. **16**(10): p. 505-13.
126. Picco, A., et al., *Visualizing the functional architecture of the endocytic machinery*. Elife, 2015. **4**.
127. Carlsson, A.E. and P.V. Bayly, *Force generation by endocytic actin patches in budding yeast*. Biophys J, 2014. **106**(8): p. 1596-606.
128. Dmitrieff, S. and F. Nedelec, *Membrane Mechanics of Endocytosis in Cells with Turgor*. PLoS Comput Biol, 2015. **11**(10): p. e1004538.
129. Aghamohammadzadeh, S. and K.R. Ayscough, *Differential requirements for actin during yeast and mammalian endocytosis*. Nat Cell Biol, 2009. **11**(8): p. 1039-42.
130. Basu, R., E.L. Munteanu, and F. Chang, *Role of turgor pressure in endocytosis*

- in fission yeast*. Mol Biol Cell, 2014. **25**(5): p. 679-87.
131. Pelkmans, L., et al., *Genome-wide analysis of human kinases in clathrin- and caveolae/raft-mediated endocytosis*. Nature, 2005. **436**(7047): p. 78-86.
 132. Toshima, J., et al., *Phosphoregulation of Arp2/3-dependent actin assembly during receptor-mediated endocytosis*. Nat Cell Biol, 2005. **7**(3): p. 246-54.
 133. Reiter, W., et al., *Validation of regulated protein phosphorylation events in yeast by quantitative mass spectrometry analysis of purified proteins*. Proteomics, 2012. **12**(19-20): p. 3030-43.
 134. Aebersold, R. and M. Mann, *Mass spectrometry-based proteomics*. Nature, 2003. **422**(6928): p. 198-207.
 135. Hoffmann E D, S.V., *Mass spectrometry : Principles and applications*. Vol. xii. 2001, New York: Wiley.
 136. Fenn, J.B., et al., *Electrospray ionization for mass spectrometry of large biomolecules*. Science, 1989. **246**(4926): p. 64-71.
 137. Eliuk, S. and A. Makarov, *Evolution of Orbitrap Mass Spectrometry Instrumentation*. Annu Rev Anal Chem (Palo Alto Calif), 2015. **8**: p. 61-80.
 138. Cox, J., et al., *Andromeda: a peptide search engine integrated into the MaxQuant environment*. J Proteome Res, 2011. **10**(4): p. 1794-805.
 139. Cox, J. and M. Mann, *MaxQuant enables high peptide identification rates, individualized p.p.b.-range mass accuracies and proteome-wide protein quantification*. Nat Biotechnol, 2008. **26**(12): p. 1367-72.
 140. Ong, S.E., et al., *Stable isotope labeling by amino acids in cell culture, SILAC, as a simple and accurate approach to expression proteomics*. Mol Cell Proteomics, 2002. **1**(5): p. 376-86.
 141. Ong, S.E. and M. Mann, *A practical recipe for stable isotope labeling by amino acids in cell culture (SILAC)*. Nat Protoc, 2006. **1**(6): p. 2650-60.
 142. Guilak, F., J.R. Tedrow, and R. Burgkart, *Viscoelastic properties of the cell nucleus*. Biochem Biophys Res Commun, 2000. **269**(3): p. 781-6.
 143. Guo, M., et al., *Probing the stochastic, motor-driven properties of the cytoplasm using force spectrum microscopy*. Cell, 2014. **158**(4): p. 822-32.
 144. Grevesse, T., et al., *Opposite rheological properties of neuronal microcompartments predict axonal vulnerability in brain injury*. Sci Rep, 2015. **5**: p. 9475.
 145. Munder, M.C., et al., *A pH-driven transition of the cytoplasm from a fluid- to a solid-like state promotes entry into dormancy*. Elife, 2016. **5**.
 146. Ashkin, A., *Acceleration and Trapping of Particles by Radiation Pressure*. Physical Review Letters, 1970. **24**(4): p. 156-&.
 147. Ashkin, A., *Forces of a single-beam gradient laser trap on a dielectric sphere in the ray optics regime*. Biophys J, 1992. **61**(2): p. 569-82.
 148. Mazolli, A., P.A.M. Neto, and H.M. Nussenzveig, *Theory of trapping forces in optical tweezers*. Proceedings of the Royal Society a-Mathematical Physical and Engineering Sciences, 2003. **459**(2040): p. 3021-3041.
 149. Hendricks, A.G., E.L. Holzbaur, and Y.E. Goldman, *Force measurements on cargoes in living cells reveal collective dynamics of microtubule motors*. Proc Natl Acad Sci U S A, 2012. **109**(45): p. 18447-52.
 150. Sarshar, M., W.T. Wong, and B. Anvari, *Comparative study of methods to*

- calibrate the stiffness of a single-beam gradient-force optical tweezers over various laser trapping powers.* J Biomed Opt, 2014. **19**(11): p. 115001.
151. Mason, T.G. and D.A. Weitz, *Optical measurements of frequency-dependent linear viscoelastic moduli of complex fluids.* Phys Rev Lett, 1995. **74**(7): p. 1250-1253.
 152. Muzzey, D., et al., *A systems-level analysis of perfect adaptation in yeast osmoregulation.* Cell, 2009. **138**(1): p. 160-71.
 153. Saito, H. and F. Posas, *Response to hyperosmotic stress.* Genetics, 2012. **192**(2): p. 289-318.
 154. Bodenmiller, B., et al., *Phosphoproteomic analysis reveals interconnected system-wide responses to perturbations of kinases and phosphatases in yeast.* Sci Signal, 2010. **3**(153): p. rs4.
 155. Breitkreutz, A., et al., *A global protein kinase and phosphatase interaction network in yeast.* Science, 2010. **328**(5981): p. 1043-6.
 156. Levy, E.D., C.R. Landry, and S.W. Michnick, *Cell signaling. Signaling through cooperation.* Science, 2010. **328**(5981): p. 983-4.
 157. Zheng, Y., et al., *Temporal regulation of EGF signalling networks by the scaffold protein Shc1.* Nature, 2013. **499**(7457): p. 166-71.
 158. Scott, J.D. and T. Pawson, *Cell signaling in space and time: where proteins come together and when they're apart.* Science, 2009. **326**(5957): p. 1220-4.
 159. Bhattacharyya, R.P., et al., *Domains, motifs, and scaffolds: the role of modular interactions in the evolution and wiring of cell signaling circuits.* Annu Rev Biochem, 2006. **75**: p. 655-80.
 160. Gustin, M.C., et al., *MAP kinase pathways in the yeast Saccharomyces cerevisiae.* Microbiol Mol Biol Rev, 1998. **62**(4): p. 1264-300.
 161. Chen, R.E. and J. Thorner, *Function and regulation in MAPK signaling pathways: lessons learned from the yeast Saccharomyces cerevisiae.* Biochim Biophys Acta, 2007. **1773**(8): p. 1311-40.
 162. Hersen, P., et al., *Signal processing by the HOG MAP kinase pathway.* Proc Natl Acad Sci U S A, 2008. **105**(20): p. 7165-70.
 163. Harsha, H.C., H. Molina, and A. Pandey, *Quantitative proteomics using stable isotope labeling with amino acids in cell culture.* Nat Protoc, 2008. **3**(3): p. 505-16.
 164. Willbrand, K., et al., *Identifying genes from up-down properties of microarray expression series.* Bioinformatics, 2005. **21**(20): p. 3859-64.
 165. Macia, J., et al., *Dynamic signaling in the Hog1 MAPK pathway relies on high basal signal transduction.* Sci Signal, 2009. **2**(63): p. ra13.
 166. Bilsland-Marchesan, E., et al., *Rck2 kinase is a substrate for the osmotic stress-activated mitogen-activated protein kinase Hog1.* Mol Cell Biol, 2000. **20**(11): p. 3887-95.
 167. Teige, M., et al., *Rck2, a member of the calmodulin-protein kinase family, links protein synthesis to high osmolarity MAP kinase signaling in budding yeast.* Proc Natl Acad Sci U S A, 2001. **98**(10): p. 5625-30.
 168. Proft, M. and K. Struhl, *Hog1 kinase converts the Sko1-Cyc8-Tup1 repressor complex into an activator that recruits SAGA and SWI/SNF in response to osmotic stress.* Mol Cell, 2002. **9**(6): p. 1307-17.

169. Lee, Y.J., et al., *Reciprocal phosphorylation of yeast glycerol-3-phosphate dehydrogenases in adaptation to distinct types of stress*. Mol Cell Biol, 2012. **32**(22): p. 4705-17.
170. Vaga, S., et al., *Phosphoproteomic analyses reveal novel cross-modulation mechanisms between two signaling pathways in yeast*. Mol Syst Biol, 2014. **10**(12): p. 767.
171. Yuzyuk, T., M. Foehr, and D.C. Amberg, *The MEK kinase Ssk2p promotes actin cytoskeleton recovery after osmotic stress*. Mol Biol Cell, 2002. **13**(8): p. 2869-80.
172. Yuzyuk, T. and D.C. Amberg, *Actin recovery and bud emergence in osmotically stressed cells requires the conserved actin interacting mitogen-activated protein kinase kinase kinase Ssk2p/MTK1 and the scaffold protein Spa2p*. Mol Biol Cell, 2003. **14**(7): p. 3013-26.
173. Bettinger, B.T., M.G. Clark, and D.C. Amberg, *Requirement for the polarisome and formin function in Ssk2p-mediated actin recovery from osmotic stress in Saccharomyces cerevisiae*. Genetics, 2007. **175**(4): p. 1637-48.
174. Reiter, W., et al., *Yeast protein phosphatase 2A-Cdc55 regulates the transcriptional response to hyperosmolarity stress by regulating Msn2 and Msn4 chromatin recruitment*. Mol Cell Biol, 2013. **33**(5): p. 1057-72.
175. Reiser, V., H. Ruis, and G. Ammerer, *Kinase activity-dependent nuclear export opposes stress-induced nuclear accumulation and retention of Hog1 mitogen-activated protein kinase in the budding yeast Saccharomyces cerevisiae*. Mol Biol Cell, 1999. **10**(4): p. 1147-61.
176. Rep, M., et al., *Osmotic stress-induced gene expression in Saccharomyces cerevisiae requires Msn1p and the novel nuclear factor Hot1p*. Mol Cell Biol, 1999. **19**(8): p. 5474-85.
177. Mattison, C.P. and I.M. Ota, *Two protein tyrosine phosphatases, Ptp2 and Ptp3, modulate the subcellular localization of the Hog1 MAP kinase in yeast*. Genes Dev, 2000. **14**(10): p. 1229-35.
178. Sharrocks, A.D., S.H. Yang, and A. Galanis, *Docking domains and substrate-specificity determination for MAP kinases*. Trends Biochem Sci, 2000. **25**(9): p. 448-53.
179. Lee, J., et al., *MAPK Hog1 closes the S. cerevisiae glycerol channel Fps1 by phosphorylating and displacing its positive regulators*. Genes Dev, 2013. **27**(23): p. 2590-601.
180. Tay, S., et al., *Single-cell NF-kappaB dynamics reveal digital activation and analogue information processing*. Nature, 2010. **466**(7303): p. 267-71.
181. Chou, M.F. and D. Schwartz, *Biological sequence motif discovery using motif-x*. Curr Protoc Bioinformatics, 2011. **Chapter 13**: p. Unit 13 15-24.
182. Schwartz, D. and S.P. Gygi, *An iterative statistical approach to the identification of protein phosphorylation motifs from large-scale data sets*. Nat Biotechnol, 2005. **23**(11): p. 1391-8.
183. Linding, R., et al., *Systematic discovery of in vivo phosphorylation networks*. Cell, 2007. **129**(7): p. 1415-26.
184. Mok, J., et al., *Deciphering protein kinase specificity through large-scale analysis of yeast phosphorylation site motifs*. Sci Signal, 2010. **3**(109): p. ra12.

185. Manning, G., et al., *Evolution of protein kinase signaling from yeast to man*. Trends Biochem Sci, 2002. **27**(10): p. 514-20.
186. Soufi, B., et al., *Global analysis of the yeast osmotic stress response by quantitative proteomics*. Molecular BioSystems, 2009. **5**(11): p. 1337-1346.
187. Bennetzen, M.V., et al., *PhosphoSiteAnalyzer: a bioinformatic platform for deciphering phospho proteomes using kinase predictions retrieved from NetworkKIN*. J Proteome Res, 2012. **11**(6): p. 3480-6.
188. Linding, R., et al., *NetworkKIN: a resource for exploring cellular phosphorylation networks*. Nucleic Acids Res, 2008. **36**(Database issue): p. D695-9.
189. Nguyen Ba, A.N. and A.M. Moses, *Evolution of characterized phosphorylation sites in budding yeast*. Mol Biol Evol, 2010. **27**(9): p. 2027-37.
190. Ho, C.H., et al., *A molecular barcoded yeast ORF library enables mode-of-action analysis of bioactive compounds*. Nat Biotechnol, 2009. **27**(4): p. 369-77.
191. Chowdhury, S., K.W. Smith, and M.C. Gustin, *Osmotic stress and the yeast cytoskeleton: phenotype-specific suppression of an actin mutation*. J Cell Biol, 1992. **118**(3): p. 561-71.
192. Stewart, M.P., et al., *Hydrostatic pressure and the actomyosin cortex drive mitotic cell rounding*. Nature, 2011. **469**(7329): p. 226-30.
193. Kondo, T. and S. Hayashi, *Mitotic cell rounding accelerates epithelial invagination*. Nature, 2013. **494**(7435): p. 125-9.
194. Lancaster, O.M., et al., *Mitotic rounding alters cell geometry to ensure efficient bipolar spindle formation*. Dev Cell, 2013. **25**(3): p. 270-83.
195. Michelot, A., et al., *Actin filament elongation in Arp2/3-derived networks is controlled by three distinct mechanisms*. Dev Cell, 2013. **24**(2): p. 182-95.
196. Reider, A., et al., *Syp1 is a conserved endocytic adaptor that contains domains involved in cargo selection and membrane tubulation*. EMBO J, 2009. **28**(20): p. 3103-16.
197. Qiu, W., et al., *A novel septin-associated protein, Syp1p, is required for normal cell cycle-dependent septin cytoskeleton dynamics in yeast*. Genetics, 2008. **180**(3): p. 1445-57.
198. Stimpson, H.E., et al., *Early-arriving Syp1p and Ede1p function in endocytic site placement and formation in budding yeast*. Mol Biol Cell, 2009. **20**(22): p. 4640-51.
199. Moseley, J.B. and B.L. Goode, *Differential activities and regulation of Saccharomyces cerevisiae formin proteins Bni1 and Bnr1 by Bud6*. J Biol Chem, 2005. **280**(30): p. 28023-33.
200. McClelland, M.L., et al., *The highly conserved Ndc80 complex is required for kinetochore assembly, chromosome congression, and spindle checkpoint activity*. Genes Dev, 2003. **17**(1): p. 101-14.
201. Richardson, H., et al., *Cyclin-B homologs in Saccharomyces cerevisiae function in S phase and in G2*. Genes Dev, 1992. **6**(11): p. 2021-34.
202. Irminger-Finger, I. and N. Mathis, *Effect of microtubule-associated protein MHP1 on microtubule assembly and cell cycle progression in Saccharomyces cerevisiae*. Cell Struct Funct, 1998. **23**(4): p. 209-19.
203. Al-Bassam, J., et al., *Stu2p binds tubulin and undergoes an open-to-closed*

- conformational change*. J Cell Biol, 2006. **172**(7): p. 1009-22.
204. Blake-Hodek, K.A., L. Cassimeris, and T.C. Huffaker, *Regulation of microtubule dynamics by Bim1 and Bik1, the budding yeast members of the EB1 and CLIP-170 families of plus-end tracking proteins*. Mol Biol Cell, 2010. **21**(12): p. 2013-23.
 205. Zimniak, T., et al., *Phosphoregulation of the budding yeast EB1 homologue Bim1p by Aurora/Ipl1p*. J Cell Biol, 2009. **186**(3): p. 379-91.
 206. Ideker, T. and N.J. Krogan, *Differential network biology*. Molecular Systems Biology, 2012. **8**: p. 565.
 207. Lynch, M., *The evolution of genetic networks by non-adaptive processes*. Nat Rev Genet, 2007. **8**(10): p. 803-13.
 208. Olsen, J.V., et al., *Global, in vivo, and site-specific phosphorylation dynamics in signaling networks*. Cell, 2006. **127**(3): p. 635-648.
 209. Tawfik, D.S., *Messy biology and the origins of evolutionary innovations*. Nat Chem Biol, 2010. **6**(10): p. 692-6.
 210. Moses, A.M. and C.R. Landry, *Moving from transcriptional to phospho-evolution: generalizing regulatory evolution?* Trends Genet, 2010. **26**(11): p. 462-7.
 211. Martins, B.M. and P.S. Swain, *Trade-offs and constraints in allosteric sensing*. PLoS Comput Biol, 2011. **7**(11): p. e1002261.
 212. Landry, C.R., *Cell biology. A cellular roadmap for the plant kingdom*. Science, 2011. **333**(6042): p. 532-3.
 213. Wu, R., et al., *A large-scale method to measure absolute protein phosphorylation stoichiometries*. Nat Methods, 2011. **8**(8): p. 677-83.
 214. Kanshin, E., S.W. Michnick, and P. Thibault, *Displacement of N/Q-rich peptides on TiO2 beads enhances the depth and coverage of yeast phosphoproteome analyses*. J Proteome Res, 2013. **12**(6): p. 2905-13.
 215. Rappsilber, J., Y. Ishihama, and M. Mann, *Stop and go extraction tips for matrix-assisted laser desorption/ionization, nanoelectrospray, and LC/MS sample pretreatment in proteomics*. Anal Chem, 2003. **75**(3): p. 663-70.
 216. Ishihama, Y., J. Rappsilber, and M. Mann, *Modular stop and go extraction tips with stacked disks for parallel and multidimensional Peptide fractionation in proteomics*. J Proteome Res, 2006. **5**(4): p. 988-94.
 217. Cox, J., A. Michalski, and M. Mann, *Software lock mass by two-dimensional minimization of peptide mass errors*. J Am Soc Mass Spectrom, 2011. **22**(8): p. 1373-80.
 218. Futschik, M.E. and B. Carlisle, *Noise-robust soft clustering of gene expression time-course data*. J Bioinform Comput Biol, 2005. **3**(4): p. 965-88.
 219. Nock, R. and F. Nielsen, *On weighting clustering*. IEEE Trans Pattern Anal Mach Intell, 2006. **28**(8): p. 1223-35.
 220. Kumar, L. and M.E. Futschik, *Mfuzz: a software package for soft clustering of microarray data*. Bioinformatics, 2007. **2**(1): p. 5-7.
 221. Schwammle, V. and O.N. Jensen, *A simple and fast method to determine the parameters for fuzzy c-means cluster analysis*. Bioinformatics, 2010. **26**(22): p. 2841-8.
 222. Huang da, W., B.T. Sherman, and R.A. Lempicki, *Systematic and integrative*

- analysis of large gene lists using DAVID bioinformatics resources*. Nat Protoc, 2009. **4**(1): p. 44-57.
223. Huang da, W., B.T. Sherman, and R.A. Lempicki, *Bioinformatics enrichment tools: paths toward the comprehensive functional analysis of large gene lists*. Nucleic Acids Res, 2009. **37**(1): p. 1-13.
 224. Franceschini, A., et al., *STRING v9.1: protein-protein interaction networks, with increased coverage and integration*. Nucleic Acids Res, 2013. **41**(Database issue): p. D808-15.
 225. Shannon, P., et al., *Cytoscape: a software environment for integrated models of biomolecular interaction networks*. Genome Res, 2003. **13**(11): p. 2498-504.
 226. Cline, M.S., et al., *Integration of biological networks and gene expression data using Cytoscape*. Nat Protoc, 2007. **2**(10): p. 2366-82.
 227. Smoot, M.E., et al., *Cytoscape 2.8: new features for data integration and network visualization*. Bioinformatics, 2011. **27**(3): p. 431-2.
 228. Breitkreutz, B.J., C. Stark, and M. Tyers, *The GRID: the General Repository for Interaction Datasets*. Genome Biol, 2003. **4**(3): p. R23.
 229. Chatr-Aryamontri, A., et al., *The BioGRID interaction database: 2013 update*. Nucleic Acids Res, 2013. **41**(Database issue): p. D816-23.
 230. Beltrao, P., et al., *Systematic functional prioritization of protein posttranslational modifications*. Cell, 2012. **150**(2): p. 413-25.
 231. Ye, J., et al., *Primer-BLAST: a tool to design target-specific primers for polymerase chain reaction*. BMC Bioinformatics, 2012. **13**: p. 134.
 232. Malleshaiah, M.K., et al., *The scaffold protein Ste5 directly controls a switch-like mating decision in yeast*. Nature, 2010. **465**(7294): p. 101-5.
 233. Sheff, M.A. and K.S. Thorn, *Optimized cassettes for fluorescent protein tagging in Saccharomyces cerevisiae*. Yeast, 2004. **21**(8): p. 661-70.
 234. Xue, B., et al., *PONDR-FIT: a meta-predictor of intrinsically disordered amino acids*. Biochim Biophys Acta, 2010. **1804**(4): p. 996-1010.
 235. Cherry, J.M., et al., *Saccharomyces Genome Database: the genomics resource of budding yeast*. Nucleic Acids Res, 2012. **40**(Database issue): p. D700-5.
 236. Kaksonen, M., C.P. Toret, and D.G. Drubin, *A modular design for the clathrin- and actin-mediated endocytosis machinery*. Cell, 2005. **123**(2): p. 305-20.
 237. Holehouse, A.S., et al., *CIDER: Classification of Intrinsically Disordered Ensemble Regions*. Biophys. J., 2015. **108**(2).
 238. Pollard, T.D. and J.A. Cooper, *Actin, a central player in cell shape and movement*. Science, 2009. **326**(5957): p. 1208-12.
 239. Haviv, L., et al., *A cytoskeletal demolition worker: myosin II acts as an actin depolymerization agent*. J Mol Biol, 2008. **375**(2): p. 325-30.
 240. Meshcheryakov, A., E. Steudle, and E. Komor, *Gradients of turgor, osmotic pressure, and water potential in the cortex of the hypocotyl of growing ricinus seedlings : effects of the supply of water from the xylem and of solutes from the Phloem*. Plant Physiol, 1992. **98**(3): p. 840-52.
 241. Harold, F.M., *To shape a cell: an inquiry into the causes of morphogenesis of microorganisms*. Microbiol Rev, 1990. **54**(4): p. 381-431.
 242. Boulant, S., et al., *Actin dynamics counteract membrane tension during*

- clathrin-mediated endocytosis*. Nat Cell Biol, 2011. **13**(9): p. 1124-31.
243. Li, D., et al., *Extended-resolution structured illumination imaging of endocytic and cytoskeletal dynamics*. Science (New York, NY), 2015.
 244. Avinoam, O., et al., *ENDOCYTOSIS. Endocytic sites mature by continuous bending and remodeling of the clathrin coat*. Science, 2015. **348**(6241): p. 1369-72.
 245. Drubin, D.G., et al., *Cytoskeletal networks and pathways involved in endocytosis*. Novartis Found Symp, 2005. **269**: p. 35-42; discussion 43-6, 223-30.
 246. Scher-Zagier, J.K. and A.E. Carlsson, *Local Turgor Pressure Reduction via Channel Clustering*. Biophys J, 2016. **111**(12): p. 2747-2756.
 247. Boettner, D.R., et al., *The F-BAR protein Syt1 negatively regulates WASp-Arp2/3 complex activity during endocytic patch formation*. Curr Biol, 2009. **19**(23): p. 1979-87.
 248. Hertz, H.R., *Ueber die Beruehrung elastischer Koerper (On Contact Between Elastic Bodies)*. Gesammelte Werke (Collected Works). Vol. Vol. 1. 1882, Leipzig, Germany, 1895.
 249. Johnson, K.L.K., K.;Roberts, A. D., *Surface energy and the contact of elastic solid*. Proc. R. Soc. Lond. A. , 1971. **324**: p. 301-313.
 250. Style, R.W., et al., *Surface tension and contact with soft elastic solids*. Nat Commun, 2013. **4**: p. 2728.
 251. Ewers, H., et al., *GM1 structure determines SV40-induced membrane invagination and infection*. Nat Cell Biol, 2010. **12**(1): p. 11-8; sup pp 1-12.
 252. Idrissi, F.Z., et al., *Distinct acto/myosin-I structures associate with endocytic profiles at the plasma membrane*. J Cell Biol, 2008. **180**(6): p. 1219-32.
 253. Wheeler, J.R., et al., *Distinct stages in stress granule assembly and disassembly*. Elife, 2016. **5**.
 254. Rog, O., S. Kohler, and A.F. Dernburg, *The synaptonemal complex has liquid crystalline properties and spatially regulates meiotic recombination factors*. Elife, 2017. **6**.
 255. Khurana, R., et al., *Mechanism of thioflavin T binding to amyloid fibrils*. J Struct Biol, 2005. **151**(3): p. 229-38.
 256. Watson, H.A., et al., *In vivo role for actin-regulating kinases in endocytosis and yeast epsin phosphorylation*. Mol Biol Cell, 2001. **12**(11): p. 3668-79.
 257. Godlee, C. and M. Kaksonen, *Review series: From uncertain beginnings: initiation mechanisms of clathrin-mediated endocytosis*. J Cell Biol, 2013. **203**(5): p. 717-25.
 258. Feric, M., et al., *Coexisting Liquid Phases Underlie Nucleolar Subcompartments*. Cell, 2016. **165**(7): p. 1686-97.
 259. Kendall, K., *Adhesion: molecules and mechanics*. Science, 1994. **263**(5154): p. 1720-5.
 260. Young, T., *An essay on the cohesion of fluids*. Philosophical Transactions of the Royal Society of London, 1805. **95**: p. 65-87.
 261. Dupré, A. and P. Dupré, *Théorie mécanique de la chaleur* 1869: Gauthier-Villars. 517.
 262. da Silva Pedrini, M.R., et al., *Osmoporation: a simple way to internalize*

- hydrophilic molecules into yeast*. Appl Microbiol Biotechnol, 2014. **98**(3): p. 1271-80.
263. Hendricks, A.G. and Y.E. Goldman, *Measuring Molecular Forces Using Calibrated Optical Tweezers in Living Cells*. Methods Mol Biol, 2017. **1486**: p. 537-552.
 264. Fischer, M., et al., *Active-passive calibration of optical tweezers in viscoelastic media*. Rev Sci Instrum, 2010. **81**(1): p. 015103.
 265. Cross, R., *Elastic and viscous properties of Silly Putty*. American Journal of Physics, 2012. **80**: p. 870-75.
 266. Guo, M., et al., *The role of vimentin intermediate filaments in cortical and cytoplasmic mechanics*. Biophys J, 2013. **105**(7): p. 1562-8.
 267. Sunthar, P., *Polymer Rheology*. 1 ed. Rheology of Complex Fluids, ed. J.M. Krishnan, A.P. Deshpande, and P.B. Sunil Kumar. 2010: Springer New York. 258.
 268. Guo, H., et al., *Entanglement-controlled subdiffusion of nanoparticles within concentrated polymer solutions*. Phys Rev Lett, 2012. **109**(5): p. 055901.
 269. Lieleg, O., et al., *Cytoskeletal polymer networks: viscoelastic properties are determined by the microscopic interaction potential of cross-links*. Biophys J, 2009. **96**(11): p. 4725-32.
 270. Broedersz, C.P., et al., *Cross-link-governed dynamics of biopolymer networks*. Phys Rev Lett, 2010. **105**(23): p. 238101.
 271. Dooling, L.J., et al., *Programming Molecular Association and Viscoelastic Behavior in Protein Networks*. Adv Mater, 2016. **28**(23): p. 4651-7.
 272. Koenderink, G.H., et al., *High-frequency stress relaxation in semiflexible polymer solutions and networks*. Phys Rev Lett, 2006. **96**(13): p. 138307.
 273. Mahadevi, A.S. and G.N. Sastry, *Cooperativity in Noncovalent Interactions*. Chem Rev, 2016. **116**(5): p. 2775-825.
 274. Busch, D.J., et al., *Intrinsically disordered proteins drive membrane curvature*. Nat Commun, 2015. **6**: p. 7875.
 275. Pietrosevoli, N., R. Pancsa, and P. Tompa, *Structural disorder provides increased adaptability for vesicle trafficking pathways*. PLoS Comput Biol, 2013. **9**(7): p. e1003144.
 276. Foty, R.A., et al., *Surface tensions of embryonic tissues predict their mutual envelopment behavior*. Development, 1996. **122**(5): p. 1611-20.
 277. Tallinen, T., et al., *On the growth and form of cortical convolutions*. Nature Physics, 2016. **12**: p. 588–593.
 278. Gupta, K., et al., *The role of interfacial lipids in stabilizing membrane protein oligomers*. Nature, 2017. **541**(7637): p. 421-424.
 279. Huh, W.K., et al., *Global analysis of protein localization in budding yeast*. Nature, 2003. **425**(6959): p. 686-91.
 280. Dill, K.A. and S. Bromberg, *Molecular driving forces : statistical thermodynamics in biology, chemistry, physics, and nanoscience*. 2nd ed. 2011, London ; New York: Garland Science. xx, 756 p.
 281. Ford, M.G., et al., *Curvature of clathrin-coated pits driven by epsin*. Nature, 2002. **419**(6905): p. 361-6.
 282. Youn, J.Y., et al., *Dissecting BAR domain function in the yeast Amphiphysins*

- Rvs161 and Rvs167 during endocytosis*. Mol Biol Cell, 2010. **21**(17): p. 3054-69.
283. French, J.B., et al., *Hsp70/Hsp90 chaperone machinery is involved in the assembly of the purinosome*. Proceedings of the National Academy of Sciences, 2013. **110**(7): p. 2528-2533.
 284. Gleisner, M., et al., *Epsin N-terminal Homology Domain (ENTH) Activity as a Function of Membrane Tension*. J Biol Chem, 2016. **291**(38): p. 19953-61.
 285. Derganc, J. and A. Copic, *Membrane bending by protein crowding is affected by protein lateral confinement*. Biochim Biophys Acta, 2016. **1858**(6): p. 1152-9.
 286. Helfrich, W., *Elastic properties of lipid bilayers: theory and possible experiments*. Z Naturforsch C, 1973. **28**(11): p. 693-703.
 287. Harmandaris, V.A. and M. Deserno, *A novel method for measuring the bending rigidity of model lipid membranes by simulating tethers*. J Chem Phys, 2006. **125**(20): p. 204905.
 288. Zhang, W., et al., *Tuning the Poisson's Ratio of Biomaterials for Investigating Cellular Response*. Adv Funct Mater, 2013. **23**(25): p. 3226-3232.
 289. Roman, B. and J. Bico, *Elasto-capillarity: deforming an elastic structure with a liquid droplet*. J Phys Condens Matter, 2010. **22**(49): p. 493101.
 290. Chang, H.C., et al., *Hsc70 is required for endocytosis and clathrin function in Drosophila*. J Cell Biol, 2002. **159**(3): p. 477-87.
 291. Yu, A., et al., *Protein aggregation can inhibit clathrin-mediated endocytosis by chaperone competition*. Proceedings of the National Academy of Sciences of the United States of America, 2014. **111**(15): p. E1481-90.
 292. Bhattacharyya, N.P., M. Banerjee, and P. Majumder, *Huntington's disease: roles of huntingtin-interacting protein 1 (HIP-1) and its molecular partner HIPPI in the regulation of apoptosis and transcription*. FEBS J, 2008. **275**(17): p. 4271-9.
 293. Wu, F. and P.J. Yao, *Clathrin-mediated endocytosis and Alzheimer's disease: an update*. Ageing Res Rev, 2009. **8**(3): p. 147-9.
 294. Bradford, M.K., K. Whitworth, and B. Wendland, *Pan1 regulates transitions between stages of clathrin-mediated endocytosis*. Mol Biol Cell, 2015. **26**(7): p. 1371-85.
 295. Sun, Y., et al., *A Pan1/End3/Sla1 complex links Arp2/3-mediated actin assembly to sites of clathrin-mediated endocytosis*. Mol Biol Cell, 2015. **26**(21): p. 3841-56.
 296. Alberts, B., *The cell as a collection of protein machines: preparing the next generation of molecular biologists*. Cell, 1998. **92**(3): p. 291-4.
 297. Alberts, B., *Cell biology: the endless frontier*. Mol Biol Cell, 2010. **21**(22): p. 3785.
 298. Collins, S.R., et al., *Toward a comprehensive atlas of the physical interactome of Saccharomyces cerevisiae*. Mol Cell Proteomics, 2007. **6**(3): p. 439-50.
 299. Gavin, A.C., et al., *Proteome survey reveals modularity of the yeast cell machinery*. Nature, 2006. **440**(7084): p. 631-6.
 300. Gavin, A.C., et al., *Functional organization of the yeast proteome by systematic analysis of protein complexes*. Nature, 2002. **415**(6868): p. 141-7.

301. Hein, M.Y., et al., *A Human Interactome in Three Quantitative Dimensions Organized by Stoichiometries and Abundances*. Cell, 2015. **163**(3): p. 712-723.
302. Ho, Y., et al., *Systematic identification of protein complexes in Saccharomyces cerevisiae by mass spectrometry*. Nature, 2002. **415**(6868): p. 180-3.
303. Krogan, N.J., et al., *Global landscape of protein complexes in the yeast Saccharomyces cerevisiae*. Nature, 2006. **440**(7084): p. 637-643.
304. Jain, S., et al., *ATPase-Modulated Stress Granules Contain a Diverse Proteome and Substructure*. Cell, 2016. **164**(3): p. 487-498.
305. Buxbaum, A.R., B. Wu, and R.H. Singer, *Single β -actin mRNA detection in neurons reveals a mechanism for regulating its translatability*. Science (New York, NY), 2014. **343**(6169): p. 419-422.
306. Cougot, N., et al., *Dendrites of mammalian neurons contain specialized P-body-like structures that respond to neuronal activation*. Journal of Neuroscience, 2008. **28**(51): p. 13793-13804.
307. Park, H.Y., et al., *Visualization of Dynamics of Single Endogenous mRNA Labeled in Live Mouse*. Science (New York, NY), 2014. **343**(6169): p. 422-424.
308. Malinovska, L., et al., *Dictyostelium discoideum has a highly Q/N-rich proteome and shows an unusual resilience to protein aggregation*. Proceedings of the National Academy of Sciences of the United States of America, 2015: p. 201504459.
309. Strzelecka, M., et al., *Coilin-dependent snRNP assembly is essential for zebrafish embryogenesis*. Nat Struct Mol Biol, 2010. **17**(4): p. 403-9.
310. Parker, R. and U. Sheth, *P Bodies and the Control of mRNA Translation and Degradation*. Molecular Cell, 2007. **25**(5): p. 635-646.
311. Ramaswami, M., J.P. Taylor, and R. Parker, *Altered Ribostasis: RNA-Protein Granules in Degenerative Disorders*. Cell, 2013. **154**(4): p. 727-736.
312. Teixeira, D. and R. Parker, *Analysis of P-body assembly in Saccharomyces cerevisiae*. Molecular biology of the cell, 2007.
313. Landau, L.D., et al., *Theory of elasticity*. 3rd English ed. Course of theoretical physics. 1986, Oxford ; New York: Pergamon Press. viii, 187 p.